SYNTHESIS OF ZINC OXIDE NANOSTRUCTURES AND THEIR APPLICATIONS AS FIELD ELECTRON EMISSION CATHODES AND PHOTOCATALYSTS

HARTINI BINTI AHMAD RAFAIE

FACULTY OF SCIENCE
UNIVERSITY OF MALAYA
KUALA LUMPUR

2016

SYNTHESIS OF ZINC OXIDE NANOSTRUCTURES AND THEIR APPLICATIONS AS FIELD ELECTRON EMISSION CATHODES AND PHOTOCATALYSTS

HARTINI BINTI AHMAD RAFAIE

THESIS SUBMITTED IN FULFILLMENT OF
THE REQUIREMENTS FOR THE DEGREE OF
DOCTOR OF PHILOSOPHY

FACULTY OF SCIENCE
UNIVERSITY OF MALAYA
KUALA LUMPUR

2016

UNIVERSITI MALAYA

ORIGINAL LITERARY WORK DECLARATION

Name of Candidate: **Hartini Ahmad Rafaie**

Registration/Matric No: **SHC120001**

Name of Degree: The Degree of Doctor of Philosophy

Title of ~~Project Paper~~/~~Research Report~~/~~Dissertation~~/Thesis ("this Work"):
SYNTHESIS OF ZINC OXIDE NANOSTRUCTURES AND THEIR APPLICATIONS AS FIELD ELECTRON EMISSION CATHODES AND PHOTOCATALYSTS

Field of Study: **Advanced Materials**

I do solemnly and sincerely declare that:

1) I am the sole author/writer of this Work;
2) This Work is original;
3) Any use of any work in which copyright exists was done by way of fair dealing and for permitted purposes and any excerpt or extract from, or reference to or reproduction of any copyright work has been disclosed expressly and sufficiently and the title of the Work and its authorship have been acknowledged in this Work;
4) I do not have any actual knowledge nor do I ought reasonably to know that the making of this work constitutes an infringement of any copyright work;
5) I hereby assign all and every rights in the copyright to this Work to the University of Malaya ("UM"), who henceforth shall be owner of the copyright in this Work and that any reproduction or use in any form or by any means whatsoever is prohibited without the written consent of UM having been first had and obtained;
6) I am fully aware that if in the course of making this Work I have infringed any copyright whether intentionally or otherwise, I may be subject to legal action or any other action as may be determined by UM.

Candidate's Signature Date

Subscribed and solemnly declared before,

Witness's Signature Date

Name:
Designation:

ABSTRACT

Pure and Fe, Al or Mg doped zinc oxide nanostructures were synthesized by the sol-gel method using conventional (HMTA) or biomaterial (*Citrus aurantifolia*(CA)) reagent as the reducing agents. The effect of substrate (Al, glass, stainless steel) using HMTA was studied. It was discovered that glass was the most efficient substrate, while stainless steel was the least efficient in terms of ZnO nanorods growth rate. This was due to the reactivity of the metallic substrates with the chemicals used during synthesis. The effect of deposition time from 0.5 hour to 4 hours showed improved crystallinity, uniformity and increase in diameter with deposition time. Doping with Fe and Al at different concentrations was verified by shifts in the XRD peak of the zinc oxide (001) diffraction plane towards smaller or higher angle and EDX analysis. Using CA as the reducing agent, growth rate was significantly affected by the solution pH. ZnO nanorods prepared at different pH values using CA. Enhanced ZnO formation was observed in neutral and alkaline compared to acidic solution. This was due to the abundance of OH- ions in non acidic solutions which promoted the formation of the $Zn(OH)_2$ intermediate species. A direct correlation between doping level and the concentration of Mg used was observed. XRD peak shiftstoward higher angleagain indicated dopingwhich was further verified using EDX. FEE properties of pure ZnO synthesized at between 0.5 and 4 hours showed marked differences due to the geometrical affect. Increase in ZnO nanorods aspect ratio for sample synthesized at longer time yielded higher field enhancement factor values while reducing the turn-on and threshold electric field values. ZnO doped with different level of Alsynthesized at constant deposition time, gave similar field enhancement values due to the similar geometrical structure of the samples. The effect of Al doping was observed in the form of reducing the turn-on and threshold electric field values. Similar effects were observed for Mg-doped ZnO samples. On the effect of AgNPs decoration on the efficiency of ZnO as photocatalysts revealed that microsized ZnO particles decorated with nanosized Ag were significantly more efficient than nanosized ZnO particles decorated with nanosized Ag. This phenomena was explain in terms of the light shield effect in the nanosized samples based on commonly accepted photocatalytic degradation of dye.

ABSTRAK

Zink oksida tulen dan yang didop (Fe, Al atau Mg) berstruktur nano telah disintesis dengan kaedah sol-gel menggunakan bahan konvensional (HMTA) atau bahan semulajadi (*Citrus aurantifolia* (CA)) sebagai agen penurunan.Kesan penggunaan substrat yang berbeza telah dikaji (Al, kaca, keluli tahan karat) menggunakan HMTA.Hasil penemuan mendapati bahawa kaca adalah substrat yang paling berkesan untuk penghasilan ZnO berstruktur rod bersaiz nano, manakala keluli tahan karat adalah sebaliknya. Ini disebabkan oleh tindak balas substrat logam dengan bahan kimia yang digunakan semasa proses sintesis. Kesan dop ZnO dengan Fe dan Al pada kepekatan yang berbeza telah dikenalpasti dengan anjakan pada puncak XRD (001) zink oksida ke arah sudut yang lebih kecil atau besar dan juga melalui analisis EDX.Kadar pembentukan ZnO dipengaruhi oleh nilai pH cecair yang disediakan.ZnO berstruktur nano berbentuk rod berbeza nilai pH telah disediakan menggunakan CA. Peningkatan pembentukan ZnO berstruktur nanorod di dalam larutan neutral dan beralkali berbanding larutan berasid. Ini adalah kerana lebihan ion OH^- dalam larutan bukan berasid membantu pembentukan spesies perantara iaitu $Zn(OH)_2$. Korelasi secara berterusan antara kadar dop dan kepekatan Mg dikaji. Puncak XRD ZnO yang di dopkan dengan Mg beranjak ke sudut yang lebih tinggi yang menunjukkan proses dop telah berlaku dan ini turut dibuktikan melalui analisis EDX. Sifat pelepasan electron (FEE) ZnO tulen yang disintesis di antara tempoh masa 0.5 dan 4 jam menunjukkan perbezaan sifat disebabkan kesan geometri ZnO. ZnO berstruktur rod bersaiz nano yang disintesis pada tempoh masa yang lebih panjang menghasilkan nilai faktor peningkatan medan elektrik yang paling tinggi. Manakala memberikan nilai *turn-on* dan *threshold*medan elektrik yang rendah.ZnO yang di dopkan dengan Al pada kepekatan yang berbeza yang disintesis pada tempoh masa yang constant memberikan nilai faktor peningkatan medan elektrik yang sama disebabkan oleh ciri geometri berstruktur nano

yang sama. ZnO yang didopkan dengan Al telah diperhatikan mempunyai kecenderungan nilai *turn-on* dan *threshold* medan elektrik yang menurun. Kesan yang sama telah diperhatikan bagi sampel ZnO yang didopkan dengan Mg. Kesan efisiensi dekorasi AgNPs terhadap ZnO sebagai fotopemangkin telah membuktikan bahawa ZnO partikel bersaiz mikro yang didekorasi dengan Ag bersaiz nano secara signifikannya lebih efisienberbanding ZnO partikel bersaiz nano yang didekorasi dengan Ag bersaiz nano. Fenomena ini menjelaskan dari segi perlindungan kesan cahaya bagi sampel bersaiz nano berdasarkan penurunan penyurutan cahaya yang biasa berlaku.

ACKNOWLEDGEMENTS

The completion of this thesis would not possible unless by the support and guidance from people around me. Truly, words are not enough to express my gratitude to all of them.

I would like to express my deepest gratitudeto my inspiring supervisor, Assoc. Prof. Dr. Roslan Md Nor for his guidance, advice, encouragement and opportunities to learn a lot of new things throughout the research.

My sincere appreciations isalso extend to Prof. Dr. Yusoff Mohd Amin. Special thanks to all of my laboratory mates: Nurul Rozullyah, Siti Shafiqah, Nor Azmina, Nurul Najua, Siti Nur Asiah, Nor Fadira for their helpful discussion, guidance and kindness and sharing knowledge as it has added to my work. Not forgetting my collaborators from the photonics laboratory; Fauzan, An, Malathy, Zuraidah and Rafis for their team work.

Special thanks to Mrs. Zurina, Mrs. Endang, Mrs. Aida Hani, Mr. Amir, and Mr. Mohammad from Physics Department, University of Malaya for their assistance in the FESEM, Micro-Raman, Photoluminescence and TEM analysis and Mr. Abdul Rahman Yusoff from the Chemistry Department, University of Malaya for assisting me in the XRD characterization.

I thank Universiti Teknologi MARA, University of Malaya and Ministry of Higher Education for the scholarship and financial support.

Last but not least, a trillion thanks to my husband, Mohd Haniff Abu Bakar, daughter, Nur Qalesya Dania Mohd Haniff, my lovely mom Hjh Halimatu Sadiah Abdul Karim, parents-in-law Abu Bakar Madin and Domiah Othman and family members, Saiful Anuar, Hazreen, Haryati, Asmawi, Syakirah, Umie Nadia, for their love, support and understanding throughout my work. All the hard work and sacrifices has finally paid off.

Hartini Ahmad Rafaie

2016

TABLE OF CONTENT

LIST OF FIGURE

Chapter 2

Chapter 3

Chapter 4

Chapter 5

LIST OF TABLE

Chapter 2

Chapter 3

Chapter 4

Chapter 5

LIST OF ABBREVIATIONS

1D	One dimension
2D	Two dimensions
3D	Three dimensions
AgNPs	Silver nanoparticle
CA	*Citrus aurantifolia*
CB	Conduction band
DI	Deionized water
EDX	Energy dispersed X-ray spectroscopy
eV	Electron volt
FEE	Field electron emission
FESEM	Field emission scanning electron microscopy
FN	Fowler Nordheim
FWHM	Full width half maximum
HMTA	hexamethylenetetramine
HRTEM	High resolution transmission electron microscopy
HT-XRD	High temperature X-ray diffraction
I-V	Current-voltage
J-E	Current density-electric field
MB	Methelyne blue
meV	Mili electron volt
NPs	Nanoparticles
PL	Photoluminescence spectroscopy
TEM	Transmission electron microscopy
UV	Ultra violet
UV-Vis	Ultra violet visible spectroscopy
VB	Valence band
XRD	X-ray diffraction

CHAPTER 1: INTRODUCTION

1.1 Introduction to Nanomaterial

Nanomaterials have attracted much attention recently due to their specific features that differed from bulk materials. Nanomaterials are commonly defined as materials which have dimensions of up to 100 nm. In practical terms, nanomaterials can be defined as materials that exhibit novel electrical, optical, chemical, mechanical and thermal properties not present in the bulk. The control and manipulation of matter within the nanometer range has the potential for the fabrication of nanoscale devices.There is a number of nanostructured materials that has been explored specifically to benefit from their various new properties. Among these are carbon nanomaterials such as carbon nanotubes and graphene, and oxide nanomaterials, for example TiO_2, ZnO, SiO_2, MgO.

Over the last few years research on nanostructured ZnO has been centred on its excellent properties such as larger thermal conductivity, large exciton binding energy at 60 meV and a band gap of 3.37 eV. A variety of potential applications such as field emission display, photocatalyst, sensors, electronic-devices and photonic-devices from nanostructured ZnO-based devices were being developed.

1.2 Synthesis of ZnO Nanomaterials

The synthesis of ZnO nanomaterials and their implementation in devices is of significant importanceand are actively studied. On the synthesis of nanostructured ZnO, attention has focused on the fabricationof different shapes of ZnO such as nanowires (Willander et al., 2009), nanorods (Ahmed et al., 2013), nanoneedles (Lee et al., 2007), nanotetrapod (Rackauskas et al., 2012) and nanoflower (Kim et al., 2012). These nanostructures are desirable for many applications, however direct fabrication of certain nanostructured shapes with controlled crystalline morphology, orientation and surface structure remains a challenge. Here, the main challenge for the realization of ZnO nanodevices is related to the development of a simple and economical method of ZnO nanomaterial synthesis. Besides, methods for large scaled fabrication of 1D nanostructured ZnO still technically difficult.(Xu et al., 2002)(Rezapour & Talebian, 2014).

Various physical and chemical deposition techniques including chemical vapor deposition (CVD), molecular beam epitaxy, pulsed laser deposition, hydrothermal and sol-gel methods have been used to synthesis nanostructured ZnO. Among these techniques, the sol-gel synthesis method has the advantages of low temperature, large scale, and economics, making it very suitable for the industrial mass production (Huang & Lin, 2008)(Mamat et al., 2010). However, insight on the growth mechanisms of ZnO nanostructures grown by sol-gel method, where the influence of synthesis parameters such as concentration of the precursor solution, growth temperature, growth time, temperature, type of substrate used are still not completely understood. Understanding of the underlying growth mechanism is essential for controlled and optimized synthesis conditions. Also, the type of precursor, solvent, reducing agent and stabilizing agent played significant role in determining the end product. Conventionally, for synthesizing ZnO nanostructures using the sol gel technique, HMTA and CTAB have been used as the reducing agent. There has been reports on the use of biomaterial such as aloe vera (Sangeetha, Rajeshwari, & Venckatesh, 2011) and lime (Samat & Nor, 2013) as the active medium in the growth solution. The main motivation of utilizing these sources was to provide green alternatives of low-cost raw materials and non-toxic ZnO-based application such as for photocatalysis and medical.

1.3 Objectives of the study

In general, from the perspective of nanostructured ZnO synthesis research, the most important challenges that have been focused in current study are:

i. An optimized and controlled growth is required to determine the specified type of nanostructures for specific applications, since the morphology and structure of ZnO is highly sensitive to the growth environment such as precursor, concentration, temperature, substrate and growth time;

ii. A simple and good technique to synthesis the aligned ZnO nanorods array. An aligned array of nanostructures will give great advantages due to their tunable electronic and optoelectronic properties; and

iii. Insufficient knowledge of ZnO growth and its mechanism.

Awareness of green technology has attracted intensive interest due to demand of a nontoxic and environmentally friendly chemical. Green technology is required that involve of methodologies, process and materials enhancement for generating a clean product and environment. Based on this, the objectives of the study reported in this thesis are summarized as follows;

i. Parametric study of ZnO nanorods synthesis by low temperature sol-gel method, including the investigation of the effect of utilizing biomaterial i.e. *Citrus aurantifolia* in the formation of ZnO nanostructures.

ii. To investigate the field electron emission properties of pure ZnO and doped ZnO nanostructures.

iii. To study the effect of AgNP decorated micro and nanostructured ZnO as photocatalysts in uv photodegradation of dye.

1.4 Scopes of study

The synthesis of pure and Al, Fe or Mg doped ZnO nanostructures were done by a low temperature sol-gel method. Investigation on the effect of parameters such as type of substrate i.e aluminum, glass and stainless steel and effect of deposition time was done.

Study on the synthesis of ZnO nanstructures using biomaterial i.e *Citrus aurantifolia* as an alternative to the conventional reducing agent by sol-gel method was also conducted. The effect of pH and doping were studied. Effect of temperature to the ZnO nanoparticles was also investigated by employed in-situ high temperature XRD measurement. The samples were analyzed using field emission scanning electron microscope (FESEM), transmission electron microscope (TEM), X-ray diffraction (XRD) and micro Raman spectroscopy to investigate the structural properties of ZnO nanostructures. Elemental identification was determined using EDX. Photoluminescence and uv-visible spectroscopy were used to determine the optical properties of ZnO nanostructures.

The potential applications of the pure ZnO and doped ZnO nanostructures for field electron emission (FEE) and photocatalysis application were studied. For FEE applications, pure ZnO and Al-doped ZnO nanorods were used as emission cathodes and the characteristic such as turn-on field, threshold field and field enhancement factor value were determined. Photocatalytic activity was evaluated by examining the degradation of methylene blue (MB) as a model for dye pollutant in water. Effects of silver nanoparticles (AgNPs) decoration on microstructured and nanostructured ZnO photocatalyst were evaluated.

1.5 Thesis organization

This thesis consists of 6 chapters. Chapter 1 provides a broad overview of the thesis that covered the background of study, problem statements, and objectives of the research and also scope of the study.

Chapter 2 consists of research background of ZnO nanostructures. The form of nanomaterials and its classification were discussed. An introduction of ZnO nanostructures was discussed including its crystal structure, physical, electrical, optical and field electron emission properties. The basic theory on Fowler-Nordhiem Theorem and past research on field electron emission from ZnO nanostructures also covered. A review on variety of low dimensional ZnO nanostructures and their synthesis method also discussed. For synthesis method, vapor phase and aqueous phase method are reviewed. In addition, a discussion on growth mediated of ZnO nanostructures by HMTA and biomaterial from previous literature also discussed. Some potential applications of ZnO nanostructures such as field electron emission and photocatalysis were briefly discussed in this thesis. In concluding Chapter 2, the growth mechanism of ZnO nanostructures was presented.

Chapter 3 covers all the synthesis method, results and discussion of ZnO nansotructures. 5 set of experiments will be discussed which are 1) the effect of substrate on the morphology and crystal structure of ZnO nanorods, 2) the effect of deposition time to the formation of aligned ZnO nanorods array, 3) the effect of iron (Fe) doped on aligned Zno nanorods array, 4) the effect of aluminum (Al) doping on ZnO nanorods and 5) Green synthesis of ZnO nanostructures using *Citrus aurantifolia*. Work on green synthesis of ZnO will cover on the pH effect, different temperature and also effect of Magnesium doping to the ZnO nanostructures.

In Chapter 4 and 5, the applications of ZnO nanostructures were described. Two applications have been done which are (i) field electron emission cathodes and (ii) photocatalysis. Field electron emission measurement was done on selected sample. While for photocatalysis, two set of experiments which are AgNPs decorated microstructures and nanostructures ZnO are discussed on photodegradation of MB dye performance. Finally, the findings were summarized in Chapter 6 and some suggestions were also presented for future work.

CHAPTER 2: LITERATURE REVIEW

2.1 Introduction

In this chapter a review on the topics relevant to the present work is presented. These include brief accounts on the properties of ZnO and methods for the synthesis of ZnO nanostructures. Applications of ZnO nanostructures as field electron emission cathodes and as photocatalyst in the degradation of dyes in waste water are also reviewed.

2.2 Forms of nanomaterials

Nanomaterials are the main enabler of nanotechnology and can be defined as materials with size in the range of approximately 1 and 100 nanometers, such that size effect led to novel properties in the nanomaterials not observed in the bulk. Novel properties such surface area, electrical conductivity, surface plasmon resonance and chemical reactivity are of great interest to basic science and industrial applications. Nanomaterial can be classified into four categories according to its dimension, namely, zero, one, two or three dimensional nanomaterials. Examples are show in Figure 2.1. Zero dimensional (0D) are quantum dots or spherical nanoparticles of radius between 1 and 100 nm. These materials exhibit novel properties such high chemical reactivity, quantum confinement and surface plasmon resonance. One dimensional (1D) are nanowires, nanotubes, and nanobelts with thickness the size of nanometers. Examples are carbon nanotubes, nanowires and nanobelts of a variety of metals and oxides. These materials have huge potentials in nanoelectronics, catalysis, field electron emission and chemical sensing. Two-dimensional (2D) are materials with bulk size surface area but nanometer sized thickness. The most well known example is the graphene sheet where the electrical properties are significantly different from its bulk counterpart, graphite.

Finally, three-dimensional (3D) are nanomaterials in the form of nanoplates and nanoflowers.

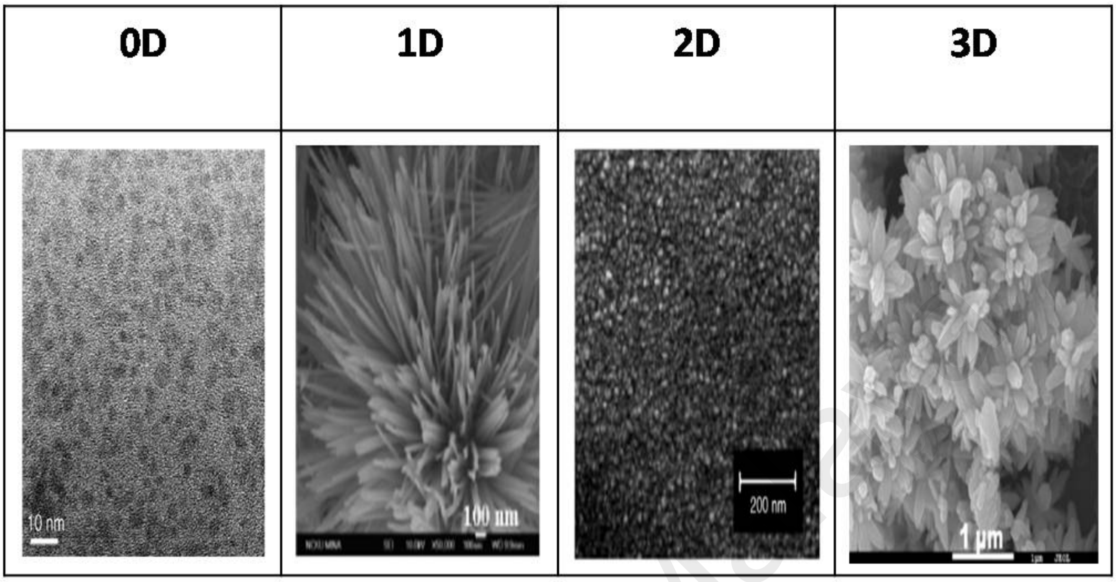

Figure 2.1: Image demonstrating nanomaterials classification.

2.3 Zinc oxide nanostructures

ZnO is a semiconductor compound which consists of zinc ion (Zn^{2+}) and oxygen ion (O^{2-}). Zinc belongs to Group II transition metal while oxygen belongs to group VI element. Being an n-type semiconducting material, together with its many useful optical, electrical and non-toxic properties, ZnO is a candidate for potential applications such as nanoelectronics devices, chemical sensors, field effect transistor materials, photocatalysts and solar cells. ZnO has extremely large exciton binding energy (60 meV) compared to 25 meV of gallium nitride (GaN), resulting in more efficient luminescence light emission (Janotti & Walle, 2009). Excitons in ZnO are thermally stable at room temperature giving it an added advantage for optoelectronic and ultraviolet laser applications.Among the 1D nanostructures, ZnO nanowires and nanorods have been widely studied because of their excellent carrier transport properties and large surface area that have potential for new generation nanodevices with high performance.

2.3.1 Crystal structure of zinc oxide

ZnO is one of the II-VI compound semiconductors which have a crystal structure of wurtzite (hexagonal symmetry), zinc blend or rock salt (cubic symmetry). Generally, ZnO is most commonly stable in the wurtzite structure. Figure 2.2 represents the schematic diagrams of three type crystal structure of ZnO.

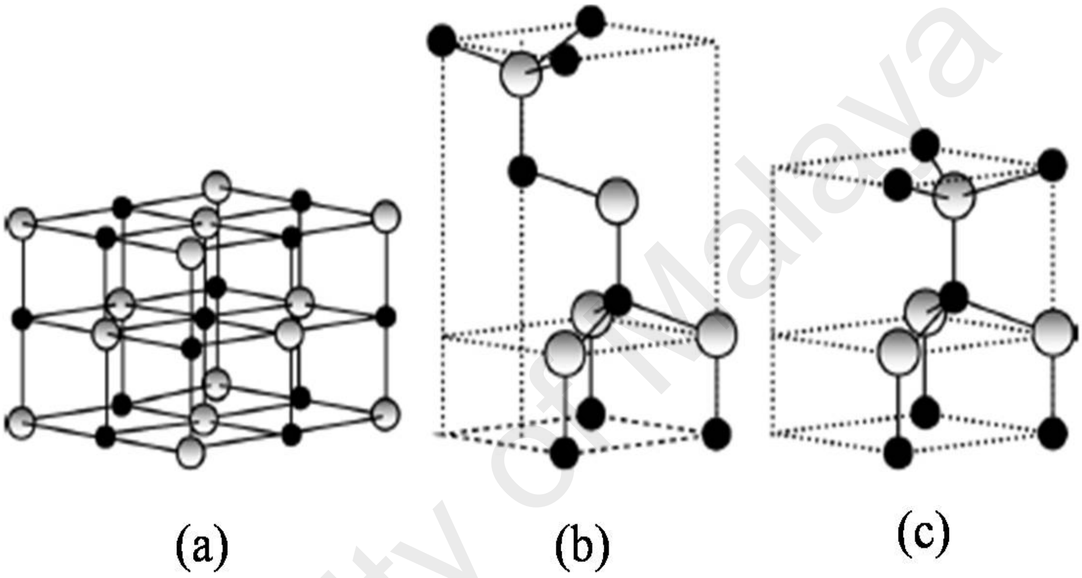

Figure 2.2: Schematic diagram of three type crystal structure of ZnO (a) cubic rocksalt, (b) cubic zinc blend and (c) hexagonal wurtzite structure. The shaded gray and black spheres denote zinc and oxygen atoms respectively (Hadis & Özgur, 2009)**.**

The wurtzite structure of ZnO has a hexagonal unit cell (space group *P63mc*) with lattice parameter ‘a’ = 0.3296 nm and ‘c’= 0.50265 nm at 300 K. Each sublattice consists of four atoms per unit cell and each atom of one kind is surrounded by four atoms of the other kind. Both zinc and oxygen atoms are tetrahedrally coordinated to each other and this coordination exhibits a positive polar symmetry along the c-axis (Al-Owais, 2013)(Liu et al., 2007). In polar ZnO crystal faces as shown in Figure 2.3, both Zn terminated (0001) and O terminated (000-1) faces are polar in nature. The other important faces in the wurtzite ZnO structure are non-polar (11-20) and (10-10).

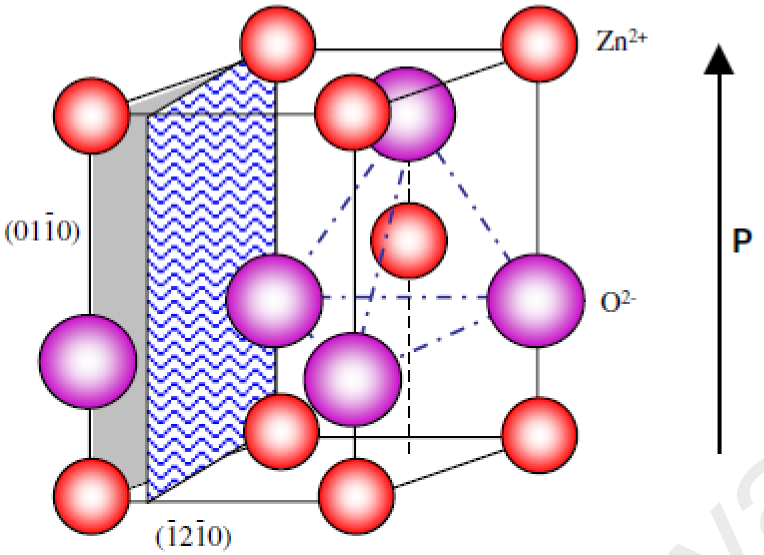

Figure 2.3: Wurtzite ZnO and its polar and non-polar surfaces (Wang, 2004).

2.3.2 Electrical properties of zinc oxide

The electrical conductivity of ZnO is due to defects created either by oxygen vacancies or zinc interstitial (Fan & Lu, 2005)(Dinesha et al., 2009) that made it an intrinsically n-type semiconductor. These defects introduce donor states in the forbidden band slightly below the conduction band resulting in the semiconducting behavior of ZnO. The electrical properties of ZnO can be modified either by doping, thermal treatment or change the thickness of the thin film. The changed of conductivity of ZnO nanostructures can be influenced by doping with Al (Qiang, Yan, & Hang, 2006), Ag (Kuo et al., 2007), Li and Mg (Liu et al., 2005).

Zhou et al. (Zhou et al., 2007) reported that the electrical conductivity of ZnO is directly related to the number of electron formed by the ionization of the interstitial zinc atom and the oxygen vacancies. In their observation, the electrical resistivity of ZnO thin films increased as the dopant concentration increased which might be due to thedecrease in mobility of carriers caused by the segregation of the dopant at the grain boundary.

Ruan et al. (Ruan et al., 2012) observed that, with increase Mn doping level, severe suppression of electron was induced. As Mn doping level increases, the electron concentration of the films decreases and the corresponding mobility is reduced. The decrease in mobility might be related to the increase in impurity scattering centers and grain boundaries of the films with higher Mn content.

The morphology and optimum surface structure of ZnO nanostructures has been shown to influence its electrical properties. Well aligned sheets, rods, or wires of ZnO may exhibit better conductivity, because of fast and effective path for electron transportation (Hong et al., 2008). Therefore, a high quality c-axis oriented ZnO nanostructures and optimum surface roughness significantly influenced the electrical properties.

2.3.3 Optical properties of zinc oxide

ZnO with its wide direct band gap (3.34 eV) and large exciton binding energy (60 meV) at room temperature, is a promising semiconductor material for the fabrication of lasers and light emitting diodes (LEDs) in the visible region. The luminescence efficiency of nanostructured ZnO is generally higher than that of films due to the reduced structural defect density in nano-sized materials. Photoluminescence (PL) spectra of ZnO nanostructures have been extensively reported. Typical ZnO PL emission bands are in the ultraviolet and visible (green, yellow, blue and violet) regions (Deus et al., 2014)(Gokarna et al., 2013). The uv emission generally resulted from the recombination of near band-edge (NBE) free exciton or the exciton combination (Zeng et al., 2013). While the visible emissions known as deep level emission (DLE) are attributed to the several defects levels due to vacancies of oxygen and zinc, interstitial oxygen and zinc, as well as other extrinsic impurities in ZnO. Table 2.1 represents a summary of the possible scheme of deep level PL transistions from ZnO (Yogamalar & Bose, 2013).

Table 2.1: Possible scheme of deep level transition in ZnO.

Emission color	Proposed deep level transition
Violet	Zn_i to VB
Blue	Zn_i to VB or CB to V_{Zn}
Green	V_o to V_{Zn}
Yellow	CB to O_i
Orange	CB to O_i or Zn_i to O_i
Red	Lattice disorder along the c-axis

In order to extend the application to broader wavelength region, the PL characteristics of ZnO nanostructures are affected by doping, size and structure (Panin et al., 2008)(Liu et al., 2009). Liu et al. (Liu et al., 2010) reported the effect of Al doping on the photoluminescence properties of ZnO nanofibers. Al-doped ZnO nanofibers were prepared by electrospinning technique with concentration of Al ranged from 0 to 5 % (mole ratio of Al/ (Zn+Al)). They observed that all photoluminescence spectra consist of two luminescence bands at green and orange region. Both bands decreased simultaneously with increasing of Al doping and this situation might be due to the inwards penetration of excess oxygen. They also reported that, the PL centers of the green and orange bands were attributed to oxygen vacancies and excess oxygen, which might be located inside the polycrystalline grains and near the grain boundaries.

Deus et al. (Deus et al., 2014) reported ZnO nanocolumns synthesized by hydrothermal method and their photoluminescence properties. The characteristic photoluminescence peaks in the blue-green emission (at 490 nm) and green emission (at 580 nm) were preported. The uv band emission was due to direct recombination of electron, while the visible emission band was suggested to be due to the points defects such as oxygen vacancies.

Mousavi et al. (Mousavi, Haratizadeh, & Minaee, 2011) examined the effect of doping and morphology on the photoluminescence of ZnO nanostructures. They suggested that the intensity of uv–green emission was affected by size. ZnO with larger structures was found to have strong uv emission than the visible emission. The PL properties of ZnO nanostructures were affected by the surface structure of ZnO itself. They also observed the enhancement of deep level emission for thinner nanostructures which was attributed to their larger surface area. Similar observation was made by Fan et al. (Fan & Lu, 2005), who reported the green emission intensity increased with decreasing nanowires diameters. According to Fan et al., larger surface-to-volume ratio of thinner nanowires caused higher of defects density and surface recombination.

2.4 Synthesis techniques of ZnO nanostructures

The synthesis of ZnO nanostructures generally has been mainly carried out by two based methods, which are vapor based method and liquidbased method. Vapor based methods are based on gaseous environment in closed chambers and usually requires high temperatures of 300 – 1500 °C for achieving better crystallinity of ZnO products . Liquid based method is a preparation of ZnO products using an aqueous or ethanol solvent and mineralizer under low temperatures typically below 100 °C.

2.4.1 Vapor-phase method

In vapor-phase synthesis of nanoparticles, conditions are created where the vapor phase mixture is thermodynamically unstable relative to formation of the solid material to be prepared in nanoparticulate form. This includes usual situation of a supersaturated vapor. It also includes what we might call ‘chemical supersaturation’ in which it is thermodynamically favorable for the vaporphase molecules to react chemically to form a condensed phase. If the degree of supersaturation is sufficient, and the reaction condensation kinetics permits, particles will nucleate homogeneously. Once nucleation occurs, remaining supersaturation can be relieved by condensation or reaction of the vapor-phase molecules on the resulting particles, and particle growth will occur rather than further nucleation (Palmqvist, 2003).

In order to control the diameter, aspect ratio, and crystallinity, diverse techniques have been exploited including chemical vapor deposition (CVD), metal organic chemical vapor deposition (MOCVD), molecular beam epitaxy (MBE), radio frequency magnetron sputtering and pulsed laser deposition.These vapor-phase growth methods are based on two mechanisms which are vapor-liquid-solid (VLS) and vapor-solid (VS).

(a) Vapor-Liquid-Solid Mechanism

The VLS mechanism is well recognized and most widely accepted among the various mechanisms for an isotropic growth of nanostructures. VLS method is a simpler and cheaper process, and is advantageous for growing ZnO on large wafers. The VLS process has been widely used for the growth of 1D nanowires and nanorods. A typical VLS process is used with nanosized liquid metal droplets as catalysts. The gaseous reactants interact with the nanosized liquid facilitating nucleation and growth of single crystalline rods and wires under the metal catalyst. Typical metal catalysts in the VLS process are Au (Song et al., 2013), Ag (Panda & Jacob, 2009) and Ni (Kim et al., 2004) prepared by CVD, spray pyrolysis, thermal evaporation (Weigand et al., 2012)(Liu & Cai, 2008)(Rajabi, Dariani, & Zad, 2011). Wagner and Ellis were proposed the VLS mechanism in 1964 to explain the growth of whisker which using Au as a metal catalyst (Wagner & Ellis,1965). Basically, VLS is a catalyst-assisted growth process which uses metal nanoclusters or nanoparticles as the nucleation seeds. These nucleation seeds determined the interfacial energy, growth direction and diameter of the nanostructure. Therefore proper choice of a catalyst is critical.

The VLS process consists primarily of three steps: (1) formation of the liquid alloy droplet, (2) crystal nucleation upon gas adsorption and supersaturation, and (3) axial growth from the crystalline seeds to form nanowires/ rods. According to the VLS mechanism, a liquid phase is formed initially, due to formation of a eutectic phase or the presence of a low melting point phase in an alloy system, which consists of the substrate or gas phase constituent. The liquid surface adsorbs the reactant gaseous species much more efficiently than does the solid surface. On supersaturation of the liquid alloy, a nucleation centre forms, and serves as a preferred site for the axial growth of nanowires/ rods. The adsorbed gas reactants are then diffuse through the liquid phase to solid/liquid interface, and the growth of the solid phase proceeds. Due to the much larger accommodation coefficient of the reactants in the liquid, growth is much faster at the solid/liquid interface compared to the solid/vapour interface (Steiner, 2004). Figure 2.4 illustrates the growth of nanowires/ rods by a VLS mechanism (Steiner, 2004).

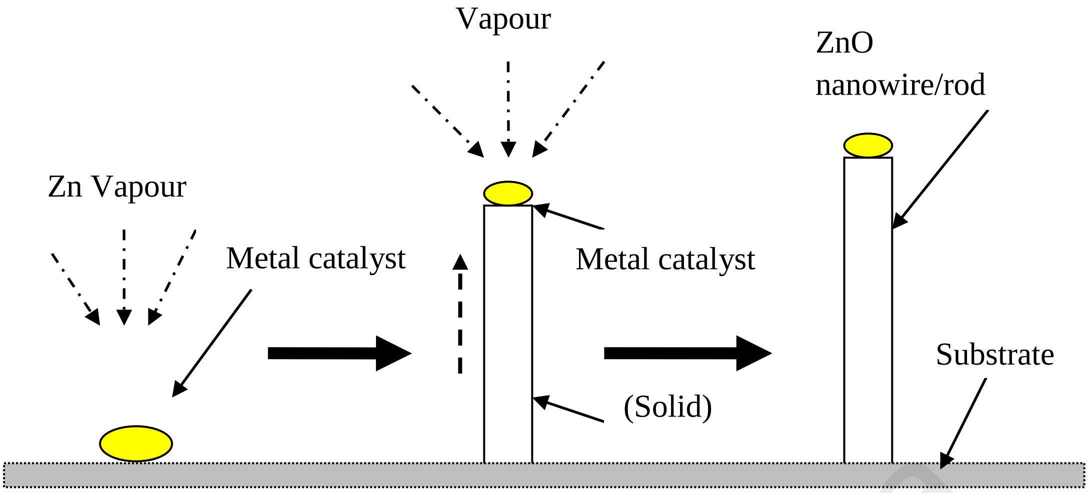

Figure 2.4: Illustration of growth of a nanowire/rod by VLS mechanism (Steiner, 2004).

(b) Vapor-Solid Mechanism

VS mechanism occurs in many catalyst-free growth processes which it also referred as evaporation-condensation process (Khan et al., 2007)(Wang et al., 2013). This process involves direct vaporization of the solid at high temperature, followed by the deposition of the nanostructures at lower temperature. The preparation method that typically involved this mechanism is thermal evaporation, CVD and rapid evaporation (Kong, Fan, & Zhu, 2012)(Wang et al., 2009)(Huang et al., 2008). The minimization of surface free energy has been proposed by several experimental and theoretical work governs by the VS process. Under high temperature condition, source materials are vaporized and then directly condensed on the substrate placed in the low temperature region. Once the condensation happens, the initially condensed molecules form seed crystal serving as the nucleation sites. As a result, they facilitate directional growth to minimize the surface energy. As shown in Figure 2.5 ZnO nanowire/ rod can grow without the presence of catalyst assisted.

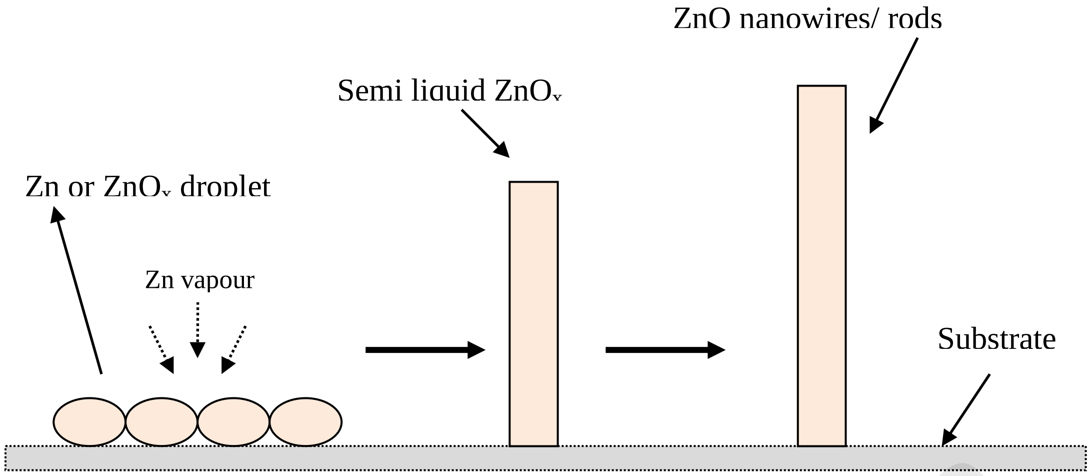

Figure 2.5: Illustration of growth of a nanowire/rod by VS mechanism (Steiner, 2004).

2.4.2 Liquid-phase method

In general, the liquid based preparation of ZnO products involves the reaction of a metal salt with hydroxide ions in water or alcohol based solvent. Compared with the vapor based method, liquid based synthesis routes have many advantages, such as low cost and non-vacuum instruments needed, convenience in handling, and easiness in composition control, making it very promising for the large-scale and environmentally benign synthesis of 1D semiconductor nanostructures (Feng et al., 2013)(Jung et al., 2013). Liquid-phase methods such as sol-gel, hydrothermal, template assisted solution method, immersion, solvothermal and chemical bath deposition has been proven successful for the reproducible growth of ZnO nanostructures with specific size and shape (Znaidi et al., 2003)(Ahmed et al., 2012)(Kai et al., 2012)(Baviskar et al., 2013). The sol-gel and hydrothermal methods are among the recognized method for the preparation of 1D ZnO nanostructures with characteristic of narrow size distribution, good crystallization, and high quality orientation.

Prabakar et al. (Prabakar & Kim, 2010) synthesized ZnO nanorod by low temperature sol-gel method by controlling the volume ratios of precursor solution. They employed 2 step processes which were seeding by dip-coated technique and grow the ZnO nanorods by immersion method. They used $Zn(NO_3)_2.6H_2O$ and hexamethylenetetramine (HMTA) as a precursor and reducing agent with concentration was set at 20 mM at different volume ratios (Zn:HMTA) of 1;1, 1:0:8, 1:0:6 and 1:0:4 at 90 °C growth temperature for 4 hours growth time. Dense and large diameters of hexagonal ZnO nanorods were formed when the volume ratio 1:1 was employed. However, reduced in density and diameter was discovered as they reduced the amount of HMTA. Figure 2.6 represent the FESEM images of obtained ZnO nanorods at different volume ratios.

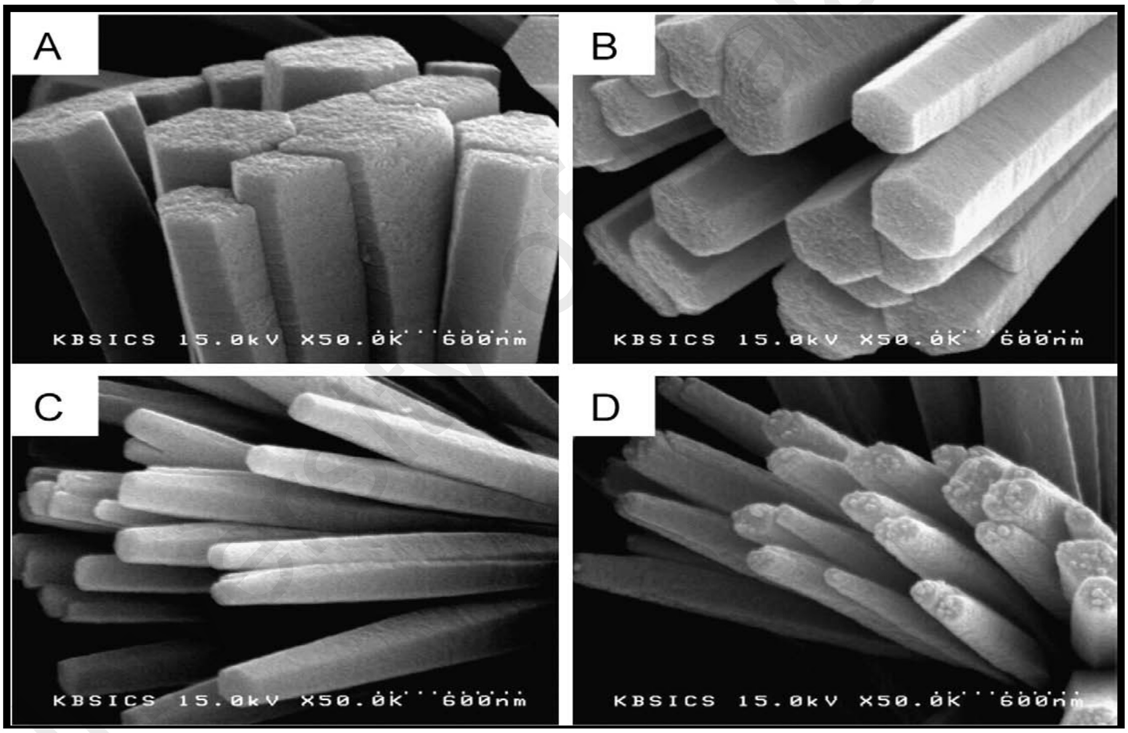

Figure 2.6: SEM images of ZnO nanorods grown at 20mM zinc nitrate and HMTA volume ratios of (A) 1:1, (B) 1:0.8, (C) 1:0.6 and (D) 1:0.8 at 90 °C for 4h (Prabakar & Kim, 2010).

Vertically aligned ZnO nanorods arrays prepared on Si substrate was reported by Jia et al. (Jia, Wang, & Yao, 2012). A simple and low temperature sol-gel combine with chemical bath deposition method was used. They employed two step processes involving seeding process by pulling process and growing the ZnO nanorods by chemical bath deposition method. The precursor solution was prepared by mixing the $Zn(CH_3COO)_2.2H_2O$ as a precursor and HMTA as a reducing agent with equimolar (1:1) concentration. The seeded substrate was immersed and suspended in the precursor solution at 90 °C for 1.5 hours. They observed that, the ZnO nanorods were aligned perpendicular to the substrate with diameter in the range 70 – 100 nm and length of about 1.5 mm (see Figure 2.7 a and b).

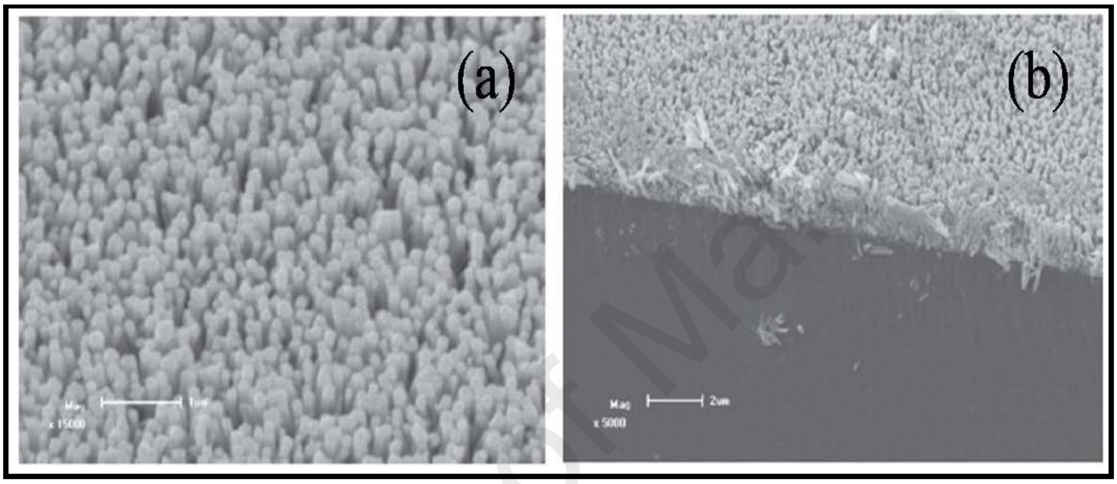

Figure 2.7: SEM image of the ZnO nanorods (a) top view image, (b) cross-sectional view (Jia et al., 2012).

Kao et al. (Kao et al., 2009) reported on fabrication of ZnO nanowires using low temperature solution-synthesis method. They dissolved $Zn(CH_3COO)_2.2H_2O$ in a water and grow at temperature of 50 °C for 24 hours. The obtained precipitate was collected and heat at 150 °C for 24 hours, followed by annealing process for about 4 hours at different annealing temperatures in the range 200 - 400 °C. As shown in Figure 2.8, the nanowires obtained were high density and distribute randomly with diameter less than 100 nm.

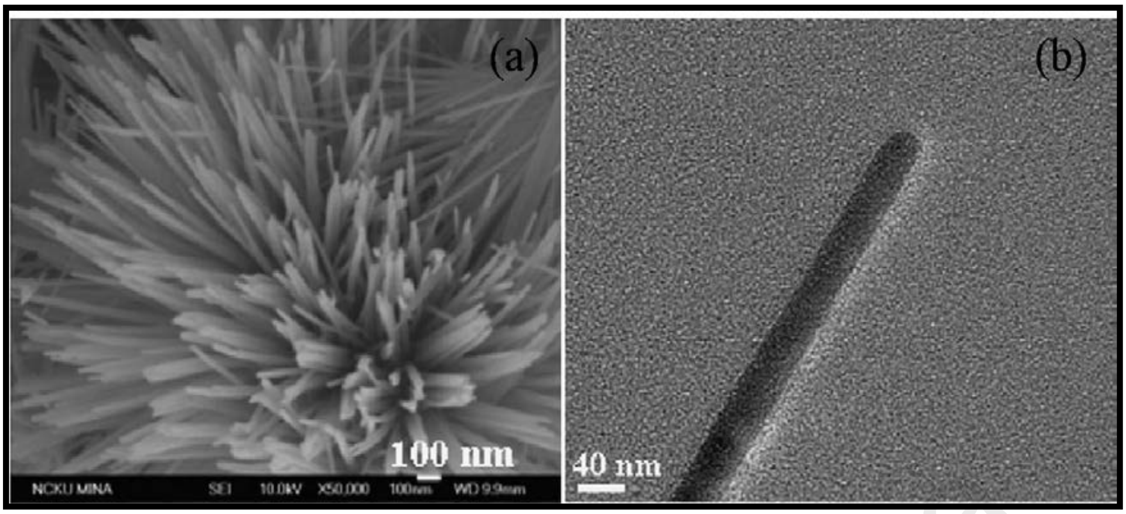

Figure 2.8: (a) FESEM and (b) TEM image of ZnO nanowires (Kao et al., 2009).

(a) Sol-gel technique and the process

Sol-gel method is a chemical synthesis technique for the fabrication of materials. In general, the sol-gel process involves the transition of a system through the formation of a colloidal suspension *(sol*) to form a network in a continuous liquid phase (*gel*). In sol-gel process, the starting material will face two types of reactions which are hydrolysis and polymerization in order to form a colloidal suspension (*sol*). Recently, due to the development of many applications and devices, sol-gel method has gain an interest as it reached its full potential for fabricating materials. In addition, the emerging of nanotechnology nowadays is one of the factor that sol-gel has become one of the promising nanomaterial synthesis technique.

Sol-gel techniques require low temperature (as low as 90 °C) and low energy during the deposition (Huang & Lin, 2008) compared to other method such as MOCVD (Zhang et al., 2004) and thermal evaporation (Kong, Fan, & Zhu, 2012). Other than that sol-gel method can be implemented for mass production and it’s suitable for commercialization as the process is cost-effective, produce high quality coatings and the process can be highly controllable (Yin, Que, & Kam, 2009)(Zhao, Li, & Lou, 2014).

A variety of processing in sol-gel method offers a variation of final product. Figure 2.9 illustrating the final product that resulted from sols but experiencing different processes. Thin films can be produced by preparing the sols on substrate either by using spin coating or dip coating method. Sols also can be extended become a wet gel by ageing process. If the ageing process is continuous until the solvent dried, the resultant product is dried gel.

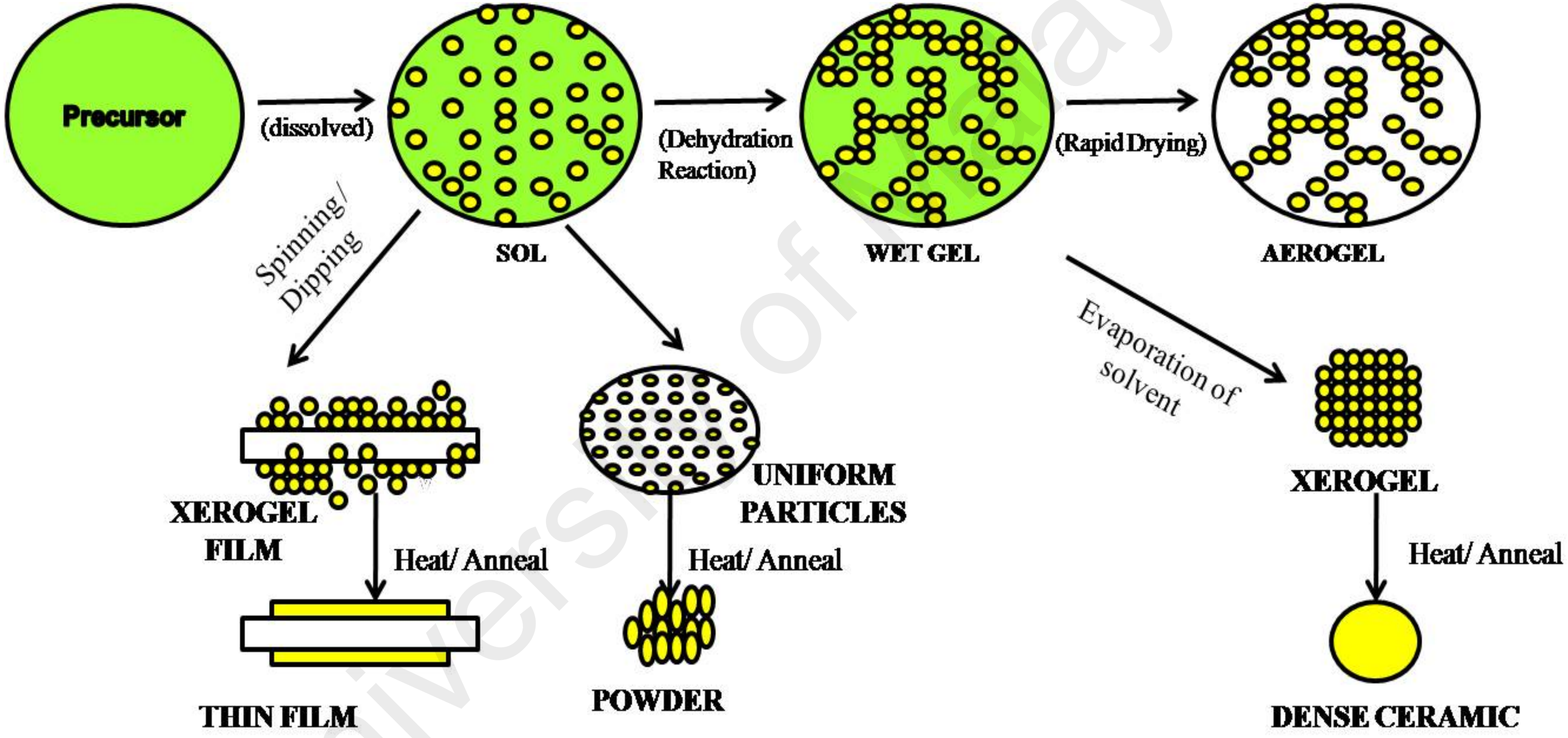

Figure 2.9: Schematic representation of different stages and routes of the sol-gel process (Brinker & Scherer, 1990).

(b) Zinc oxide nanostructures growth using HMTA aqueous solution

The most commonly used chemical agents in the existing literature for the liquid-phase chemical synthesis of ZnO nanostructures especially nanorods and nanowires are Zn nitrate, Zn acetate and HMTA (Qiu et al., 2009)(Ye & Chen, 2012). It has been reported that, the combination of these materials is an effective way to achieve high quality ZnO nanorods/ nanowires.

The molecular structure of HMTA was shown in Figure 2.10. Even though the exact role of HMTA during the ZnO nanorod/ nanowire growth is still unclear, it has been suggested that it acts as a bidentate Lewis base that coordinates and bridges two Zn^{2+} ions in a stock solution (Lopez et al., 2014)(Xu & Wang, 2011). Another significant role of HMTA during the synthesis process is it supplies the OH^{-} ions to drive the precipitation reaction by thermal degradation. HMTA also has been reported acts as a pH buffer by slowly releasing OH^{-} ions through thermal decomposition. The hydrolysis rate of HMTA is decreased with an increase in pH and vice versa. The existence of HMTA also facilitates the anisotropic growth of nanorod/ nanowire towards [0001] growth direction (Yangyang et al., 2012).

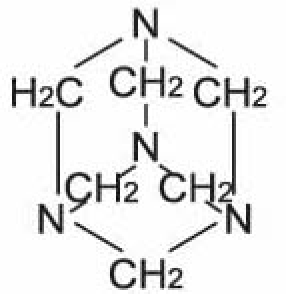

Figure 2.10: Molecular structure of HMTA.

Hsiao et al. (2013) synthesized Ga-doped ZnO nanorods on a glass substrate using hydrothermal method (Hsiao et al., 2013). Seeding method was performed at first by radio frequency (rf) magnetron sputtering using a ZnO target with 99.99% purity at room temperature. The synthesis solution was prepared by mixing zinc nitrate hexahydrate ($Zn(NO_3)_2 \cdot 6H_2O$), gallium nitrate hydrate ($Ga(NO_3)_3 \cdot xH_2O$) and HMTA. $Zn(NO_3)_2$ is the source of Zn^{2+} ions and the HMTA play a role as a pH buffer, maintaining a constant pH. They stated that, the presence of more surface defects at a lower pH reflects the presence of more H^+ ions, which absorb more OH groups and O^{2-} ions. Low growth temperature (≤ 90 °C) was conducted for the fabrication of undoped and doped ZnO nanarods (Hsiao et al., 2013). Yin et al. also used HMTA in the synthesis solution of ZnO nanorods. HMTA acts as a weak base which going through a hydrolysis process in water and releases the OH^- ion, hence maintaining the pH in mild condtion (Yin, Liu, & Liu, 2014). Tan et al. (Tan et al., 2014) demonstrated that the presence of HMTA assists the formation of rod-like structure along the c-axis. They indicate that the chelation of HMTA on the non-polar surfaces of the nanorods prevents radial growth due to inhibition of Zn^{2+} ions absorption. Moderate temperature (usually ≤ 100 °C) will cause the decomposition of HMTA to produce hydroxyl ions for the formation of ZnO. This is supported by Sugunan et al.(Sugunan et al., 2006) who suggested that HMTA acts a chelating agent that attaches to the nonpolar facet of ZnO nanorods. Due to this situation, epitaxial growth along the c-axis is facilitated because only the (0001) plane is exposed during the synthesis process**.**

The general mechanism of the sol-gel process of growing ZnO nanorods/nanowires with HMTA mediated is described by the following chemical reactions (Khusaimi et al., 2010) :

$$Zn(NO_3)_2(aq) \;+\; C_6H_{12}N_4(aq) \;+\; 4H_2O \;\leftrightarrow\; Zn(NO_3)_2(aq) \;+ \qquad (2.1)$$

$C_6H_{12}N_4H_4^{+}$ + $4OH^{-} \rightarrow [Zn(C_6H_{12}N_4]^{2+}(aq) + 2NO_3^{-}(aq)$

$$[Zn(C_6H_{12}N_4)]2+(aq) + 4OH^{-} (aq) \rightarrow Zn(OH)_4^{2-(}aq) + C_6H_{12}N_4 \quad (2.2)$$

$$Zn(OH)_4^{2-(}aq) \rightarrow Zn(OH)_2(s) + 2OH^{-}(aq) \quad (2.3)$$

$$Zn(OH)_2(s) \rightarrow ZnO\ (s) + H_2O \quad (2.4)$$

As a stabilizer, HMTA (as shown in Figure 2.11 (a)) reduce agglomeration and this process may slow down the growth and lead to formation of thinner rods.

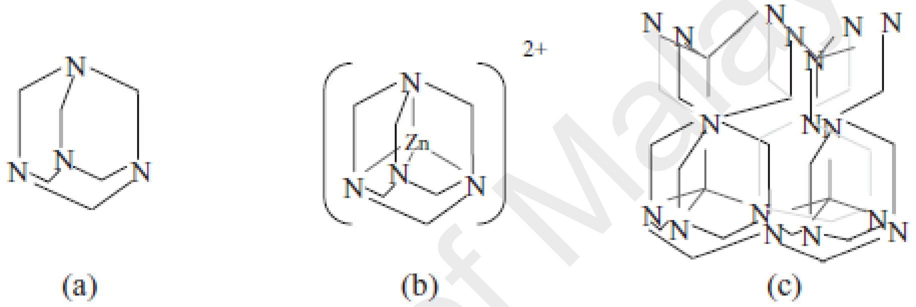

Figure 2.11: Illustrations showing structures of (a) HMTA, (b) chelation of HMTA to Zn ion complex, (c) stacking of the complexes in rod-like manner.

In solution, $Zn(NO_3)_2$ form a hexaaquazinc ion complex. As mentioned earlier, HMTA is a stronger Lewis base than water as well as tetradenate ligand. HMTA is able to displace water and chelate the Zn^{2+} ion (as shown in Figure 2.11 (b)) through the four nitrogen atoms (Equation 2.1). HMTA also acts as a source of OH- ions (Equation 2.2), which displaces the bonding with Zn-HMTA complex and form $Zn(OH)_4^{2-}$ (Equation 2.3). In hexagonal wurtzite structure of ZnO, each Zn atom is tetrahedrally surrounded by O atom and vice versa. These complexes will have intermolecular hydrogen bonding linkage and arranges itself into continuous stacking positions of rod-like structure (as shown in Figure 2.11 (c)). Heat will cause $Zn(OH)_4^{2-}$ to precipitate out as $Zn(OH)_2$ and form ZnO (Equation 2.4) upon drying (Khusaimi et al., 2010).

(c) Zinc Oxide nanostructures growth using biomaterial

Recently the awareness of green technology has attracted intensive interest due to demand of a nontoxic and environmentally friendly chemical. Green technology is an initiative evolving various kinds of methodologies, process and materials enhancement for generating a clean product and environment. The development of green technology towards green nanotechnology has attracted a great deal in nanoscience research. Since the development of the concept of green nanoparticle preparation by Raveendran et al. (Raveendran, Fu, & Wallen, 2003), there is a growing need for environmentally benign metal - nanoparticle synthesis processes that do not use toxic chemicals in the synthesis protocols to avoid adverse effects in various application especially medical. Although nanomaterials may be synthesized using chemical approaches, it is now possible to introduce and utilize the biological materials.

Utilization of plant extracts has been recognized for the ability in reducing the metal ions, although the nature process of reducing agents involved was not well understood (Mittal, Chisti, & Banerjee, 2013). Plant extracts also can act as a stabilizing agent and the source of the plant extract is known to influence the characteristics of the nanoparticles (Kumar and Yadav, 2009).

Recently, preparation of metal oxide nanoparticles particularly Ag an Au nanoparticles using environmentally benign materials using plant extracts have received attention due to its simple, economical and require a little or no maintenance. For instant, Prathna et al. (Prathna et al., 2011) reported the synthesis of silver nanoparticles by Citrus limon (lemon) aqueous extract. The Citrus limon (lemon) were used as a bioreductant and the results showed that the silver nanoparticles below 50 nm size with nearly spherical shape was produced. Khalil et al. (Khalil, Ismail, & El-Magdoub, 2012) demonstrated a biosynthesis of Au nanoparticles using olive leaf extracts as reducing agent. Characterizations showed that the Au nanoparticles formed in nanotriangle shape with diameters ranging from 50 to 100 nm. Moreover, Philip (Philip, 2010) reported a biological synthesis of gold and silver nanoparticles using the leaf extract of Hibiscus rosa sinensis. The extract acted as a reduction agent and stabilizer.Various shapes and different sizes of nanoparticles were obtained. In recent, synthesis of ZnO nanoparticles using biomaterial also was considerably getting attention from researchers. For example, Sangeetha et al. (Sangeetha et al., 2011) demonstrated the synthesis of ZnO nanoparticles using *Aloe barbadensis miller* leaf extract. The results showed that the ZnO nanoparticles were predominantly spherical in shape with average size range from 25 to 40 nm. Fu et al. (Fu & Fu, 2015) were successfully synthesized ZnO nanoparticles using leaf extract of *Plectranthus amboinicus* as a reducing agent. SEM results revealed that the ZnO nanoparticles exhibit a rod shape structure with an average size of 88 nm. Darroudi et al. (Darroudi et al., 2013) synthesized zinc oxide nanoparticles using gum tragacanth. From TEM results, the formation of ZnO nanoparticles in the size range of below 50 nm. Work done by Samat and Nor (Samat & Nor, 2013) demonstrated the synthesis of ZnO nanoparticles using *Citrus aurantifolia* as a reducing agent. In their work, spherical zinc oxide nanoparticles were produced using different concentration of zinc acetate in the size range of 50 – 200 nm.

(d) Doping of zinc oxide

Doping is the process of adding impurities to intrinsic (pure) semiconductor to alter their electrical, optical and magnetic properties. The addition of impurities may add charge carrier elements to the semiconductor. Generally, the doping process of ZnO achieved by

replacing Zn^{2+} atoms with atoms of elements which have higher valence electron such as aluminium (Srinivasan, Kumar, & Kumar, 2007), magnesium (Cetin et al., 2012), manganese (Rekha et al. , 2010) and indium (Wang et al., 2007). Controlling the doping level plays an important role in many nanotechnology applications. In addition, doping will assist increase the conductivity of the ZnO thin film or nanostructures. Electronegativity and difference between ionic radius of dopant and zinc influenced the efficiency of the dopant element (Nunes et al., 2002).

2.5 Applications of zinc oxide nanostuctures

Realising the unique behaviors and properties of ZnO nanostructures, several applications have emerged since it was discovered. ZnO forms a wide range variety of nanostructures such as nanowires, nanorods, nanotubes and nanoparticles. Due to an excellent quality and properties, tremendous efforts have been implemented to use the semiconductor ZnO nanostructures as elements in devices for instant for applications in optoelectronic, nanoelectronic and nanochemical system (Table 2.2).

Table 2.2: Important applications of ZnO nanostructures

NANOELECTRONICS	*Field emission sources *Field effect transistor *Solar cell system *Nanogenerator
OPTOELECTRONICS	*Laser diodes (LDs) *Photodetector *Optical devices, data storage *Light emitting diode (LEDs)
NANOCHEMICAL	*Photocatalysis *Chemical/Biochemical sensor

2.5.1 Field electron emission from zinc oxide nanostructures

Field electron emission (FEE) phenomenon is the process when electrons tunnel out from the surface of metal or semiconductor in vacuum when a sufficiently high electric field is applied (Bhattacharya et al., 2011). It occurs because the wave function of an electron does not vanish at the classical turning point, but decays exponentially into the barrier where the electron's total energy is less than the potential energy. Thus, there is a finite probablility that the electron will be found on the outside of the barrier. The tunneling emission current – field strength relation was modeled by Fowler and Nordheim in 1928 (Fowler & Nordheim, 1928). Under the influence of a high electric field the effective energy barrier of the metal orsemiconductor surface will be modified from an infinite square well to a triangular barrier resulting in the probability of electron tunneling to be finite.

Field emission properties of ZnO nanostructures have been investigated by many researchers due to its compatibility and usefulness as electron sources in cold cathode in flat panel display, portable x-ray, microwave generator, electron guns in SEM/TEM and vacuum microelectronic devices (Mahmood, Park, & Sung, 2013). The FEE applications of several ZnO nanostructures has been reported previously in the literature (Lin, Huang, & Lin, 2014)(Yilmazoglu et al., 2012)(Li et al., 2007) due to following properties that make ZnO favorable and potential electron field emitters application such as low electron affinity, high aspect ratio, chemical stability, and stable at high temperature (Liao et al., 2005)(Jin et al., 2009)(Zhang et al., 2013). It has been discovered that the emitter density is very critical to the emission efficiency. It is well known that CNTs has a low turn-on field of about 0.5–2 V/μm and high emission current density of about several mA/cm^2 (Ling-min et al., 2011). However, CNTs can be easily degraded in oxygen ambient even though they show good emission property as a field emitter. Therefore, a discovery on ZnO nanostructures which are more stable at high temperature in an oxygen environment and have a more controllable electronic property, have been considered more as alternative FE sources instead of CNTs.

(a) The Fowler-Nordheim model

From Schrödinger's wave theory, Fowler and Nordheim satisfactorily explained field emission as the quantum mechanical tunneling of electrons from flat metal surfaces into vacuum under the influence of the applied electric field. The Fowler-Nordheim (F-N) equation (Fowler & Nordheim, 1928), describes the relation between the emission current density J, the surface work function ϕ, and the applied electric field strength, F. Figure 2.12 shows the potential energy diagram of an electron at a distance z from the metal surface, with the applied field strength being F at the surface of the metal.

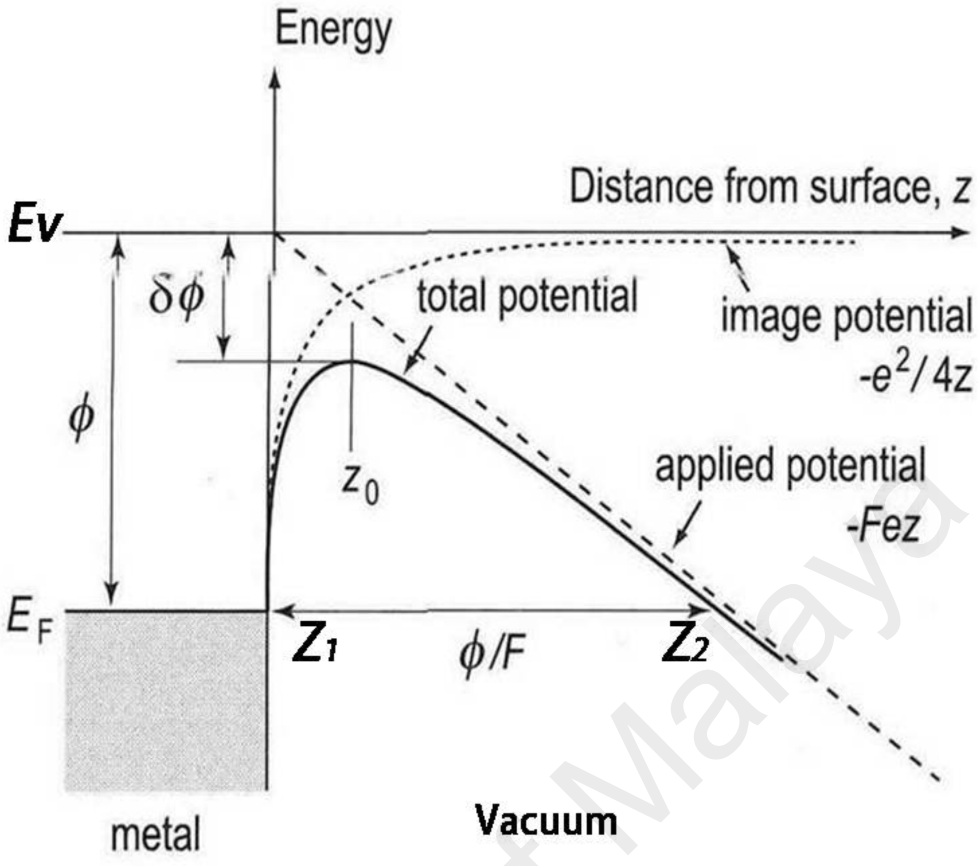

Figure 2.12: Diagram of the energy-level scheme for field emission from a metal surface.

As illustrate in Figure 2.12, free electrons in the metal occupy states up to the Fermi level, energetically separated from the vacuum by the work function, ϕ. For electrons to escape from a metal surface, they need to have sufficient energy to overcome the potential barrier across the metal-vacuum interface. In the presence of an electric field, F, the infinite square potential barrier is modified to the the electric field and image potential, $-e^2/4z$, resulting in an triagular potential barrier. Z_1 –Z_2 represent the width of potential barrier in the presence of an electric field which is finite for the metallic free electrons. Based on the assumptions described above Fowler and Nordheim (Fowler & Nordheim, 1928) modeled the FEE phenomenon for flat metal surfaces with the mathematical expression:

$$J = \frac{\mathrm{AE}^2}{\emptyset}\exp\left(-\frac{B\emptyset^{\frac{3}{2}}}{E}\right) \tag{2.5}$$

where J is the current density, E is the applied electric field, A and B are constants with values of 1.56 x 10^{-6} AeV V^{-2} and 6.83 x 10^{9} $eV^{-3/2}$ Vm^{-1}, and ϕ= 5.3 eV is the work function of ZnO, respectively.

The FN model has been used on rough field electron emitter surfaces giving a modified field electron emission equation:

$$J = A\ \frac{(\beta E)^2}{\emptyset}\exp\left(-\frac{B\emptyset^{\frac{3}{2}}}{\beta E}\right) \tag{2.6}$$

The local electric field at the field emitter tip, F, is defined as;

$$F = \beta E \tag{2.7}$$

where β is the field enhancement factor.

The FN plot, which is the linearized form of Equation (2.6), is;

$$\ln\left(\frac{J}{E^2}\right) = \ln\left(\frac{A\beta^2}{\emptyset}\right) - \ \frac{B\emptyset^{\frac{3}{2}}}{\beta}\frac{1}{E} \tag{2.8}$$

According to Fowler and Nordheim model,the slope of fitted straight line obtained from experimental data can determine the β value which corresponds to $\beta = -B\phi^{3/2}$. The work function, ϕ for ZnO is 5.3 eV (Minami, Miyata, & Yamamoto, 1998)(Li et al., 2007). A negative linear slope from the plot demonstrates that the FE from the material follows the FN model.

The parameters associated with the FEE properties of a field electron emitters are the field enhancement factor, β, turn-on field, thresholdfield and emission stability. The field enhancement factor, β is defined as the local electric field divided by the average electric field, and is calculated from the slope of the FN slope. The definition of the turn-on and the threshold field are the electric field required to initiate the field emission process and that to produce useful emission current respectively. No specific values defined turn-on and threshold fields. Thedifference in defining turn-on field and threshold field values depends on the applications, for example, flat display and x-ray sources that required a threshold value of 10 mA/cm^2 and 100mA/cm^2 for their operations respectively. Different emission current density values has been defined, for instance, Maiti et al. (Maiti et al., 2008) and (Xiao et al., 2008) defined the turn-on field as the electric field required to produce a current density of 10 μA/cm^2 and threshold field was defined as the field required to draw current density of 1 mA/cm^2, respectively. Chen et al. (Chen et al., 2008) specified the current density of 0.2 μA/cm^2 for turn-on field and 1 mA/cm^2 for the threshold field, respectively. Sheini et al. (Sheini, Joag, & More, 2010) defined the turn on field as the field required to produce an emission current density at 1μA/cm^2 and the threshold field for emission current density reached at 100μA/cm^2. Huang et al. (Huang, Yu, & Zhu, 2007) stated that the turn on field as an electric field which produced a current density of 0.1μA/cm^2 and the threshold field current density arrives at 1mA/cm^2. Emission stability can be defined as a constancy of emission current flow in certain time.

(b) Field electron emission from zinc oxide nanostructures

Field electron emissions from 1D nanostructures have been widely studied for their significance in both fundamental research and technical applications. In the past decade, carbon nanotubes were particularly being researched as it was found to be an excellent candidate for FEE application. The characteristic of high aspect ratio enhances the electric field on the sharp end of their structures (Fransen, Rooy, & Kruit, 1999). Besides, FEE from 1D nanostructure of oxide and semiconductor have also found their importance and reported in this area. ZnO has been regarded as one of the promising material for FEE application since it has properties of higher thermal stability, easy to tune the electronic property, chemical stability and stronger radiation-oxidation resistance (Li et al., 2007)(Ramgir et al., 2006). Various 1D nanostructures of ZnO such as nanowires, nanorods and nanofibers can be a potential alternative for producing field emission electrons with low threshold fields and high efficiency.

Lee et al. (Lee et al., 2002) studied FEE of ZnO nanowires prepared by vapor deposition and reported that, the turn-on field value for the ZnO nanowires of 6.0 V/μm at current density of 0.1 μA/cm^2, and the threshold field value of 11.0 V/μm at 1 mA/cm^2. Ren et al. (Ren et al., 2003) improved the FEE performance to get better ZnO-based field emitter by coating gold (Au) on the silicon substrate before growth process. They observed that with low areal density of Au, the turn on value is 6.46 V/μm for the electric field required to obtain the FEE current density of 1 mA/cm^2 comparable to that of carbon nanotubes. Yu et al. (Yu et al., 2005) developed a catalyst-free method and fabricated ZnO nanostructures with sharp emission end to enhance the FE properties. They observed anode-cathode separation affected the value of the turn-on and threshold fields at 1.8 V/μm and 3.9 V/μm at 300 μm spacing, and 2.2 V/μm and 4.6 V/μm at 100 μm, respectively. Small electrodes separation leads an increase of current density hence enhanced the FEE properties.

The fabrication and growth process for controlling the geometry especially the tip of field electron emitters was found to be a challenge in the FEE applications (Johnson et al., 2006). Efforts have been made to investigate the role of tip morphology on 1D ZnO nanostructures. Pan et al. (Pan et al., 2010) reported on the FE properties from well-aligned ZnO nanorod arrays with three kinds of tip morphology: abruptly sharpened, tapered and plane. The field enhancement factor, β which quantifies the ability of a specific emitter to amplify E showed that the abruptly sharpened tip has the highest value (~2.3 × 10^3) compared to tapered and plane tip morphologies (~1.0 × 10^3

and ~8.7 × 10^2 respectively). Another approach to enhance the FEE properties of ZnO nanostructures is by the doping process. To understand this approach, it is necessary to have some idea of the theory behind it. Electrons in solid materials are confined by a potential-energy barrier. The potential energy of a planar cold cathode with micro-roughness was described earlier in Equation 2.1. According to the FN equation (Equation 2.2), an effective approach to achieving strong electric fields is to employ sharp tips as electron emitters. In addition, lowering the electron barrier is beneficial to FE. Therefore, doping is found to be an effective approach to adjusting the Fermi energy level for semiconductors. The relationship between electron concentration and the Fermi level can be written as:

$$n = 2\left(\frac{2\pi m * kT}{h^2}\right)^{\frac{3}{2}} \exp\left[\frac{(E_F - E_C)}{kT}\right] \tag{2.9}$$

where n is the electron concentration, m* is the electron effective mass, k is Boltzmann’s constant, h is Planck’s constant, T is the absolute temperature, and E_F and E_C are energies at the Fermi level and the bottom of conduction band, respectively. This indicates that the FE performance can be improved through n-type doping because the Fermi level is lifted and, hence, the work function is reduced. It is even possible to realize negative electron affinity very advantageous for electron emission through heavy doping under certain conditions (Sun et al., 2006).

Pan et al. (Pan et al., 2006) synthesized MgZnO tetrapods by thermally oxidizing Zn and Mg powders. They observed that Mg-doped ZnO exhibited better field emission properties with higher emission current density and lower turn-on field value compared to pure ZnO nanowires. They also reported that, ZnO with higher Mg content exhibited better field emission properties with higher emission current density than ZnO with lower Mg content. Wang et al. (Wang et al., 2013) fabricated pure ZnO and Al-doped ZnO nanowires using low-temperature hydrothermal growth to investigate the field emission properties. The Al doping level was varied from 0 at. %. 1 at.%, 2 at.% and 3 at. % and they observed that the turn-on fields and threshold field values reduced with Al contents. Similar trend was observed for the field enhancement factor, β where the values for Al-doped ZnO nanowires emitters were apparently increase corresponding to the Al contents. Yu et al. (Yu et al., 2010) also observed that, the field emission properties of Sn-doped ZnO with a turn-on field value of 1.94 V/µm and threshold field value of 3.23 V/µm. They claimed that the good FE performance according to the sharp tips structure and the decrease of work function

2.5.2 ZnO as photocatalyst

At present, environmental pollution has become a major challenge during the development of modern human society (Vu et al., 2013). This serious problem was generating a much attention on how to eliminate the pollutant particularly from water. The waste water treatment especially utilizing environmentally friendly photocatalysts has been extensively studied. ZnO, aside from TiO_2 has been considered as a promising material for purification and disinfection of water (Kenanakis & Katsarakis, 2014). ZnO nanostructures are excellent photocatalyst for photodegradation of the organic dyes molecules owing to its high photoactivity, environment-friendly feature, cost effective, stability, and non toxic (Pung, Lee, & Aziz, 2012)(Tian et al., 2012). ZnO nanostructures have a great potential in photocatalyst applications by serving as active compositions or as supports by tailoring size, concentration of oxygen defects, doping and surface area (Height et al., 2006)(Fu, Han, & Meng, 2012).

2.6 Growth techniquesof zinc oxide nanostructures by sol-gel method

Several growth techniqueshave been reported to illustrate the growth process of ZnO nanostructures using the sol gel technique. Various mechanisms that have been used in ZnO synthesis process will be illustrated in detailed. In liquid based sol-gel method, the growth mechanisms of ZnO nanostructures in particular ZnO nanorods have been reported on two step process involving seeding process, continued with the growth process. A simple spin coating method or dip coating method has been employed for generating the seeding layer of ZnO nanocrystal. The growth technique of ZnO nanorods arrays has been reported by Huang et al. (Huang et al., 2011).

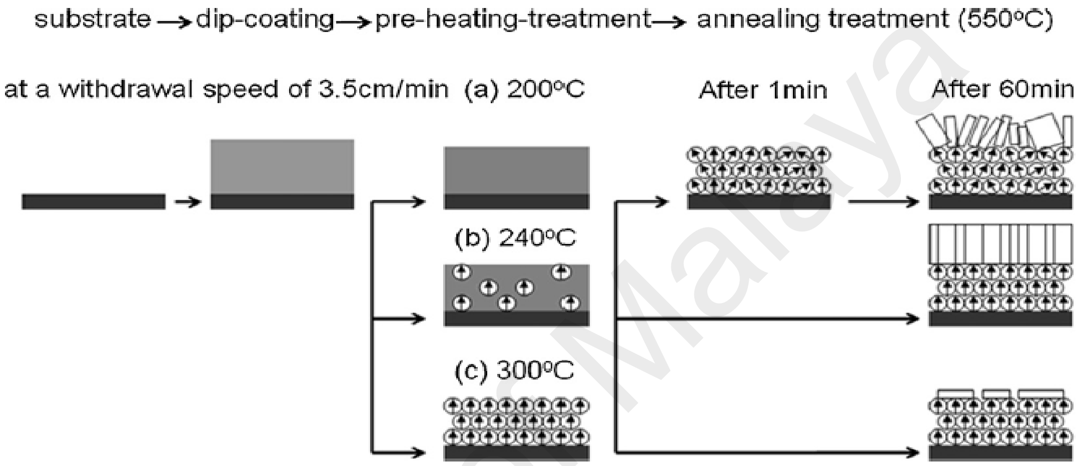

Figure 2.13: Schematic illustration of the ZnO nanorod arrays aligned on the glass substrate influenced by pre-heating temperature (Huang et al., 2011).

As shown in Figure 2.13, they suggested that the ZnO nanorods arrays generated from template-free sol-gel technique by tailoring the heating temperatures (200, 240 and 300 °C) and the withdrawal speed of seed layer. For the film pre-heated at 200 °C, no crystallization was happened resulting improper preferred orientation of ZnO nanorods, while at 300 °C, only a few nanorods were nucleated from the seeded layer. Well-aligned ZnO nanorod arrays were obtained from the oriented nanocrystalline film pre-heated at 240 °C.

Another growth technique was suggested by Liu et al. (Liu et al., 2015). The ZnO nanorods was prepared by two step process which are seeded process by spin coating method of ZnO thin film at various layer (2, 4, 6 and 8 layers) followed by hydrothermal method for the ZnO growth. The synthesis process with suggested fabrication process is represents in Figure 2.14.

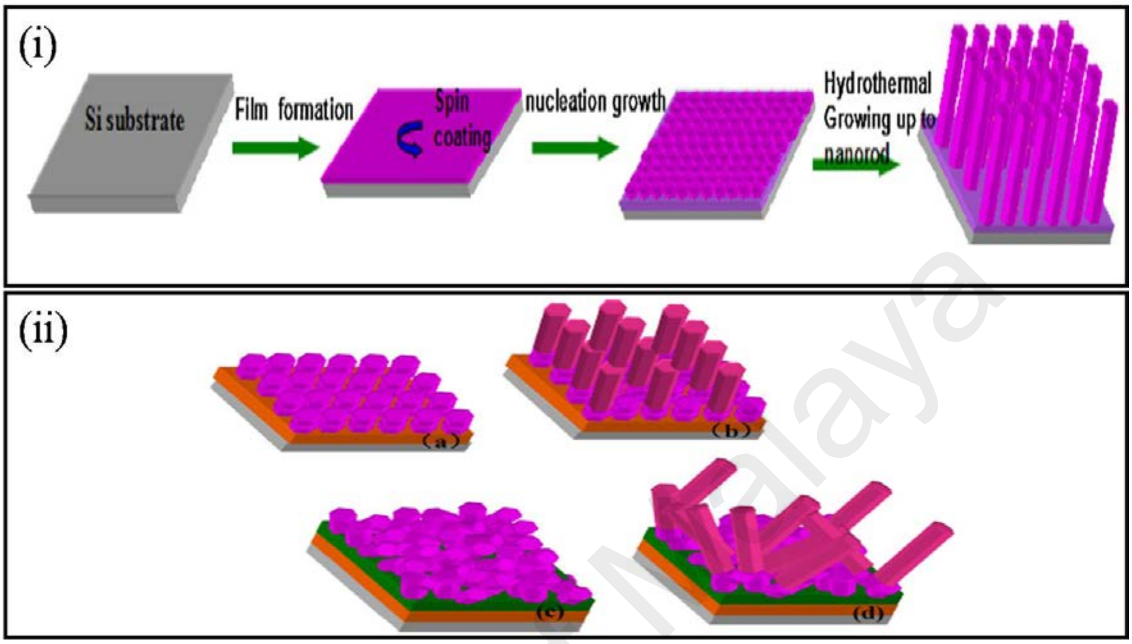

Figure 2.14: (i) Synthesis process of ZnO nanorods and (ii) Schematic of fabrication process of ZnO nanorod arrays assisted growth by the ZnO seed layers ((Yufang Liu et al., 2015).

SEM results reveal that the seed layer influenced on diameter, density, length and orientation of ZnO nanorods arrays. They observed that ZnO nanorods array grown on the 4 seed layer shows a higher density and vertical orientation compared to other sample.

Ekthammathat et al. (Ekthammathat et al., 2013) synthesized ZnO nanorods on Zn substrates by hydrothermal method with controlling the pH of precursor solution of 9-12. They also proposed a growth technique on the simple method that has been employed (as shown in Figure 2.15).

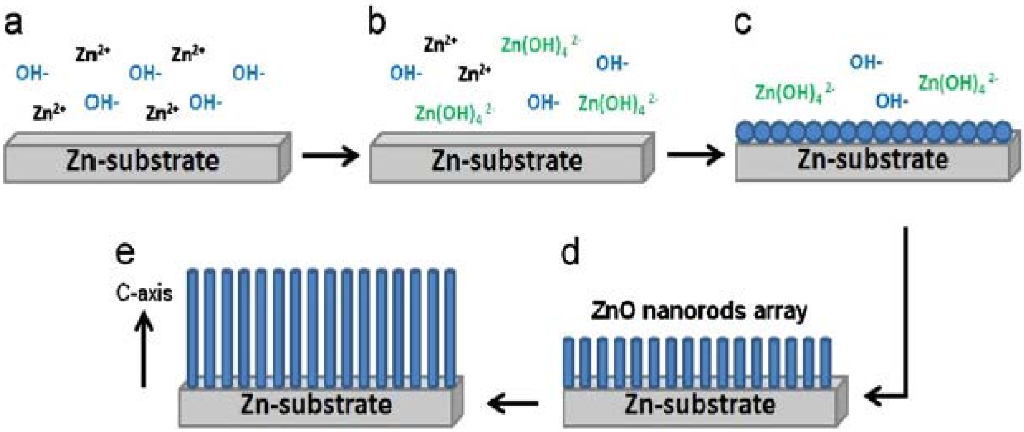

Figure 2.15: Schematic diagram of a possible growth technique of hexagonal prism ZnO nanorods on Zn substrates (Ekthammathat et al., 2013).

They suggested and proposed the growth technique of ZnO nanorods based on following steps: (i) Zn substrate was dissolved in basic solution and Zn^{2+} ions formed. (ii) $[Zn(OH)4]^{2-}$ complex ions was formed to create multiple nuclei on the zinc substrate. (iii) homoepitaxial growth of nuclei proceeded as hexagonal prism ZnO nanorods at 120 °C and 24 hours hydrothermal reaction.

2.7 Summary

The overall review of ZnO which includes the nanomaterials and its classification, introduction of ZnO and its properties on crystal structure, physical, electrical, optical (luminescence) and FEE properties have been summarized. A variety low dimensional ZnO nanostructure and various synthesis methods also discussed. Growth mediated of ZnO nanostructures by HMTA and biomaterials also being explained. The applications of ZnO nanostructures particularly field electron emission and photocatalyst also presented. The growth techniqueof ZnO which has been postulated by several studies is also briefly decribed.

CHAPTER 3: SYNTHESIS AND CHARACTERIZATION OF ZINC OXIDE NANOSTRUCTURES USING THE SOL-GEL METHOD

In this chapter, an account on the synthesis and characterization of ZnO nanostructures using different sol-gel synthesis strategies is presented. ZnO nanostructures were synthesized using the conventional methods and using a biomaterial namely *Citrus aurantifolia* (CA).

The content of this chapter is divided into three main sections. The first section synthesis and characterization method of ZnO nanostructures by utilizing conventional reduction agent i.e. hexamethylenetetramine (HMTA, $C_6H_{12}N_4$) is described. Under this section, four set experiments were conducted which are;

i. the effect of substrate materials on the formation of ZnO;
ii. the effect of deposition time on the formation of ZnO on glass substrates;
iii. the effect of Fe-doping on glass substrates; and
iv. the effect of Al-doping on aluminum.

In the second section, we presented the synthesis and characterization of ZnO nanostructures by utilizing CAjuices as the reducing agent. The three experiments are as follows;

i. the effect of pH on the structural and optical properties of ZnO;
ii. high temperature XRD (HT-XRD) study of ZnO nanoparticles; and
iii. the effect of Mg-doping on the structural and optical properties of ZnO nanostructures.
iv. Finally, the synthesis and characterization of silver nanoparticles (AgNP) decorated micro- and nanostructured ZnO are described. All the AgNP decorated samples were used in dye photodegradation applications that will be discussed in Chapter 5.

All samples were characterized using x-ray diffraction (XRD), Raman spectroscopy, field emission scanning electron microscopy (FESEM), energy dispersive x-ray spectroscopy (EDX) to characterize the crystallinity, morphology and chemical composition of the samples. Transmission electron microscope (TEM) was employed to study the structural properties of the samples. Photoluminescence spectroscopy was used to study the optical properties.

3.1 Synthesis and characterization of zinc oxide nanostructures using HMTA

The overall experimental work done is summarized in a flowchart shown in Figure 3.1. Detailed descriptions of each step are as follows.

3.1.1 Preparation of substrates

The substrates were cut into squares of 2 cm × 2 cm and ultrasonic cleaned in deionized (DI) water, acetone and ethanol each for ten minutes. The substrates were then rinsed thoroughly in DI water and keep dried for further used. Two types of seeding methods were used which were spin-coating and dip-coating method. The seed solution was prepared by mixing 0.55 g zinc acetate dehydrates into 100 ml isopropanol with continuous stirring at 60 °C for 2 hours. For spin-coating method, the spin rate was maintained at 3000 rpm for 30 s. After deposition, the substrates were heated at 300 °C for 1 hour to evaporate the solvent and remove organic residuals. The process was repeated for 10 times for all substrates. For dip-coating method, a similar seed solution was used. The substrates were dipped in a solution for 5 minutes followed by heating process. The seeded substrates then were characterized using FESEM and XRD to determine the morphology and structural properties.

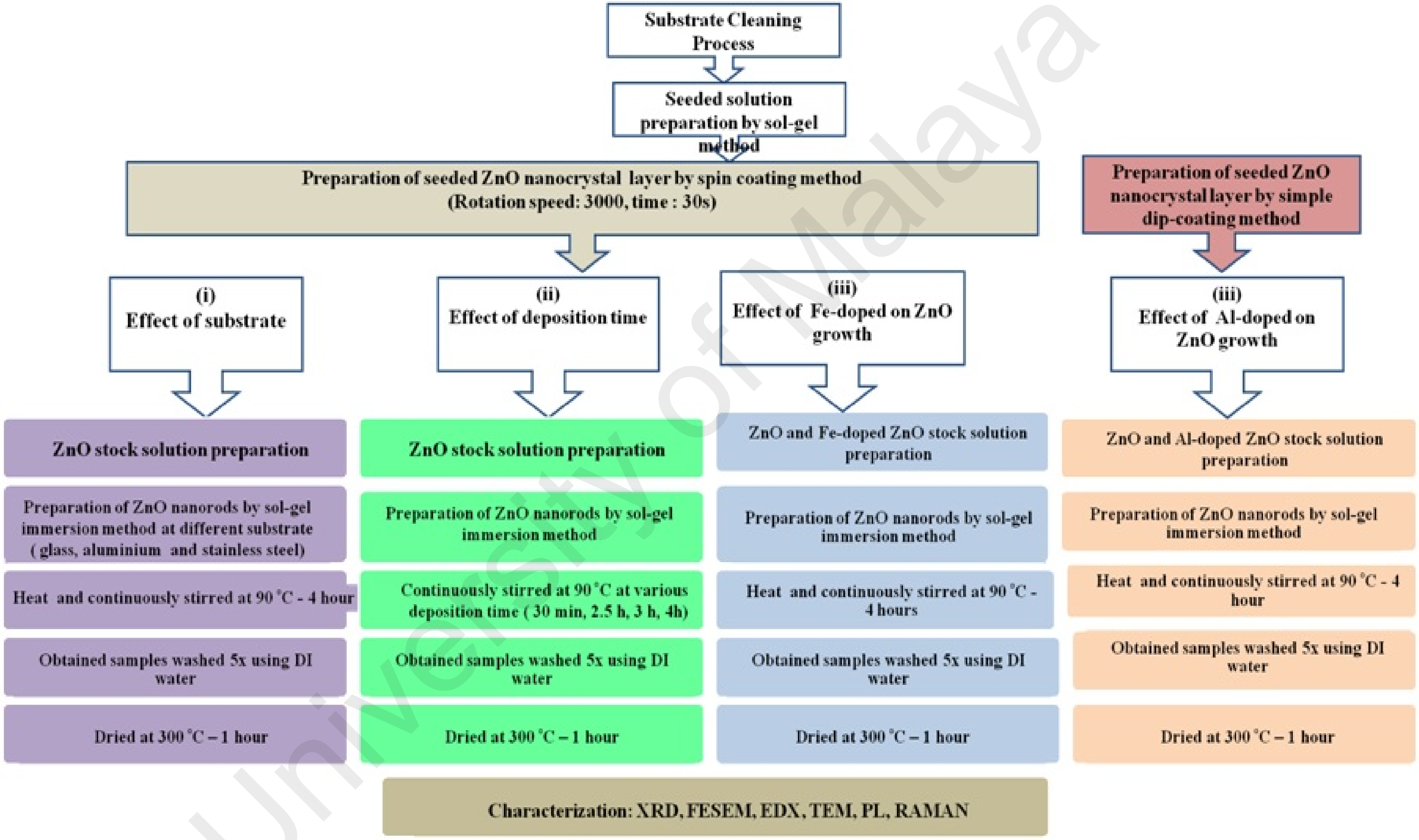

Figure 3.1: The flow chart showing the synthesis process of ZnO nanostructures (i) the effect of substrate, (ii) the effect of deposition time, (iii) Fe-doped to ZnO nanorods, and (iv) Al-doped to ZnO nanorods.

Figure 3.2 shows the normalized XRD pattern of seeded ZnO nanoparticles in the range of 2θ: 20 – 60 °. Figure 3.2 (a) is a XRD pattern for seeded ZnO nanoparticles prepared on glass substrates by spin-coating method, while Figure 3.2 (b) is for seeded ZnO nanoparticles prepared on aluminum substrates by dip-coating method. Both graph show an identical pattern with the diffraction peaks can be assigned to (100), (002), (101), (102), and (110) for the standard wurtzite ZnO structure. It was observed that the seeded ZnO nanoparticles prepared by spin-coating and dip-coating method have a sharp diffraction peak indicates that the seeded substrates were highly crystalline. No impurity peak was detected showing that the seeded ZnO substrates are pure ZnO.

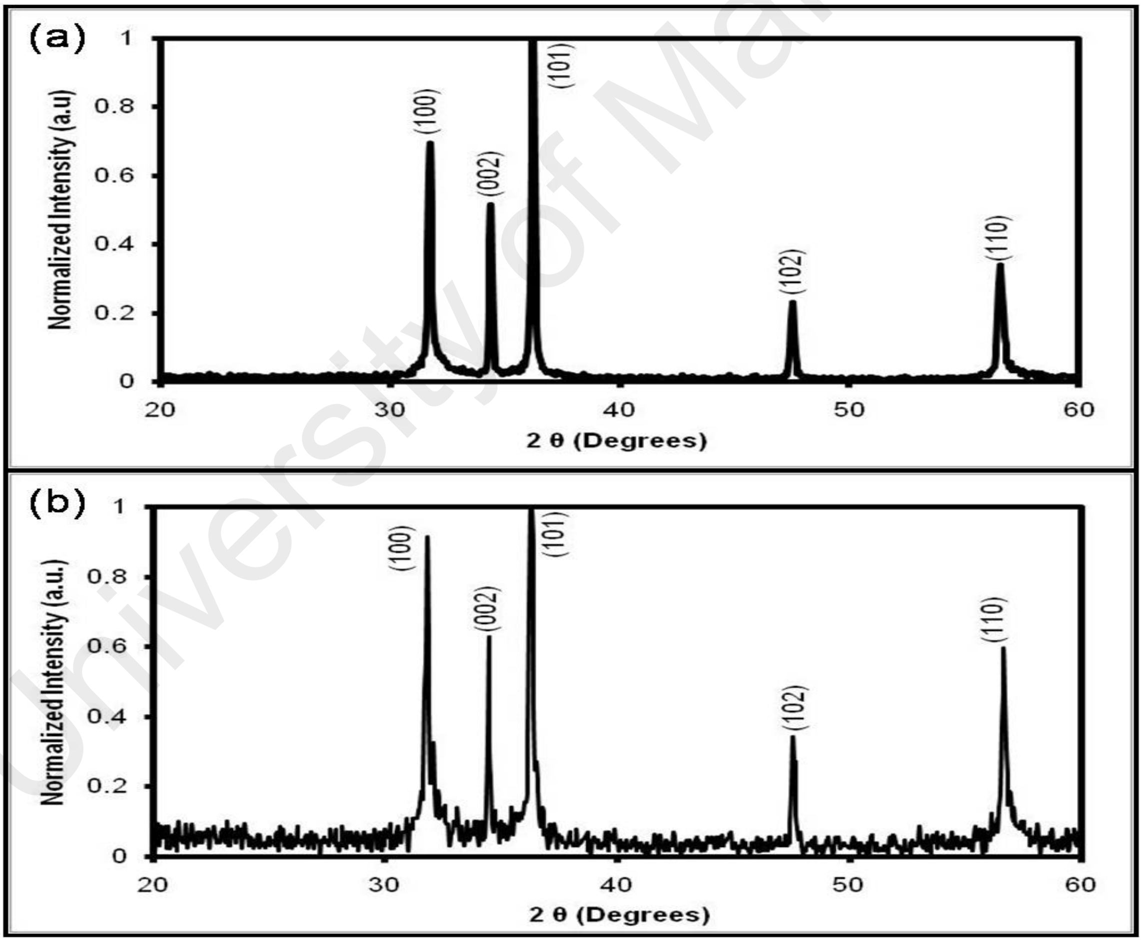

Figure 3.2: The X-ray diffraction pattern for seeded ZnO prepared by (a) spin-coating method on glass substrates and (b) dip-coating method on aluminum substrates.

Figure 3.3 shows the FESEM images of seeded ZnO nanoparticles. Figure 3.3 (a) and (b) shows the images of seeded ZnO nanoparticles prepared on glass substrates by spin-coating method, while Figure 3.3 (c) and (d) shows the images of seeded ZnO nanoparticles prepared on aluminum substrates by dip-coating method.

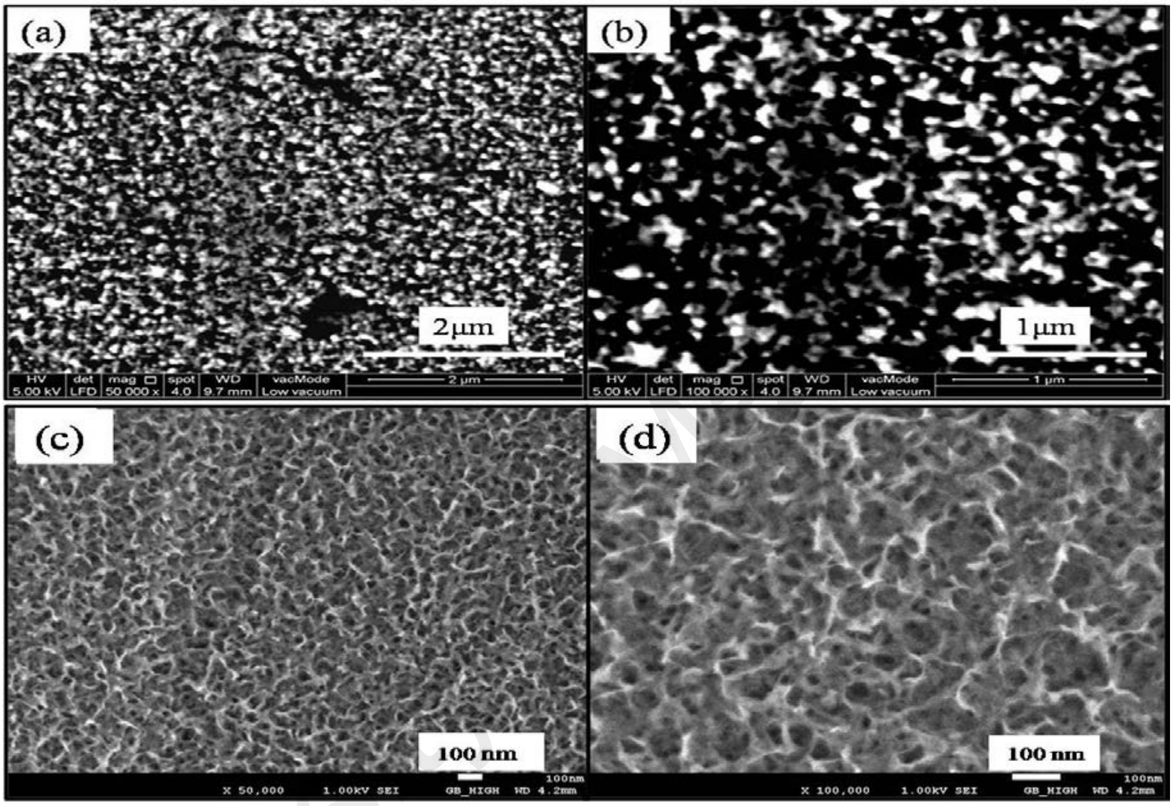

Figure 3.3: FESEM images of seeded ZnO prepared by (a-b) spin-coating method and (c-d) dip-coating method.

The ZnO nanoparticles seeds prepared by spin-coating method (Figure 3.3 (a and b)) consisted of uniform particles with estimated size of 20 – 30 nm. The ZnO nanoparticles seeds prepared by dip-coating method (Figure 3.3 (c and d)) consisted of particles like connected sheets. The seed layer will provide a low free energy barrier to the relative substrate and act as the active nucleation sites for the growth of ZnO nanorods (Chiu & Huang, 2012). When the interface energy between the crystal nuclei and the substrate is low, the nucleation barrier will be decreased (Wang et al.,2008).

3.1.2 Deposition of zinc oxide nanorods

The stock solution was prepared by dissolving 0.249 g zinc nitrate hexahydrate ($Zn(NO_3)2·6H_2O$) and 0.46 g hexamethylenetetramine (HMTA, $C_6H_{12}N_4$) in 100 ml DI water and stirred at 60 °C for 2 hours to yield a clear and homogenous solution. The solution was left overnight for aging. To deposit the ZnO nanorods the seeded glass, aluminum and stainless steel substrates were immersed vertically in the stock solution. Deposition was conducted for 4 hours at 95 °C. After deposition, the samples were removed from the solution and rinsed thoroughly in DI water and dried at 150 °C for 10 min and then annealed at 300 °C for 1 hour.

Another set of samples with same process was done by using glass as substrate and the deposition time was varied for about 0.5, 2, 3 and 4 hours to study the time evolution of ZnO NP growth.

To synthesize iron doped ZnO nanorods, 12.1, 24.2 and 36.3 mg iron nitrate nanohydrate ($Fe(NO_3)_3.9H_2O$) was added to the stock solution which corresponded to 5, 10 and 15 mol % Fe with respect to zinc, respectively. The sample was deposited on glass substrates and deposition time was set up for 4 hours.

For the synthesis of Al doped ZnO nanorods, 5.7, 17.4 and 29.6 mg $Al(NO_3)_3.9H_2O$ were added to the stock solution at concentrations of 1, 3 and 5 mol % Al with respect to zinc, respectively. The overall experimental work done is summarized in a flowchart shown in Figure 3.1.

The morphology of the ZnO nanorods was characterized by field emission scanning electron microscope (FESEM). The chemical composition of the obtained ZnO nanorods was observed using EDX attached to a FESEM. Transmission electron microscope (TEM) was further used to characterize the structure of ZnO nanorods. The crystal structure of the samples was investigated using X-ray diffraction patterns with

Cu-Kα (λ=1.5418Å) radiation as the probe beam. Raman shift were measured using micro-Raman spectrometer with Nd: YAG laser operating at the second harmonic wavelength of 532 nm as the excitation source. Photoluminescence (PL) spectroscopy was conducted using a He-Cd laser source at 325 nm.

3.2 Results and discussion

3.2.1 Substrates effects on the morphology and crystal structure of zinc oxide nanorods

Figure 3.4 shows the normalized XRD patterns of ZnO nanorods prepared on various substrates. Figure 3.4 (a) – (c) correspond to XRD patterns for ZnO nanorods deposited on the seeded glass, aluminium, and stainless steel substrates, respectively. The observed diffraction peaks of ZnO nanorods deposited on three different substrates have an identical XRD pattern that can be indexed to standard hexagonal wurtzite ZnO structure. The diffraction peaks at 31.70°, 34.43°, 36.27°, 47.61°, 56.65°, 62.92°, 66.43°, 68.01°, and 69.14° are assigned to the (100), (002),(101), (102), (110), (103), (200), (112), and (201) planes of hexagonal wurtzite ZnO consistent with the data of JCPDS No. 36-1451. The intense peaks suggest the good crystallinity of ZnO. No peaks related to impurities materials were detected.

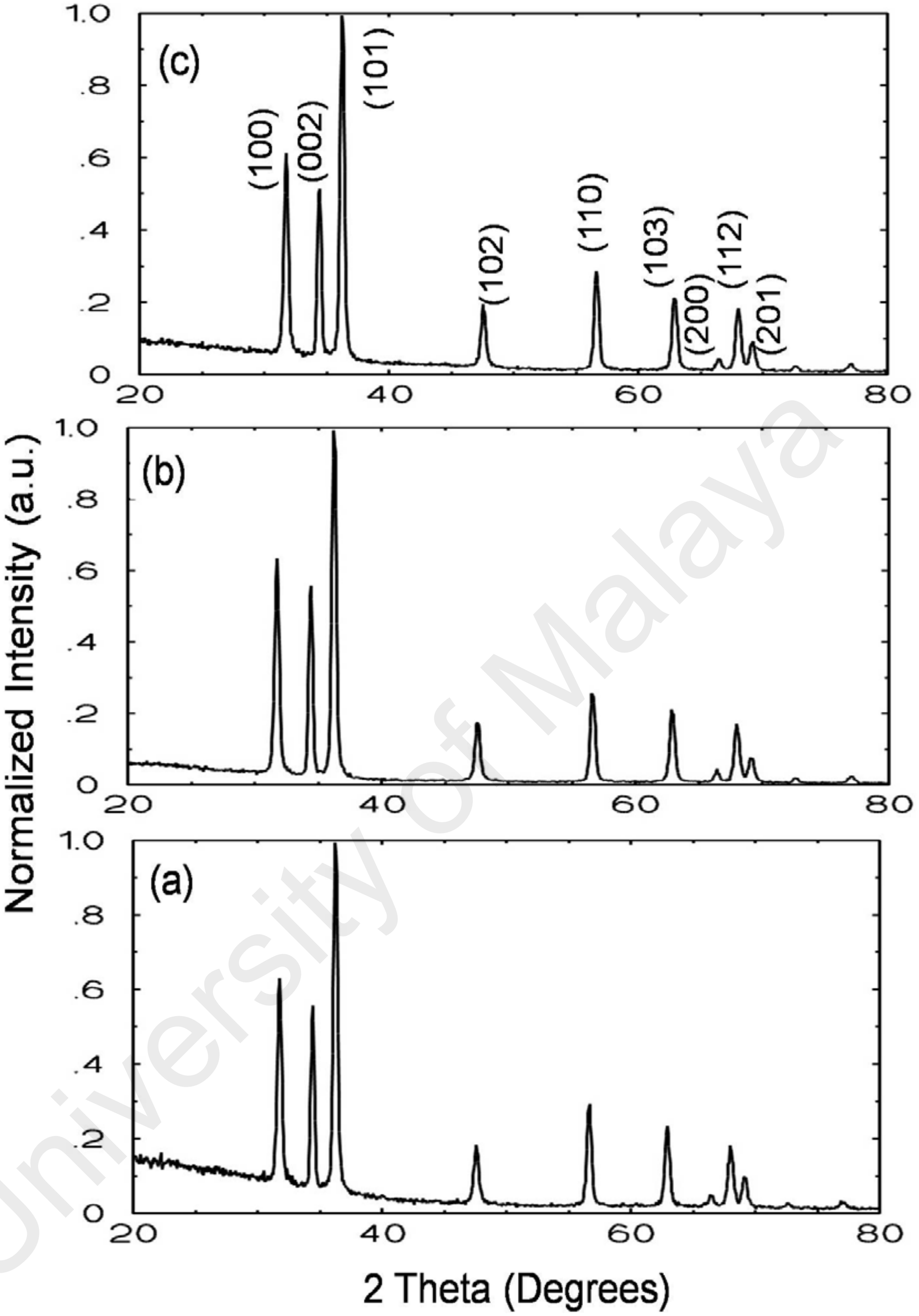

Figure 3.4: XRD patterns of ZnO nanorods deposited on (a) glass, (b) aluminium, and (c) stainless steel substrates by sol-gel method.

Figure 3.5 shows the FESEM images of ZnO nanorods deposited on glass, aluminum and stainless steel substrates. For all samples, dense and quasi-aligned nanorods were obtained but varying in diameter and length. The image for ZnO nanorods deposited on glass (Figure 3.5 (a) and (b)) shows the ZnO nanorods with average diameter of 40 to 80 nm. For ZnO nanorods deposited on aluminum substrates (Figure 3.5 (c) and (d)) the estimated diameter of nanorods is about 50 to 150 nm, while for ZnO nanorods deposited on stainless steel substrate (Figure 3.5 (e) and (f)) the estimated diameter of the nanorods were in the range of 80 to 200 nm. Enhancement on the diameter size of nanorods has been observed for the three different substrates. Glass substrates were discovered to have the smallest range of diameter size and uniform distribution of rods compared to aluminum and stainless steel. This occurrence may be due to the reactivity of HMTA towards the substrate. The structure of glass substrate was amorphous with smoother surface compared to other substrate. Aluminum and stainless steel substrates were expected to react with the HMTA solution, hence increase the surface structure defect on the formation of ZnO nanorods (Yang et al., 2008).

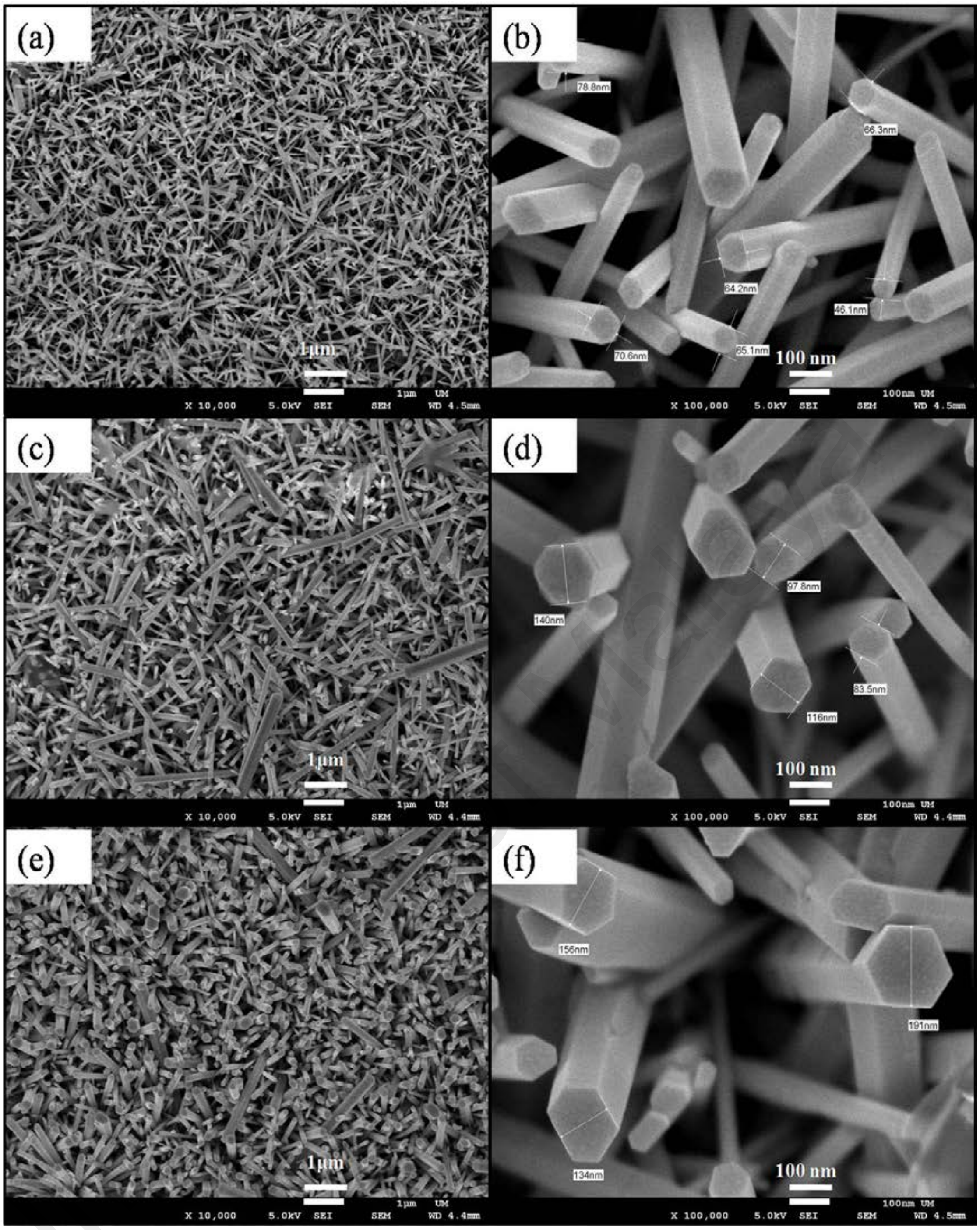

Figure 3.5: FESEM images of ZnO nanorods deposited on (a, b) glass, (c, d) aluminum, (e, f) stainless steel substrates

Figure 3.6 shows the cross-sectional view from FESEM image of ZnO nanorods deposited on glass, aluminum and stainless steel substrates. The cross-sectional view for ZnO nanorod deposited on glass (Figure 3.6 (a)) shows a uniform quasi-aligned array formation of nanorods with length approximately 2.8 μm. For ZnO nanorods deposited on aluminum substrate (Figure 3.6 (b)), the nanorods length was about 3.45 to 4.31 µm which was longer compared to those deposited on glass substrates. While for ZnO nanorods deposited on stainless steel (Figure 3.6 (c)) shows much less pronounced layer of a non-uniform lengthed nanorods. The good alignment of ZnO nanorods deposited on glass may be attributed to the non-reactivity of the HMTA solution towards the glass substrate compared to aluminum and stainless steel.

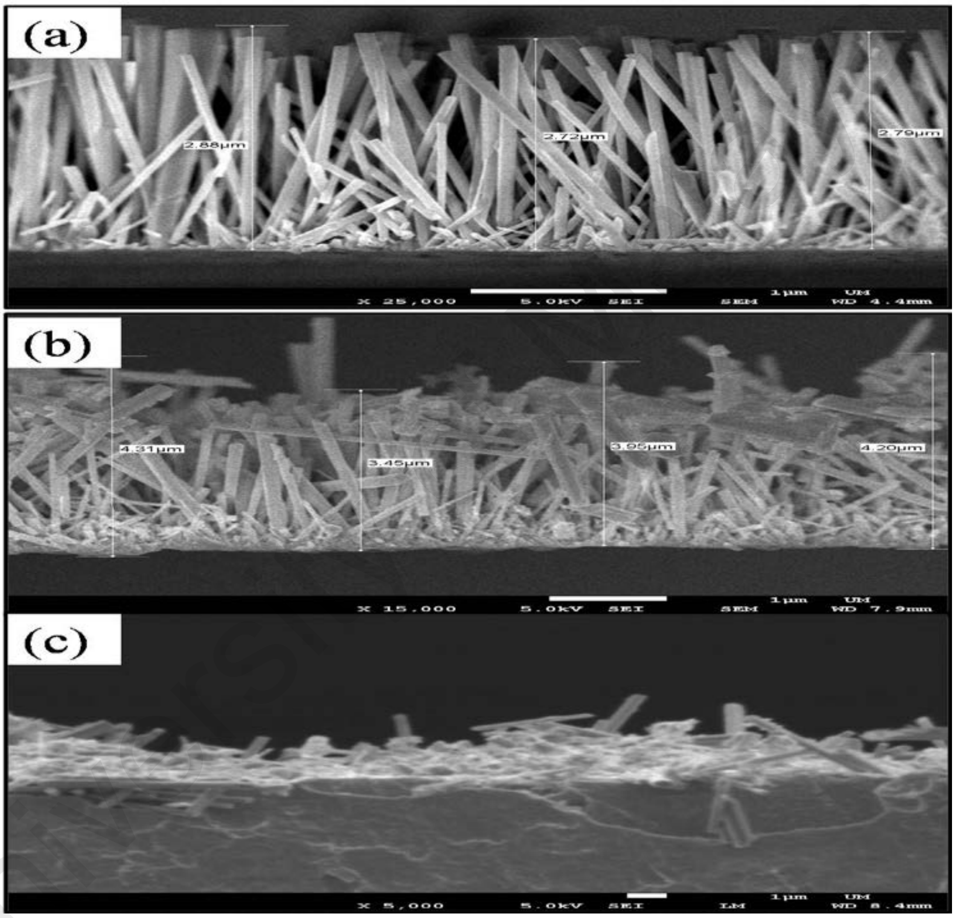

Figure 3.6: Cross-sectional FESEM images of ZnO nanorods deposited on (a) glass, (b) aluminum, and (c) stainless steel substrates.

Typical TEM images of ZnO nanorods deposited on different substrates are shown in Figure 3.7. Figure 3.7 (a) - (c) shows the TEM images of ZnO nanorod deposited on glass, (d) – (f) on aluminum and (g) – (h) on stainless steel substrates. All samples having a rod-like structure as proven earlier from FESEM results. The HRTEM images of ZnO nanorod deposited on glass substrate (Figure 3.7 (c)) shows that the nanorod has a single-domain wurtzite structure with a high crystal quality. The spacing between adjacent lattice planes is about 0.24 nm. For ZnO nanorods deposited on aluminum and stainless steel substrates (Figure 3.7 (f) and (i)), the lattice spacing between adjacent lattice planes is about 0.25 nm. These adjacent lattice plane was attributed to the (002) planes of the hexagonal structure. The (002) planes were perpendicular to the growth direction, confirming that the nanorods have grown along the [001] direction.

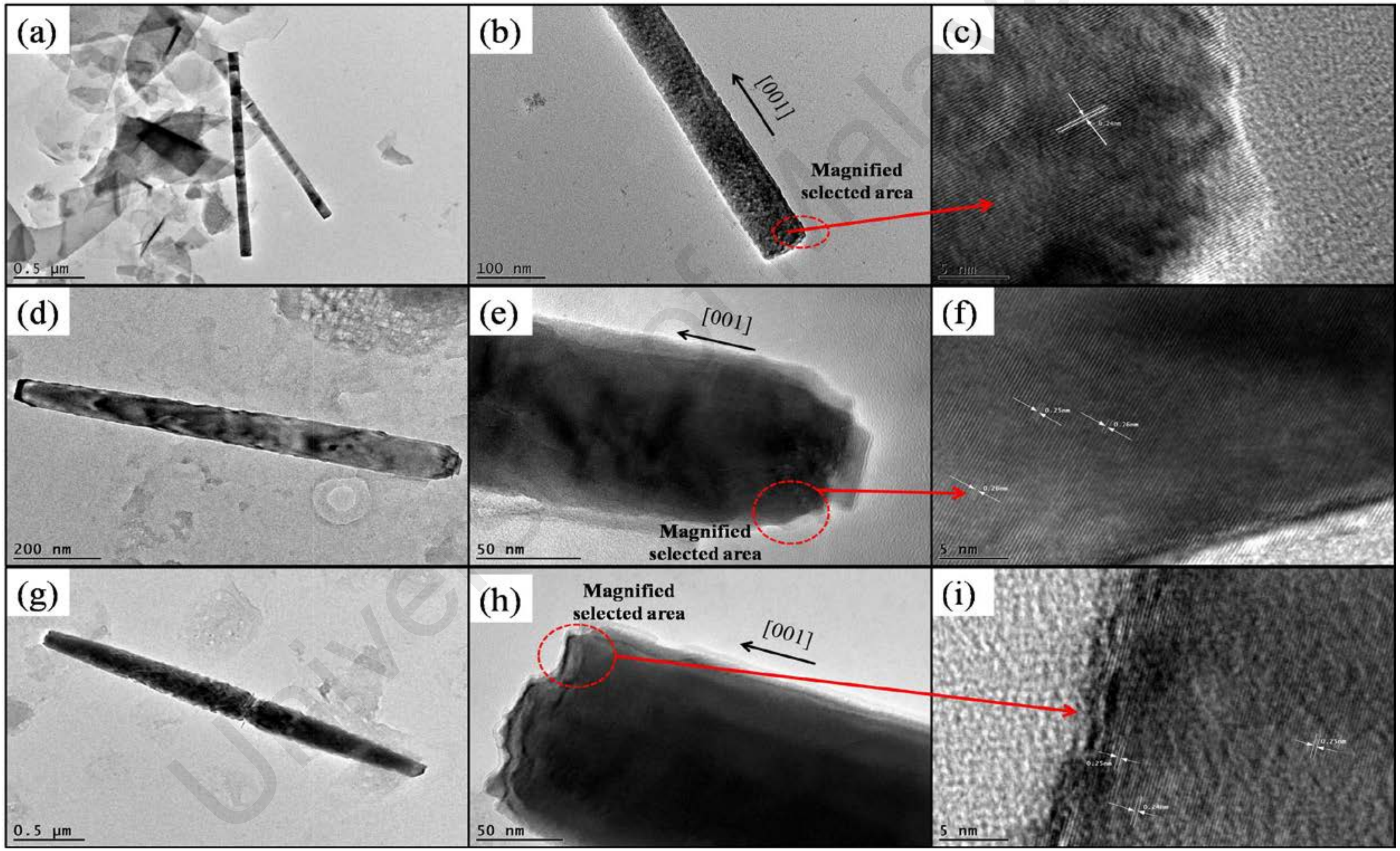

Figure 3.7: TEM and HRTEM images of ZnO nanorods synthesized on (a-c) glass, (d-f) aluminium and (g-i) stainless steel substrates.

In summary, ZnO nanorods were successfully synthesized on glass, aluminium, and stainless steel substrate. To some degree all samples exhibited similar rod-liked structure but with different aspect ratio. From FESEM results, the estimated size of ZnO nanorods deposited on glass substrates is about 40-80 nm in diameter, and 2.8 μm in length. For ZnO nanorods synthesized on aluminum substrate, the estimated size is about 50 – 150 nm in diameter and 3.45 – 4.31 μm in length. An increasing of size was observed for ZnO nanorods deposited on stainless steel substrate with estimated size of 80 – 200 nm in diameter and the length is negligible as the rods did not well form in a vertical direction. The different in diameter and length of the nanorods deposited on different substrate was attributed to the reactivity of HMTA aqueous solution and surface defect on the substrates during the synthesis process. From XRD analysis, ZnO nanorods that deposited on glass, aluminum and stainless steel substrates showed a typical XRD pattern of ZnO that match well with wurtzite hexagonal ZnO. TEM analysis show that ZnO nanorods deposited on glass, aluminum and stainless substrates grow along the c-axis and are single crystals.

3.2.2 The effect of deposition time to the formation of zinc oxide nanorods deposited on glass substrates

The ZnO nanorods deposited on seeded glass substrate were synthesized at deposition times of 0.5, 2, 3 and 4 hours. Figure 3.8 shows the XRD patterns for the ZnO nanorods prepared at the different deposition times. The XRD diffraction peaks can be assigned to (100), (002), (101), (102) and (110) hexagonal wurtzite structure and consistent to the JCPDS Card No. 079-2205.

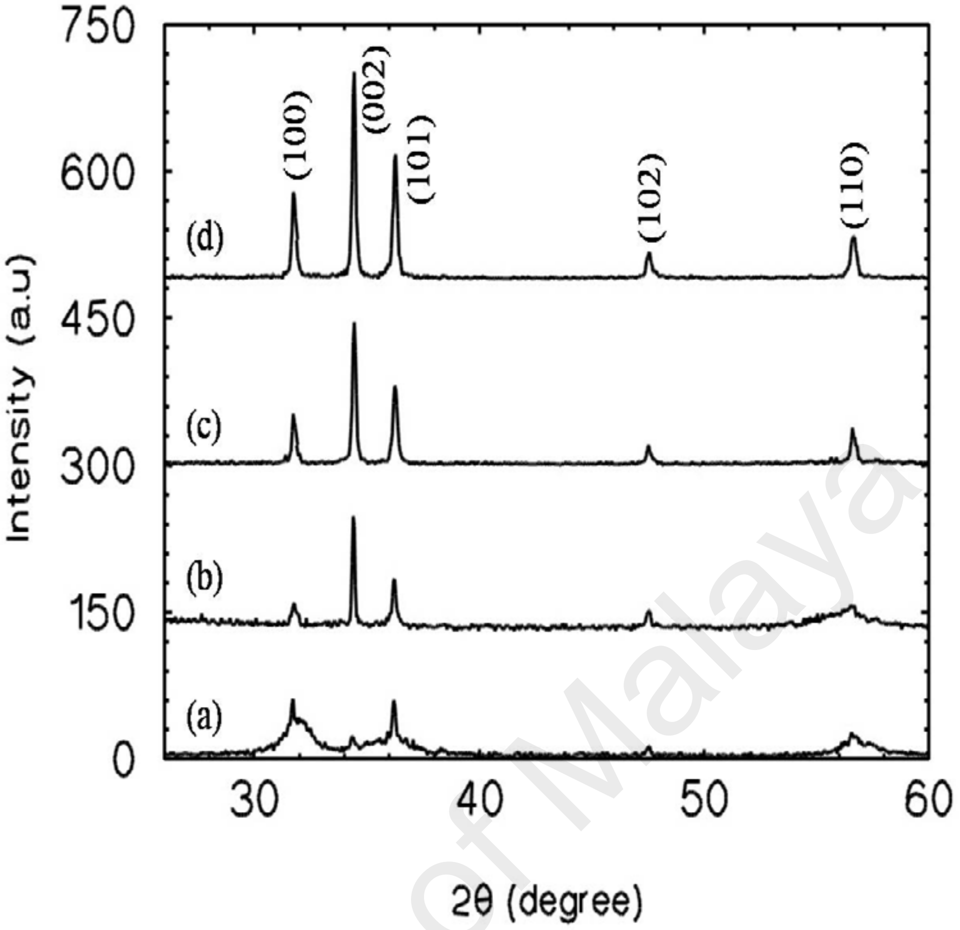

Figure 3.8: XRD patterns of ZnO nanorods synthesized by sol gel method at different deposition times (a) 0.5 hour (b) 2 hours, (c) 3 hours and (d) 4 hours.

The ZnO nanorods deposited for 0.5 hour (Figure 3.8 (a)) shows a broad background peak of (100), (101) and (110) that indicates the low density of nanoparticles and small thickness of the ZnO layer. Figure 3.8 (b) shows the XRD spectrum of ZnO nanorods deposited for 2 hours where the (100), (002) and (101) diffraction peak were more pronounced with sharp and intense peaks. Deposition duration of 3 and 4 hours (Figure 3.8 (c) and (d)), gave similar sharp and intense XRD peaks. This enhancement showed the formation of ZnO nanorods crystallinity over time. No impurity peak was detected showing that the obtained ZnO nanorods were pure ZnO. Similar observation was discovered by Liu et al. (Liu et al., 2014) that reported the diffraction peak of ZnO prepared at different reaction time by hydrothermal microemulsion route become narrower and indicating that the crystallization of the sample increased with reaction time.

The FESEM images of ZnO nanorods prepared at different deposition time are shown in Figure 3.9. The ZnO samples that deposited for 0.5 hours (Figure 3.9 (a)), composed of dense and homogeneous nanoparticles. The dense nanoparticles were due to the seed layer nanoparticles deposited before the deposition process. The ZnO nanorods deposited for 2, 3 and 4 hours showed identical density of formation. As the deposition time was increased to 2 hours, the nanorods structure started to form (Figure 3.9 (b)). The nanorods were uniform and formed a quasi-aligned structure. At 3 hours (Figure 3.9 (c)) and 4 hours (Figure 3.9 (d)), hexagonal-shaped nanorods were uniformly formed over the entire substrate surface with similar density and orientation. The diameter of ZnO nanorods increased proportionally with the increased of the deposition time, estimated at 27 nm to 80 nm for the deposition time of 0.5 hour to 4 hours. This phenomenon is related to the Ostwald ripening process which describes particle coarsening in term of their size (Eduardo et al., 2006).

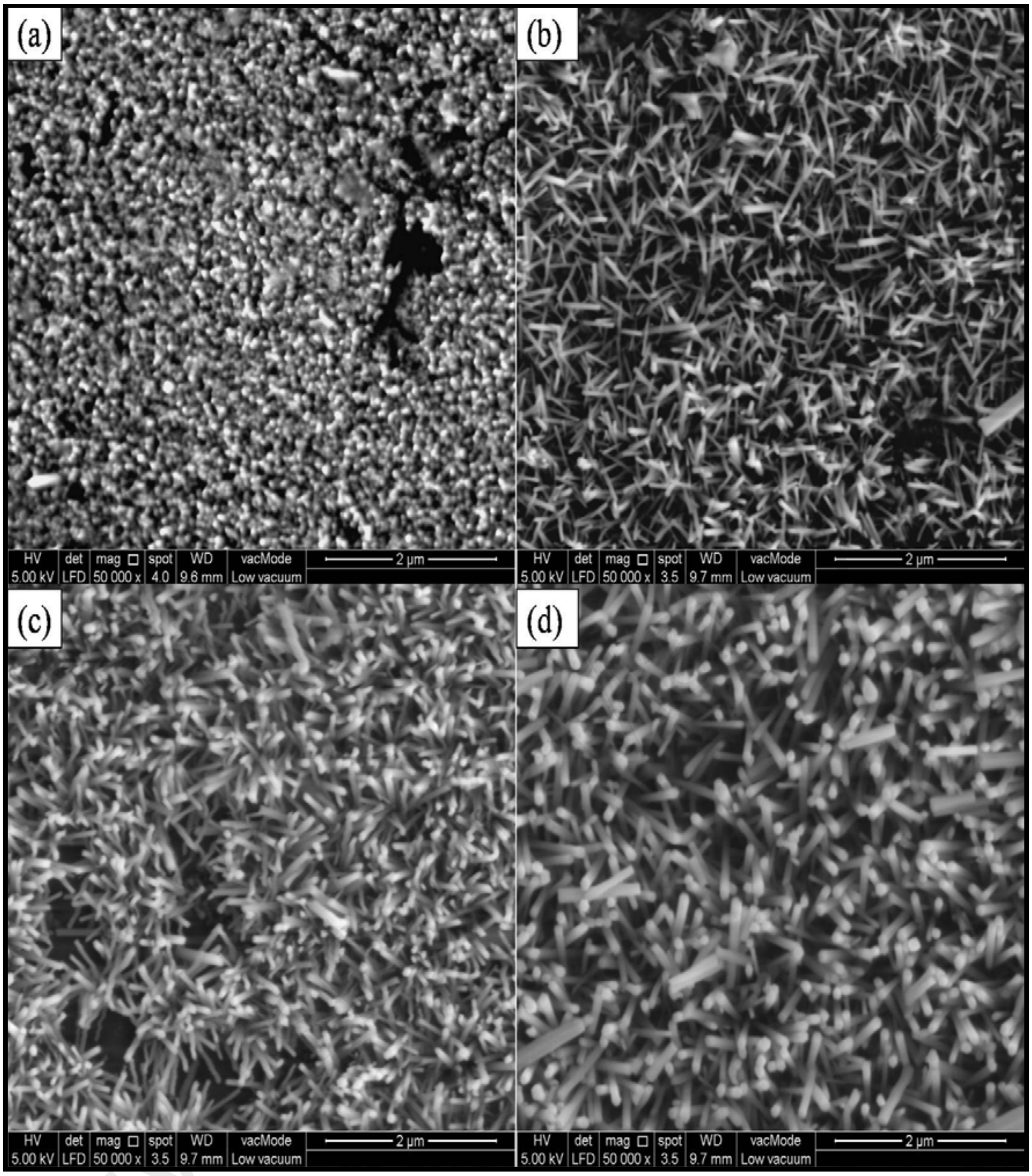

Figure 3.9: FESEM images of ZnO nanorods synthesized by sol gel method at different growth times (a) 0.5 hour, (b) 2.0 hours, (c) 3 hours and (d) 4 hours.

As a summary, XRD result was showed that all of the diffraction peaks for ZnO nanorods which prepared at different deposition times can be well indexed to the hexagonal ZnO wurtzite structure. With longer deposition time, the peak intensity increased hence performed better crystallization. From FESEM results, ZnO nanorod deposited for 0.5 hour, yield nanoparticles formed on the ZnO seeds. After 2 hours nearly vertical aligned ZnO nanorods were formed. After 3 and 4 hours, the ZnO nanorods formed increased in size. The density of ZnO nanorods at 4 hours deposition time is almost uniform with the formation of hexagonal shapes. It can be summarized that the 4 hours deposition time for synthesis of ZnO nanorods was sufficient and selected to futher used in other experiment and applied for the field electron emission application.

3.2.3 Iron doped zinc oxide nanorods deposited on glass substrates

The effect of pure and iron doped ZnO nanorods at various concentrations was studied. Seeded glass substrate was used to deposit the pure and Fe-doped ZnO nanorods. The FESEM images ofpure and Fe-doped ZnO nanorods at various Fe concentrations are shown in Figure 3.10. For all samples, uniform shapes and aligned structure of hexagonal ZnO nanorods were exhibited but with varying diameters. The nanorods were well-defined hexagonal shaped with flat end facets. Pure ZnO nanorods (Figure 3.10 (a) and (b)) and 5 mol % Fe-doped ZnO nanorods (Figure 3.10 (c) and (d)) shows similar morphology. The diameters of the nanorods were estimated to be in the range of 50 and 75 nm formed in quasi-aligned arrays. The diameter of 10 mol % Fe-doped ZnO nanorods (Figure 3.10 (e) and (f)) and 15 mol % Fe-doped ZnO nanorods (Figure 3.10 (g) and (h)) increased compared to those obtained in pure ZnO and 5 mol % Fe-doped ZnO nanorods. The average rod diameter increases approximately to between 150 and 200 nm when 10 and 15 mol % Fe were added. This may be due to the capacity of the Fe ions to disrupt the normal order of the ZnO crystal lattice, resulting in crystal growth expansion (Chen et al., 2007)(Wang et al. , 2009).

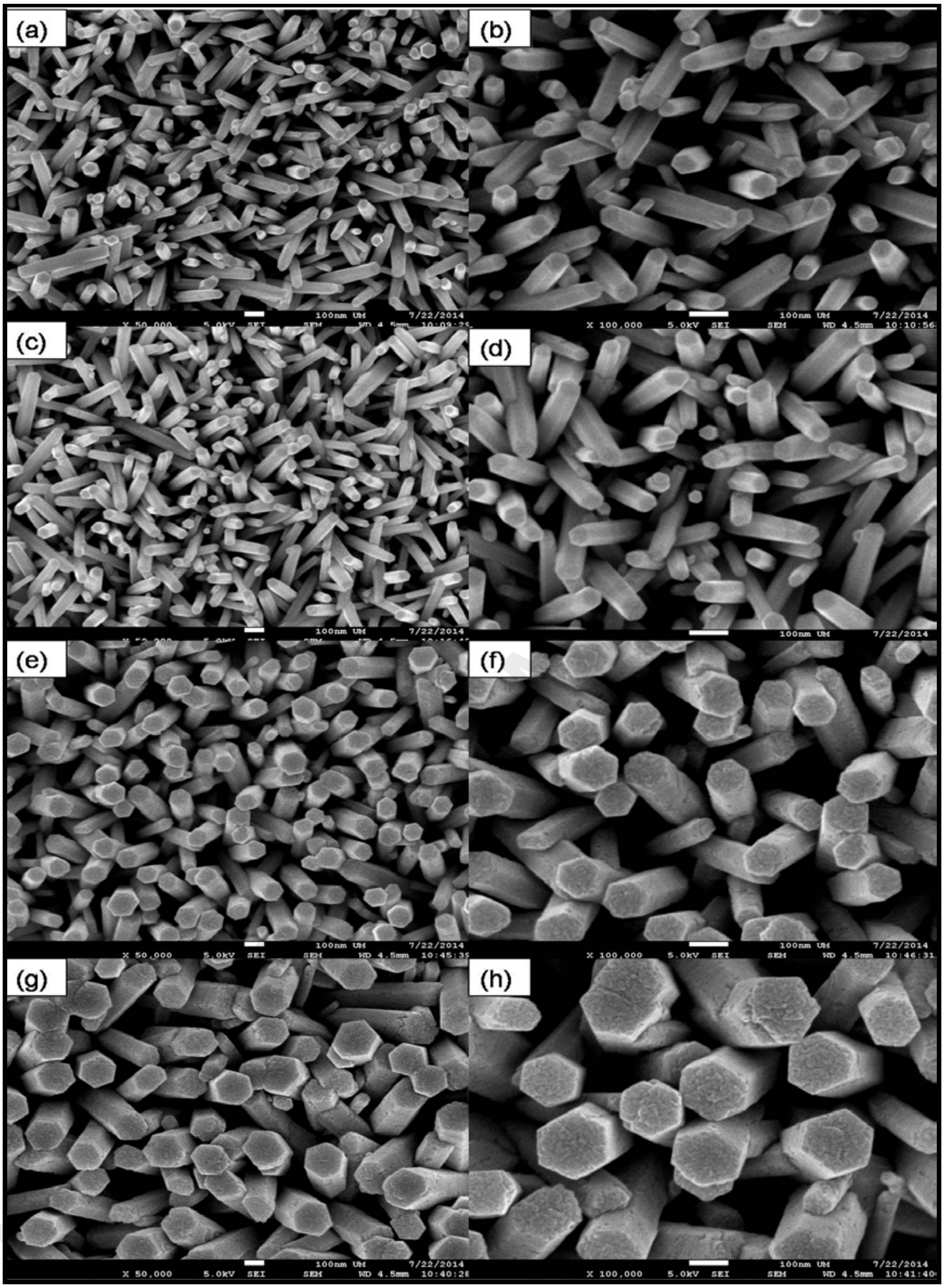

Figure 3.10: FESEM images of (a,b) pure ZnO nanorods, (c,d) 5, (e,f) 10 and (g,h) 15 mol % Fe-doped ZnO nanorod at 50, 000 and 100k magnification.

The morphology and structure of Fe-doped ZnO nanorods have been characterized in detail using TEM. Figure 3.11 shows the TEM images of ZnO nanorods. The nanorods appeared to be well formed (Figure 3.11 (a)). The corresponding HRTEM image is shown in Figure 3.11 (b) and (c). The HRTEM image for an area marked by red circle in Figure 3.11 (a) gave a d-spacing value of 0.25 nm for ZnO nanorods which was attributed to (002) plane indicating growth along [001] direction(Uhm, Sun Han, Rhee, & Choi, 2013).

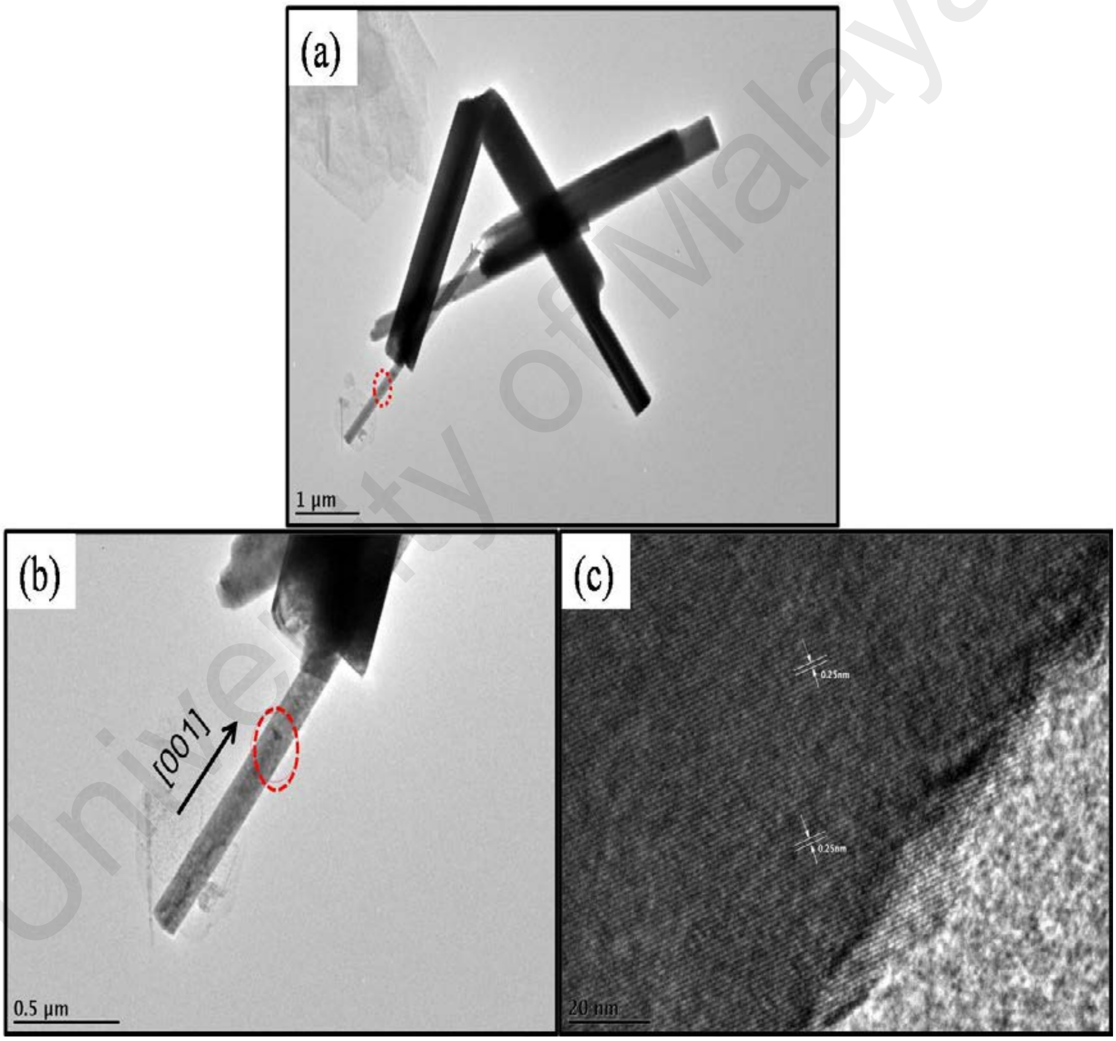

Figure 3.11: TEM images at (a) low, (b) high resolution and (c) HRTEM image of ZnO nanorods.

Figure 3.12 depicts the XRD patterns for the pure and Fe-doped ZnO nanorods grown with various dopant concentrations. The XRD pattern shown in Figure 3.12 (i) indicate all the ZnO nanorods exhibited polycrystalline with a structure that belongs to the ZnO hexagonal wurtzite type. For pure ZnO nanorods, it exhibits a broad background peak in the XRD spectrum. A sharp and intense peak was produced when Fe was doped into the ZnO stock solution.

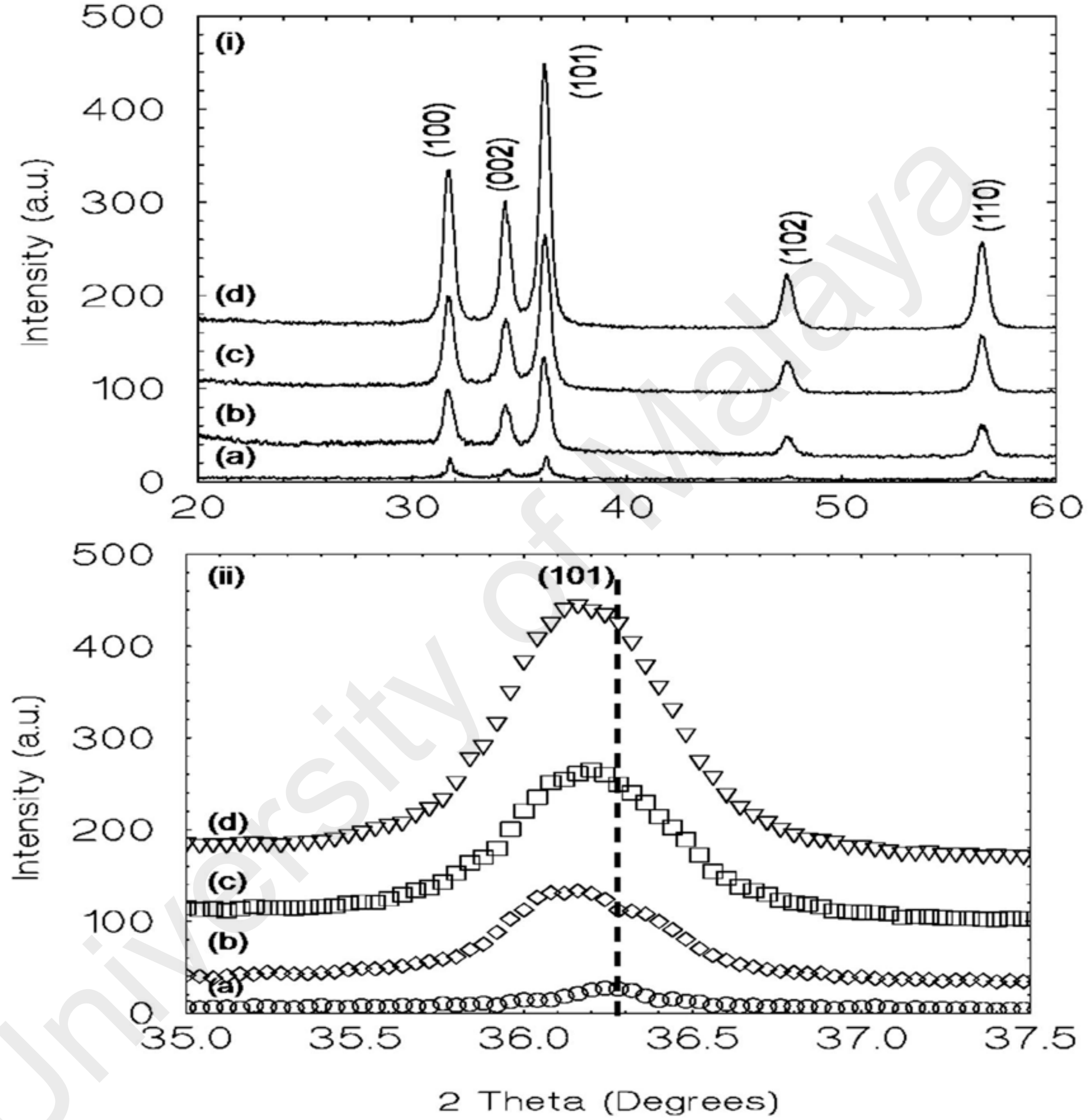

Figure 3.12: (i) XRD pattern and (ii) enlargement of XRD pattern between range 35-37.5° for (a) pure ZnO nanorods, (b) 5, (c) 10 and (d) 15 mol % Fe-doped ZnO nanorods.

From Figure 3.12 (ii), the XRD was analyzed between the ranges of 30 – 37.5°. The position of (101) peak was at 2θ = 36.26°, 36.20°, 36.16° and 36.12° for pure ZnO, 5,10 and 15 mol % Fe-doped ZnO nanorods, respectively which indicated that the position of (101) peak shifted to lower angles with increasing Fe concentration. The lattice constant, ‘c’ increased from 5.207 Å to 5.220 Å, indicating that Fe^{2+} was substituted into the ZnO lattice. The increase in "c" might be due to the difference of ionic radii of Fe^{2+} and Fe^{3+} at 0.078 nm and 0.068 nm, respectively, with Zn^{2+} at 0.074 nm (Xu & Li, 2010)(Chen et al., 2007)(Wang et al., 2009). Difference valence state of Fe ions (Fe^{2+} or Fe^{3+}) that replaced Zn^{2+} in lattice site will affect the degree of lattice distortion which resulted in lattice strain in ZnO thin film (Chen et al., 2006) . Hence, this will affect the ZnO crystal structure which shows the degradation in crystallinity. However, this observation contradicted the result reported by Linhua et al. (Linhua et al., 2010) and Hassan et al. (Hassan et al., 2012) who showed that the peak position of (002) reflection plane shifted to the larger diffraction angle, hence results in decreasing in lattice constant ‘c’ values.

The full width at half maximum of the (100) reflection peak (Figure 3.12 (ii))become wider as Fe ions were incorporated into ZnO lattice which is 0.55, 0.52 and 0.56^o for 5 mol % Fe-doped ZnO nanorods, 10 mol % Fe-doped ZnO nanorods and 15 mol % Fe-doped ZnO nanorod, repectively, compared to 0.30^o for pure ZnO nanorods (Table 3.1).

Table 3.1: Measured XRD properties of pure ZnO and Fe-doped ZnO nanorods.

Sample	**XRD (101) Peak Position (2θ)**	**Lattice constant, *a* (Å) (hkl)**	**Lattice constant, *c* (Å)(hkl)**	**d-spacing (nm)**	**FWHM (2θ)**
Pure ZnO nanorods	36.22	2.861	5.207	2.478	0.30
5 mol % Fe-doped ZnO	36.16	2.866	5.218	2.482	0.55
10 mol % Fe-doped ZnO	36.14	2.868	5.220	2.483	0.52
15mol % Fe-doped ZnO	36.13	2.868	5.220	2.483	0.56

It indicates that the doping of Fe ions occupies the regular lattice site of Zn^{2+} and degradation of crystallinity occurred. The lattice constant "a" and "c" were calculated using following equations (Suryanarayana & Norton, 1998):

$$a = \frac{\lambda}{\sin\theta\sqrt{3}} \tag{3.1}$$

and

$$c = \frac{\lambda}{\sin\theta} \tag{3.2}$$

where λ is the X-ray wavelength of the incident CuKα radiation (0.154056 nm). The calculated lattice constant 'a' and 'c' for pure and Fe-doped ZnO nanarods are shown in Table 3.1.

The Raman shift spectra of pure ZnO and Fe-doped ZnO nanorods are shown in Figure 3.13. Figure 3.13 (i) shows a typical Raman shift of (a) pure, (b) 5 mol %, (c) 10 mol % and (d) 15 mol % Fe-doped ZnO nanorods in the range of 250 and 700 cm^{-1}.

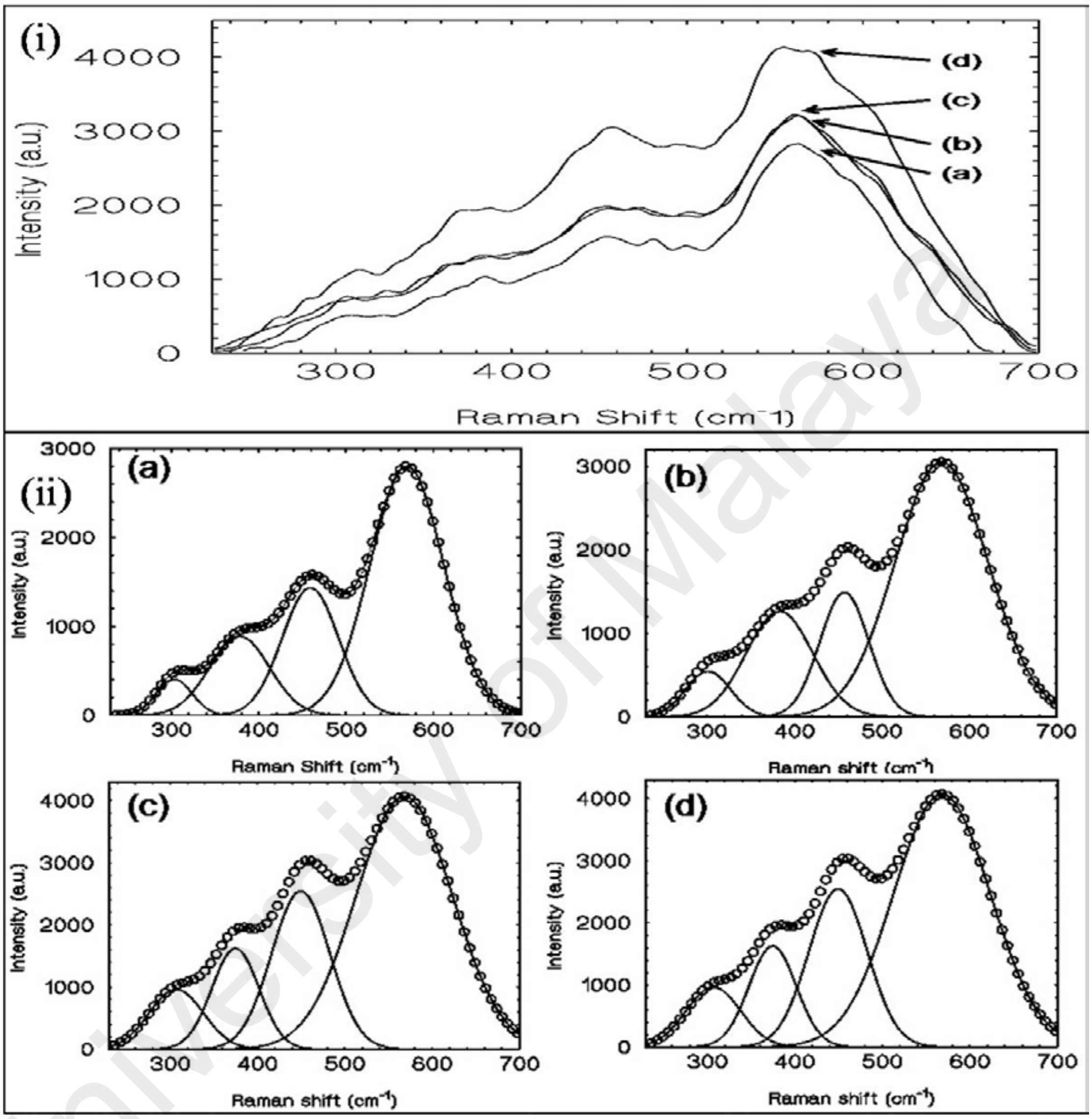

Figure 3.13: (i) Raman spectra and (ii) Gaussian fitting of Raman spectra of (a) pure ZnO nanorods, (b) 5, (c) 10 and (d) 15 mol % Fe-doped ZnO nanorods.

Pure ZnO and Fe-doped ZnO nanorods showed identical Raman spectra shape. Crystalline ZnO has sets of optical phonon at the zone center which is $A_1 + E_1 + 2B_1 + 2E_2$. Group theory predicts that there are two A_1, two E_1, two E_2 andtwo B_1 in the Raman spectra of ZnO. $A_1 + E_1 + 2E_2$ are attributed to Raman active mode, $2B_1$ is Raman silent modes and $A_1 + E_1$ is infrared actives modes. In addition, the vibration of A_1 and E_1 modes can polarize in unit cell, which creates a long range electrostatic field splitting the polar modes into longitudinal optical (LO) and tranverse optical (TO) components (Fonoberov & Balandin, 2004)(Damen, Porto, & Tell, 1966).

The Raman peak position was also fitted to the Gaussian functions and the graph are presented in Figure 3.13 (ii). Four Gaussian curves were extracted from the spectrum and details of symmetry and wave number (cm^{-1}) for all samples are tabulated in Table 3.2 below.

Table 3.2: Measured Raman shifts from pure and Fe doped ZnO and possible peak assignment (Damen et al., 1966).

Symmetry	***Peak position ZnO bulk ($cm^{-1)}$**	**Peak position of nanorods**			
		Pure ZnO	**5 mol % Fe ZnO**	**10 mol % Fe ZnO**	**15 mol % Fe ZnO**
-	-	303.2	301.2	297.7	307
A_1 (TO)	380	377.9	382.9	385.8	374.7
Quasi A_1 (TO)	395	-	-	-	-
E_1 (TO)	413	-	-	-	-
E_2 (high)	444	459	457.1	457.8	449.5
[E_2 (high) + E_2 (low)]	-	569.6	568.3	569.4	568.1

The Raman spectrum of pure ZnO nanorods and Fe-doped ZnO nanorods shows four prominent peaks. For pure ZnO nanorods, peaks were observed at 377, 459 and 569 cm^{-1} assigned to A_1 (TO), E_2 (high) and [E_2 (high) + E_2 (low)] modes, respectively as shown in Table 3.2. The peak at 303.2 cm^{-1} cannot be explained within the framework of bulk single phonon modes but can be attributed to the multiphonon scattering process (Liu et al., 2007)(Adhyapak et al., 2014).

Figure 3.14 shows the room temperature photoluminescence spectra of pure and Fe-doped ZnO nanorods. There are three emission bands appeared in PL spectra for all samples.

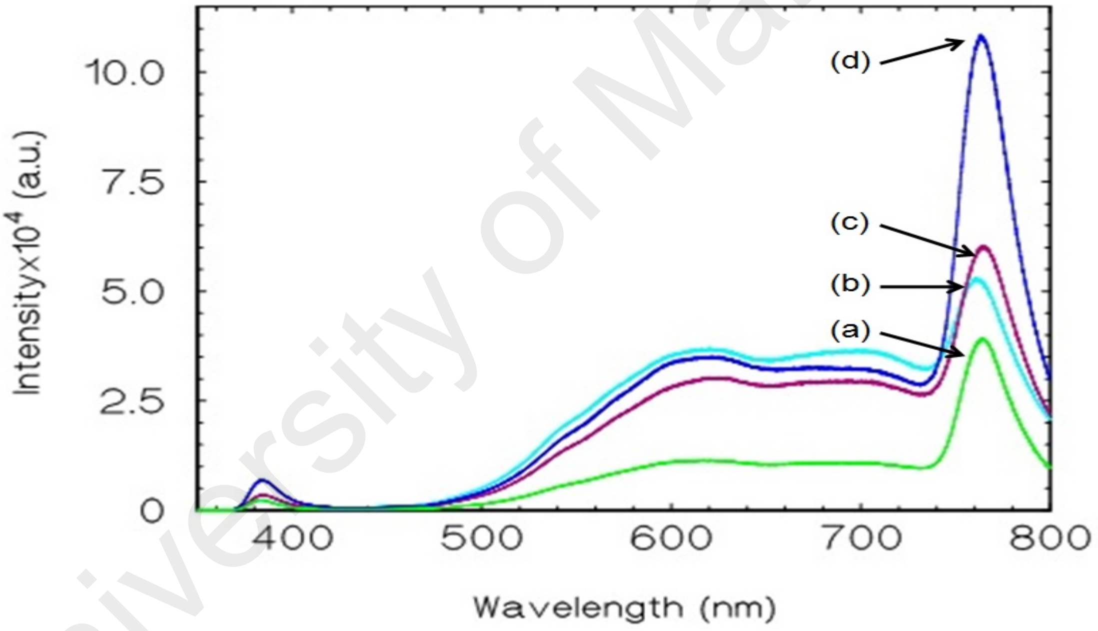

Figure 3.14: PL spectra of (a) pure ZnO nanorods, (b) 5, (c) 10 and (d) 15 mol % Fe-doped ZnO nanorods.

Emission in the ultraviolet which called the near band edge (NBE) emission is associated with exciton emission. From Figure 3.14, NBE emission was observed for (a) pure ZnO nanorods and Fe-doped ZnO nanorods at different concentrations of (b) 5, (c) 10 and (d) 15 mol %. The PL peak position at NBE emission for all samples were similar centered approximately at 384 nm. Another characteristic PL emission form ZnO is the deep level emission (DLE) caused by radial recombination of photogenerated hole with an electron that belongs to the native defect in the surface or sub-surface of materials. From the PL spectra (Figure 3.14 (a)-(d)), a broader green-yellow emission around 590 nm was observed similar to those observed elsewhere(Giri et al., 2011)(Tian et al., 2013). From Figure 3.14, a relatively stronger peak in the near-infrared (IR) wavelength range around 760 nm for pure and Fe-doped ZnO nanorods. Fang et al., and Lee et al., reported that, the peak around 750 and 765 nm attributed to near-IR region which is due to second order diffraction (Fang, Wu, Lee, & Hsien, 2008)(Lee et al., 2007). In order to quantify the emission peaks, the broad spectrum has been deconvoluted by Gaussian fitting as illustrated in Figure 3.15.

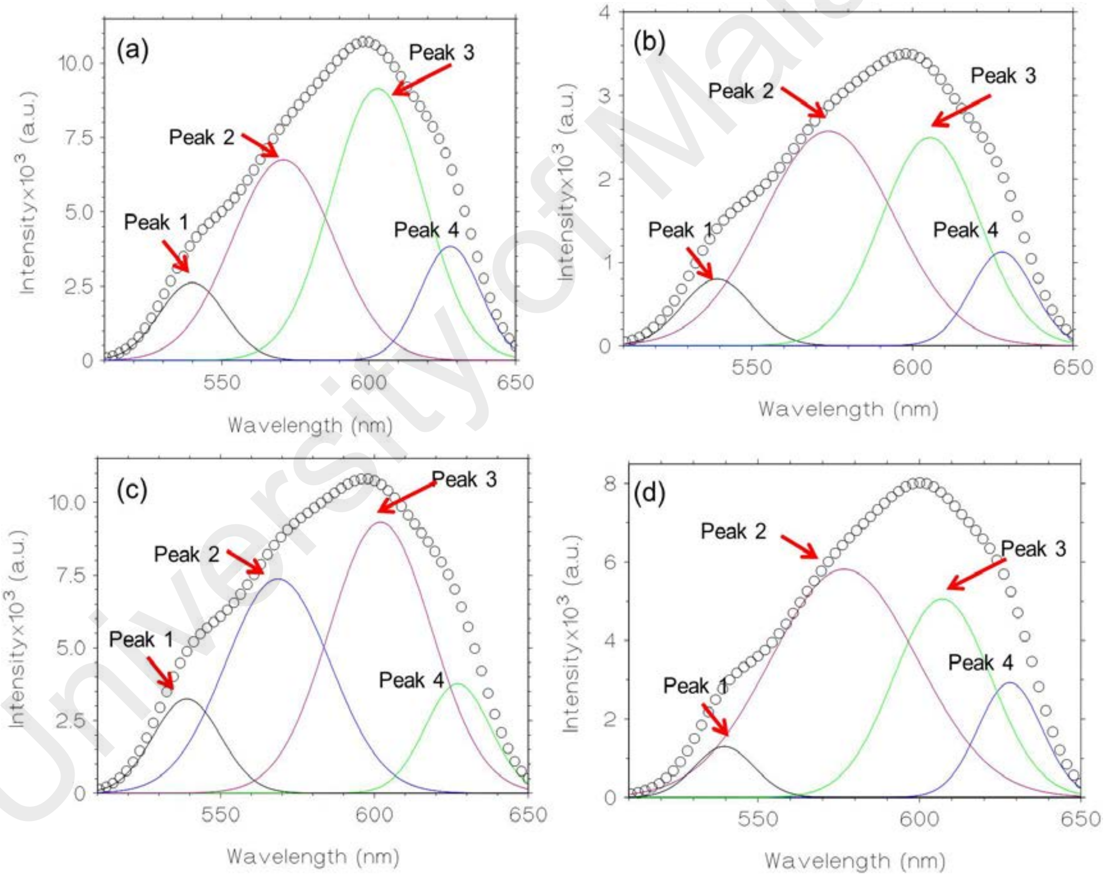

Figure 3.15: Gaussian fitted PL spectrum of (a) pure ZnO nanorods, (b) 5, (c) 10 and (d) 15 mol % Fe-doped ZnO nanorods.

The Gaussian fitting was made in order to find the various emission peaks contained in the visible emission region spectra, which is referred to as deep-level emission and attributed to recombination of electrons deeply trapped in oxygen vacancies and zinc interstitials, with photogenerated holes (Srivastava et al., 2009)(Dijken et al., 2000). The details of fitted peaks are shown in Table 3.3 where pure and Fe-doped ZnO samples exhibited similar PL peaks for all band emission.

Table 3.3: Gaussian fitting decomposition data of the PL emission spectra for pure ZnO nanorod and Fe- doped ZnO nanorods at various concentrations.

Sample	**Peak 1 (nm)**	**Peak 2 (nm)**	**Peak 3 (nm)**	**Peak 4 (nm)**
Pure ZnO nanorods	539	568	602	626
5 mol % Fe-doped ZnO nanorods	540	572	601	622
10 mol % Fe-doped ZnO nanorods	539	568	602	627
15 mol % Fe-doped ZnO nanorods	539	574	605	625
Proposed transition	Transition from deep donor level by the oxygen vacancies to valence band.	Transition of Zn_i to V_{Zn}	Hydroxyl group	Oxygen interstitial
References	(Ding, Yan, & Xue, 2012) (Liu et al., 2004)	(Karthikeyan & Pandiyarajan, 2010)	(Tam et al., 2006) (Djurišić et al., 2007)	(Liu et al., 2004)

Similar emission peak at about 539 and 540 nm for pure ZnO, 5, 10 and 15 mol % Fe-doped ZnO nanorods spectra were attributed to transition from hole trapped at the doubly ionized oxygen vacancy (Ding et al., 2012)(Liu, 2004). The emission at 568 nm for pure ZnO and 10 mol % Fe-doped ZnO nanorods, 572 nm and 574 nm for 5 and 15 mol % Fe-doped ZnO nanorods were attributed to the transition of zinc interstitial to zinc vacancies (Karthikeyan & Pandiyarajan, 2010). The orange-yellow emission observed at 602 nm for pure ZnO and 10 mol % Fe-doped ZnO nanorods, 601 nm and

605 nm for 5 and 15 mol % Fe-doped ZnO nanorods, respectively may originated fromstructural defect, single ionized vacancy and impurities (Vanheusden et al., 1996)(Wu & Liu, 2002). Previous literature reported that this emission peak might be attributed to the presence of hydroxyl groups (Tam et al., 2006)(Djurišić et al., 2007). Lastly, PL peak at 626 nm for pure ZnO nanorod, 622 nm, 627 nm and 625 nm for 5, 10 and 15 mol% Fe-doped ZnO nanorods were ascribed to the oxygen interstitial (Liu, 2004).

In summary quasi-aligned pure ZnO and Fe-doped ZnO nanorods were prepared by sol-gel immersion method. The diameter of nanorod increased as the concentration of Fe-doping increased. The diameter of pure ZnO nanorods in average between 50 and 75 nm, while when Fe was incorporated to the ZnO samples, the diameter increasedto between 150 and 200 nm, respectively. XRD spectrum showed that ZnO nanorods were wurtzite hexagonal crystal structure with good crystal quality and peak positions were shifted to the lower diffraction angles with Fe doping. The lattice constant ‘c’ increased as Fe incorporated to the ZnO, indicating that Fe^{2+} was substituted into the ZnO lattice. Raman spectra for pure ZnO and Fe-doped ZnO nanorods also revealed the inhibition of surface defects with Fe doping. The photoluminescence of pure and Fe-doped ZnO nanorodswere similar major bands in the uv and green regions.

3.2.4 Aluminum doped zinc oxide nanorods deposited on aluminum substrates

Pure and aluminum (Al) doped ZnO nanorods were synthesized by sol-gel synthesis method on seeded Al substrates. Figure 3.16 shows the FESEM images of pure and Al-doped ZnO nanorods at various doping level. All samples exhibited rod-like structure but different in distribution and aspect ratio.

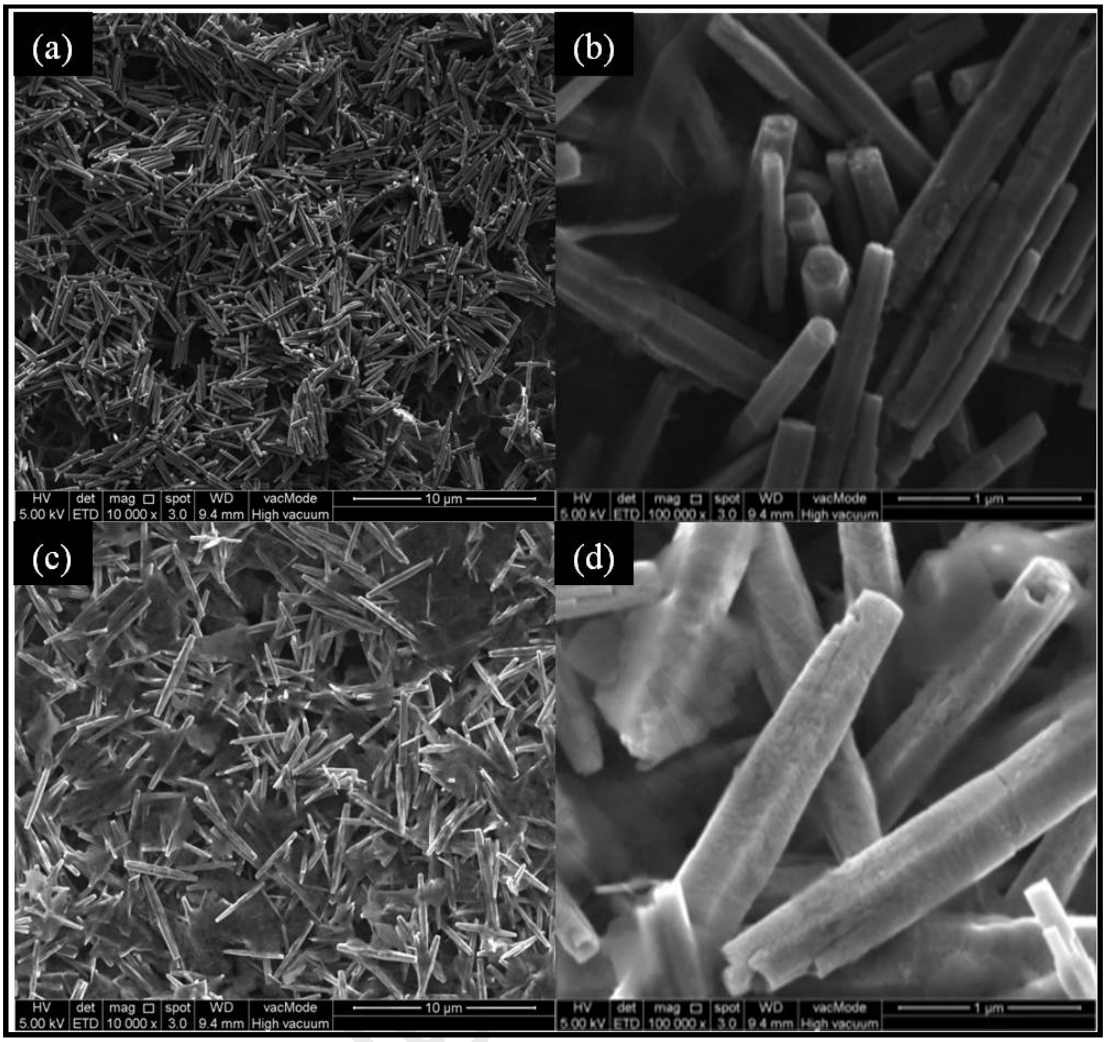

Figure 3.16: FESEM images of (a, b) pure ZnO, (c, d) 1, (e, f) 3 and (g, h) 5 mol % Al - doped ZnO nanorods.

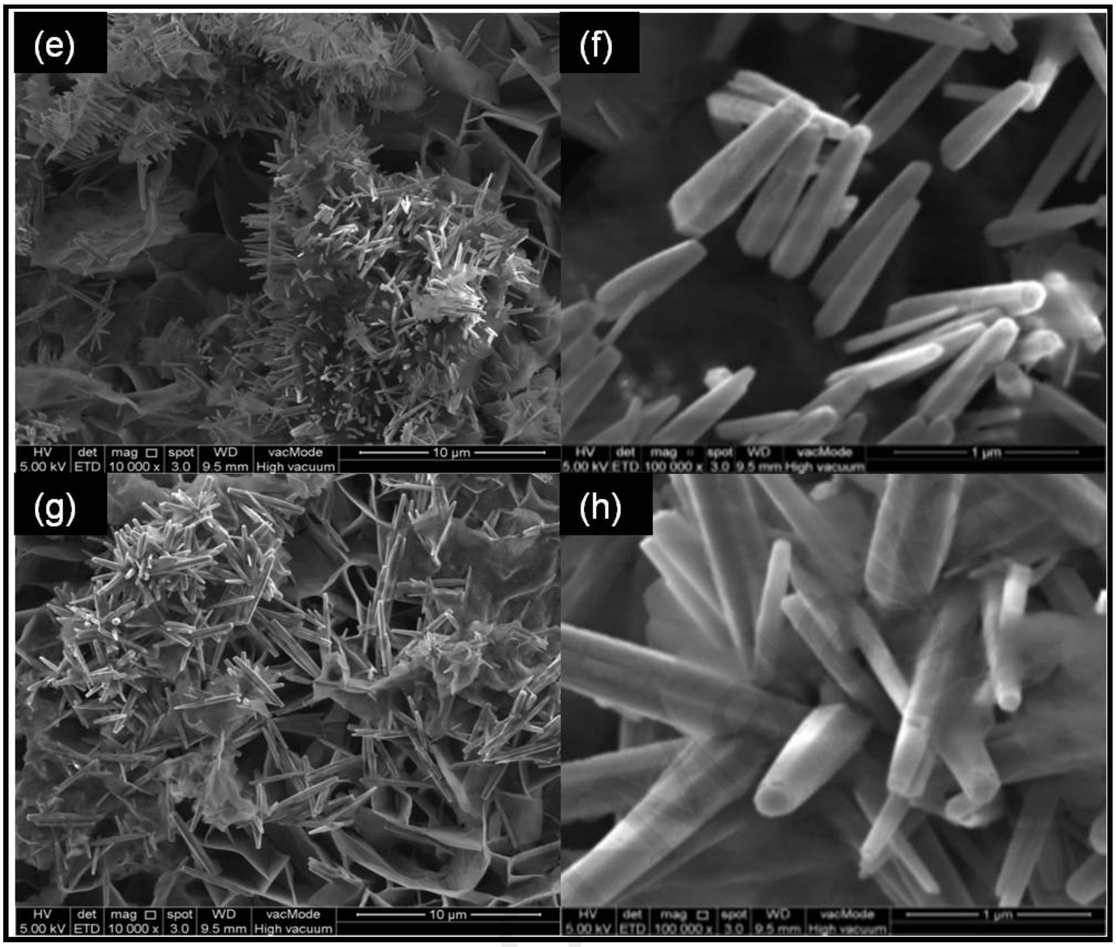

'Figure 3.16, continued': FESEM images of (a, b) pure ZnO, (c, d) 1, (e, f) 3 and (g, h) 5 mol % Al -doped ZnO nanorods.

For pure ZnO nanorods (Figure 3.16 (a)), the nanorods were randomly distributed with estimated similar rod size of 2 -3 μm in length and 100 – 250 nm in diameter. From higher magnification image (Figure 3.16 (b)), the end of the rod formed a flat hexagonal structure. For 1 mol % Al-doped ZnO nanorods (Figure 3.16 (c)), the nanorods were formed randomly distributed. The estimated size of the rod is about 3 – 4 μm in length and diameter of 100 – 200 nm. The end of the rod appeared not well formed compared to pure ZnO nanorods. For 3 mol % Al-doped ZnO nanorods (Figure 3.16 (e)), the cone-rod liked structures formed agglomerated with a non-uniform distribution. The cone-rod like structures have sharp tips at the end of the rod (Figure 3.16 (f)). The estimated length of the cone-rod like structure was about 1 - 3 μm. Figure 3.16 (g) and (h) show the images of 5 mol % Al-doped ZnO nanorods. The ZnO nanorods were attached together and formed as a bundle on top of ZnO sheet-liked structure. The estimated size of rod was 2 - 3 μm in length and 100 - 300 nm in diameter. The density of 5 mol % Al-doped ZnO nanorods was less compared to the other samples. There was a sheet-liked layer of ZnO attached to the nanorods. Pure ZnO and Al-doped ZnO nanorods samples were randomly distributed and formed non-quasi-aligned structures. This might be due to the imperfect alignment on the seed layer during the preparation process.

Figure 3.17 shows the EDX spectrum for the pure ZnO and Al-doped ZnO nanorods. The EDX spectra of pure ZnO nanorods (Figure 3.17 (a)) composed of Zn and O element with almost stoichiometric content (Zn: O = 43.52:56.48). Figure 3.17 (b), (c) and (d) shows the EDX spectra of ZnO nanorods doped with 1, 3 and 5 mol % Al revealed the presence of O, Zn and Al elements with atomic % for each sample is (Zn:O:Al =63.17:32.59:4.24), (Zn:O:Al =67.25:28.34:4.41), and (Zn:O:Al =66.37:28.16:5.47), respectively.

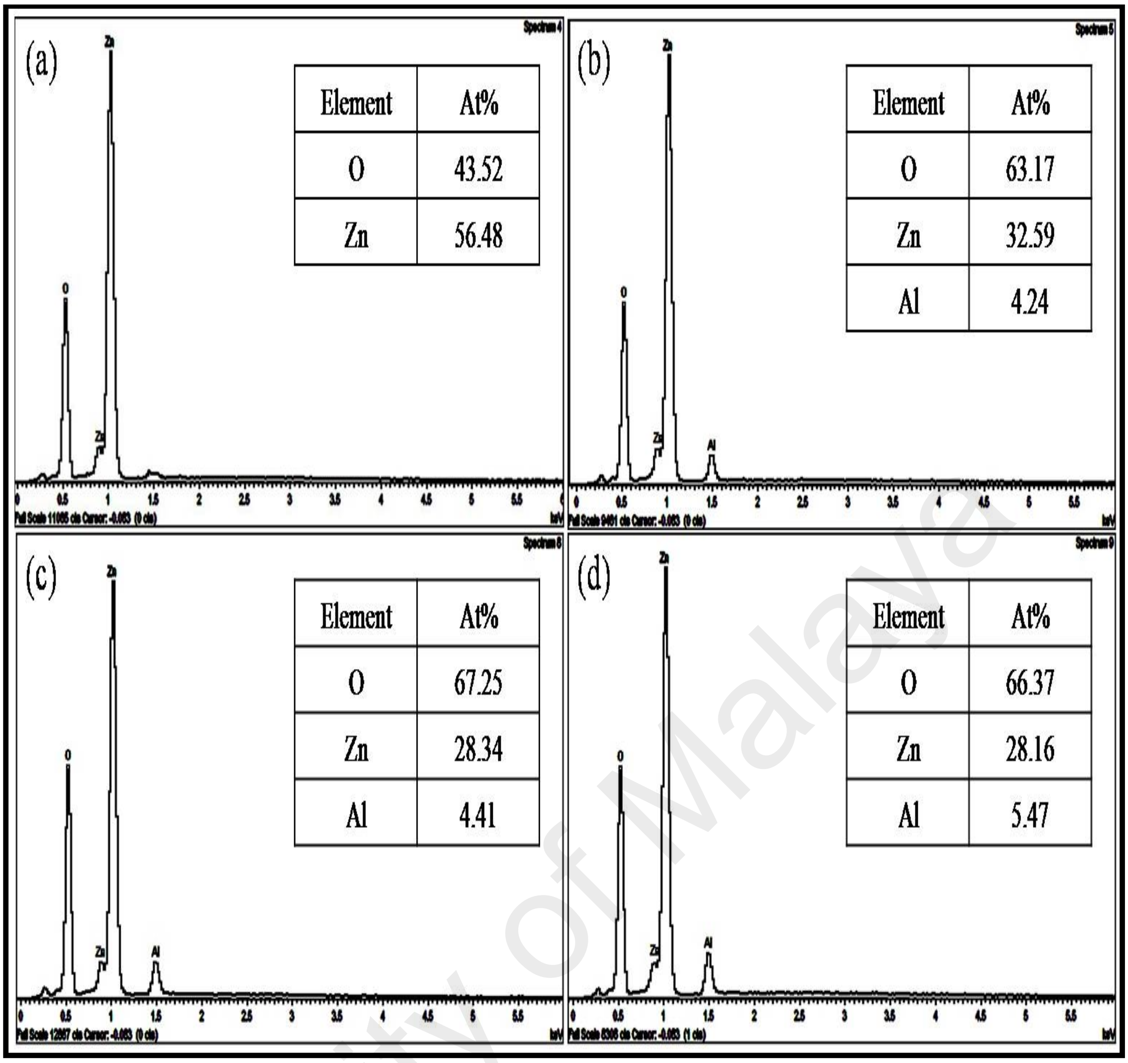

Figure 3.17: EDX spectrum of (a) pure ZnO, (b) 1, (c) 3 and (d) 5 mol % Al-doped ZnO nanorods.

Figure 3.18 shows the variation of doping levels of Al-doped ZnO nanorods prepared at different concentration obtained from quantified EDX analysis. As expected, the doping level of Al increased as the concentration of the $Al(NO_3)_3$ used during synthesis increased with value of 0.13, 0.16 and 0.19 % for 1, 3 and 5 mol % Al-doped ZnO nanorods, respectively.

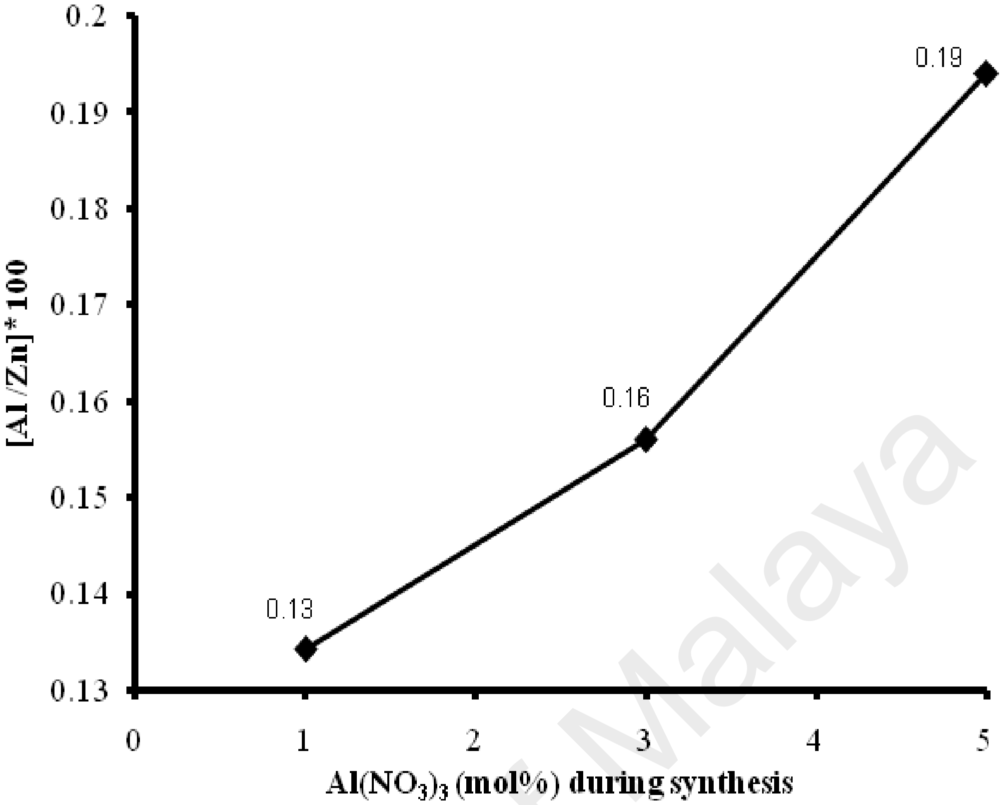

Figure 3.18: The inclusion of Al in ZnO with respect to the starting amount of Al.

The morphology and structure of Al-doped ZnO nanorods have been characterized using TEM. Figure 3.19 shows the TEM images of pure ZnO nanorods. Figure 3.19 (a) shows a typical section of nanorod. The spot used for the higher magnification micrograph is indicated (marked by a circle) and the magnified image is shown in Figure 3.19 (b). The lattice spacing is found to be approximately 0.25 nm for pure ZnO nanorods corresponding to the distance between two crystal planes.

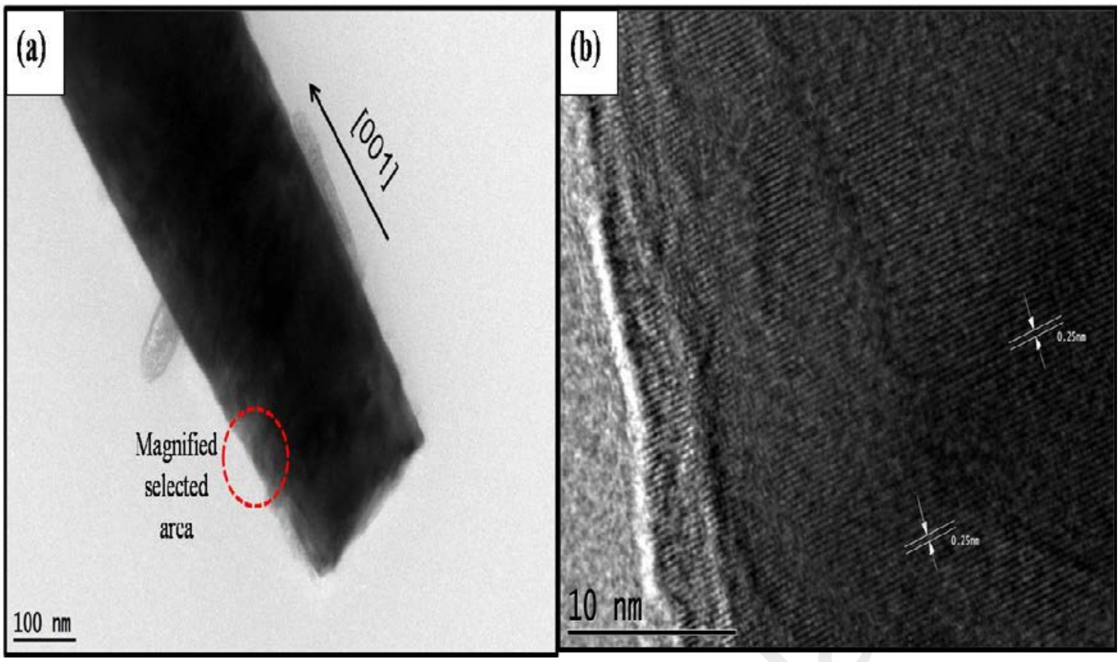

Figure 3.19: HRTEM of (a) pure ZnO nanorod and (b) showing lattice spacing of the pure ZnO nanorod.

Figure 3.20 exhibits the typical TEM image of 1 mol % Al-doped ZnO nanorod. The nanorod was appeared in a well formed (Figure 3.20 (a)). The HRTEM image in Figure 3.20 (b) showed that the interplanar spacing of the nanorod was 0.24 nm corresponding to the d-spacing of (002) plane of ZnO, which indicated that the nanorod grew along the [001] direction. From the HRTEM images, it can be verified that the synthesized products have highly crystalline structure, which have potential used in field emission display applications.

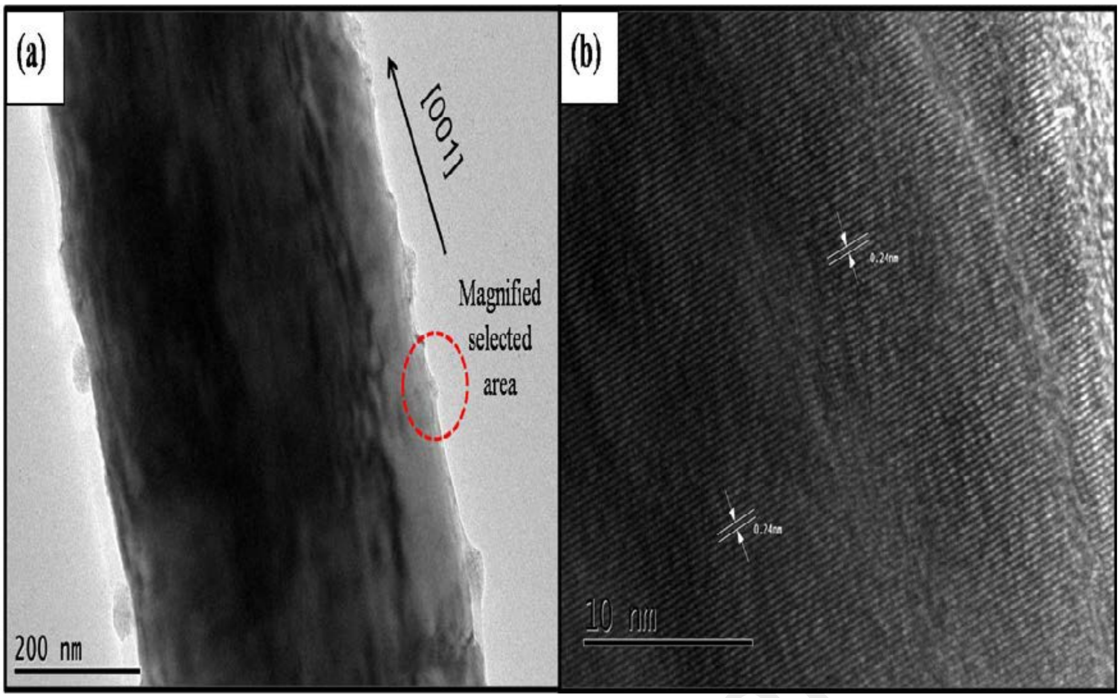

Figure 3.20: (a) TEM image and (b) HRTEM image showing lattice spacing of 1 mol % Al doped ZnO nanorods.

The XRD spectra of the pure and Al-doped ZnO nanorods are presented in Figure 3.21. The diffraction peaks were measured on the XRD spectrum in the range 2θ= 20°- 60°. All spectra exhibit crystal diffraction planes of (100), (002), (101), (102) and (110) respectively. Besides the diffraction peaks of the aluminium substrate (labelled as *), all diffraction peaks for all samples are indexed to the wurtzite phase of ZnO (hexagonal, $P6_3mc$) which fit with the standard JCPDS No. 79-2205. The diffraction peaks of pure ZnO nanorods (Figure 3.21 (a)(i)) were sharp and intense, imply the good crystallization of the ZnO sample. For 1 mol % Al-doped ZnO nanorods (Figure 3.21 (a)(ii)), the diffraction peaks was also intense and sharp similar to pure ZnO nanorods. The diffraction peaks of 3 and 5 mol % Al-doped ZnO nanorods were broader and appeared noisier indicating the effect of Al doping on the crystallinity of the ZnO samples.

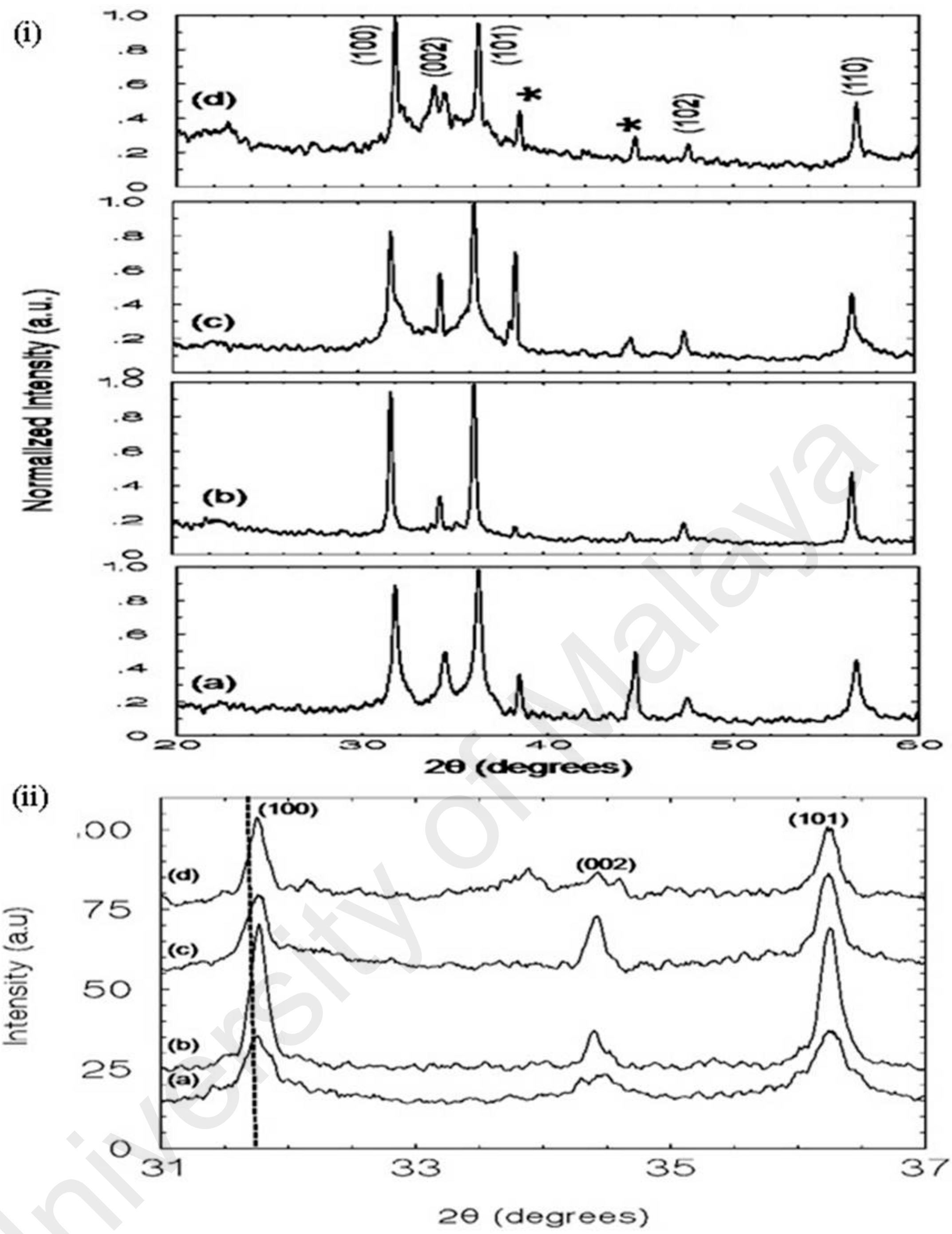

Figure 3.21: (i) XRD pattern between range 20 - 60 ° and (ii) enlargement of XRD pattern between range 31 – 37 ° for (a) pure ZnO, (b) 1, (c) 3 and (d) 5 mol % Al-doped ZnO nanorods. The (*) represent the existing of Al peak from the substrate.

As shown in Figure 3.21 (ii), there was a slight shift of peak position for (002), (101) and (100) plane for pure ZnO nanorod (a) and Al-doped ZnO nanorod deposited at (b) 1 mol %, (c) 3 mol % and (d) 5 mol %. The peak position of the (100) shifted towards higher 2θ values with increasing of Al concentration. This might be due to two factors which are the formation of stress by ion size difference between Zn and Al (ionic radii of Zn^{2+} and Al^{3+} are 72 pm and 53 pm respectively) and also the segregation of Al in the grain boundaries for high Al doping concentrations (Srinivasan et al., 2007)(Zhou et al., 2007). Similar shift also was observed by Kim et al. that have been succesfull synthesized aluminum doped zinc oxide films prepared by radio frequency magnetron sputtering (Park, Ma, & Kim, 1997). However, Zi-qiang et al. discovered shift towards lower 2θ value for the Al-doped ZnO thin films prepared by sol-gel method (Zi-qiang et al., 2006). They reported that, increasing the amount of doping will cause crystallinity deterioration of film and this occurrence may be attributed to the different ion size between zinc and aluminium.

The Raman spectra of the pure and Al-doped ZnO nanorods at different concentrations are depicted in Figure 3.22. Raman scattering measurement was done to determine the structures of the pure and Al-doped ZnO nanorod. The crystal perfection and structural defects of ZnO can be clearly defined by this measurement. As discussed earlier in Section 3.2.3, crystalline ZnO has sets of optical phonon at the zone center which is $A_1 + E_1 + 2B_1 + 2E_2$.

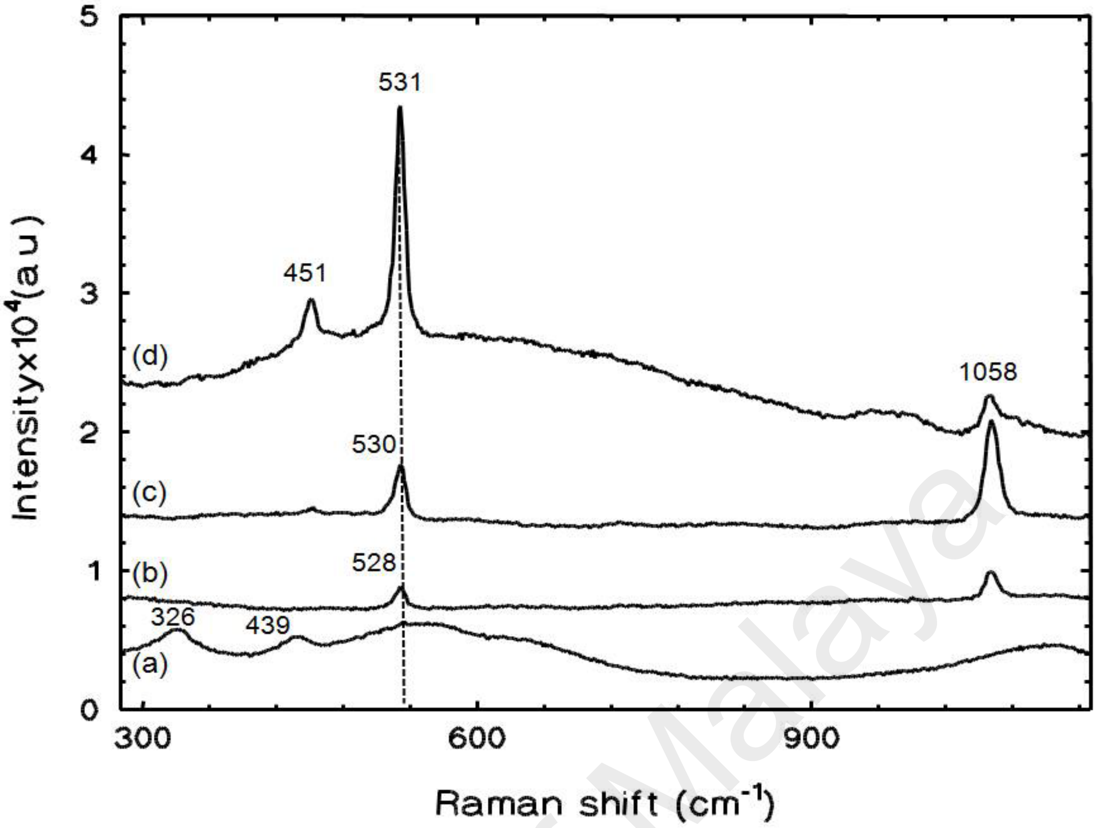

Figure 3.22: Raman spectra of (a) pure ZnO, (b) 1, (c) 3 and (d) 5 mol % Al-doped ZnO nanorods.

For the pure ZnO nanorods (Figure 3.22 (a)), two Raman peaks were observed. Raman peak at 439 cm^{-1} corresponded to the E_2 mode, the characteristic of Raman active peak for the wurtzite hexagonal phase of ZnO (Li et al., 2010). Besides, peak at 326 cm^{-1} which was attributed to the $E_{2H} – E_{2L}$ mode (multi phonon process) for the pure ZnO nanorod was observed. Raman spectra pattern was changed when Al was doped into the ZnO sample. Peak intensity at 439 cm^{-1} was not detected Figure 3.22 (b), (c) and (d), which indicated that Al-doped ZnO nanorods have much higher oxygen vacancies concentration than pure ZnO nanorod (Ruan et al., 2012). Another difference in Raman spectrum of ZnO nanorod doped with 1, 3 and 5 mol % Al was the appearance of one additional strong and sharp peak which is centered at about 528, 530 and 531 cm^{-1}, respectively. There are reports on the effect of dopant on the Raman spectra of ZnO however the issue remained controversial. Ruan et al. discovered a new Raman peak from sample Mn-doped ZnO films at 526 cm^{-1} which they believed that the additional mode is originate from the lattice defects (Ruan et al., 2012). Eskandari et al. also observed appearance of new Raman peak at about 750 cm^{-1} and suggested that this influenced by the doping of Al element which caused from the formation of defects (oxygen vacancies or zinc interstitial) or impurities (Al) (Eskandari, Ahmadi, & Ahmadi, 2010). Therefore, a possible explanation for this might be the additional Raman mode is associated with Al impurities when dopant was added to the ZnO nanorod samples.

Figure 3.23 shows the room temperature PL spectrum of pure ZnO nanorods and ZnO nanorods doped with 1, 3 and 5 mol % Al. The overlapping peaks for each graph were fitted with Gaussian curves. Each samples consist of two emission bands, a small and weak band in the uv region (~390 nm) which was attributed to the exciton-related activity (Uthirakumar et al., 2007)(Kwok et al., 2006), and a relatively strong emission band in the visible (green-orange-red; ~560 nm) region (Chen et al., 2009). The list of PL peaks obtained from Gaussian curve fittings are summarized in Table 3.4.

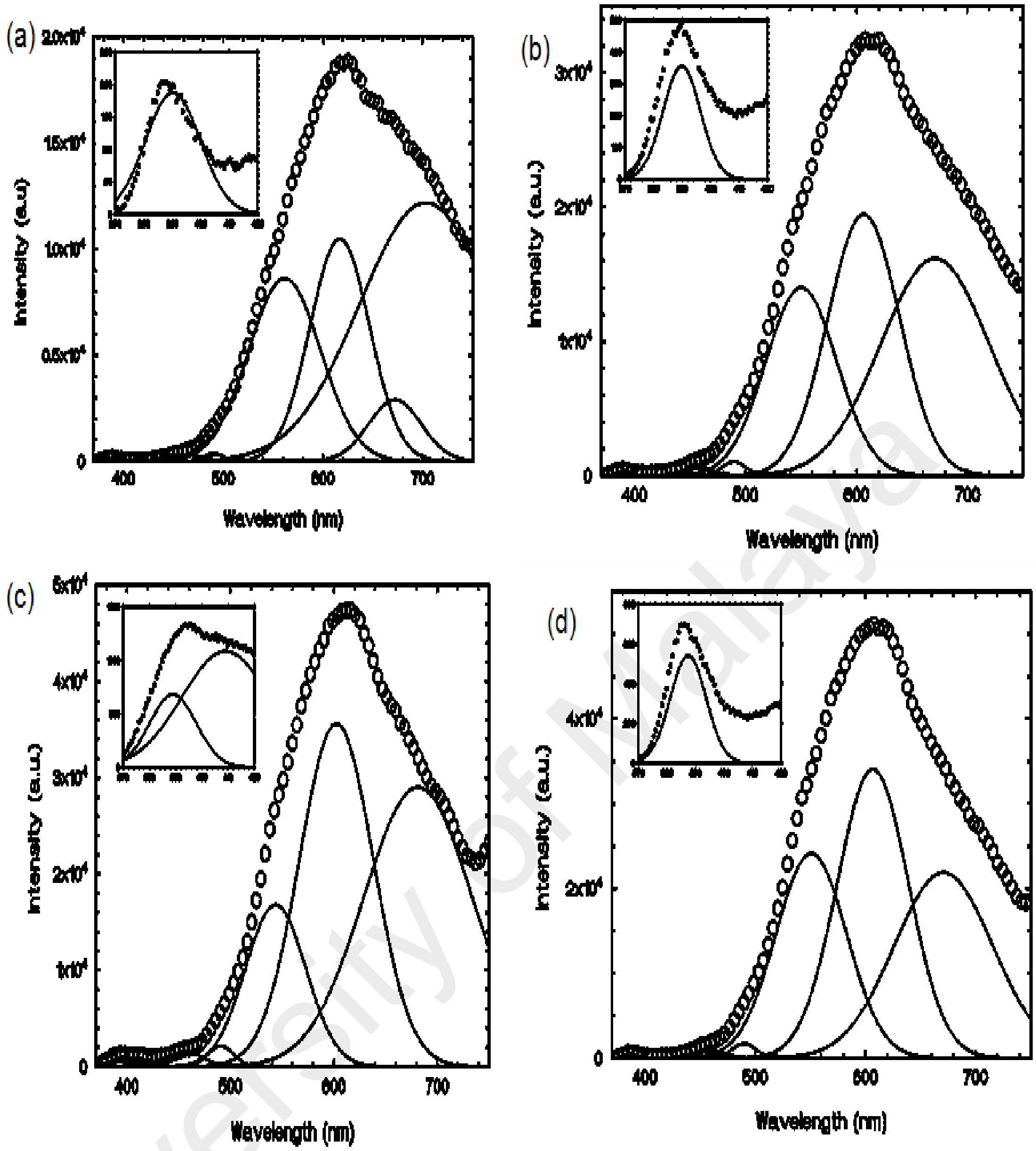

Figure 3.23: Gaussian fitted PL spectra at green emission region of (a) pure ZnO, (b) 1, (c) 3 and (d) 5 mol % Al-doped ZnO nanor

Table 3.4: De-convolution of the emission spectra of pure ZnO, 1, 3 and 5 mol% Al-doped ZnO nanorods.

Sample name	Peak position,Energy (nm) (eV)	Proposed transition	Refs.
Pure ZnO nanorod	390.2 (3.18)	UV emission (NBE)	(Uthirakumar et al., 2007)(Kwok et al., 2006)
	458.7 (2.70)	Transition of Zn_i to V_{Zn}	(Wen et al., 2005)(Alvi, Willander, & Nur, 2010)
	490.5 (2.53)	Transition of Zn_i to V_{Zn}	(Wen et al., 2005)
	561.7 (2.21)	Transition of Zn_i to V_{Zn}-	(Reddy et al., 2011)
	616.9 (2.01)	Oxygen interstitial/ Hydroxyl group	(Liu et al., 2004)(Moura et al., 2010) (Tam et al., 2006)
	672.1 (1.85)	Oxygen vacancy	(Alvi et al., 2010)
1.0 mol % Al-doped ZnO nanorod	389.9 (3.18)	UV emission (NBE)	(Uthirakumar et al., 2007)(Kwok et al., 2006)
	457.6 (2.71)	Transition of Zn_i to V_{Zn}	(Wen et al., 2005)(Alvi et al., 2010)
	489.7 (2.53)	Transition of Zn_i to V_{Zn}	(Wen et al., 2005)
	550.3 (2.25)	Transition of Zn_i to V_{Zn}-	(Reddy et al., 2011)
	606.6 (2.04)	Oxygen interstitial/ Hydroxyl group	(Liu, 2004)(Moura et al., 2010) (Tam et al., 2006)
	670.7 (1.85)	Oxygen vacancy	(Alvi et al., 2010)
3.0 mol % Al-doped ZnO nanorod	389.0 (3.19)	UV emission (NBE)	(Uthirakumar et al., 2007)(Kwok et al., 2006)
	409.0 (3.03)	Exciton recombination	(Kim et al., 2007)(Ni et al., 2008)
	456.1 (2.72)	Transition of Zn_i to V_{Zn}	(Wen et al., 2005)(Alvi et al., 2010)
	490.6 (2.53)	Transition of Zn_i to V_{Zn}	(Wen et al., 2005)
	543.8 (2.28)	Transition of Zn_i to V_{Zn}-	(Reddy et al., 2011)
	602.6 (2.06)	Oxygen interstitial/ Hydroxyl group	(Liu, 2004)(Moura et al., 2010) (Tam et al., 2006)
	681.5 (1.82)	Oxygen vacancy	(Alvi et al., 2010)

'Table 3.4, continued': De-convolution of the emission spectra of pure ZnO, 1, 3 and 5 mol % Al-doped ZnO nanorods.

Sample name	Peak position,Energy (nm) (eV)	Proposed transition	Refs.
5.0 mol % Al-doped ZnO nanorod	387.4 (3.20)	UV emission (NBE)	(Uthirakumar et al., 2007)(Kwok et al., 2006)
	458.2 (2.71)	Transition of Zn_i to V_{Zn}	(Wen et al., 2005)(Alvi et al., 2010)
	490.0 (2.53)	Transition of Zn_i to V_{Zn}	(Wen et al., 2005)
	551.0 (2.25)	Transition of Zn_i to V_{Zn}-	(Reddy et al., 2011)
	606.9 (2.04)	Oxygen interstitial/ Hydroxyl group	(Liu, 2004)(Moura et al., 2010) (Tam et al., 2006)
	671.0 (1.85)	Oxygen vacancy	(Alvi et al., 2010)

The NBE emission was observed at the uv region at 390 nm for pure ZnO nanorod, 389 nm for 1 mol % Al-doped ZnO nanorod, 388 nm for 3 mol % Al-doped ZnO nanorod and 387 nm for 5 mol % Al-doped ZnO nanorod. This transition was due to the recombination of free excitons through the exciton-exciton collision process (Yun et al., 2010)(Li et al., 2006). It has also been assigned to the exciton transition from the localized level below the conduction band to the valance band. A slight blue-shift in the DLE emission peak occured for the doped ZnO with increasing of Al doping level. This might be due to the reduction of deep level emission and also possible to tune the uv emission of ZnO (Reddy et al., 2011)(Janotti & Walle, 2009). A peak centered at 458 nm was observed for pure ZnO nanorod while peak at 456 nm have been observed for ZnO nanorod doped with 3 mol % Al which was attributed to the recombination of electron from neutral deep donor level of Zinc interstitials (Zn_i) to an acceptor level of neutral Zinc vacancies (V_{Zn}) energy level (Reddy et al., 2011)(Wen et al., 2005)(Alvi et al., 2010). Additional peak in the UV band centered at 408 nm was also observed for doped ZnO nanorod which may arise from exciton recombination (Kim et al., 2007). Peak at about 489-490 nm attributed to transition energy from zinc interstitial to zinc vacancy have been observed for all samples (Wen et al., 2005). This transition also suggested that all Al-doped ZnO samples showed a trend of being blue-shifted with increasing the Al dopant concentration (Yun et al., 2010)(Zi-qiang et al., 2006).

There are possible defects that can contribute in a visible emission region (green-yellow -red region) in ZnO nanomaterial such as oxygen vacancies (V_o), Zinc vacancies (V_{Zn}), oxygen interstitials (O_i), Zinc interstitials (Zn_i) and oxygen antisites (substitution O at Zn position) (O_{Zn}) (Reddy et al., 2011)(Janotti & Walle, 2009)(Behera & Acharya, 2008). However, the origin of the visible emission is still rather controversial issue inZnO. It was observed that peak at 561 nm was found for pure ZnO nanorod while 543 nm for ZnO doped with 3 mol % Al in the green region which attributed to the radiative transition of an electron from deep donor level of Zn_i to an acceptor level which caused by singly ionized charged state of defect V_{Zn}- (Reddy et al., 2011).Broad peak around ~ 600 – 680 nm wasattributed to yellow-red emission have been observed in all samples which may ascribed to the oxygen atoms in interstitial (Alvi et al., 2010)(Liu, 2004)(Moura et al., 2010). The red emission in the range of 650 nm to 750 nm also may be attributed to oxygen vacancies (V_o). Tam et al. reported that the visible (green-yellow) emission may also exhibit by the presence of hydroxyl groups on the surface which the preparation is commonly done by solution-based method (Tam et al., 2006). For pure ZnO nanorod there was an additional peak around 703nm which attributed to the red emission, however the peak did notexist when dopant was added to the samples. Therefore, taking into account the condition of growth, it is reasonable to assume that the peak was shifted to green-yellow emission due to the contribution of Al dopant. The suggested energy band diagram illustrated as Figure 3.24. This figure illustrates the above assignment.

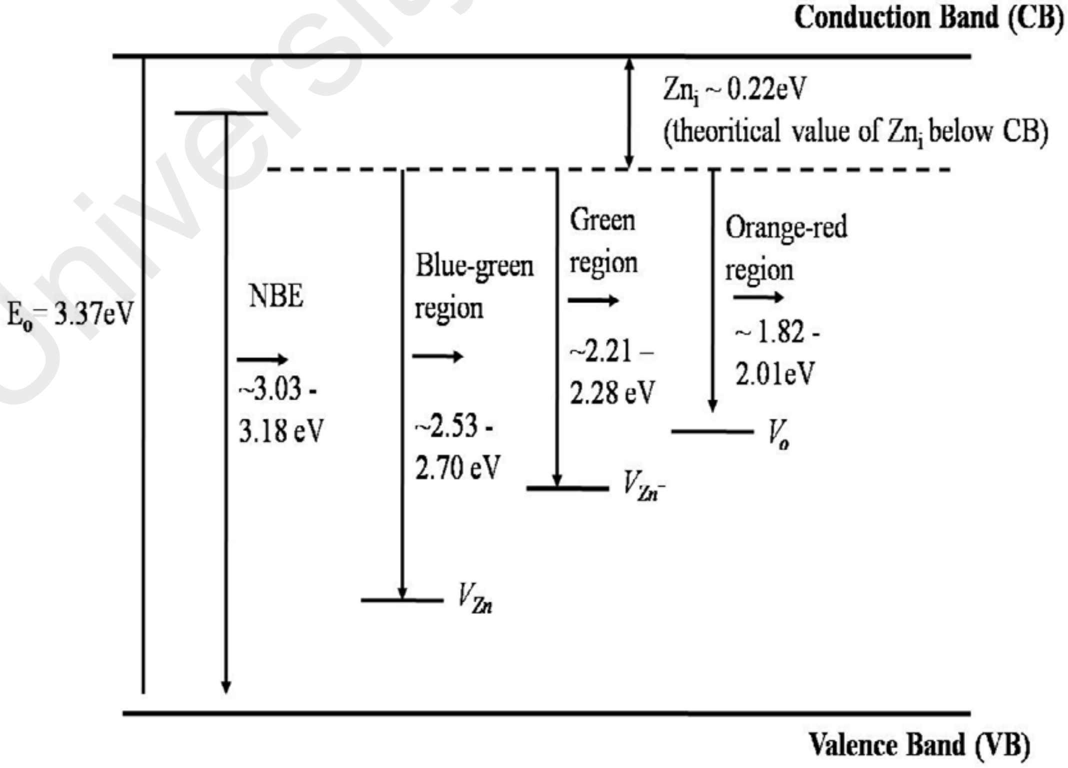

Figure 3.24: Suggested energy band diagram of ZnO nanorods.

In summary, the pure ZnO and Al-doped ZnO nanorods were synthesized on seeded Al substrates. From FESEM results, all samples exhibited rod-like structure but different in densityand aspect ratio. For pure ZnO nanorods, the rods were randomly distributed, highly dense and uniform in term of their length (2 – 3 μm) and diameter (100 – 250 nm). When 1, 3 and 5 mol % of Al was added, the nanorods were bundled with length of 1- 4 μm. EDX analysis showed inclusion of Al at 0.13, 0.16, and 0.19at % in the ZnO nanorods synthesized using 1, 3 and 5 mol % $Al(NO_3)_3$.HRTEM results indicated the nanorods grow in [001] direction and the lattice between two adjacent plane is about 0.24 – 0.25 nm. The XRD pattern of pure ZnO and Al-doped ZnO nanorods were in agreement with typical hexagonal wurtzite structure of pure ZnO. The XRD peak obtained also shifted towards higher 2θ value indicating that Al ion was incorporated into the ZnO lattice. Raman results shows that, peak at 439 cm^{-1} was reduced and another additional mode at 528 cm^{-1} was appeared. PL spectra of all samples presented two luminescence bands at uv and green-red emission region. The PL result shows the peak position shifted to the blue emission range as increasing the Al doping concentration.

3.3 Green synthesis of zinc oxide nanostructures using *Citrus aurantifolia*

Citrus aurantifolia(CA) fruits have the characteristic of highly a polyembryonic species that describe the phenomenon of two seedlings emerging from one seed. The fruit surface is smooth, greenish-yellow in colour and the juice is highly acidic (Yadav et al., 2004). As tested in this experiment the pH of the fresh juice was about 3.5. The major flavour components of the fresh CA fruits have been reported as limonene. Figure 3.25 shows a picture of CA fruits and the chemical structure of limonene. Three experiments were conducted using CA juice as a reducing agent which is to study (i) the effect of pH on the formation ZnO nanorods, (ii) high temperature effect to the crystal structure of ZnO nanoparticles and (iii) Mg-doped ZnO nanostructures.

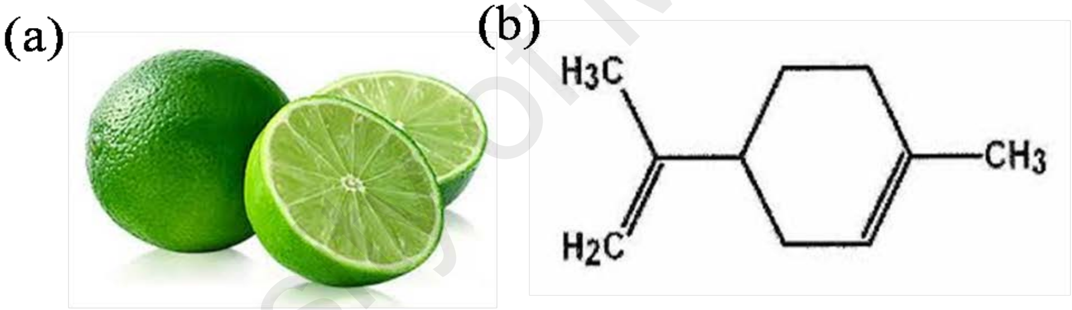

Figure 3.25: (a) CA fruits used in the synthesis process and (b) the chemical structure of limonene.

The overall experimental work done is summarized in a flowchart shown in Figure 3.26. Detailed description of each step will be given as follows.

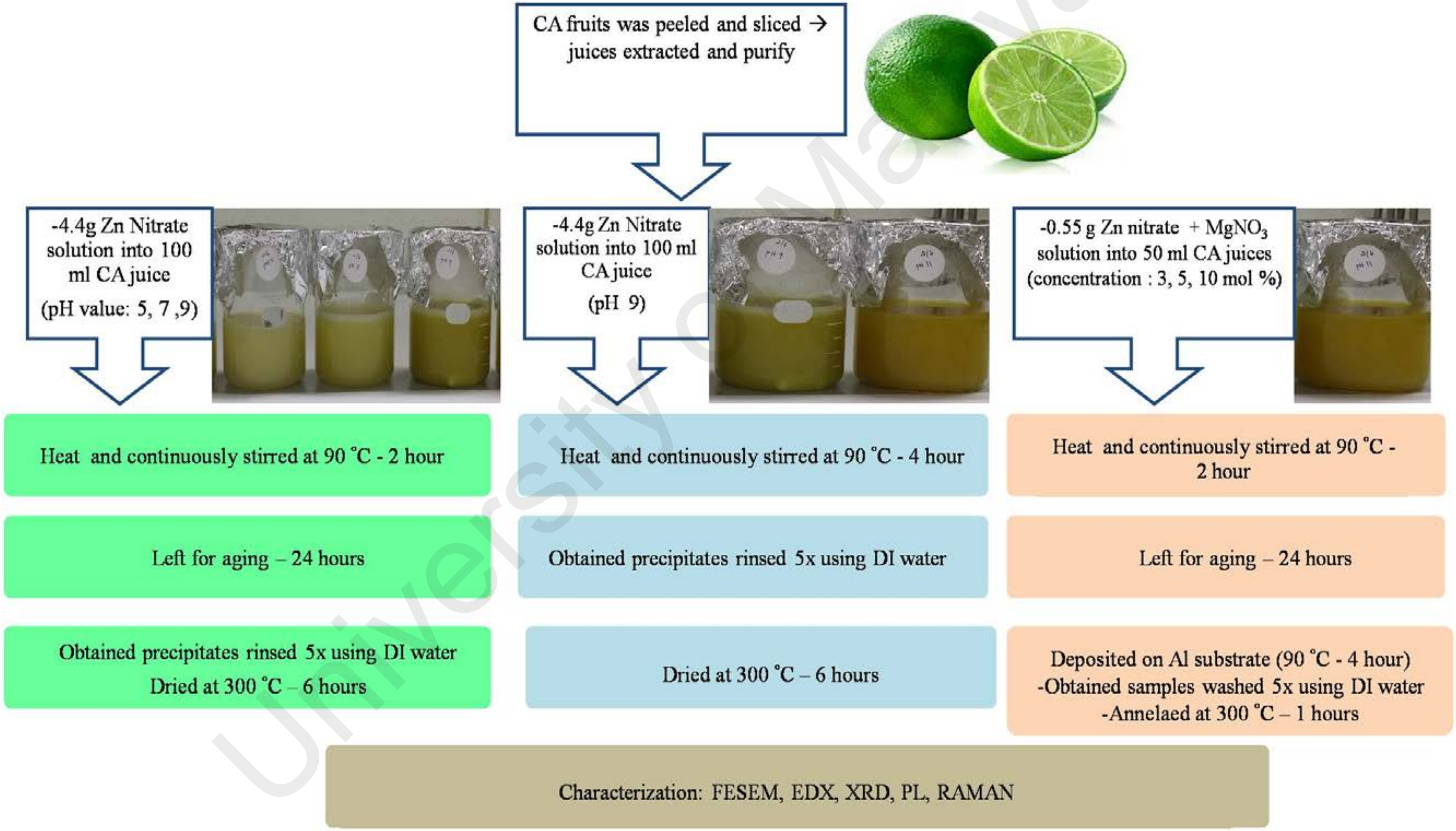

Figure 3.26: Process flow for the synthesis ZnO nanostructures using CA juices.

3.3.1 Experimental details

The CAfruits used werepurchased from the local market. About 200 g CA fruits were peeled and the pulp obtained was blended with 500 ml DI water. The blended slurry was initially filtered with muslin cloth to remove large solid particles. Then the filtrate was further filtered with a 200 nm pore syringe filter. Finally, the juice was centrifuged at 3000 rpm. The filtered juice was kept at 4 ^{o}C until used.

To study the effect of pH on the formation of ZnO nanorods, stock solutions were prepared by dissolving about of 4.4 g $Zn(NO)_3.6H_2O$ in 100 mL CA juice at three different pH value of stock solution. The initial pH of the stock solutions was about 3.5. To change the pH of the stock solution, 0.1 M NaOH solution was added until pH values of 5, 7 and 9 were obtained. Then the solutions were heated at 90 ^{o}C under continuous stirring for 2 hours and aged for 24 hours at room temperature. White precipitates recovered from the solutions were thoroughly rinsed in DI water and then dried in air at 300 ^{o}C for 6 hours.

To study the effect of high temperature XRD on ZnO nanoparticles (NPs) using CA juice, the stock solution was prepared with same amount as earlier experiment**.** The stock solution was prepared at pH 9. The solution was kept under vigorous stirring at 90 °C for 4 hours, allowed to cool at room temperature and then the supernatant was discarded. The precipitates (pale white solid product) obtained was rinsed several times thoroughly in DI water and dried at 300 °C for 6 hours. In-situ high temperature X-ray diffraction (HT-XRD) analysis over the range of 20 − 80 ° at temperature ranging from 25 - 375 °C have been employed. The X-Ray source was Cu Kα radiation (1.546 Å) and scanning at 0.01 ° step size. The heating rate was at 10 °C/min.

Synthesis of pure ZnO and Mg-doped ZnO nanostructures was done using sol-gel immersion technique. 0.55 g of $Zn(NO)_3.6H_2O$ was dissolved in 50 ml of CA juice and then, 0.1 M NaOH were added drop by drop to the solution for adjusting the pH of the solution become 11. The process followed by adding 3, 5 and 10 mol % amount of magnesium nitrate hexahydrate ($Mg(NO_3)_2.6H_2O$) with respect to zinc were dissolved in a stock solution as the magnesium source. The stock solution was stirred continuously for 2 hours at 60 °C for obtaining the growth solution and then aged for 24 hours before deposition process. The glass substrates were immersed in the stock solution and kept at 90 °C for 4 hours. Finally the samples are taken out of solution and cleaned through DI water and annealed at 300 °C for 1 h.

For all samples, structural characterization was carried out by XRD, FESEM, EDX, Raman and PL using similar setting as discussed earlier in Section 3.1.2.

3.4 Results and discussion

3.4.1 Effect of pH on the formation zinc oxide nanorods usingCAjuice

Figure 3.27 shows the surface morphologies of the ZnO nanorods obtained using solutions pH 5, 7 and 9. FESEM images in Figure 3.27 (a) shows ZnO nanorods prepared in pH 5, (b) pH 7 and (c) pH 9 solution.

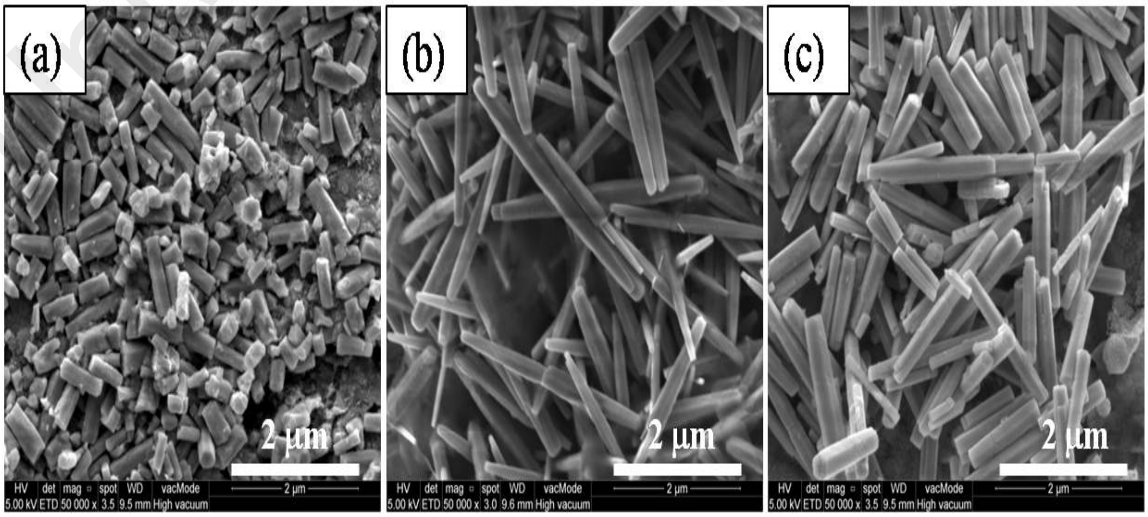

Figure 3.27: FESEM images of ZnO nanorods synthesized using CAby sol-gel method in pH (a) 5, (b) 7 and (c) 9.

From the FESEM images, nanorods structure was obtained for all samples but with slightly different aspect ratios. The nanorods formed in the neutral and alkaline solutions appeared to longer than those obtained from the acidic solution. The aspect ratio of ZnO nanorods synthesized in neutral and alkaline solution were about 10 and those synthesized in acidic solution were about 5. Similar observation was reported by Baruah & Dutta(Baruah & Dutta, 2009). They reported that the enhanced growth of nanorod in alkaline solutionwhere the abundance of OH ions contributed to the formation of the intermediate molecule, $Zn(OH)_2$ which facilitated the formation of ZnO. However, our results showed that there seemed to be a little difference between ZnO nanorods synthesized using neutral (Figure 3.27 (b)) and alkaline (Figure 3.27 (c)) solutions. The shorter and smaller diameter nanorods obtained using acidic solution can be attributed to the preferential erosion of the (0001) compared to other ZnO crystal faces (Lin et.al, 2006).

In order to verify the role of CA juice as a reducing agent during the ZnO nanostructures growth, we conducted control experiments without using CA juice with same growth parameter and characterized the obtained controlled sample using FESEM to investigate the morphology.

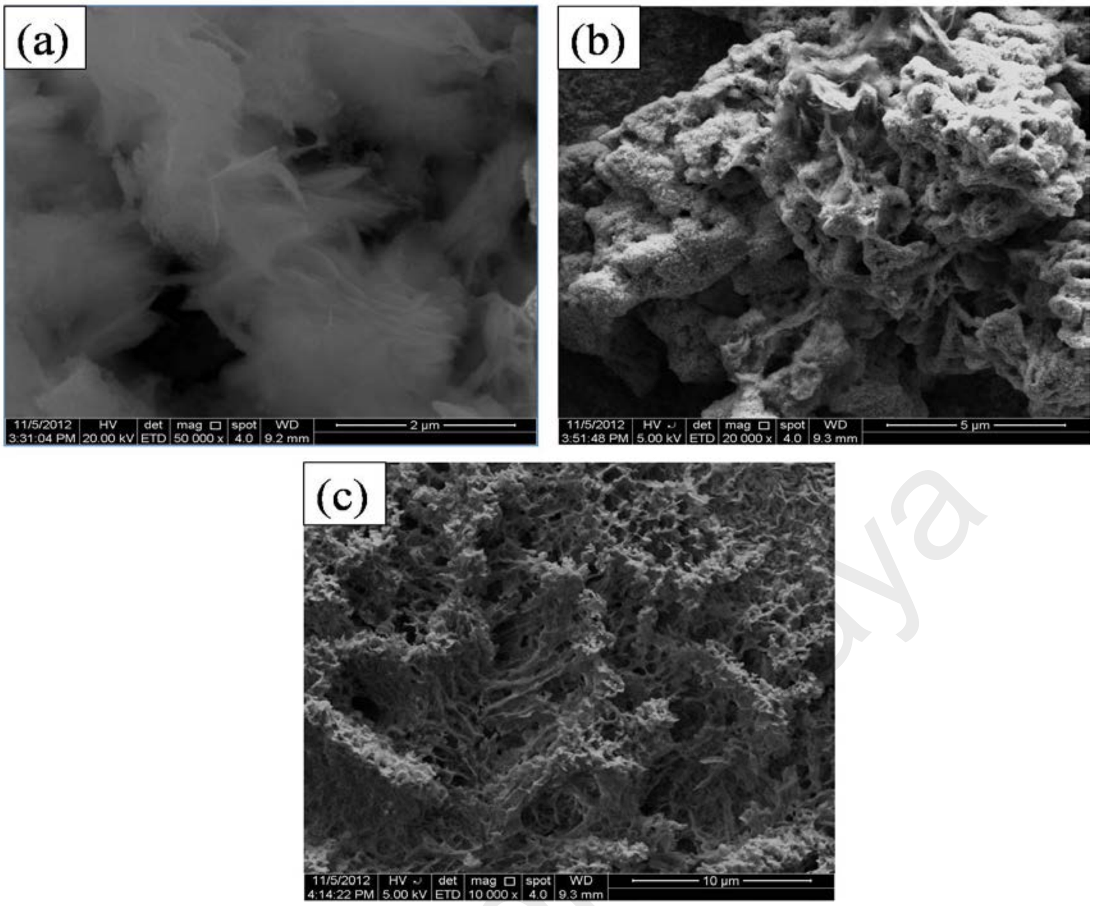

Figure 3.28: FESEM images of ZnO particulates obtained in control experiments without using CA at (a) pH 5, (b) 7 and (c) 9.

As shown in Figure 3.28 (a), (b) and (c), ZnO with sheet-like structures were observed for sample prepared in acidic solution and particulates ZnO structures for samples prepared in neutral and alkaline solution. From this result, it can be concluded that CA juice which act as a reducing agent influenced the formation of ZnO nanorods obtained in this work.

Figure 3.29 shows the normalized XRD patterns of ZnO nanorods obtained at various pH values. The main diffraction peaks located at 2θ values of about 31.6^{o}, 34^{o}, 36.2^{o}, 47^{o} and 56.5^{o} were assigned to the (100), (002), (101), (102) and (110) reflection planes of ZnO, respectively. The diffraction patterns are indexed to the hexagonal zinc oxide with lattice constants a = 0.3249 and c = 0:5206 nm.

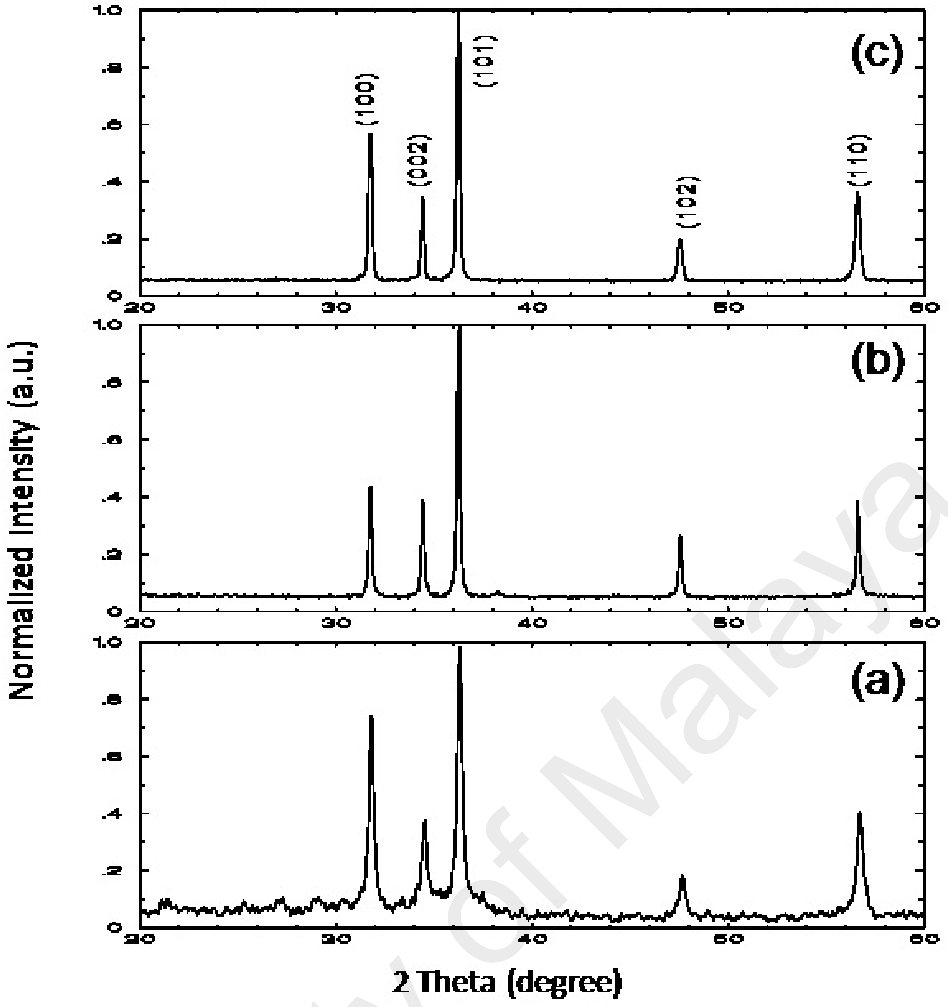

Figure 3.29: Normalized XRD patterns of ZnO nanorods synthesized using CAby sol-gel method at pH (a) 5, (b) 7 and (c) 9.

The XRD pattern for ZnO nanorods prepared at pH 5, 7 and 9 showed sharp and intense diffraction peaks. There was a slightly dominant peak due to the (101) reflection plane for samples synthesized at pH 7 (Figure 3.29 (b)) and 9 (Figure 3.29 (c)). This can be due to the direction of the nanorods which were generally inclined at an angle with respect to the direction of the incident x-ray beam as evident from the FESEM images in Figure 3.27. As for the sample synthesized at pH 5 (Figure 3.29 (a)), the peak due to the (101) reflection plane was less dominant due to smaller aspect ratio resulting in a more random orientation of the nanorods with respect to the direction of x-ray probe beam. This is an indication that the nanorods growth was along the c-axis.

Figure 3.30 shows the PL spectra of ZnO nanorods prepared at pH 5, 7 and 9. The broad spectra were fitted to Gaussian curves. It can be seen that, all ZnO nanorods synthesis at pH 5, 7 and 9 exhibits almost similar PL spectra patterns. However on closer inspection there seemed to be peaks shifted towards red emission region for ZnO nanorods grown from pH 5 to pH 9 solutions. The resulting peak positions were summarized in Table 3.5.

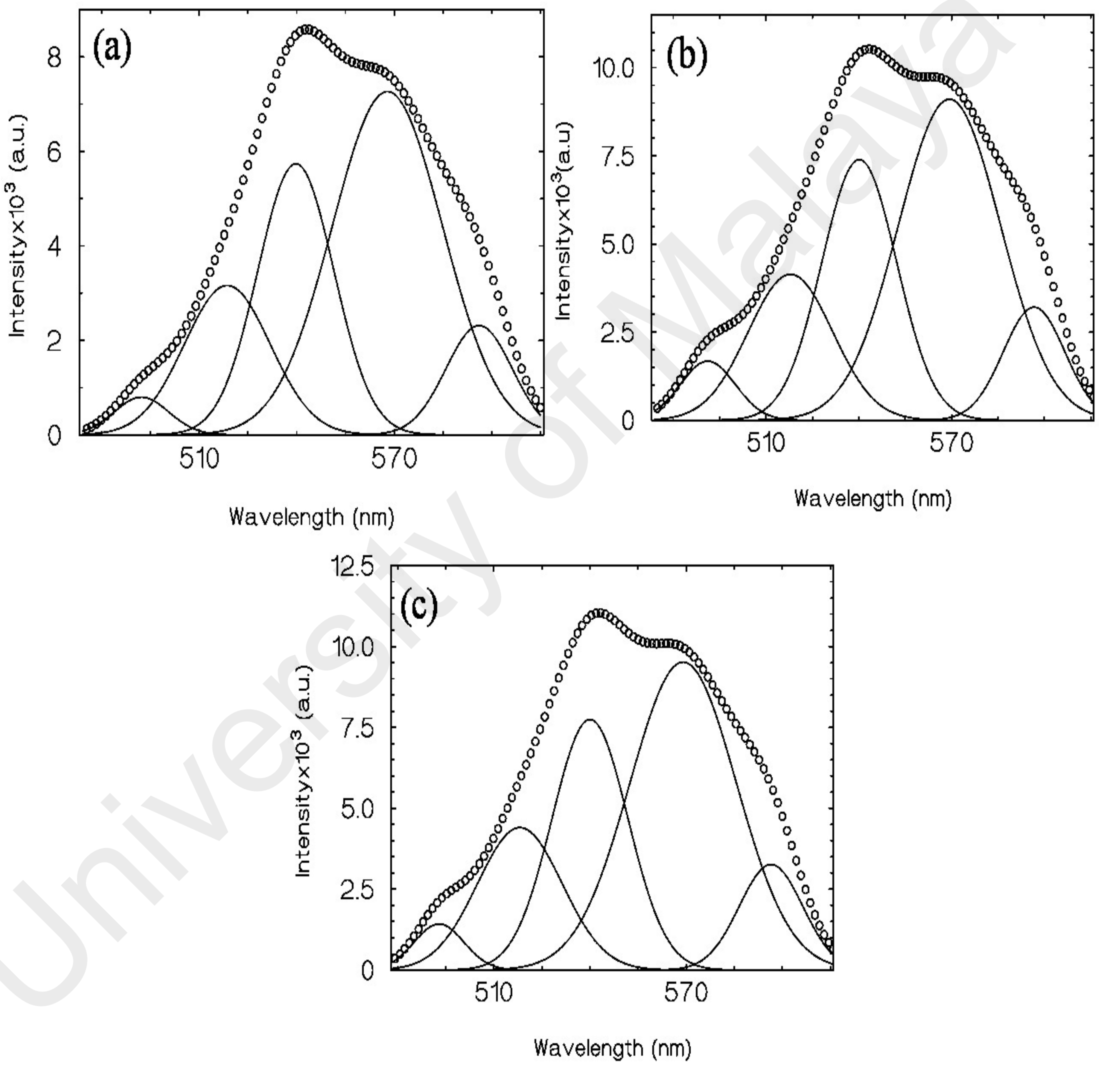

Figure 3.30: PL spectra in the yellow-green region fitted to Gaussian curves for ZnO nanorods synthesized using CAby sol-gel method at pH (a) 5, (b) 7 and (c) 9.

Table 3.5: De-convolution of the emission spectra of ZnO nanorods synthesized using *Citrus aurantifolia* juice by sol-gel method at pH (a) 5, (b) 7 and (c) 9.

Sample name	**Peak position (nm)**	**Proposed transition**	**Refs.**
pH 5	487.2	Transition from oxygen vacancy	(Patra, Manzoor, Manoth, Vadera, & Kumar, 2008)
	518.6	Singly ionized oxygen vacancy	(Vanheusden et al., 1996)
	536.7	Transition from deep donor level by the oxygen vacancies to valence band	(Ding et al., 2012)
	559.1	Transition of Zn_i to V_{Zn}	(Karthikeyan & Pandiyarajan, 2010)
	589.1	Oxygen interstial	(Uthirakumar et al., 2007)
pH 7	491.1	Transition from oxygen vacancy	(Patra et al., 2008)
	517.9	Singly ionized oxygen vacancy	(Vanheusden et al., 1996)
	540.1	Transition from deep donor level by the oxygen vacancies to valence band	(Ding et al., 2012)
	569.3	Transition of Zn_i to V_{Zn}	(Karthikeyan & Pandiyarajan, 2010)
	596.7	Hydroxyl group	(Djurišić et al., 2010)
pH 9	492.2	Transition from oxygen vacancy	(Patra et al., 2008)
	518.6	Singly ionized oxygen vacancy	(Vanheusden et al., 1996)
	539.7	Transition from deep donor level by the oxygen vacancies to valence band	(Ding et al., 2012)
	567.9	Transition of Zn_i to V_{Zn}	(Karthikeyan & Pandiyarajan, 2010)
	596.1	Hydroxyl group	(Djurišić et al., 2010)

The blue peaks were at about 487.2 nm for ZnO nanorods at pH 5, 491.2 nm for ZnO nanorods at pH 7 and 492.2 nm for ZnO nanorods at pH 9. These peaks can be attributed to the transition from oxygen vacancy (Patra et al., 2008). The peaks at around 518.6 nm, 517.9 nm, 518.6 nm for ZnO nanorods obtained at pH 5, 7 and 9 respectively, corresponded to the recombination of a photo-generated hole with a singly charged ionized state of oxygen vacancy (Vanheusden et al., 1996) and the peaks at about 536.7 nm, 540.1 nm and 539.7 nm were attributed to transition from deep donor level by the oxygen vacancies to valence band for ZnO nanorods obtained at pH 5, 7 and 9, respectively (Ding et al., 2012).

Dominant peaks at about 559.1 nm, 569.3 nm and 567.9 nm were observed for ZnO nanorods at pH 5, 7 and 9 respectively that can be attributed to transition of zinc interstial (Zn_i) to zinc vacancies (V_{Zn}) (Karthikeyan & Pandiyarajan, 2010). The peak at 589 nm observed in the sample synthesized at pH 5 can be due to oxygen interstial (O_i) in the ZnO nanorods as a result of the acidic environment (Uthirakumar et al., 2007). For the samples synthesized in neutral and alkaline solutions, peaks at about 596 nm were observed which may be due to the presence of hydroxyl groups on the sample surface (Djurišić, Ng, & Chen, 2010).

In summary, ZnO nanorods have been synthesized using CA juice at different pH values by the sol–gel method. XRD analysis showed all the samples were pure ZnO with wurzite structure with evidence of single crystal nanorods with growth along the c-axis. The aspect ratio of ZnO nanorods synthesized in neutral and alkaline solution were about 10 and those synthesized in acidic solution were about 5. Room temperature PL in the visible region consisted of a few overlapping peaks arising from recombination on common points and surface defects. Growth inhibition was observed in the samples synthesized at pH 5 which can be due to preferential erosion of ZnO (0001) face. Enhanced growth in alkaline solution at pH 9 was due to the more abundance OH^- ion compare to acidic solution, which promoted the intermediate molecule $Zn(OH)_2$. Equally efficient growth at pH 7 indicated that erosion process dominated the inhibition of nanorod growth over enhancement due to the presence of OH^- ion.

3.4.2 In-situ high temperature effect of zinc oxide nanoparticles using CA juice

In-situ high temperature XRD study was done at temperatures between 125 and 375 °C. The effect of high temperature on crystal phase, particle size and lattice constant of the samples were investigated. Figure 3.31 shows the room temperature XRD pattern for ZnO NPs at pH 9 solution.

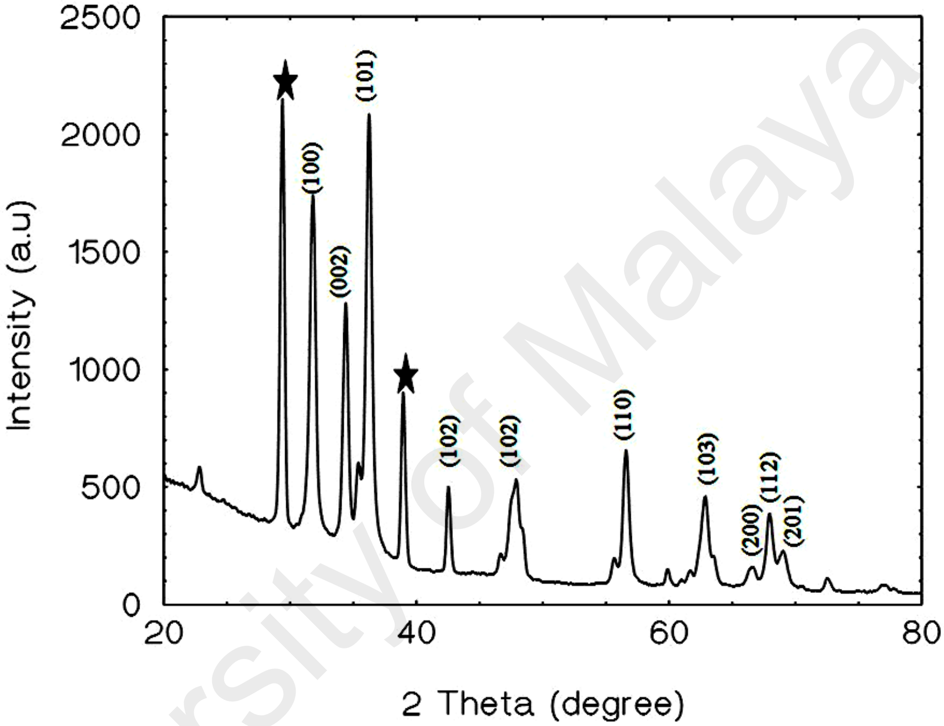

Figure 3.31: Room temperature XRD pattern of precipitates ZnO NPs (star labelled in the graph represent nitratine ($Na_6N_6O_{18}$)).

The XRD results for all samples were consistent with the standard values for ZnO hexagonal structure that showed strong prominent peaks due to diffraction planes (100), (002), and (101) (according to peak fitting based on library data No. 98-016-2843 from Highscore Plus Software). There were two additional peaks detected for thesample which assigned to nitratine ($Na_6N_6O_{18}$) (labeled as star in the graph) which have a characteristic of hexagonal crystal structure with space group R3C (according to peak fitting based on library data No. 96-900-7560 from Highscore Plus Software). This occurrence may due to the addition of NaOH to set the solution pH at 9 during the sample preparation.

The FESEM images ZnO NPs are shown in Figure 3.32. The nanoparticles formed in a spherical-like structure with various sizes. The formation of larger spherical particles could be attributed to the high surface energy of ZnO nanoparticles (Hong et al., 2006)(Raoufi, 2013). A clear magnified image (Figure 3.32 (b)) of ZnO exhibit high density distributions with particle size in the range 100 – 300 nm.

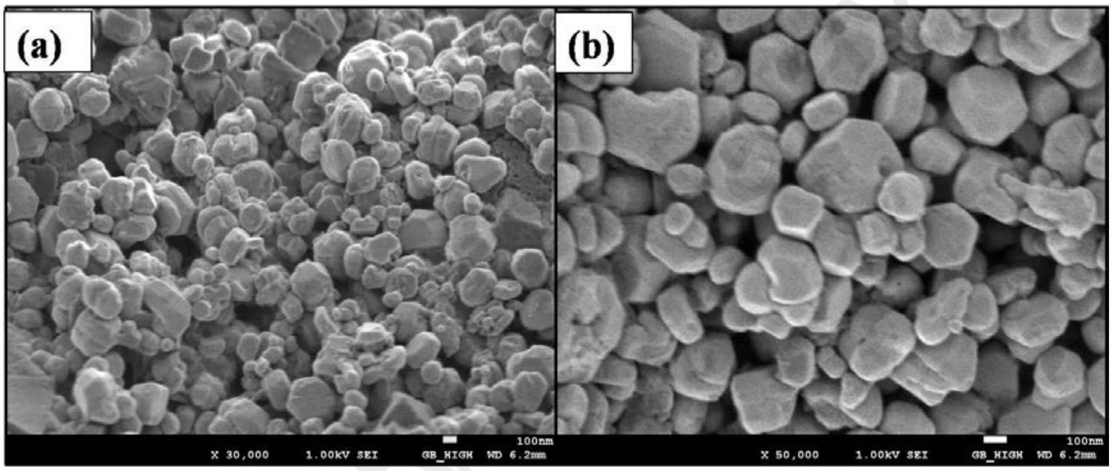

Figure 3.32: FESEM images of ZnO NPs

Figure 3.33 shows the HT-XRD pattern of ZnO NPs. Figure 3.33 (a) shows the HT-XRD profile of ZnO NPs in the range 30°- 60° while Figure 3.33 (b) presented the enlargement of the profile at range 30°- 38°.

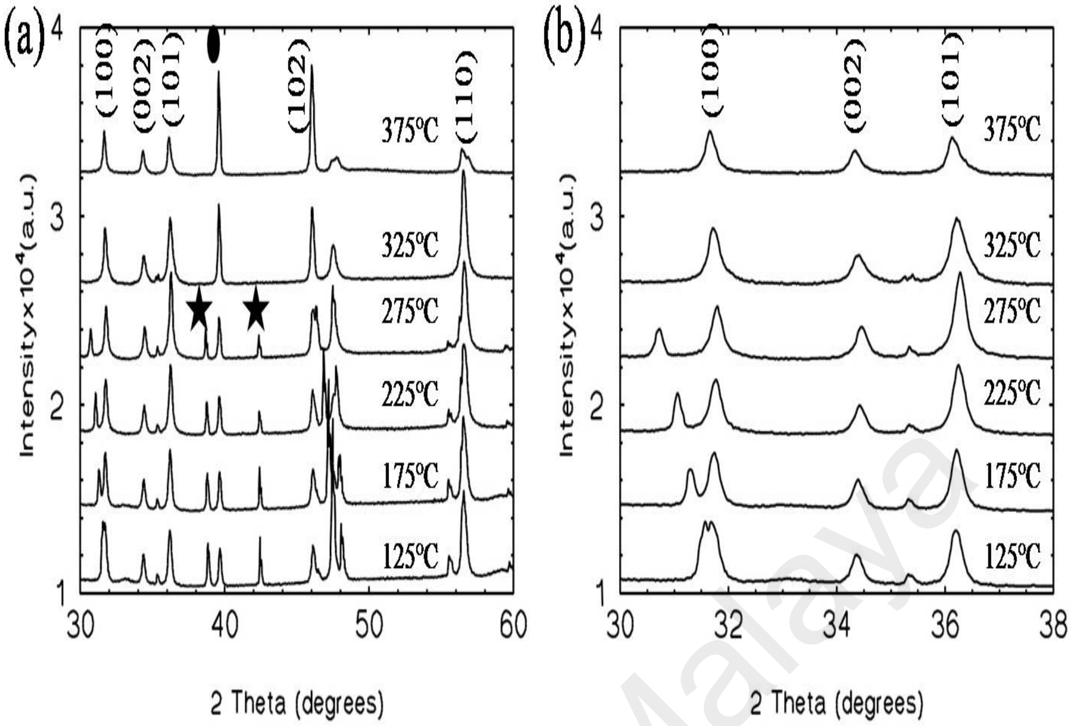

Figure 3.33: HT-XRD pattern of the ZnO NPs at temperature ranging from 125 to 375 °C and (b) enlargement of HT-XRD pattern of ZnO NPs at range 2θ= 30°-38° (star represent Nitratine, $Na_6N_6O_{18}$ and circle represent zinc hydroxide; $Zn(OH_2)$).

The ZnO NPs peaks show the crystalline nature of wurtzite ZnO with diffraction peaks corresponding to the reflection plane (100), (002), (101), (102), (110), (103) and (112), respectively. The XRD spectrum also exhibited extra diffraction peak of nitratine and zinc hydroxide in the spectrum. It can be seen that, the nitratine peak existed at temperature 125°C to 275°C and disappeared when temperature increase to 325°C. From Figure 3.33 (b), there was a slight shift in the peak position towards lower 2θ values. This was due to the change in lattice parameter related to temperature increase during XRD measurement. It has been reported that an increased in temperature will lead to lattice expansion (Raoufi, 2013).

The average crystallite size of ZnO NPs was estimated using Scherer’s formula which is given by:

$$D = \frac{0.9\lambda}{\beta \cos\ \theta} \tag{3.3}$$

where D is the mean crystallite size, λ is the wavelength of X-ray radiation (1.5406Å), β is the full-width at half maximum (FWHM in radian) of the peak due to plane (101) and θis the diffraction angle. The calculated crystallite size is presented in Table 3.6. From values obtained, the crystallite size increased from 35.07 nm to 46.42 nm as temperature increased from 125 to 375 °C. The merging process of the ZnO NPs induced from the temperature during the experiment explained this observation. At high temperature, the grain boundary migration was promoted which caused the coalescence of crystallite and the process seemed to increase with increasing temperature. The coalescence of neighboring crystallites formed larger crystallites.

The line broadening was influence by the heating process. Figure 3.34 shows the FWHM of the (101) diffraction line as a function of temperature of ZnO NPs. There was a clear trend of decreasing in the FWHM with increasing temperatures, indicating the crystallinity of ZnO NPs is caused by the rise of temperature.

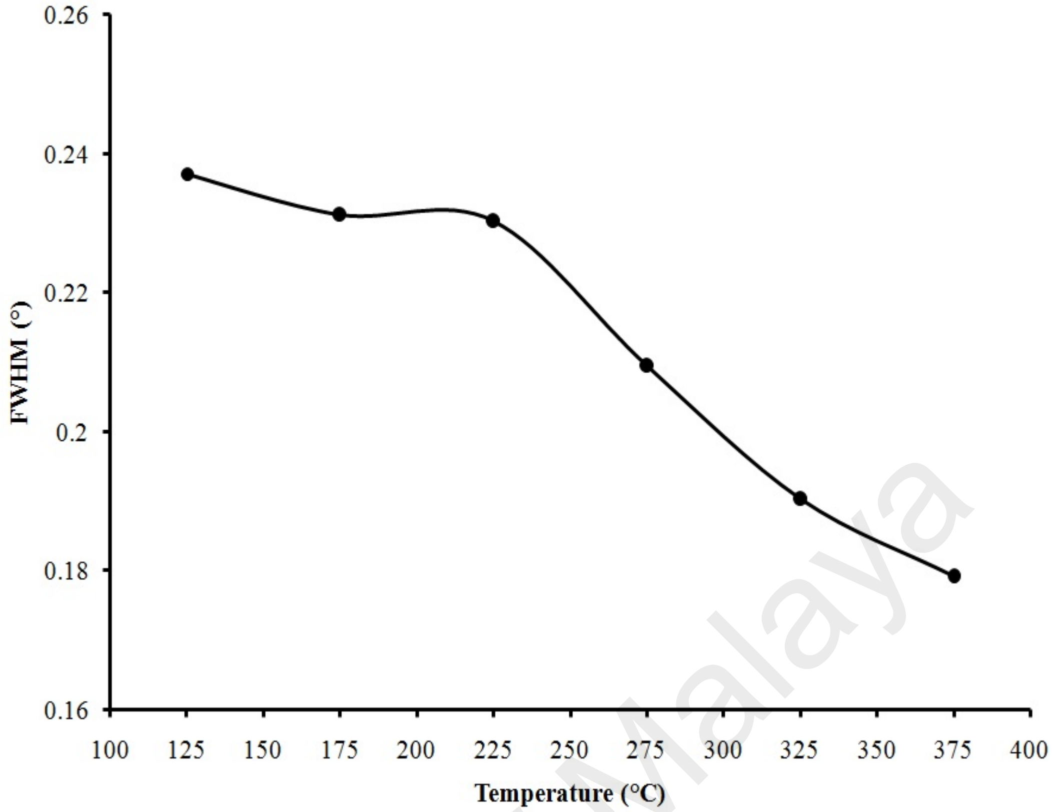

Figure 3.34: FWHM of (101) diffraction line as a function of temperature of ZnO NPs.

ZnO has a hexagonal unit cell with two lattice parameters ‘a’ and ‘c’. For the ZnO wurtzite structure the lattice constants can be calculated based on Bragg’s law.

$$2d_{hkl} \sin\theta = n\,\lambda \tag{3.4}$$

Where d_{hkl} is the spacing between lattice planes of Miller indices (h, k and l), n is the order of diffraction (n=1 for first order diffraction), λ is the X-ray wavelength of CuKα radiation (1.5406Å), and θ is the Braggs angle.

The hexagonal unit cell of ZnO is characterized by the lattice parameters and the plane spacing equation for the hexagonal structure can be expressed in the following equation(Gondal et al., 2009):

$$\frac{1}{d^2} = \frac{4}{3}\left(\frac{h^2 + hk + k^2}{a^2}\right) + \frac{l^2}{c^2} \tag{3.5}$$

Thus, for n=1, the relationship between Equation 3.4 and 3.5 can be expressed as below:

$$\sin^2\theta = \frac{\lambda^2}{4a^2}\left[\frac{4}{3}(h^2 + hk + k^2) + \left(\frac{a}{c}\right)^2 l^2\right] \tag{3.6}$$

For the measurement of lattice constant ‘a’ and ‘c’, the (100) and (002) diffraction planes were selected. Hence, the lattice constant ‘a’ can be written as:

$$a = \frac{\lambda}{2\sin\theta_{(100)}}\sqrt{\frac{4}{3}(h^2 + hk + k^2) + \left(\frac{a}{c}\right)^2 l^2} \tag{3.7}$$

$$a = \frac{\lambda}{\sqrt{3}\sin\theta_{(100)}} \tag{3.8}$$

And the lattice constant ‘c’, the (002) plane orientation was chosen using the equation:

$$c = \frac{\lambda}{2\sin\theta_{(002)}}\sqrt{\frac{4}{3}\left(\frac{c}{a}\right)^2 (h^2 + hk + k^2)l^2} \tag{3.9}$$

$$c = \frac{\lambda}{\sin\theta_{(002)}} \tag{3.10}$$

The lattice parameters were calculated using Equation 3.8 and 3.10 and are tabulated in Table 3.6. The lattice parameter values of ‘c’ and ‘a’ all increased as the temperature increased.

Table 3.6: Lattice parameters and crystallite size of ZnO NPs calculated from XRD results.

Temperature (°C)	**a (Å)**	**c (Å)**	**c/a**	**FWHM $_{(101)}$**	**Crystallite size, D (nm)**
125	3.2520	5.2119	1.6026	0.2371	35.07
175	3.2544	5.2134	1.6019	0.2312	35.96
225	3.2548	5.2148	1.6022	0.2303	36.10
275	3.2545	5.2145	1.6020	0.2094	39.71
327	3.2564	5.2166	1.6019	0.1903	43.69
375	3.2608	5.2194	1.6006	0.1791	46.42

Figure 3.35 shows the lattice parameter ‘a’ and ‘c’ and crystallite size as a function of temperature for ZnO NPs. Figure 3.35 (a) shows the lattice parameter ‘a’ and crystallite size and Figure 3.35 (b) lattice parameter ‘c’ and crystallite size as a function of temperature. The graph shows a steady increase of lattice parameter ‘a’ value i.e. 3.2520 Å, 3.2544 Å, 3.2548 Å, 3.2545 Å, 3.2564 Å and 3.2608 Å of temperature 125 °C, 175 °C, 225 °C, 275 °C, 327 °C, and 375 °C, respectively.

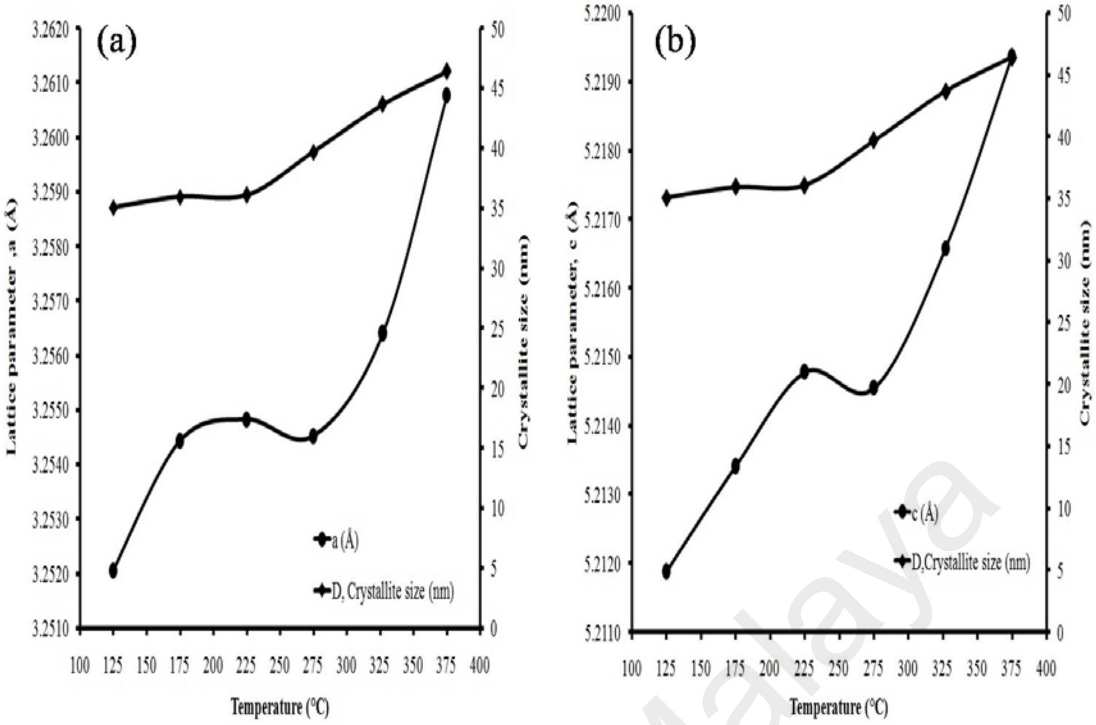

Figure 3.35: The lattice parameter ‘a’ and ‘c’ and crystallite size as a function of temperature for ZnO NPs.

The same trend was observed for lattice parameter ‘c’ as shown in Figure 3.35 (b), the values significantly increased as temperature increases i.e. 5.2119 Å, 5.2134 Å, 5.2148 Å, 5.2145 Å, 5.2166 Å and 5.2194Å for temperature 125 °C, 175 °C, 225 °C, 275 °C, 327 °C, and 375 °C, respectively. The crystallite size and lattice parameters ‘a’ and ‘c’ have also increased with temperature.

In summary, HT-XRD study of ZnO NPs, shows that the crystallite size and lattice parameter (‘a’ and ‘c’) were significantly affected by temperature. The crystallite size and lattice parameter increased as temperature increased. This was due to the incorporation of small crystallite into larger crystallite which related to Ostwald ripening.

3.4.3 The effect of Mg-doping to the formation of zinc oxide nanostructures using CA juice

In section 3.4.1 and 3.4.2 we have discussed the synthesis and characterization of the ZnO nanorods and nanoparticles utilizing biomaterial i.e CA juice by the sol-gel method. Here the effect of Mg doping of ZnO nanostructures synthesized using CA juice is described.

Figure 3.36 shows the surface morphology of pure and Mg-doped ZnO nanostructures. All samples exhibited fiber-liked structures with different aspect ratios. The ZnO nanostructures distribution for pure and Mg doped ZnO nanostructures were sparse. This feature is favorable for field electron emission applications (will discussed in Chapter 4); since dense nanostructures will induce electric field shielding that will impede electron emission.

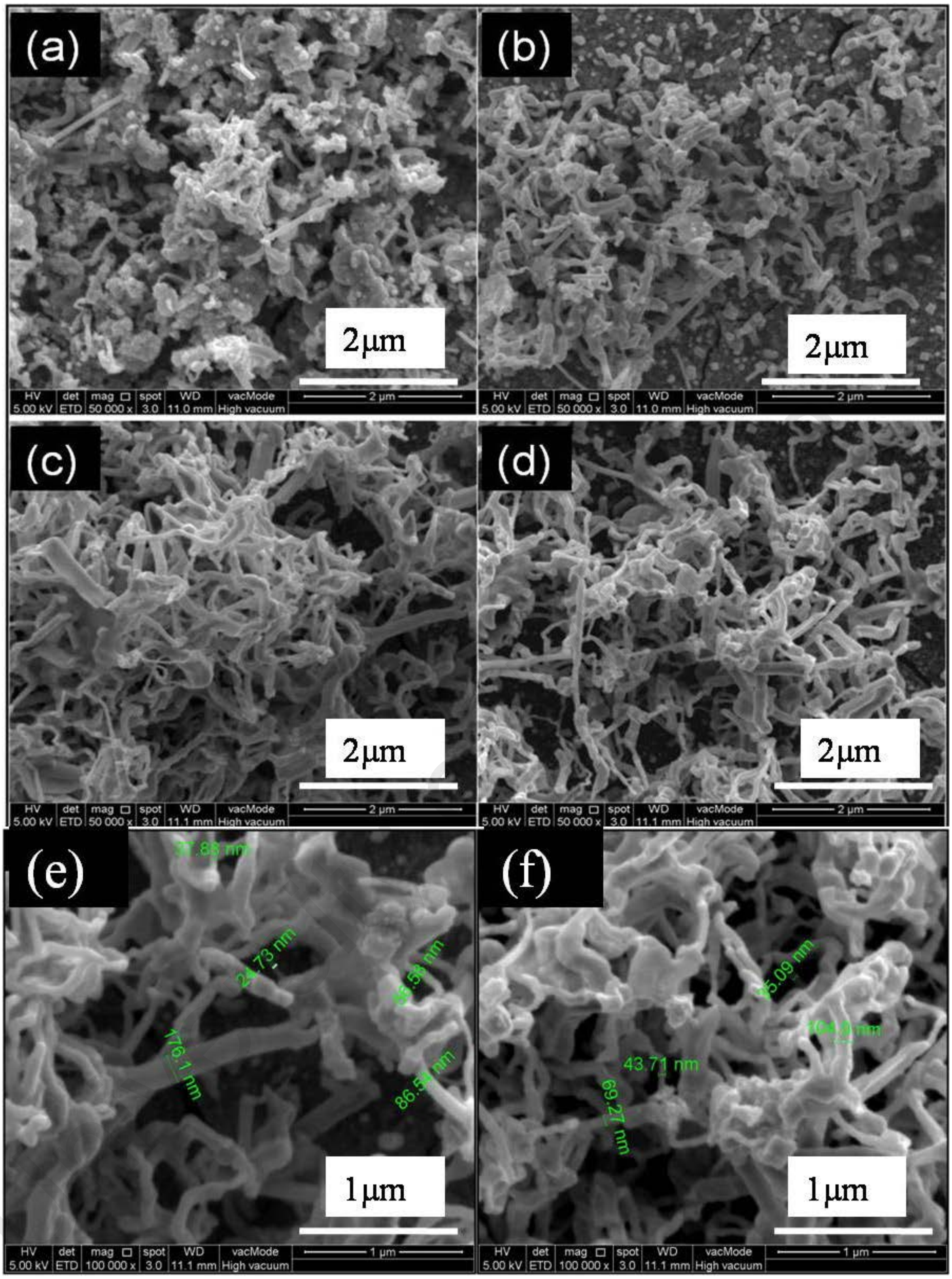

Figure 3.36: FESEM images of (a) pure ZnO (b) 3, (c) 5, (d) 10 mol % Mg-doped ZnO nanostructures at 50k magnification, (e) 5 mol % Mg-doped ZnO and (f) 10 mol % Mg-doped ZnO nanostructures

Pure and Mg-doped ZnO nanostructures produced fibres with diameters in the range 20 nm to 150 nm. Figure 3.36 (e) and (f) shows the image for 5 mol % Mg-doped ZnO and 10 mol % Mg-doped ZnO nanostructures at 100k magnification.

Figure 3.37 shows the EDX spectra of pure ZnO and Mg-doped ZnO nanostructures. Figure 3.37 (a) illustrates the normalized EDX spectra for (i) pure ZnO nanostructures, (ii) 3 mol % Mg-doped ZnO nanostructures, (iii) 5 mol % Mg-doped ZnO nanostructures and (iv) 10 mol % Mg-doped ZnO nanostructures. The presence of O, Zn and Mg element indicated Mg doping of the ZnO samples.

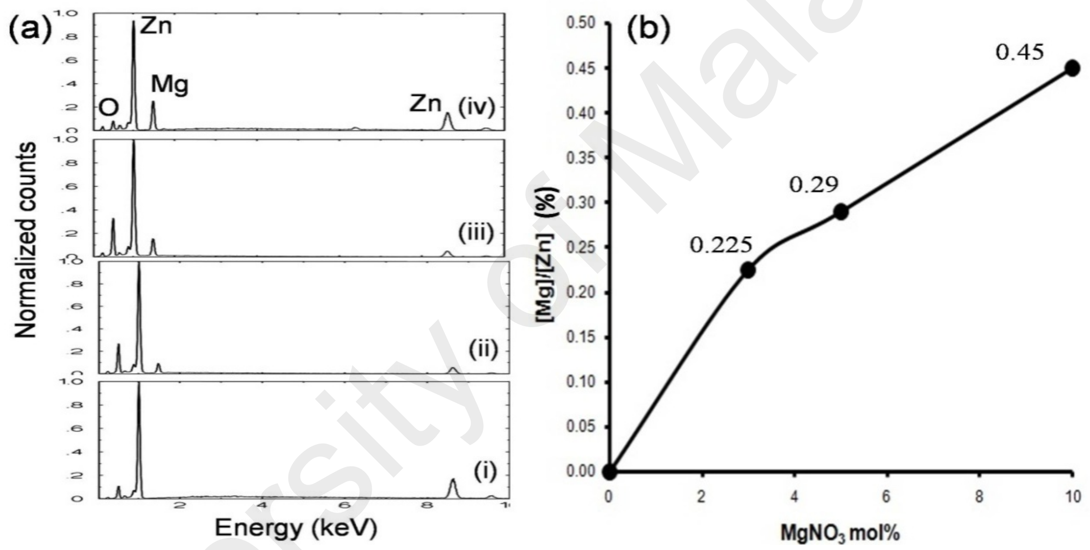

Figure 3.37: (a) EDX spectra of (i) pure ZnO (ii) 3 mol % Mg-doped ZnO, (iii) 5 mol % Mg-doped ZnO and (iv) 10 mol % Mg-doped ZnO nanostructures and (b) The inclusion of Mg in ZnO with respect to the starting amount of Mg.

From the raw data obtained by EDX analysis, the Mg atomic percentage inclusion into ZnO nanostructures was calculated and the result was plotted as Figure 3.37 (b). The plotted graph exhibits the graph of Mg/Zn ratio (in atomic percentage) versus MgNO$_3$ (in mol %) used during the synthesis process. It was observed that, the Mg/Zn ratio increased as the dopant concentrationincreased 0.225, 0.29 and 0.45 % for 3, 5 and 10 mol % Mg-doped ZnO nanostructures, respectively.

Figure 3.38 show the normalized XRD pattern for pure and Mg-doped ZnO nanostructures synthesized using CA juice. The normalized XRD spectra of pure ZnO nanostructures and ZnO nanostructures at various doping level of Mg to Zn in atomic % of 0.225%, 0.29 % and 0.45 % were present in Figure 3.38 (a) and (b) shows the enlargement of XRD pattern in the range of 2θ= 30 -37°.

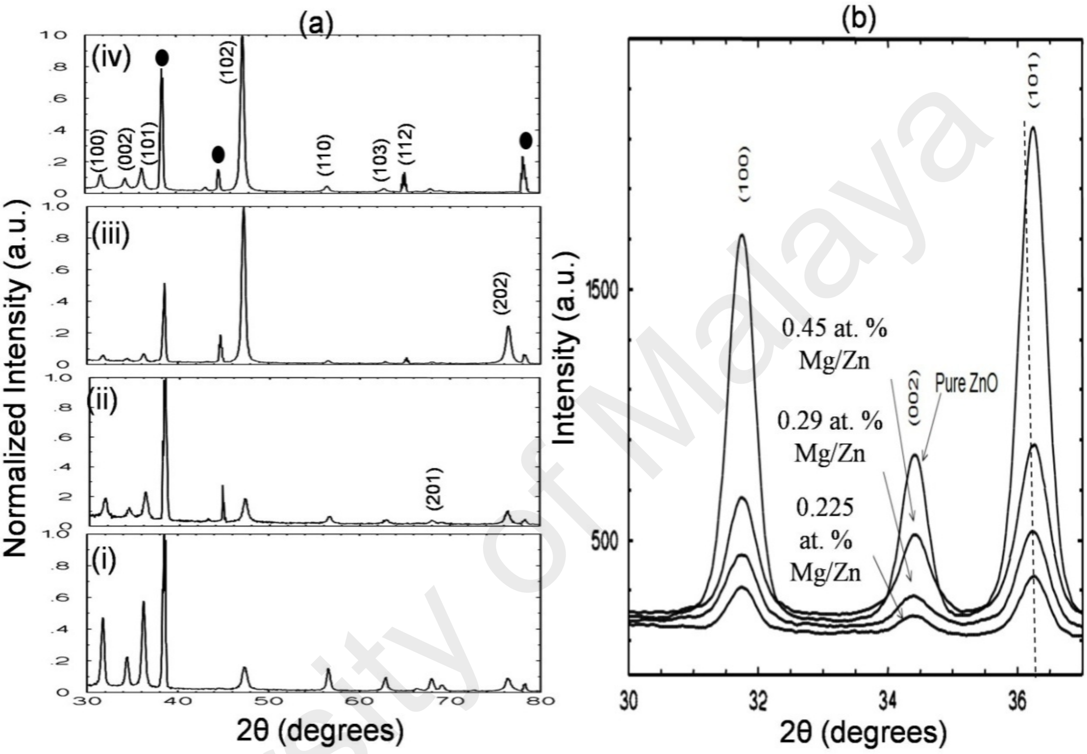

Figure 3.38: (a) Normalized XRD patterns of (i) pure ZnO, (ii) 0.225, (iii) 0.29 and (iv) 0.45 at. % Mg/Zn nanostructures(black circle represent Al peak, circle represent MgO peak) and (b) enlarged XRD patterns of pure ZnO and Mg-doped ZnO nanostructures in the range 30-37°.

The XRD patterns for all samples exhibit seven major diffraction peaks which can be assigned to (100), (002), (101), (102), (110), (103) and (112) planes respectively. The pure ZnO nanostructures and Mg-doped ZnO nanostructures at various doping level exhibit the hexagonal wurzite structure which is in good agreement with JCPDS card No. 01-079-2205. Also, present are peaks due to the Al substrates at 38.5, 44.7 and 65.1^{o} attributed to diffraction from the Al (111), (200) and (220) faces based on standard values (JCPDS No. 01-085-1327).

As shown in Figure 3.38 (b), the close up view shows the (100), (002) and (101) diffraction peaks for all samples. It was found that as the Mg concentration increased, the position of XRD peaks slightly shifted towards higher angle which was evidence of Mg doping. The increase in peak positions with increasing Mg doping level were due to Mg^{2+} ions having a smaller ionic radius compared to Zn^{2+} ion (Sengupta, Ahmed, & Labar, 2013)(Ji et al., 2004). The 2θ values for the shifted XRD peak position was tabulated in Table 3.7.

Table 3.7: Peak positions of XRD peaks of pure and Mg doped ZnO nanostructures compared to standard values.

(hkl) plane (2θ)/ Sample	**(100)**	**(002)**	**(101)**	**(102)**	**(110)**	**(103)**	**(112)**	**(201)**	**(202)**
Pure ZnO nanostructures	31.74	34.37	36.23	47.37	56.68	62.88	67.97	69.13	-
0.225 at. % Mg/Zn nanostructures	31.75	34.47	36.25	47.27	56.54	62.90	67.97	69.03	76.28
0.29 at. % Mg/Zn nanostructures	31.76	34.38	36.29	47.23	56.64	62.84	68.01	69.13	76.38
0.45 at. % Mg/Zn nanostructures	31.82	34.39	36.30	47.30	56.73	62.93	68.02	-	76.39
JCPDS No. 01-079-2205	31.766	34.419	36.251	47.536	56.591	62.852	67.942	69.080	76.953

Figure 3.39 shows the Raman spectra of pure ZnO and Mg-doped ZnO nanostructures. Figure 3.39 (a) shows the Raman spectra of pure ZnO nanostructures, (b) 0.225, (c) 0.29 and (d) 0.45 at. %% Mg/Zn nanostructures, respectively.

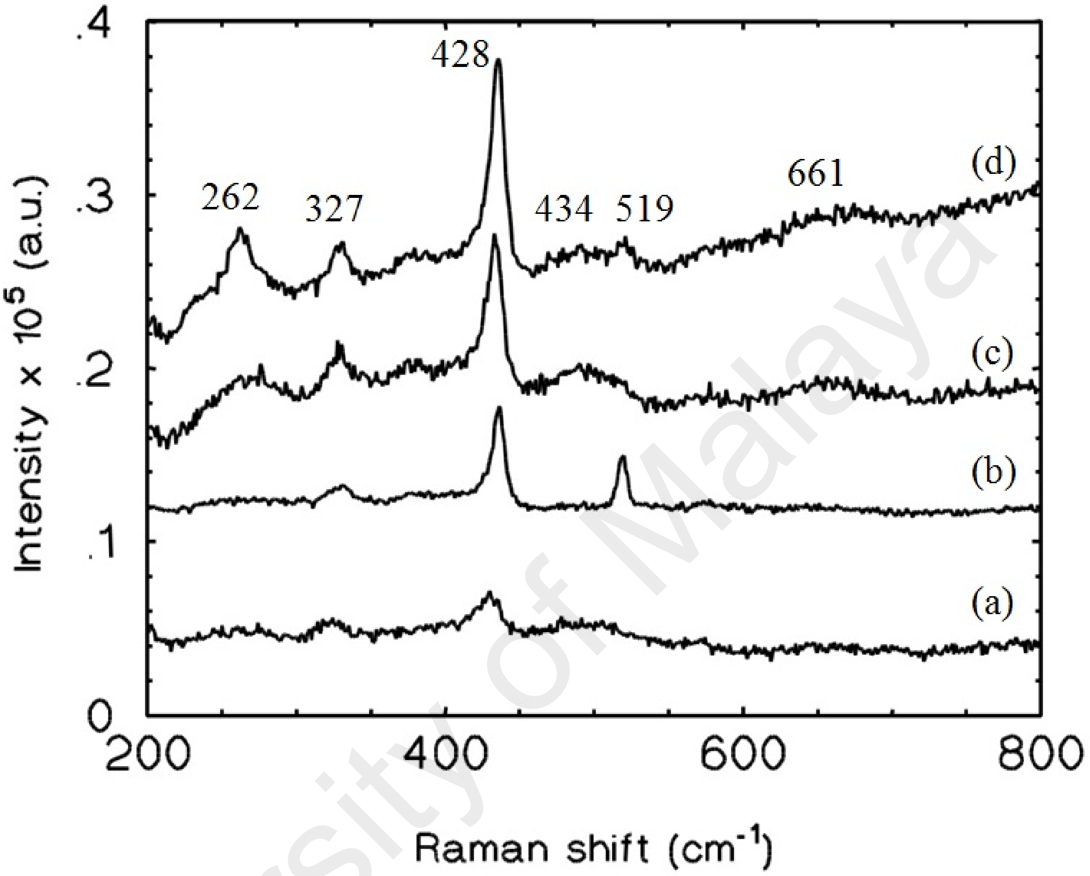

Figure 3.39: Raman spectra of (a) pure ZnO (b) 0.225, (c) 0.29 and (d) 0.45 at. % Mg/Zn nanostructures.

As shown in Figure 3.39 there are five prominent peaks at 262, 327, 427 to 434, 519 and a broad peak at 661 cm^{-1}. It can be seen that from Figure 3.39 (a-d) that the strong and dominant E_2 (high) mode of ZnO located between range 427 and 434 cm^{-1} for pure ZnO and doped ZnO nanostructures, which confirmed the characteristic of the Raman-active mode of wurtzite hexagonal ZnO. The E_2 (high) mode at 427 cm^{-1} for pure ZnO, 427.5 cm^{-1} for 0.255 % Mg-doped ZnO nanostructures, 428 cm^{-1} for 0.29 and 0.45 % Mg-doped, were red shifted by about 9-10 cm^{-1} compared to standard value of 437 cm^{-1}(Calleja & Cardona, 1977)(Sun et al.,2013). The Raman peak shifts were usually due to these reasons: (i) phonon confinement effect (Lin et. al, 2006), (ii) higher volume density of the point defects (Xiu et. al, 2006), and (iii) lattice strain (Tiwari et.al, 2002). Oxygen vacancies are one of the most important sources for point defects in ZnO nanostructure (Jiang et. al, 2007). In addition, the Raman mode of E_2 (high) – E_2 (low) was observed at ~327 cm^{-1}, which was attributed to the zone-boundary phonon scattering (Kumar et al., 2012)(Zhao et al., 2010). There was a small peak at 519 cm^{-1} and broad peak at ~660 cm^{-1} in the spectra due to the multi-phonon process and can be assigned to 2 (E_2 (high)- E_2 (low)) mode. A peak at 262 cm^{-1} observed for 0.29 and 0.45 % Mg-doped ZnO nanostructures which attributed to B1 (low) vibration mode corresponds to the silent branch mode (Calleja & Cardona, 1977)(Zhang et al. , 2009).

As a summary, pure and Mg-doped ZnO nanostructures have been synthesized using CA as a reducing agent by a biosynthesis sol-gel method. XRD results showed that all of the pure and Mg-doped ZnO exhibits peaks were consistent with the hexagonal wurtzite structure of ZnO. The Mg atomic percentage from EDX shows that the amount of Mg element in the sample was increased as the dopant concentration increases which are 0.225 %, 0.29 % and 0.45 % for 3, 5 and 10 mol % Mg-doped ZnO nanostructures respectively. Based on XRD result, there was a peak shifted toward higher 2θ which corresponds to smaller ionic radius of Mg^{2+} compared to ZnO that incorporated to ZnO structure. Raman results also exhibited a peak shifted towards red region which attributed to surface defect (oxygen vacancies) of ZnO. This phenomenon is strong evidence that Mg was successfully doped into the ZnO nanostructures.

3.5 Synthesis and characterization of silver nanoparticles decorated micro- and nanostructured zinc oxide as photocatalyst by sol-gel method

In this section, we describe the synthesis and characterization of AgNPs decorated microstructured and nanostructured ZnO to be used as photocatalysts. Microstructured ZnO were obtained from commercial ZnO powder and decorated with silver nanoparticles at different concentrations. The ZnO nanoparticles, also decorated with silver nanoparticles at different concentrations were synthesized by sol-gel method.

3.5.1 Experimental details

The AgNPs decorated microstructured and nanostructured ZnO were prepared by sol-gel method. Figure 3.40 represents the synthesis process of AgNPs decorated micro- and nanostructured ZnO.

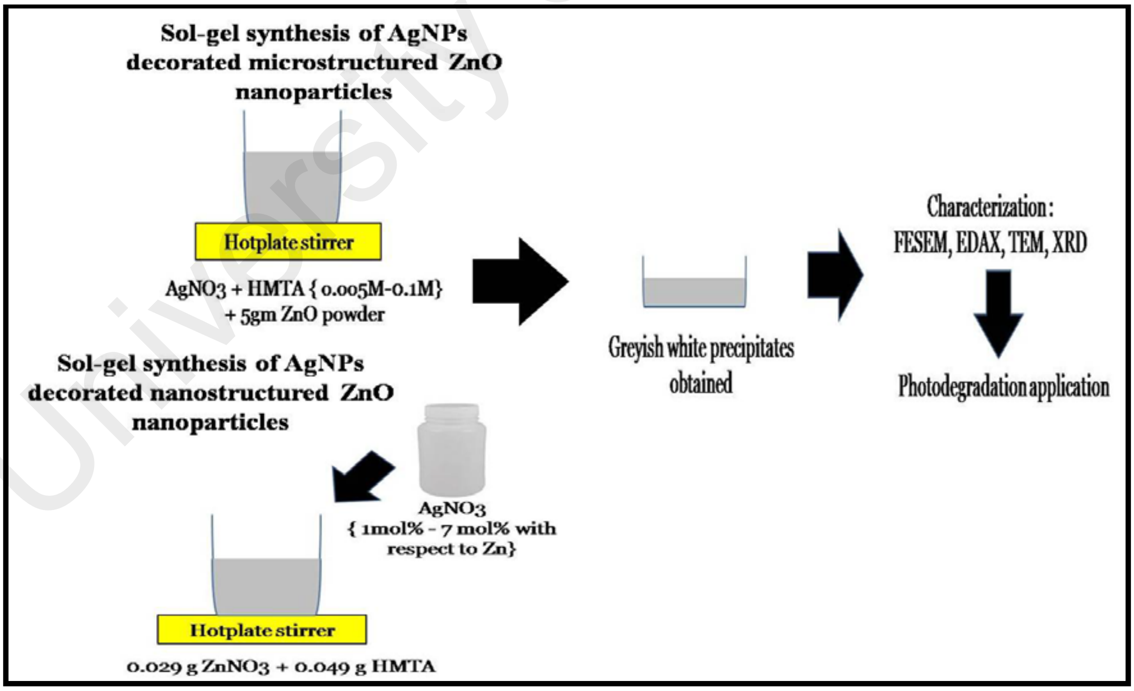

Figure 3.40: Synthesis of AgNPs decorated micro- and nanostructured ZnO**.**

For AgNPs decorated microstructured ZnO, stock solutions of silver nitrate ($AgNO_3$) and HMTA dissolved in 400 ml DI water at concentrations from 0.005 M to 0.1 M each were used. To each solution, 5 g ZnO powder was added and stirred continuously at 95 °C for 6 hours. After the reaction was completed, the solutions were centrifuged and resulting solid products washed thoroughly in DI water to remove residual unreacted chemicals. Finally, the greyish white precipitates obtained were annealed at 300 °C for 2 hours in air. For AgNPs decorated nanostructured ZnO, the synthesis process was as followed. 0.029 g of $Zn(NO_3)_2 \cdot 6H_2O$ and 0.049 g HMTA, $C_6H_{12}N_4$) were dissolved in 400 ml DI water. For the AgNPs decorated nanostructured ZnO, $AgNO_3$ was added into the stock solution at different mol % concentrations of 1, 2, 2.5, 3, 5 and 7 mol % with respect to Zn. All stock solutions for the synthesis of AgNPs decorated nanostructured ZnO undergo the same synthesis process as AgNPs decorated microstructured ZnO nanoparticles.

The pure ZnO powder, pure ZnO nanoparticles, AgNPs decorated micro- and nanostructured ZnO were characterized by field emission scanning electron microscope (FESEM) and high-resolution transmission electron microscopic (HRTEM) to study the morphological and structural relationship of the pure and modified photocatalyst. Chemical analysis was performed using electron dispersive X-ray spectroscopy (EDX), X-ray diffraction (XRD) with Cu K-alpha radiation (λ=1.4506 Å) was employed for phases and crystallinity analysis. In addition, the photoluminescence (PL) spectra were measured by photoluminescence spectrophotometer with excitation wavelength 325 nm to study the optical properties of the obtained photocatalyst.

3.5.2 Characterization of AgNPs decorated microstructured zinc oxide

Figure 3.41 shows the FESEM images of pure ZnO and AgNPs decorated microstructured ZnO. Similar structures were observed for pure ZnO particles and AgNPs decorated microstructured ZnO at various Ag content. All samples were composed of particles with average size about 500 nm. The incorporation of Ag to the ZnO samples was not visible in the FESEM images.

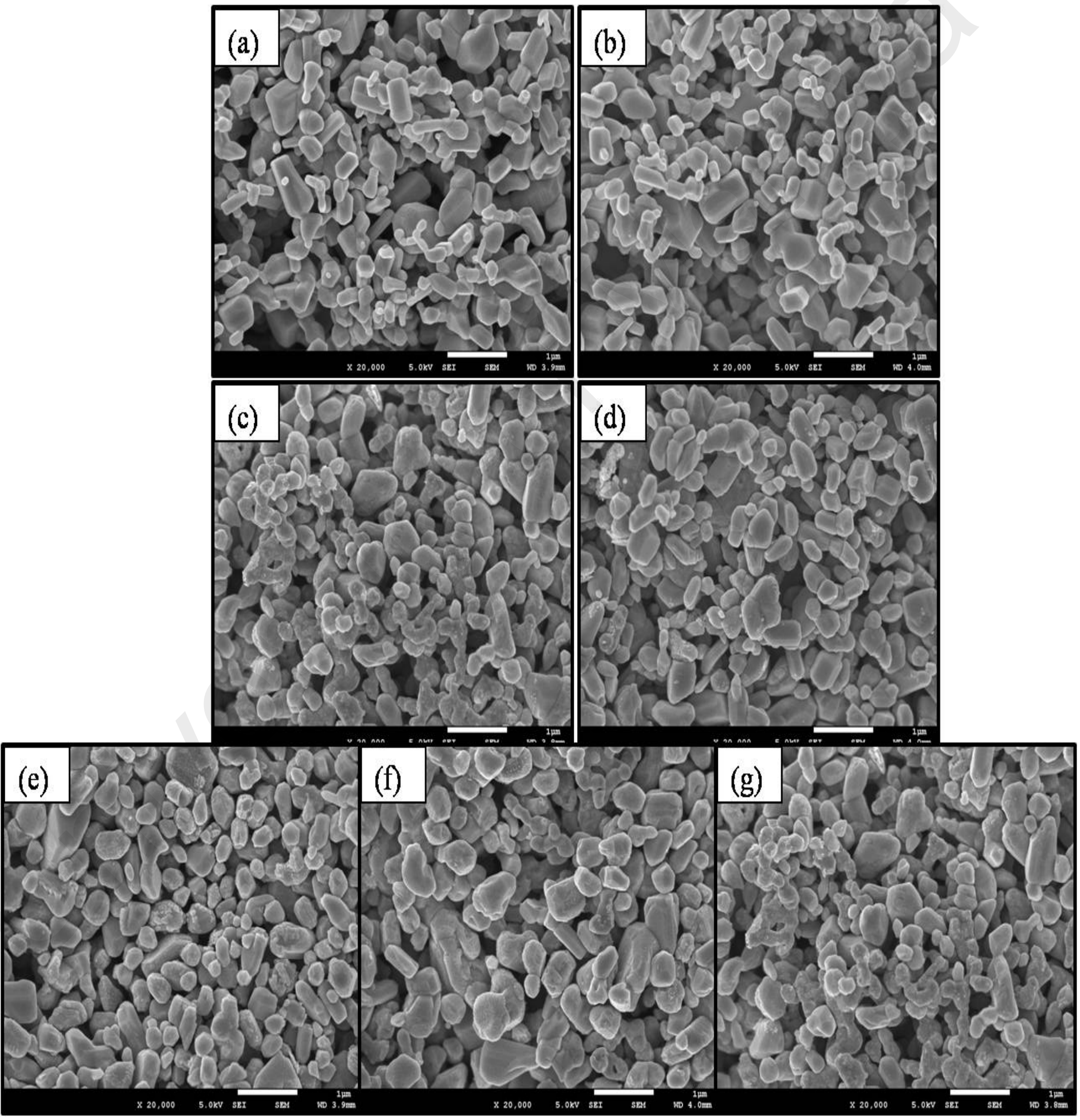

Figure 3.41: FESEM images of (a) pure ZnO, (b) 0.005 M, (c) 0.01 M, (d) 0.05 M, (e) 0.07 M, (f) 0.09 M, (g) 0.1 M AgNP decorated microstructured ZnO.

Figure 3.42 shows the EDX spectra of pure ZnO and AgNPs decorated microstructured ZnO. Figure 3.42 (a) shows the EDX spectrum for pure ZnO, (b) 0.005 M, (c) 0.01 M, (d) 0.05 M,(e) 0.07 M, (f) 0.09 M, (g) 0.1 M AgNP decorated microstructured ZnO, respectively. From the spectra only Zn, O and Ag were detected.

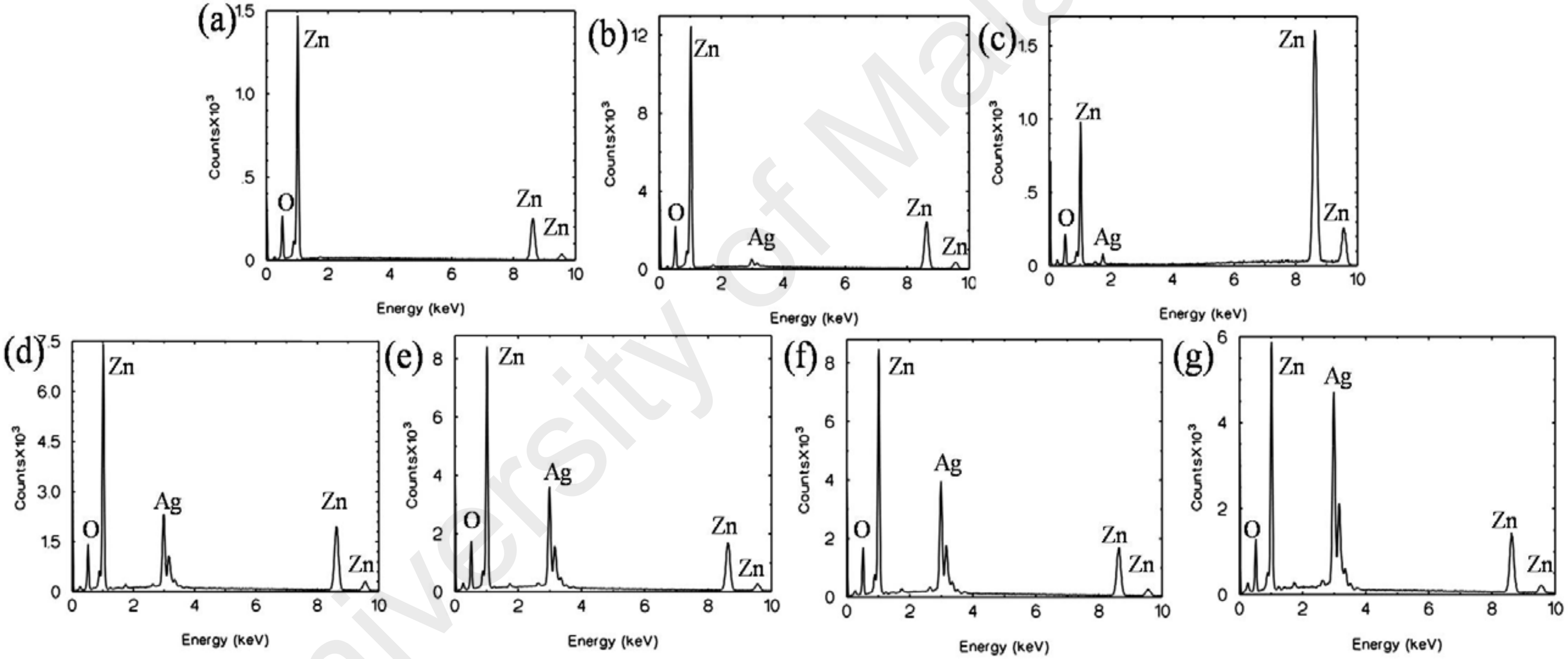

Figure 3.42: EDX spectra of (a) pure ZnO,(b) 0.005 M, (c) 0.01 M, (d) 0.05 M, (e) 0.07 M, (f) 0.09 M, (g) 0.1 M AgNPs decorated microstructured ZnO.

The concentrations of the elements for pure ZnO and AgNPs decorated microstructured ZnO are presented in Table 3.8. As expected the Ag content increased with increasing concentration of $AgNO_3$.

Table 3.8: Atomic % from EDX analysis and ratio of Ag/ZnO for pure ZnO and AgNPs decorated microstructured ZnO.

Sample	**Atomic % from EDX analysis**			**[Ag]/[Zn] (%)**
	Zn	**O**	**Ag**	
Pure ZnO	41.20	58.80	-	-
0.005M AgNPs decorated microstructured ZnO	46.60	52.85	1.073	2.33
0.01M AgNPs decorated microstructured ZnO	45.76	52.25	1.99	4.36
0.05M AgNPs decorated microstructured ZnO	39.20	56.30	4.50	11.48
0.07M AgNPs decorated microstructured ZnO	38.40	53.96	7.64	19.90
0.09M AgNPs decorated microstructured ZnO	32.70	54.05	13.25	40.40
0.1M AgNPs decorated microstructured ZnO	30.00	51.58	18.42	61.31

Figure 3.43 shows the graph of fraction of Ag/Zn as a function of $AgNO_3$ concentration for pure ZnO and AgNPs decorated microstructured ZnO. The fraction of Ag/ Zn in atomic percentage increased significantly as the amount of $AgNO_3$ used during the synthesis process increased.

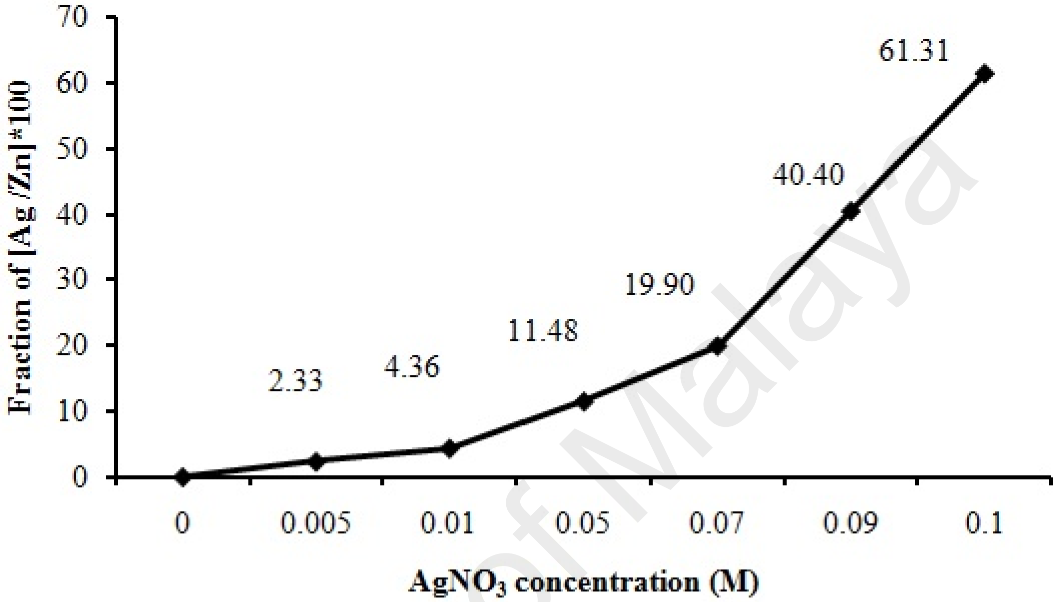

Figure 3.43: The fraction of Ag/Zn versus $AgNO_3$ concentration (M) used during the synthesis**.**

Figure 3.44 shows the chemical mapping by EDX for 0.1 M AgNPs decorated microstructured ZnO. Figure 3.44 (a) shows the SEM image of the 0.1 M AgNPs decorated microstructured ZnO in which the elemental mapping was conducted. In the images, elements were represented by blue, red and green for O, Zn and Ag atoms respectively. Figure 3.44 (b) shows the mapping for all elements where greenish tint representing Ag appeared on the surface of ZnO microparticles. As expected, the mapping of O and Zn represented in Figure 3.44 (c) and Figure 3.44 (d) showed distribution covering the whole frame. Similarly, the mapping for Ag in Figure 3.44 (e) showed complete coverage of the image frame. In generally the elemental mapping indicated that Ag was attached to the ZnO microparticles surfaces.

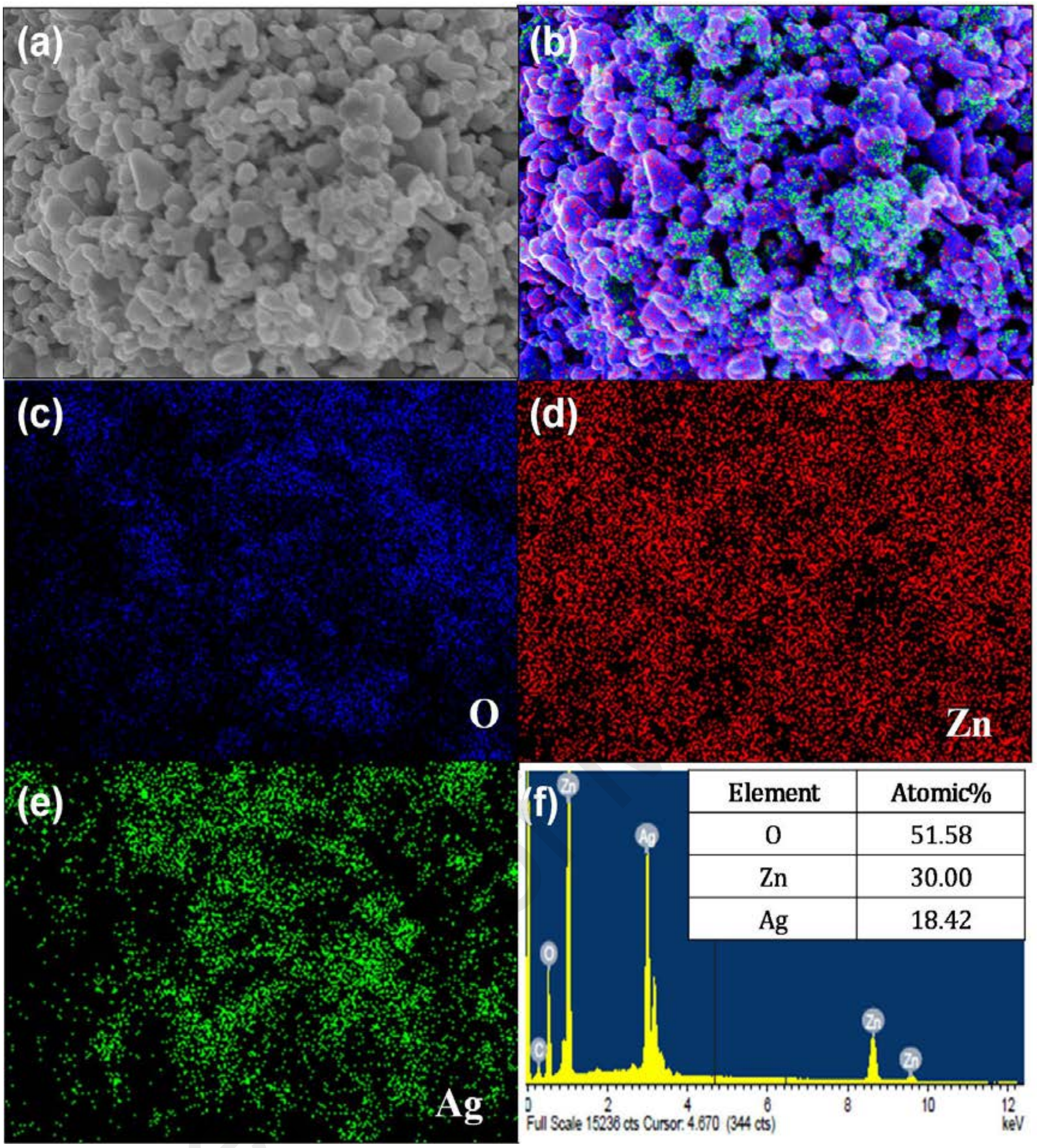

Element	Atomic%
O	51.58
Zn	30.00
Ag	18.42

Figure 3.44: (a) Selected image of 0.1 M AgNPs decorated microstructured ZnO for the EDX mapping analysis. The corresponding elemental mapping images for Zn, O and Ag are presented in (b), (c), (d) and (e), and (f) the elemental spectra and composition of the sample.

The structural properties of pure ZnO and AgNPs decorated microstructured ZnO were further analyzed with TEM. Figure 3.45 shows the TEM images of pure ZnO. Figure 3.45 (a) and (b) show the low and high magnified TEM image for pure ZnO particles.

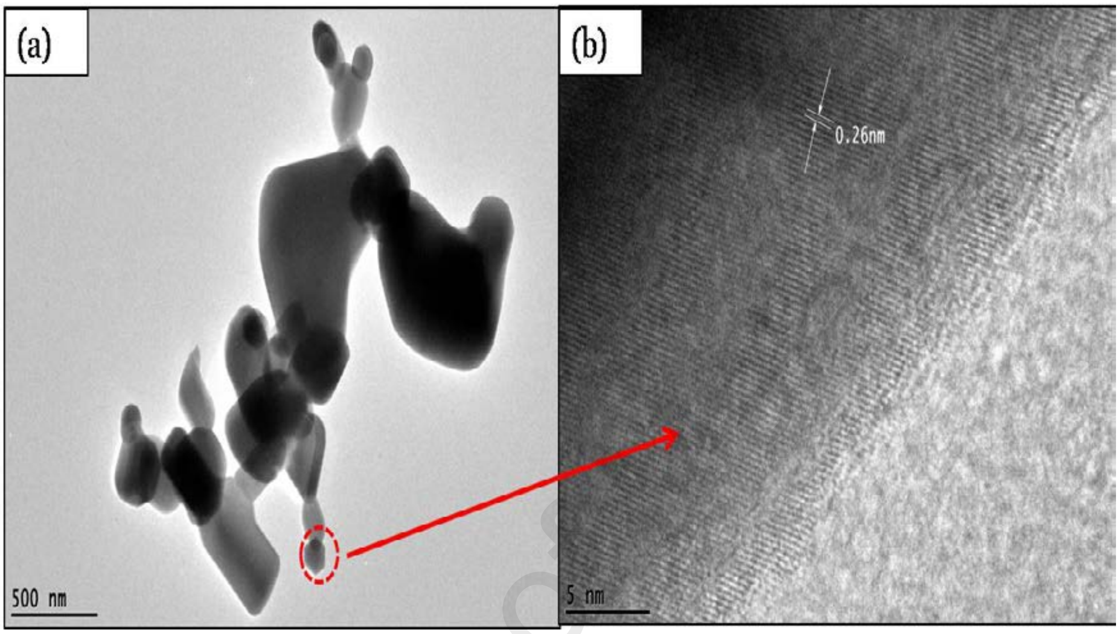

Figure 3.45: The low-magnified and high-resolution TEM image of pure ZnO.

As expected, the structure of the pure ZnO microstructures contains particles structures with size consistent with that observed in the FESEM analysis. High resolution TEM image as shown in Figure 3.45 (b) indicates that the particles of ZnO are single-crystal structures. The interplanar spacing of pure ZnO is 0.260 nm that corresponds to the ZnO (002) direction.

Figure 3.46 (a) and (b) exhibit the low magnified and high magnified TEM images of 0.005 M AgNPs decorated microstructured ZnO.

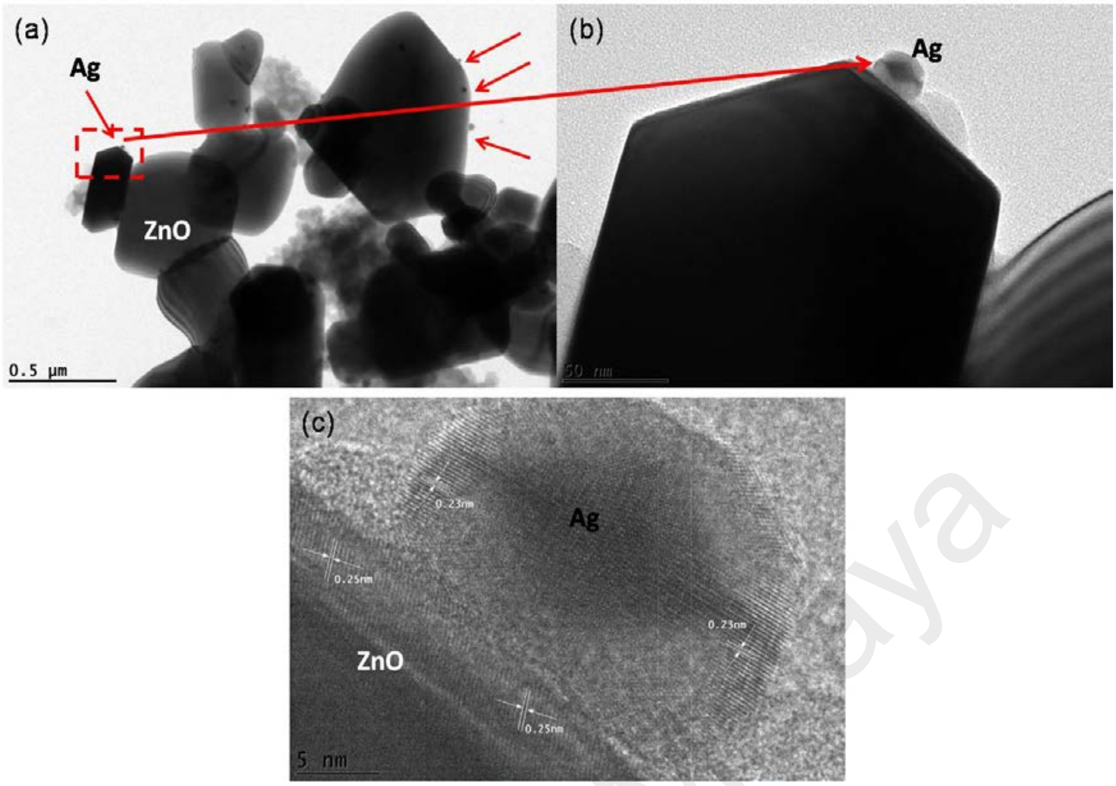

Figure 3.46: (a) and (b) The low-magnified and high-magnified TEM images of the 0.005 M AgNPs decorated microstructured ZnO, respectively (c) high-resolution TEM image of the area indicated by the square in (a).

Figure 3.46 (a) shows a low magnification of a cluster of ZnO microparticles. Here, the existence of AgNPs was not apparent. At a higher magnification shown in Figure 3.46 (b) shows the ZnO microparticle structure and an expected spherical AgNP attacted on the surface. From Figure 3.46 (c), which shows a close up view of the spherical particles yielded lattice fringe with crystalline plane spacing of 0.230 nm was assigned to the (111) plane of Ag with face centred cubic (fcc) structure. Also shown is the crystalline plane spacing of 0.250 nm corresponding to the (002) plane of ZnO. This shows that Ag NPs formed on the ZnO microparticles surface.

The XRD pattern in the range of 20 °- 60 ° for pure ZnO, 0.005 M, 0.01 M, 0.05 M, 0.07 M, 0.09 M and 0.1 M AgNPs decorated microstructured ZnO samples are shown in Figure 3.47. For pure ZnO (Figure 3.47 (a)), the diffraction peaks corresponding to (100), (002), (101) and (110) planes were in agreement with a wurtzite hexagonal ZnO crystal structure (JCPDS Card File No. 36-1451). Meanwhile, for 0.005 M, 0.01 M, 0.05 M, 0.07 M, 0.09 M and 0.1 M AgNP decorated microstructured ZnO (Figure 3.47 (b)-(g)), peaks marked with "*" which were assigned to the (111) and (200) planes were in agreement with face-centered cubic (fcc) structure of Ag (JCPDS Card File No. 04-0783), respectively (Gao et al., 2013).

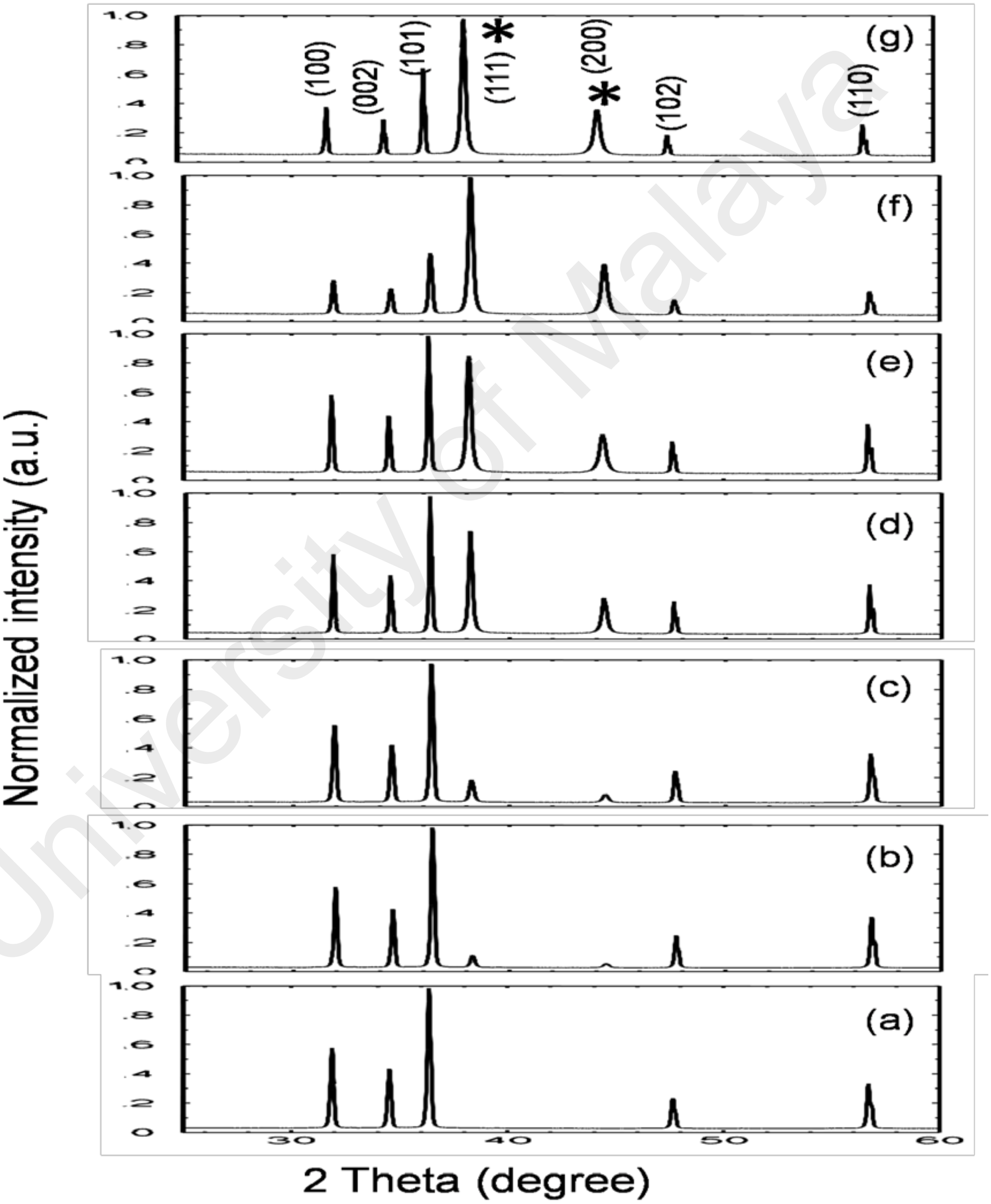

Figure 3.47: Normalized XRD patterns of (a) pure ZnO, (b) 0.005 M, (c) 0.01 M, (d) 0.05 M, (e) 0.07 M, (f) 0.09 M, (g) 0.1 M AgNPs decorated microstructured ZnO.

There are reports on the doping of ZnO with Ag, where the Ag atoms were incorporated in ZnO lattice as a substituent for Zn^{2+} or as an interstitial atom (Karunakaran, Rajeswari, & Gomathisankar, 2010)(Wang et al., 2012). If doping occured, peak shifts are expected in the XRD spectra. However, no other peaks and notable peak shift was observed in the diffraction peaks, indicating that Ag did not incorporate into the lattice of ZnO, but AgNPs formed on the surface of ZnO as reported elsewhere. (Georgekutty, Seery, & Pillai, 2008)(Xie & Wu, 2010)(Xu et al., 2008).

Figure 3.48 shows the PL spectra of pure ZnO, 0.005 M, 0.01 M, 0.05 M, 0.07 M, 0.09 M and 0.1 M AgNPs decorated microstructured ZnO samples.

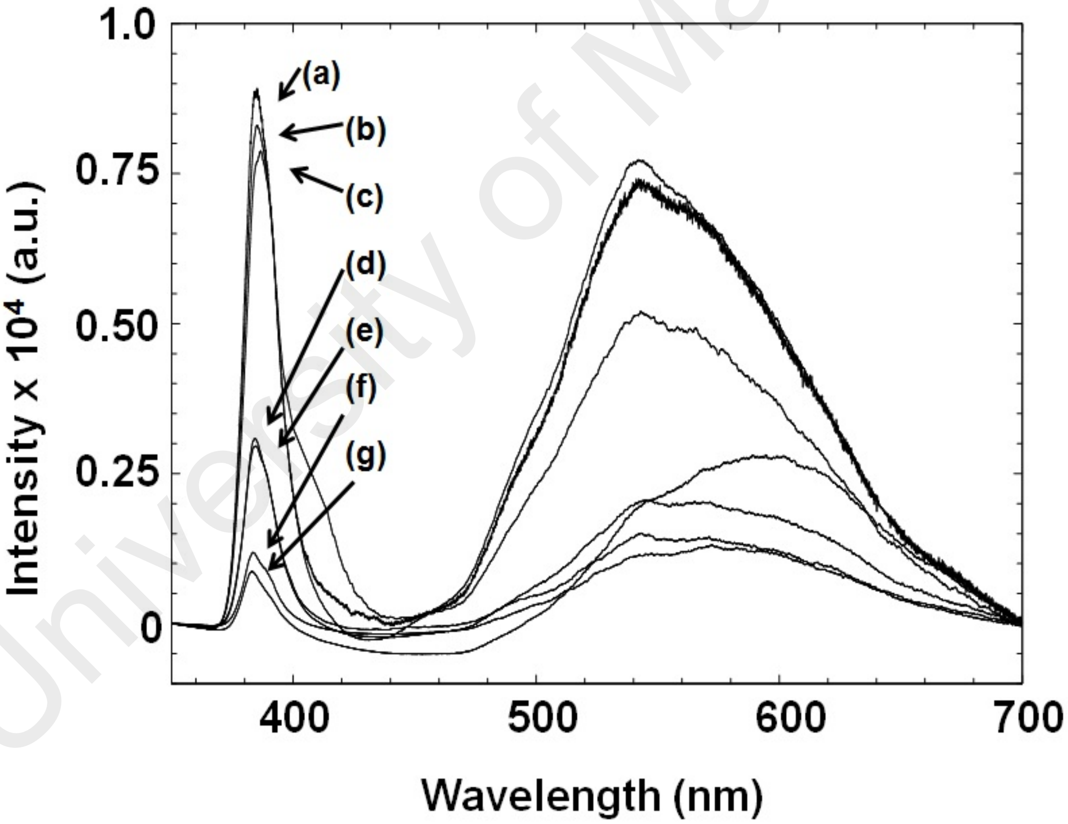

Figure 3.48: PL spectra of (a) pure ZnO, (b) 0.005 M, (c) 0.01 M, (d) 0.05 M, (e) 0.07 M, (f) 0.09 M, (g) 0.1 M AgNP decorated microstructured ZnO.

All curve similarly show two prominent emission bands, which are a near uv emission at around 380 – 400 nm and a broad green band at about ~550 nm. Near uv emission band is originated from the radiative recombination process of free excitons, while the green band emission is attributed to the recombination of electrons from conduction band edge with a hole from trap level or single ion oxygen vacancies at the particle surface (Duan et al., 2013). It was found that the PL intensity of each emission band of 0.005 M, 0.01 M, 0.05 M, 0.07 M, 0.09 M and 0.1 M AgNPs decorated microstructured ZnO is lower than pure ZnO. This might be related to the increased of Ag content that have a larger site (act as electron sinks) to accept the electrons; hence hinder the recombination of photoinduced electrons and holes (Georgekutty et al., 2008)(Ren et al., 2010).

3.5.3 Characterization of AgNPs decorated nanostructured zinc oxide

FESEM image of pure ZnO and AgNPs decorated nanostructured ZnO is shown in Figure 3.49. Figure 3.49 (a), shows the pure ZnO nanosparticles, while Figure 3.49 (b) – (g) presented the AgNP decorated nanostructured at concentration of 1, 2, 2.5, 3, 5 and 7 mol %, respectively. The pure ZnO was observed as spherical nanoparticles with uniform and homogenous distribution. From Figure 3.49 (b) – (g) the morphologies of AgNPs decorated nanostructured ZnO at various Ag concentration, showed similar structure of spherical nanoparticles like as pure ZnO. The distribution of the nanoparticles also slightly similar to each other. From this observation, it can be said that, the existence and modifying the ZnO photocatalyst with AgNPs in this experiment significantly did not influenced any morphological changes. However, in term of elemental composition in each photocatalyst, the AgNPs was significantly affecting the Ag/Zn ratio of the photocatalyst system. Hence, the changes in Ag/Zn ratio are expected to give effect in the photodegradation reaction. The pure ZnO and AgNPs decorated nanostructuctured ZnO samples obtained were homogeneous and agglomerated with a particle size ranging from 25 to 100 nm.

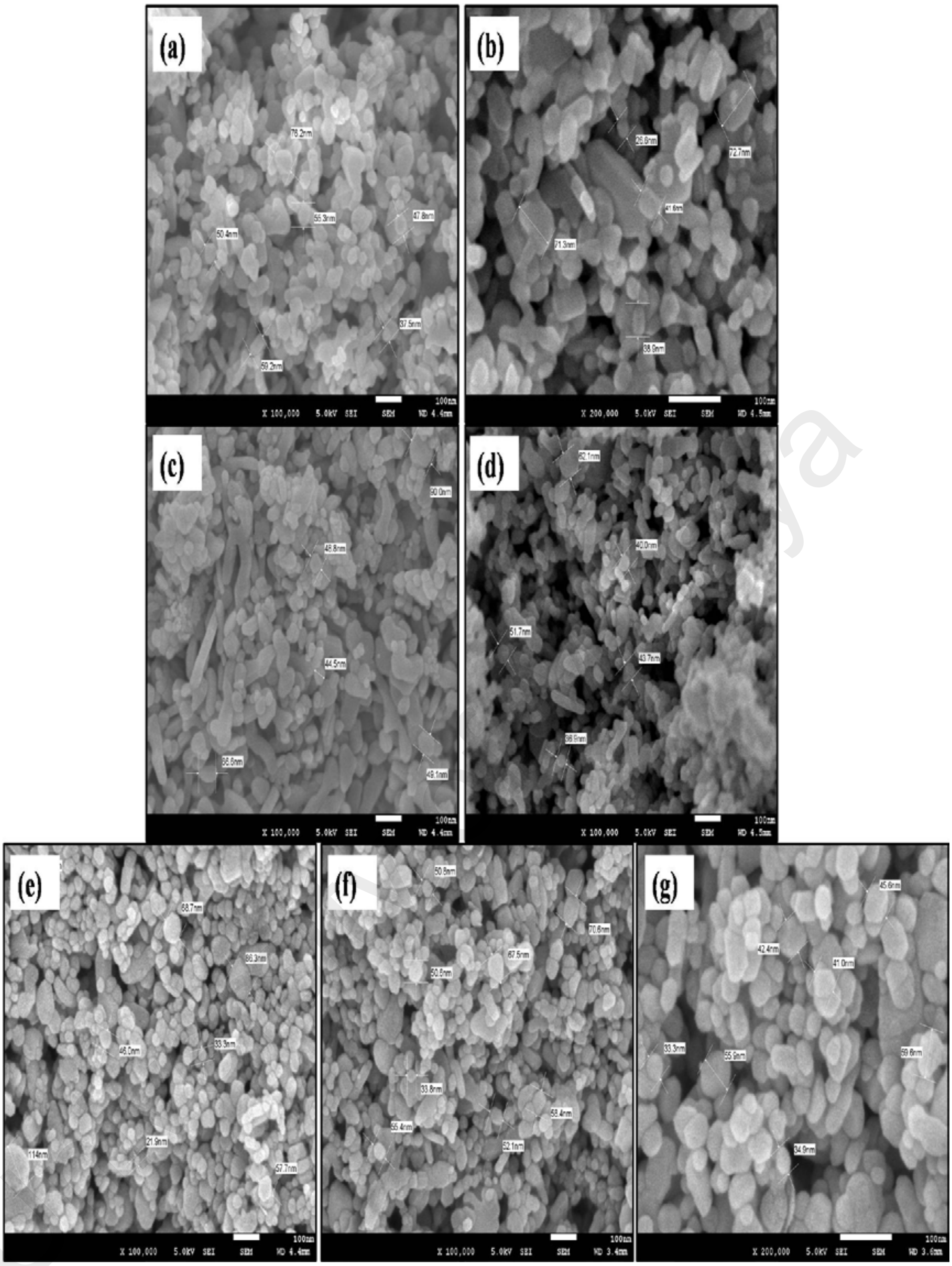

Figure 3.49: FESEM images of (a) pure ZnO (b) 1 , (c) 2, (d) 2.5, (e) 3, (f) 5 and (g) 7 mol % AgNPs decorated nanostructured ZnO.

Figure 3.50 shows the EDX spectra of pure ZnO and AgNPs decorated nanostructured ZnO. Figure 3.50 (a) shows the EDX spectra for pure ZnO, (b) 1, (c) 2, (d) 2.5, (e) 3, (f) 5, (g) 7 mol % of AgNP decorated nanostructured ZnO. It was observed that for pure ZnO, the EDX spectra mainly composed of Zn and O element while for sample AgNPs decorated nanostructured ZnO, the samples were composed of Zn, O and Ag elements.

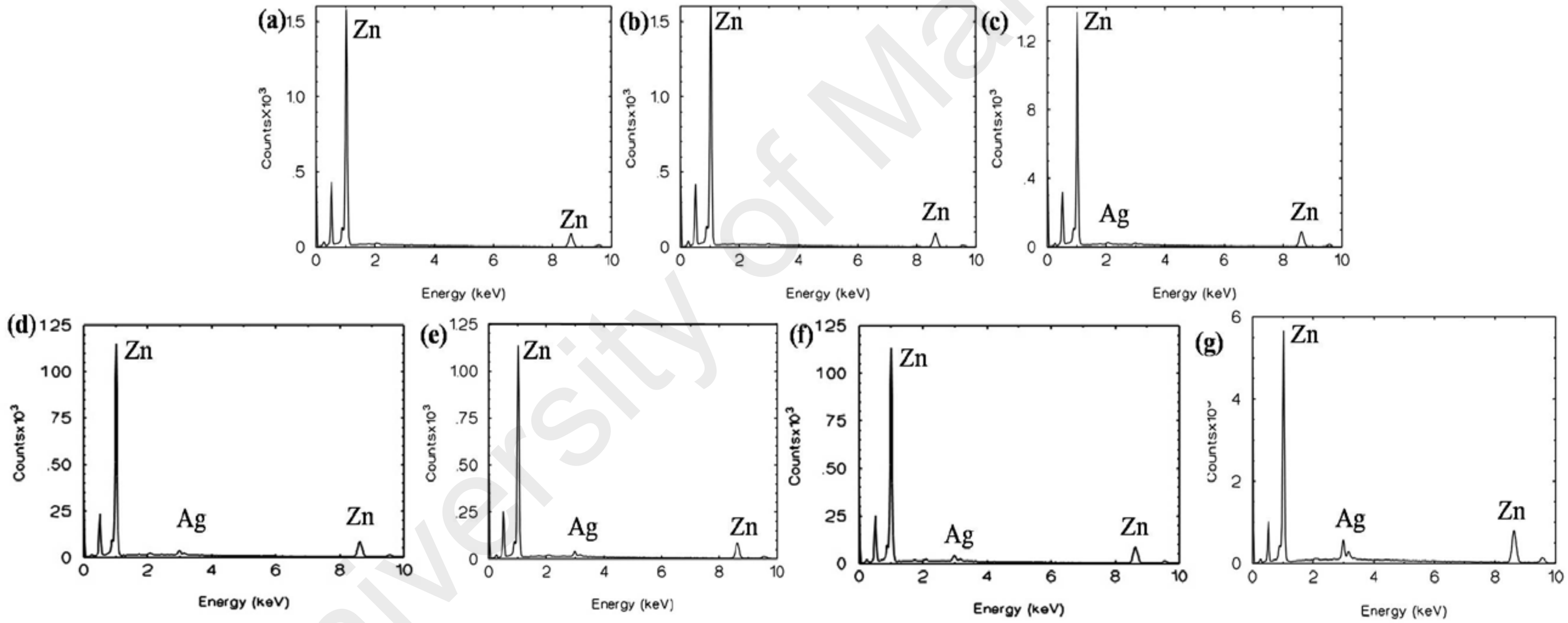

Figure 3.50: EDX spectra of (a) pure ZnO (b) 1 , (c) 2, (d) 2.5, (e) 3, (f) 5 and (g) 7 mol % AgNPs decorated nanostructured ZnO.

Composition of pure and AgNPs decorated nanostructured ZnO in atomic percentage is presented in Table 3.9.

Table 3.9: EDX analysis of pure ZnO nanoparticles and various mol % concentrations of AgNPs decorated nanostructured ZnO.

Sample	**Atomic % from EDX analysis**			**[Ag]/[Zn] (%)**
	O	**Zn**	**Ag**	
Pure ZnO	56.7	43.3	-	-
1 mol % AgNPs decorated nanostructured ZnO	55.99	43.64	0.37	0.85
2 mol % AgNPs decorated nanostructured ZnO	55.52	43.99	0.49	1.11
2.5 mol % AgNPs decorated nanostructured ZnO	51.42	47.64	0.94	1.97
3 mol% AgNPs decorated nanostructured ZnO	51.95	47.07	0.98	2.08
5 mol % AgNPs decorated nanostructured ZnO	55.15	43.18	1.67	3.87
7 mol % AgNPs decorated nanostructured ZnO	68.05	29.83	2.12	7.11

The graph of Ag/ Zn in atomic fraction as a function of $AgNO_3$ concentration is shown in Figure 3.51. As expected the Ag fraction increased significantly as the amount of $AgNO_3$ used during the synthesis process increased from 0.85 %, 1.11 %, 1.97 %, 2.08 %, 3.87 % and 7.11 % as 1, 2, 2.5, 3, 5 and 7 mol % Ag, respectively.

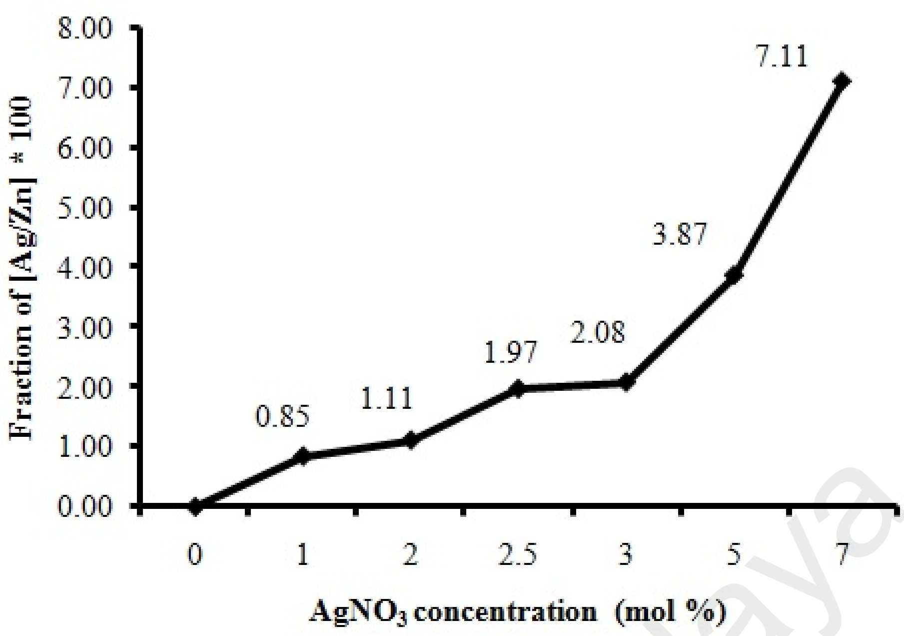

Figure 3.51: The fraction of Ag/Zn versus $AgNO_3$ concentration (mol %) used during the synthesis.

Figure 3.52 shows the chemical mapping by EDX for 7 mol % AgNPs decorated nanostructured ZnO. Figure 3.52 (b) shows the SEM image of 7 mol % AgNPs decorated nanostructured ZnO in which the elemental mapping was conducted. In the images, elements were represented by green, red and blue for O, Zn and Ag atoms respectively. Figure 3.52 (b) shows the mapping for all elements where bluish tint representing Ag appeared on the surface of ZnO nanoparticles. As expected, the mapping of O and Zn represented in Figure 3.52 (c) and Figure 3.52 (d) showed distribution covering the whole frame. Similarly, the mapping for Ag in Figure 3.52 (e) showed complete coverage of the image frame. In generally the elemental mapping indicated that Ag was attached to the ZnO nanoparticles surfaces.

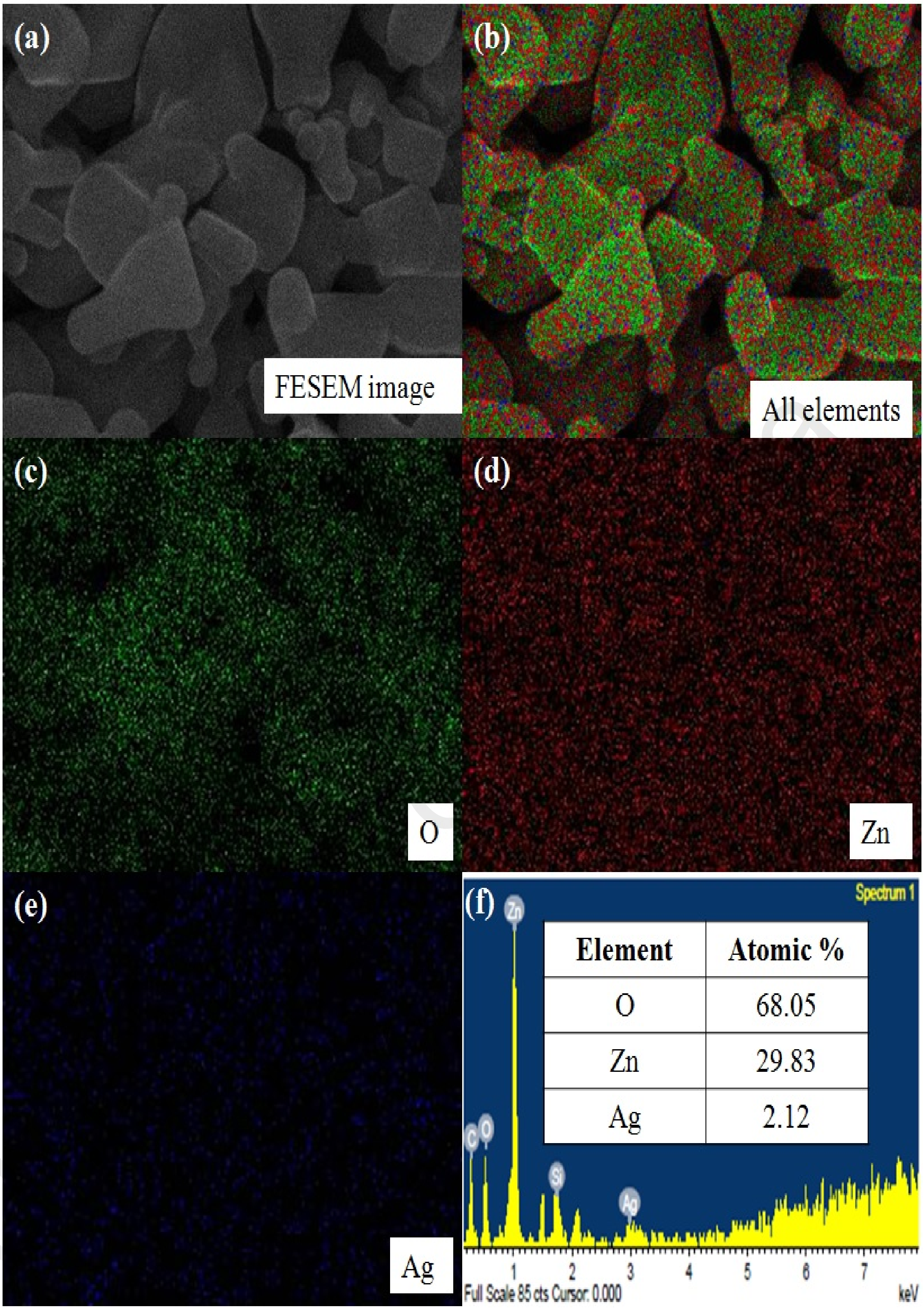

Element	Atomic %
O	68.05
Zn	29.83
Ag	2.12

Figure 3.52: (a) Image of 7 mol % AgNPs decorated nanostructured ZnO for the EDX mapping analysis. The corresponding elemental mapping images for Zn, O and Ag are presented in (b), (c), (d) and (e), and (f) the elemental spectra and composition of the sample.

The structural properties of pure ZnO and AgNPs decorated nanostructured ZnO were further analyzed with TEM. Figure 3.53 shows the TEM images of 1 mol % AgNPs decorated nanostructured ZnO. Figure 3.53 (a) and (b) show the low and high magnified TEM image for the samples.

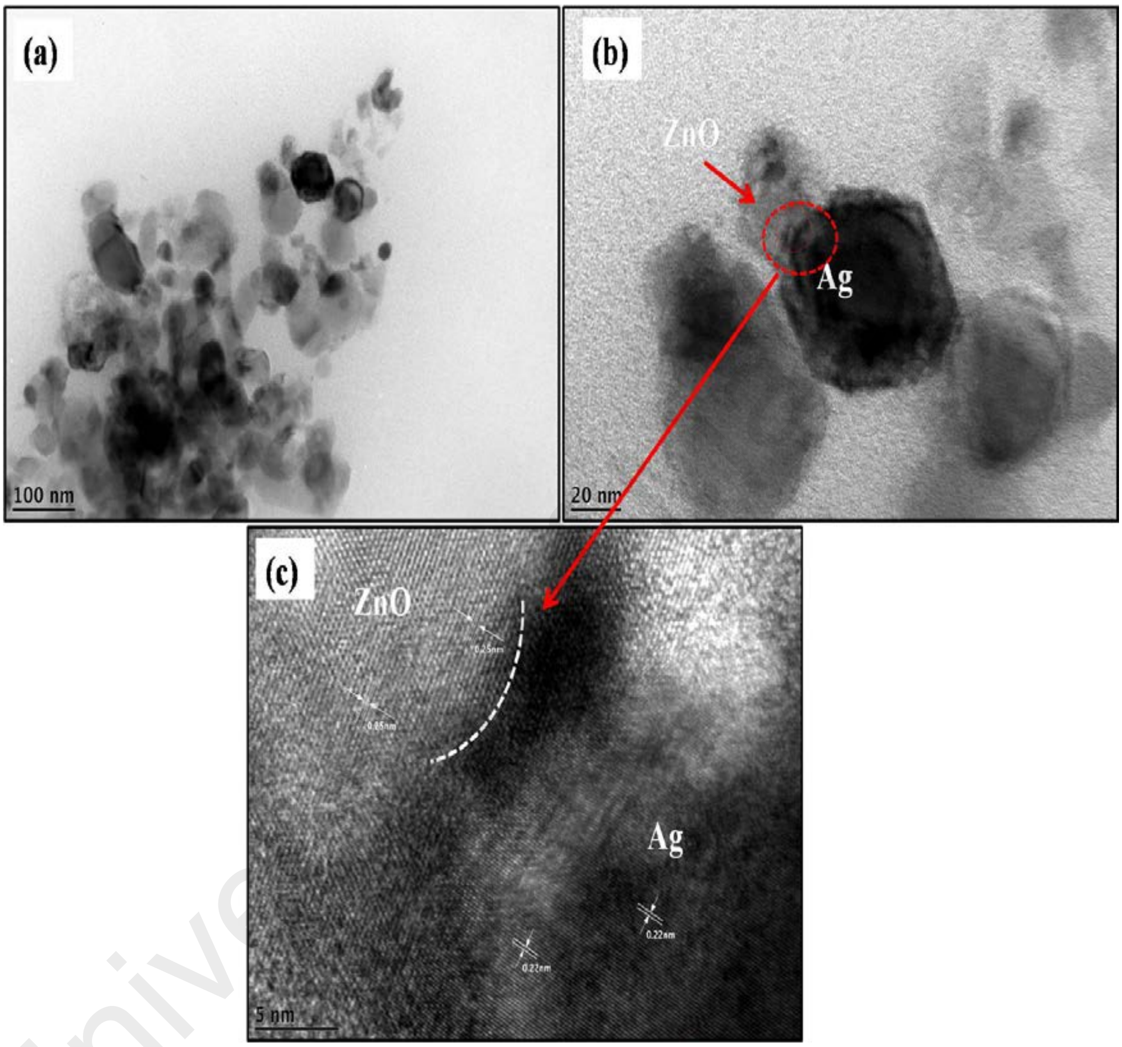

Figure 3.53: (a) and (b) The low-magnified and high-magnified TEM images of the 1 mol % AgNPs decorated nanostructured ZnO, respectively (c) high-resolution TEM image of the area indicated by the square in (a).

From Figure 3.53 (a), the heterostructures of 1 mol % AgNPs decorated nanostructured ZnOseemed to agglomerates into cluster and growth in particle like structure which in a good agreement with FESEM results. The TEM image in Figure 3.53 (b) shows the 1 mol % AgNPs decorated nanostructured ZnOconsisted of

AgNPswhere a boundary between the ZnO NPs and Ag (marked by red circle) suggested the chemical bonds between the particles. The Ag particles only formed on the ZnO surface. Figure 3.53 (c) shows a HRTEM image taken from the circle region of Figure 3.53 (b), which clearly shows the crystal lattice of Ag and ZnO. The spacing between adjacent lattice fringes in the ZnO is about 0.25 nm, which corresponds to d-spacing of the (002) plane. Also, lattice fringes with interplanar spacing of 0.22 nm attributed to {111} plane of fcc Ag was observed.

The normalized XRD patterns of pure ZnO, (b) 1, (c) 2, (d) 2.5, (e) 3, (f) 5, (g) 7 mol % of AgNP decorated nanostructured ZnOare presented in Figure 3.54 (a) - (g). For pure ZnO (Figure 3.54 (a)), a wurtzite hexagonal ZnO crystal structure (JCPDS Card File No. 36-1451) is detected. Meanwhile, for 1, 2, 2.5, 3, 5 and 7 mol % of AgNP decorated nanostructured ZnO (Figure 3.54 (b) – (g)), peaks marked with “*” which assigned to the (111) and (200) planes corresponded to the face-centered cubic (fcc) structure of Ag (JCPDS Card File No. 04-0783) was identified (Gao et al., 2013)(Song et al., 2010).

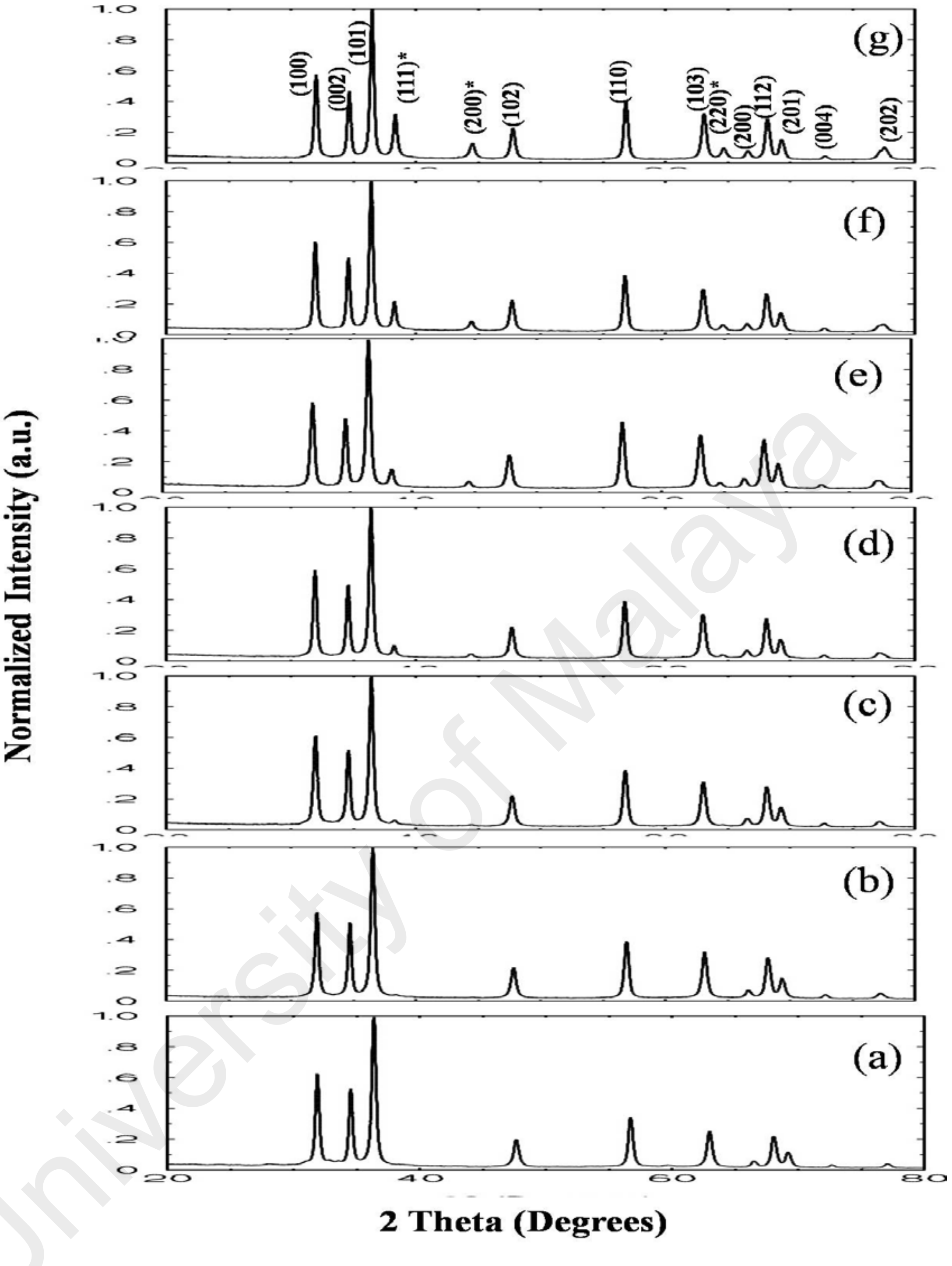

Figure 3.54: Normalized XRD patterns of the of (a) pure ZnO (b) 1 , (c) 2, (d) 2.5, (e) 3, (f) 5 and (g) 7 mol % AgNPs decorated nanostructured ZnO.

In summary, AgNPs ZnO micro- and nanostructured ZnO photocatalyst has been synthesized by a simple sol-gel method. For AgNPs decorated microstructured ZnO photocatalyst, various concentrations of Ag have been added and from electron microscopy analysis showed that all photocatalyst formed similarly in particle-like structure. No significance changes in the structure of the photocatalyst once a variation of concentration added to the ZnO. However, there was a significance difference in the amount of Ag to Zn (in atomic percentage) that measured from EDX analysis. The doping level of Ag/ Zn increased as the concentration increased. For 0.005 M AgNPs decorated microstructured ZnO, the doping level of Ag/Zn is about 2.33 %, 4.36 % for 0.01 M AgNPs decorated microstructured ZnO, 11.48 % for 0.05 M AgNPs decorated microstructured ZnO, 19.90 % for 0.07 M AgNPs decorated microstructured ZnO, 40.40 % for 0.09 M AgNPs decorated microstructured ZnO and 61.31 % for 0.1 M AgNPs decorated microstructured ZnO, respectively. For AgNPs decorated nanostrutured ZnO photocatalyst, similar particle structure of photocatalyst was obtained for all photocatalyst with average particle size beween 20 - 100 nm. However, the EDX analysis showed by increasing mol concentration of Ag, the doping level of Ag/Zn was increased. Decorated levels of Ag to Zn atomic% of 0.85, 1.11, 1.92, 2.08, 3.87 and 7.11 was obtained for 1, 2, 2.5, 3, 5 and 7 mol % AgNPs decorated nanostructured ZnO. The existence of Zn, O and Ag from EDX proved that Ag was decorated into the ZnO. From TEM result of AgNP decorated micro- and nanostructured ZnO, it was proved that Ag particle only segregated on the ZnO surface, indicating that Ag did not incorporate into the ZnO lattice. From HRTEM results, both AgNPs decorated micro- and nanostructured ZnO have a boundary between the surface of Ag and ZnO, and lattice fringes can be clearly seen for Ag and ZnO particles. The distance between the lattice is about 0.26 nm which attributed to the (002) crystal plane of the ZnO wurtzite structure. While another lattice was measured to be 0.23 nm that corresponding to (111) plane fcc metallic Ag.There was no significant peak shifted was observed from the XRD pattern for both AgNP decorated micro- and nanostructured ZnO photocatalyst, indicating that Ag particles only formed on the ZnO surface.

CHAPTER 4: APPLICATION OF ZINC OXIDE NANOSTRUCTURES AS FIELD ELECTRON EMISSION CATHODES

4.1 Introduction

In this chapter, results and discussion on field electron emission measurement and its characteristic were discussed. Three sections will be covered which are FEE characteristic on the effect of different deposition times, effect of pure and Al-doped ZnO nanorods and effect of pure and Mg-doped ZnO nanostructures.

4.2 FEE measurement of zinc oxide nanostructures

Figure 4.1 (a) schematically depicts the configuration for field emission measurements, suggesting that the emission current was generated by the tunneling of electrons from the ZnO nanostructures tip.

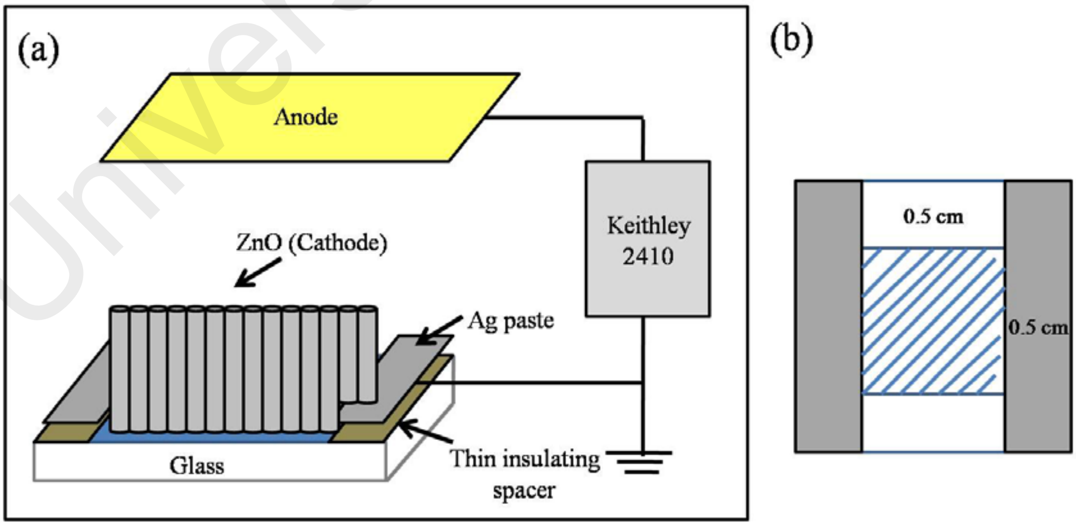

Figure 4.1: (a) configuration for field emission measurement and (b) the effective emission area, A of the ZnO nanostructures.

The field emission characteristics of the ZnO nanostructures were examined in a vacuum chamber at a pressure of 10^{-7} mbar using a Keithley 2410 source meter unit and the data acquisition was automated using the Lab tracer 2.0 software.The distance, d between the cathode of ZnO nanostructures sample and a copper anode was 120 μm measured using a micrometer gauge attached to the anode. The resolution of the micrometer gauge was 10 μm. The effective emission area, A of the ZnO nanostructures sample was 0.25 cm^2 as shown in Figure 4.1 (b). For FEE measurement of ZnO nanostructures deposited on glass substrate, a part of the glass substrate was covered with thin insulating spacer and silver paste act as electrodes (Figure 4.1 (a)). All the measurements were carried out at room temperature.

Figure 4.2 (a) shows schematics of the field electron circuit. For IV measurements voltage was increased from 0 V to 1100 V steps in 1V was applied across the electrodes and the field emission current was measured at the anode. Figure 4.2 (b) shows a typical IV curves obtained from a ZnO nanostructure cathode.

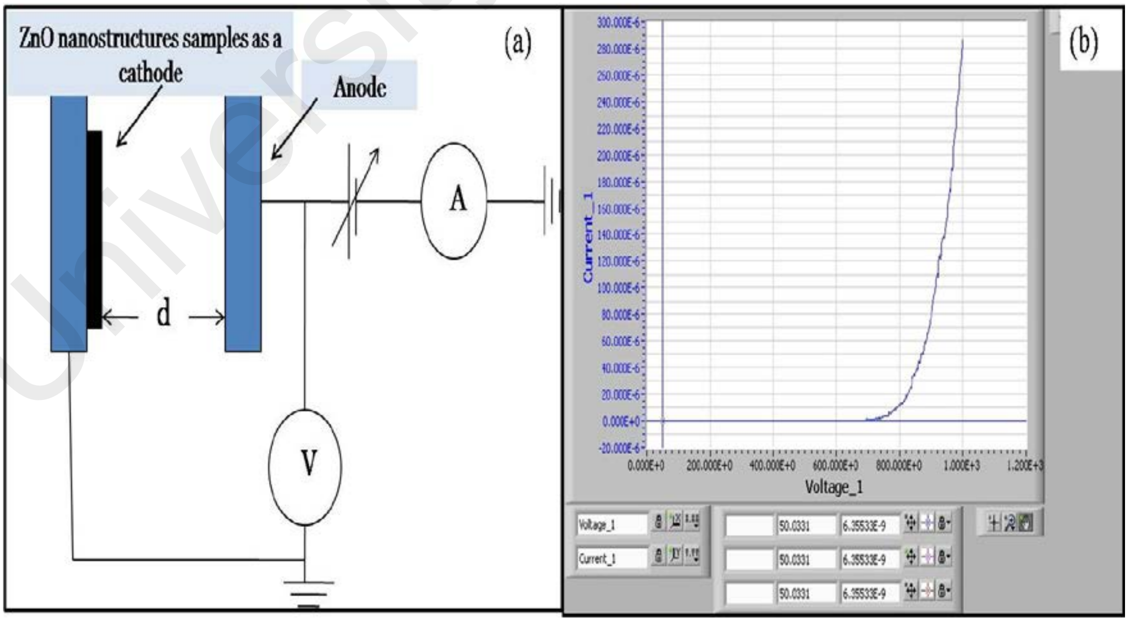

Figure 4.2: (a) Field electron schematic diagram of device and (b) picture of obtained I –V curve from the measurement.

In the experimental study of the field electron emission behavior of a sample cathode the current density versus the electric field (J-E) curves are normally fitted to the Fowler Nordheim model as described in Section (2.5.1 (a)).From the J-E curves, characteristics parameters defining the field electron emission properties of the cathode can be determined. The parameters are; (i) threshold, E_{th} (ii) turn-on electric field, E_{to}, (iii) field enhancement factor, β and (iv) the stability of the field emission. We define the turn-on field and the threshold field as the electric field that required producing 1 μA/cm^2 and 100 μA/cm^2, respectively. It is important to note that the 'field' in this measurement is not the actual local field around the ZnO nanostructures (rod/fiber-like structure which obtained in this experiment), which is not directly measurable but the average field between the anode and cathode (ZnO nanostructures sample). The applied voltage of anode – cathdode separation is denoted by E=V/d, where V is the applied potential and d is the separation between anode and cathode (120 μm). The current density is J= I/A, where I is the measured emission current and A is the total area of the emitter surface.

The field emission properties of ZnO nanostructures samples were analyzed based on the Fowler-Nordheim (FN) equation (Fowler & Nordheim, 1928) as stated earlier in equation 2.6, 2.7 and 2.8 in Section 2.51 (a)) rewritten as;

$$J = \frac{\mathrm{AE}^2}{\emptyset}\exp\left(-\frac{B\emptyset^{\frac{3}{2}}}{E}\right) \tag{2.5}$$

where J is the current density, E is the applied electric field, A and B are constants with value of 1.56 x 10^{-6} AeV V^{-2} and 6.83 x 10^{9} eV$^{-3/2}$ Vm^{-1}, and ϕ= 5.3 eV is the work function of ZnO, respectively.

The FN model has been used on rough field electron emitter surfaces giving a modified field electron emission equation:

$$J = A\,\frac{(\beta E)^2}{\emptyset}\exp\left(-\frac{B\emptyset^{\frac{3}{2}}}{\beta E}\right) \qquad (2.6)$$

The local electric field at the field emitter tip, F, is defined as;

$$F = \beta E \qquad (2.7)$$

where β is the field enhancement factor.

The FN plot, which is the linearized form of Equation (2.6), is;

$$\ln\left(\frac{J}{E^2}\right) = \ln\left(\frac{A\beta^2}{\emptyset}\right) - \frac{B\emptyset^{\frac{3}{2}}}{\beta}\frac{1}{E} \qquad (2.8)$$

4.3 Results and discussion

4.3.1 FEE measurement of zinc oxide nanorods prepared at various deposition time

The FEE measurement was carried out for ZnO nanorods sample prepared at various deposition times of 0.5 hour, 2, 3 and 4 hours (refer to Chapter 3, Section 3.22). From the measurement, the I-V characteristics exhibited an exponential-like behavior (Figure 4.3) which was found to be reproducible for all investigated samples. Figure 4.3 shows the relationship between field emission current density and electric field (J-E) of ZnO nanorods prepared at deposition time of (a) 0.5 hour, (b) 2, (c) 3, and (d) 4 hours.

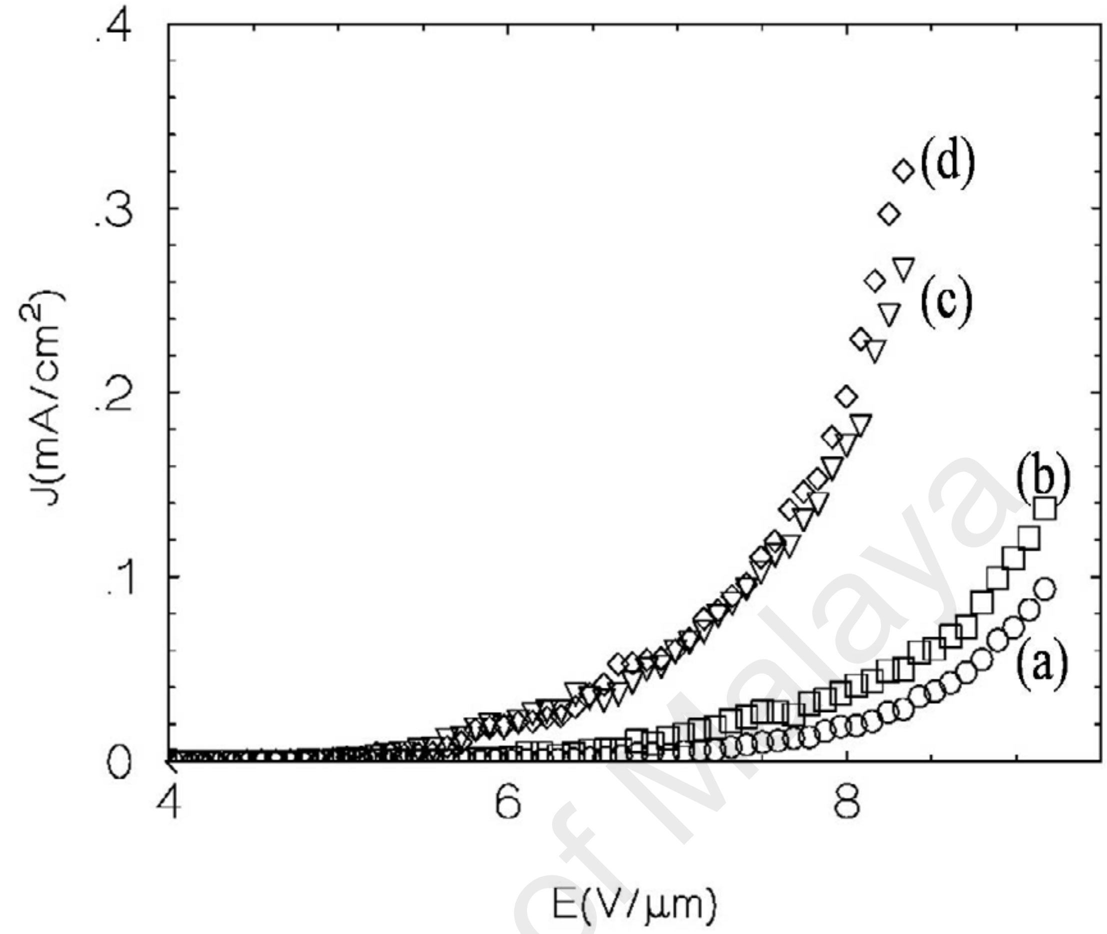

Figure 4.3: FEE measurement of the current density versus electric field (J-E) of ZnO nanorods synthesized by sol-gel method at different deposition times of (a) 0.5 hour, (b) 2 hours, (c) 3 hours and (d) 4 hours.

The turn-on field values for ZnO nanorods prepared at different deposition time of 0.5 hour, 2, 3 and 4 hours were 6.92V/µm, 6.21 V/µm, 5.45 V/µm and 5.21 V/µm, respectively.The turn-on field values decreased for ZnO nanorods prepared at longer deposition time. The threshold values also decreased with value of 10.45 V/µm, 10.12 V/µm, 9.39 V/µm and 9.12 V/µm for ZnO nanorods prepared at deposition times of 0.5 hour, 2 hours, 3 hours and 4 hour, respectively. ZnO nanorods prepared at 4 hours deposition time showed the highest field emission performance with a lower turn-on field and threshold field value.

As discussed in Chapter 3 (Section 3.2.2, page 53), the ZnO nanorods that synthesized with different deposition time initiated a different diameter and length size.

From FESEM images (Section 3.2.2, page 56), the estimated diameter of ZnO nanorods increased proportionally with the extension of the deposition time, which about 27 nm to 80 nm for the deposition time of 0.5 hour to 4 hours, respectively. The increase in diameter and length of the rods are believed to affect the FEE properties, making the ZnO nanorods become an effective field emitter in terms of reducing the turn-on and threshold fields (Ong et al., 2010)(Gayen et al., 2009). The maximum current density measured at 10 V/µm of 1.0, 1.2, 2.8 and 3.4 mA/cm^2 were obtained for ZnO nanorods samples prepared at 0.5, 2, 3 and 4 hours, respectively (as shown in Figure 4.3). Previous study by Ong reported that, ZnO nanowires that prepared within duration of 3 hours exhibited lowest turn-on field of 3.8 V/µm compared to those ZnO nanowires which were prepared within 30 minutes (8.5 V/µm) and 2 hours (5.7 V/µm) (Ong et al., 2010). Gayen also showed that the ZnO nanorods preparedin 30, 60 and 90 minutes also modulate the FEE properties (Gayen et al., 2009). Their results showed that, the turn-on field and threshold field value decreased as ZnO nanorods prepared at longer time. The turn-on field decreased and the field enhancement factor, β values increased as deposition time rises. They suggested that, the low turn-on field and increased of β value could be attributed to the different size of nanowires/ nanorod that have been prepared with longer preparation time.

To further analyze the field emission properties of the ZnO nanorods, the FN model was employed to describe the exponential dependence between the emission current and the applied field. Figure 4.4 shows the FN plot displayed with ln (J/E^2) versus 1/E graphs.

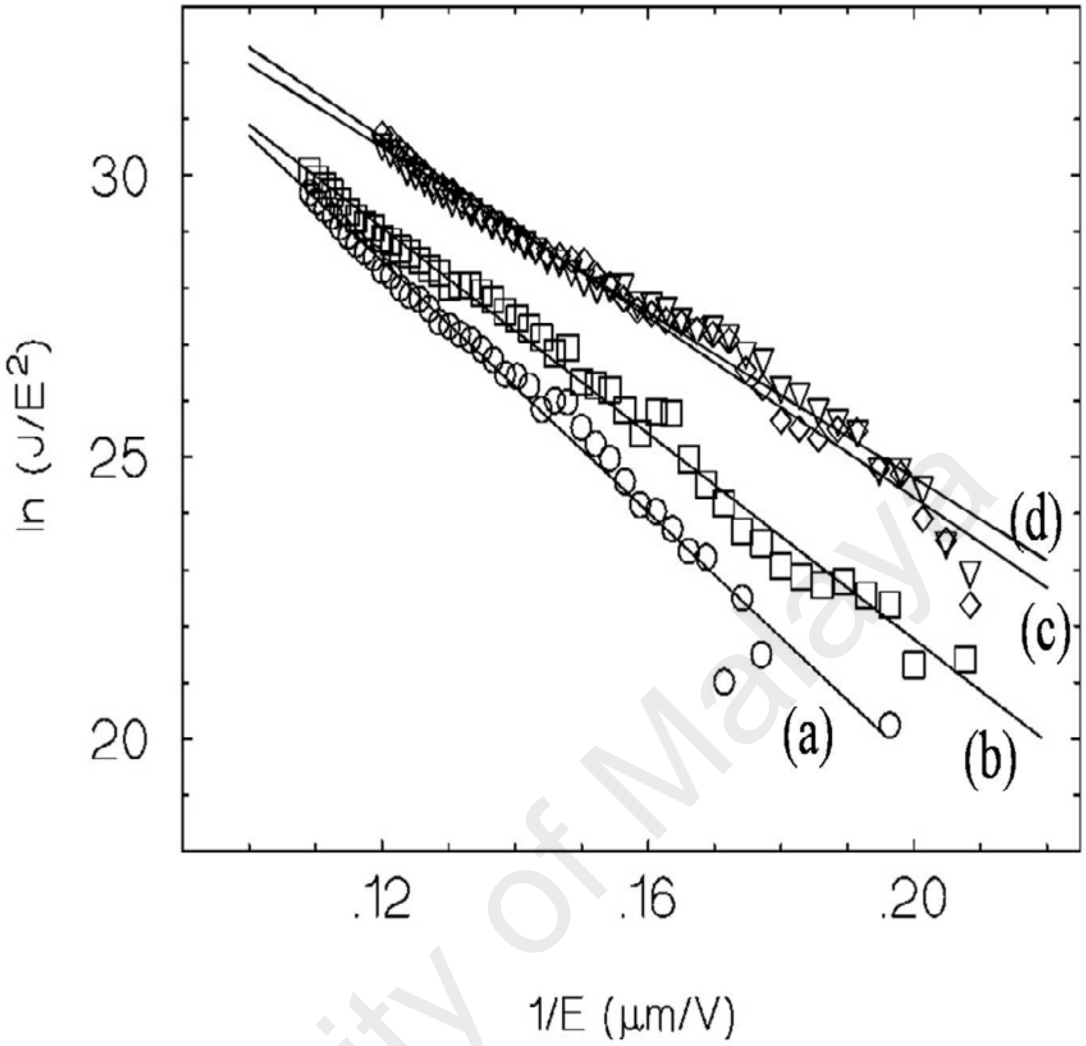

Figure 4.4: Corresponding FN plots of ZnO nanorods synthesized at different deposition time of (a) 0.5 hour, (b) 2 hours, (c) 3 hours and (d) 4 hours.

The FN plot showed good linearity over the region from the onset of the turn on field. The values of the field enhancement factor, β were calculated from the slope of the FN slope. The field enhancement factor, β was calculated to be about 3845, 4675, 5342, and 5823 for ZnO nanorod prepared at different deposition times of 0.5 hour, 2, 3 and 4 hours, respectively. The results have demonstrated that ZnO nanorods at longer deposition time with increased of diameter and length showed better FE performance. The key performance parameter for FEE measurement of ZnO nanorods at different deposition times are summarize in Table 4.1 together with previous literature.

Table 4.1: A comparison of field emission parameters of ZnO nanorods at different deposition times from present work and other literatures.

Deposition condition (mins / hours)	**Maximum current density measured at 10 V/µm (mA/cm^2)**	**Turn-on field (V/µm)**	**Threshold field (V/µm)**	**Field enhancement factor (β)**	**References**
ZnO nanorods at 0.5 hour deposition time	1.0	6.92(for 1 µA/cm^2)	9.45(for 100 µA/cm^2)	3845	Present work
ZnO nanorods at 2 hours deposition time	1.2	6.21 (for 1 µA/cm^2)	9.39 (for 100 µA/cm^2)	4675	
ZnO nanorods at 3 hours deposition time	2.8	5.45 (for 1 µA/cm^2)	8.99 (for 100 µA/cm^2)	5342	
ZnO nanorods at 4 hours deposition time	3.4	5.21 (for 1 µA/cm^2)	8.79 (for 100 µA/cm^2)	5823	
ZnO nanowires at 0.5 hours	n/a	8.5 (for 0.1 µA/cm^2)	n/a	863	(Ong et al., 2010)
ZnO nanowires at 2 hours		5.7 (for 0.1 µA/cm^2)		998	
ZnO nanowires at 3 hours		3.8 (for 0.1 µA/cm^2)		1644	
ZnO film at 30 mins		9.6 (for 10 mA/cm^2)	9.3 (for 1 mA/cm^2)	2186	(Gayen et al., 2009)
ZnO film at 60 mins		8.6 (for 10 mA/cm^2)	7.6 (for 1 mA/cm^2)	2306	
ZnO film at 90 mins		7.0 (for 10 mA/cm^2)	5.8 (for 1 mA/cm^2)	2963	

4.3.2 FEE measurement of pure ZnO and Al-doped zinc oxide nanorods

Pure and Al-doped ZnO nanorods at various doping level (atomic % of Al/Zn) synthesized using sol-gel method (refer to Chapter 3, Section 3.2.4). Details on structural and optical properties have been discussed earlier in Chapter 3 (Section 3.2.4, page 68). As presented previously, from EDX analysis (Section 3.2.4, page 72), the atomic percent amount of Al element in the sample increased as the Al dopant concentrationincreases at about 0.13, 0.16 and 0.19 % for 1, 3 and 5 mol % Al used during synthesis, respectively. FESEM results (Section 3.2.4, page 69) revealed that, the samples formed in nanorods structure with different density.

The J-E curves for pure ZnO and Al-doped ZnO nanorods at various doping level are shown in Figure 4.5. Figure 4.5 shows the J-E curve for (a) pure ZnO nanorods, Al-doped ZnO nanorods at doping level of (b) 0.13, (c) 0.16and (d) 0.19 %.

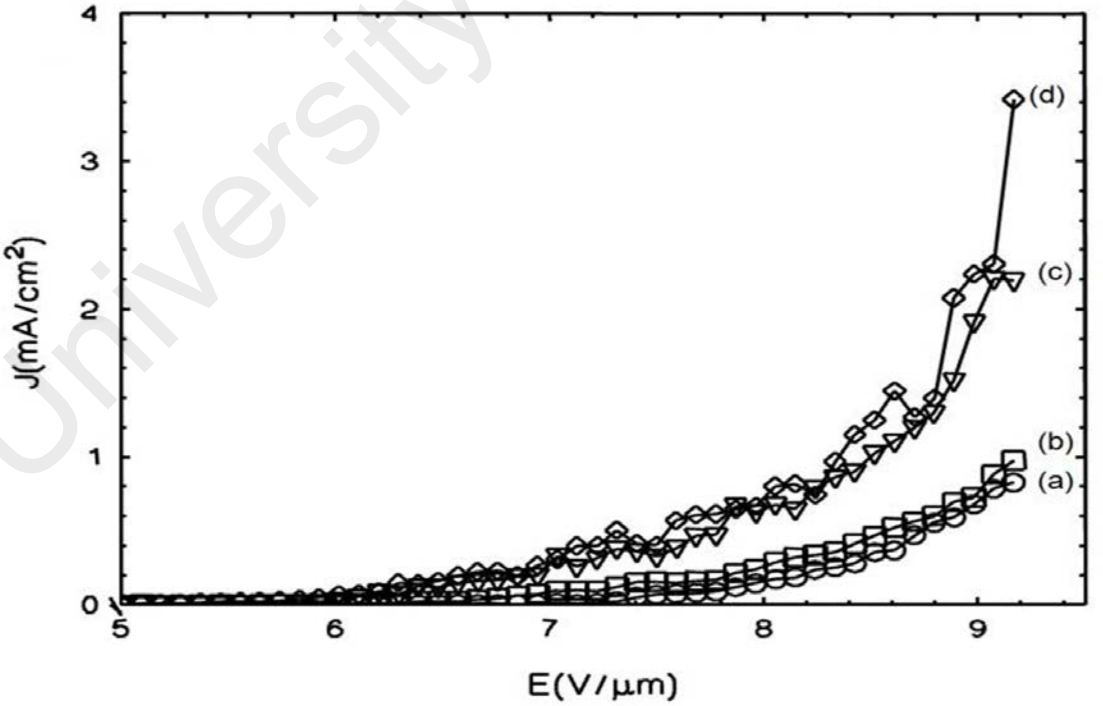

Figure 4.5: FEE measurement of the current density versus electric field (J-E) of (a) pure ZnO nanorods and ZnO nanorods at various doping level of Al to Zn in atomic % of (b) 0.13, (c) 0.16 and (d) 0.19.

From Figure 4.5, the turn-on fields were 7.2 V/μm, 6.6 V/μm, 6.0 V/μm and 5.8 V/μm at a current density of 1 μA/cm^2 for pure ZnO nanorods, Al-doped ZnO nanorods at doping level of 0.13, 0.16 and 0.19 %, respectively. The threshold fields were8.79 V/μm, 8.63 V/μm, 8.54 V/μm, and 8.49 V/μm at current density of 100 μA/cm^{2}for pure, Al-doped ZnO nanorods at doping level of 0.13, 0.16 and 0.19 %, respectively. The turn-on field and threshold field values decreased as the doping level increased.From J-E curve, the current density measured at 10 V/μm increased as the doping concentration increased. A current density of 1.0 mA/cm^2 was obtained for pure ZnO nanorods, 1.2, 2.8 and 3.4 mA/cm^2 for 0.13, 0.16 and 0.19at. % Al/Zn nanorods, respectively (as shown in Figure 4.5). The trend of increasing current density might be due to the increase of electrical conductivity with increasing doping level.Amount of doping significantly affected the the values of the turn-on field and threshold field (Fang et al., 2008).

The FN plot derived from the observed J - E characteristic is depicted in Figure 4.6. The entire FN plot can be sectioned into two regions as in the figure. This behavior of the FN plot was observed to be reproducible for all ZnO nanorods samples. This FN behavior then exhibited two different slopes at low and high electric field. The slope in high electric field (indicated by arrow in high field region on Figure 4.6) was found to be less than the low field region (indicated by arrow in low field region). The existence of dual slope may originated from the interaction between neighbouring ZnO tips, uneven surface from the sample, space-charge effect or the presence of defect which change the local density of states (Collins & Zettl, 1997)(Nor, 2011).

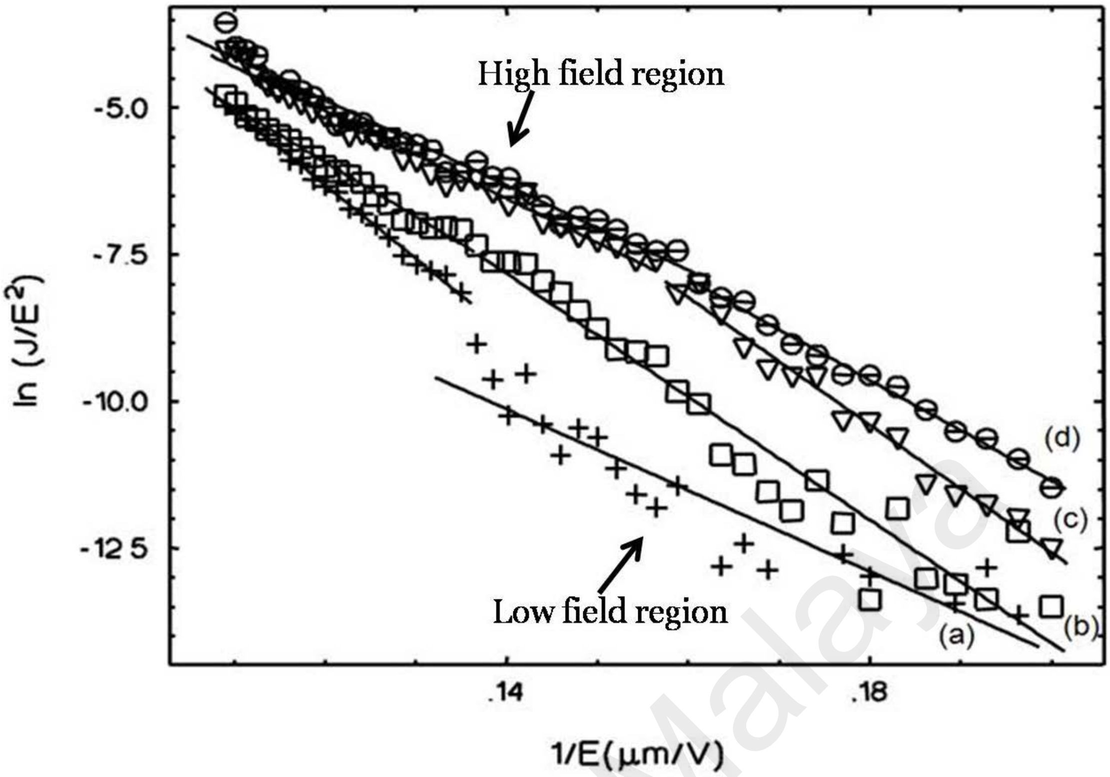

Figure 4.6: Corresponding FN plots of (a) pure ZnO nanorod and and ZnO nanorods at various doping level of Al to Zn in atomic % of (b) 0.13 %, (c) 0.16 % and (d) 0.19 %.

The slopes obtained from the F-N plots were used to estimate the field enhancement factor, β values. The field enhancement factor in the high field region is denoted as β_H and that in the low field regime as β_L. The obtained field enhancement factor β_H and β_L for pure ZnO and Al-doped ZnO nanorods were to be in the range 341.50 - 592.88 and 618.66 - 496.37. It was observed that, 0.19at. % Al/Zn nanorods gave the highest β_H value, while pure ZnO nanorods show the highest field enhancement β_L value. Generally, the low turn-on and threshold field and increase in maximum emission current density was influenced by amount of doping. The ZnO nanorods at doping level 0.19 % of Al to Zn shows better FEE characteristic compared to pure ZnO and ZnO nanorods at doping level 0.13 % and 0.16 % of Al to Zn. However, the β values showed no clear correlation with Al doping level. This is understandable since the field enhancement factor β value was influenced by the performance and ability of the emitter which enhance the local electric field at the tip compared to the average macroscopic value. The field emission properties should be greater when the structure obtained is in 1 dimension within nanorange and have high aspect ratio (Jamali et al., 2010)(Zhang et al., 2009)(Hu et al., 2006). The FEE properties of pure ZnO nanorods and Al-doped ZnO nanorods at different doping level are compared with previous literature is depicted in Table 4.2. It is clearly seen from the table, the present result has lower value of the turn-on field, threshold field and field enhancement factor, as compared to others reported in the literature. The differences in field emission properties are due to the difference in the experimental condition, such as the anode-cathode separation, level of doping and pressure (Xiao et al., 2008).

Table 4.2: A comparison of field emission parameters of Al-doped ZnO nanorods and other literatures**.**

Sample	Maximum current density (mA/cm^2)	Turn-on field (V/ µm)	Threshold field (V/µm)	Field enhancement factor (β)	References
Pure ZnO nanorods	1.0 (10 V/ µm)	7.2 (1 µA/cm^2)	8.79 (100 µA/cm^2)	$\beta_H = 341.50$, $\beta_L = 618.66$	Present work
0.13 % Al/ Zn nanorods	1.2 (10 V/ µm)	6.6 (1 µA/cm^2)	8.63 (100 µA/cm^2)	$\beta_H = 463.99$, $\beta_L = 406.55$	
0.16 % Al/ Zn nanorods	2.8 (10 V/ µm)	6.0 (1 µA/cm^2)	8.54 (100 µA/cm^2)	$\beta_H = 569.17$, $\beta_L = 391.63$	
0.19 % Al/ Zn nanorods	3.4 (10 V/ µm)	5.8 (1 µA/cm^2)	8.49 (100 µA/cm^2)	$\beta_H = 592.88$, $\beta_L = 496.37$	
1 % Al-doped ZnO nanostructure	n/a	n/a	2.0 (1 µA/cm^2)	9.3×10^3	(Navale et al., 2009)
3 % Al-doped ZnO nanostructure	n/a	n/a	2.3 (1 µA/cm^2)	3.9×10^3	
1 at. % Al-doped ZnO nanorods	n/a	2.1 (1 µA/cm^2)	5.6 (1 mA/cm^2)	3761	(Mamat et al., 2011)

4.3.3 FEE measurement of Pure ZnO and Mg-doped Zinc Oxide nanostructures

The pure ZnO and Mg-doped ZnO nanostructures were prepared at various doping level (atomic % of Mg/Zn) by sol-gel method by utilizing CA juice as a reducing agent. The synthesis process and all related results were discussed earlier in Chapter 3 (Section 3.4.3, page 104).Similar fiber-like nanostructures were formed for pure ZnO nanostructures and Mg- doped ZnO nanostructures with the estimated diameter size in the range 20 nm to 150 nm observed from FESEM results (Section 3.4.3, page 105). From EDX analysis, the Mg/Zn ratio was increased as the dopant concentrationincreased which were about 0.225 %, 0.29 % and 0.45 % for 3, 5 and 10 mol % Mg-doped ZnO nanostructures, respectively.

FEE properties of pure ZnO nanostructures and different level of doping Mg-doped ZnO nanostructures in the form of emission current density versus the applied electric field (J-E) plots are depicted in Figure 4.7.

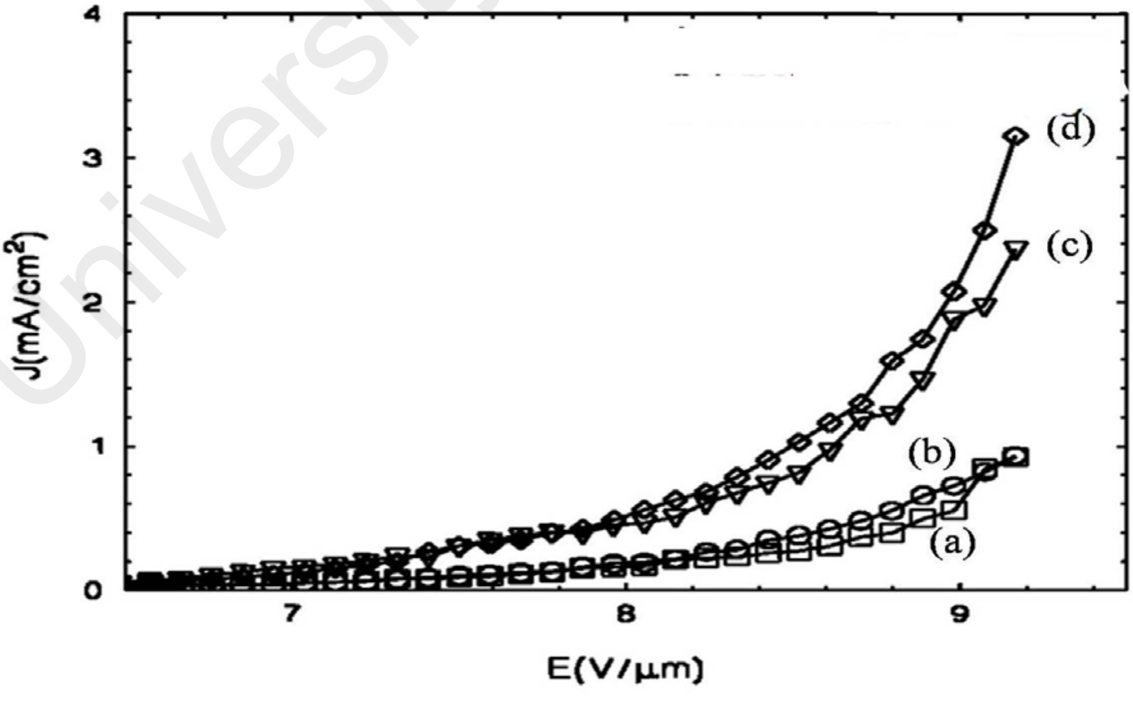

Figure 4.7: J–E field emission plot from (a) pure ZnO nanostructures, (b) 0.225 at. % Mg/Zn nanostructures, (c) 0.29 at.% Mg/Zn nanostructures, and (d) 0.45 at. % Mg/Zn nanostructures.

As stated earlier, the turn-on field and the threshold field, defined as electric fields required producing 1 μA/cm^2 and 100 μA/cm^2. The turn-on field value for pure ZnO nanostructures is 6.99 V/µm. The turn-on field values of 6.35, 6.07 and 5.99 V/µm were obtained for 0.225, 0.29 and 0.45 at. % Mg/Zn nanostructures, respectively. The turn-on field values showed a clear trend of decreasing as the level of doping of Mg/Zn increased. The threshold fields seemed to be almost equal for pure and 0.225 at. % Mg/Zn nanostructures samples at 9.16 and 9.17 V/µm before receding to 8.62 and 8.49 V/µm, for Mg-doped ZnO nanostructures at doping level of 0.29 % and 0.45 %, respectively. Apart from threshold field values for pure ZnO nanostructures and 0.225 at. % Mg/Zn nanostructures, our results showed a general trend of decreasing turn on and threshold field values with increasing Mg doping levels.

The current density was measured at 10 V/µm from J-E curve (as shown in Figure 4.7) for all samples. The current density of 0.8, 0.9, 2.4 and 3.2 mA/cm^2 were obtained for pure ZnO nanostructures, ZnO nanostrutcures at doping level of Mg to Zn of 0.225%, 0.29 % and 0.45 %, respectively. Based on the present understanding, factors that may affect the turn-on and threshold field values are emission cathode geometry and electrical conductivity. Based on FESEM imaging (Section 3.4.3, page 105), the structures and geometry of our samples were almost identical. As such, the main reason for the trend observed in the increased in the electrical conductivity of the ZnO nanostructures with increasing doping levels. Such increase in conductivity is evident in the values of the current density measured at 10 V/μm.

The F-N plots obtained for all samples are shown in Figure 4.8. For all samples, the F-N plots were well fitted to straight lines.

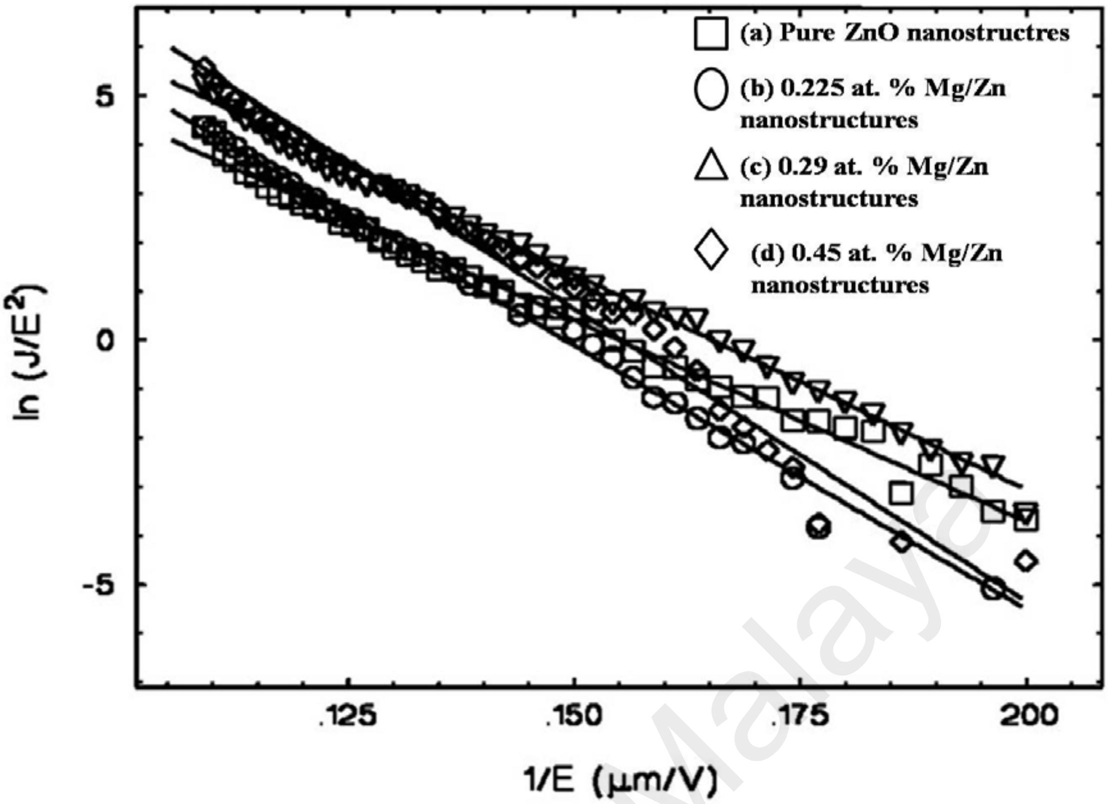

Figure 4.8: Corresponding F-N plot from (a) pure ZnO nanostructures, (b) 0.225 at. % Mg/Zn nanostructures, (c) 0.29 at.% Mg/Zn nanostructures, and (d) 0.45 at. % Mg/Zn nanostructures.

The field enhancement factors, β, obtained from the fitted straight line are 801, 965, 955 and 786 for pure ZnO nanostructures, 0.225 at. % Mg/Zn nanostructures, 0.29 at.% Mg/Zn nanostructures and 0.45 at.% Mg/Zn nanostructures, respectively. The β values showed no clear correlation with Mg doping level. This is understandable since β values are predominantly influenced by emitter geometry, for example, emitters with high aspect ratio and sharp tips tend to produce the highest enhancement (Lee et al., 2009)(Wang et al., 2005).

The emission current stability of pure and Mg-doped ZnO nanostructures has been tested for 120 minutes at a bias voltage of 1000 V and the plots for the variation of emission current with time are shown in Figure 4.9. The results show that the emission current stability for pure ZnO, 0.225 at. % Mg/Zn nanostructures and 0.45 at. % Mg/Zn nanostructures were generally good even though for 0.29 at. % Mg/Zn nanostructures, some slight fluctuations were observed. These results indicated that pure and Mg-doped ZnO nanostructures prepared by low temperature sol-gel method using CA juiceexhibit good emission current stability and is a good candidate for field emission device applications.

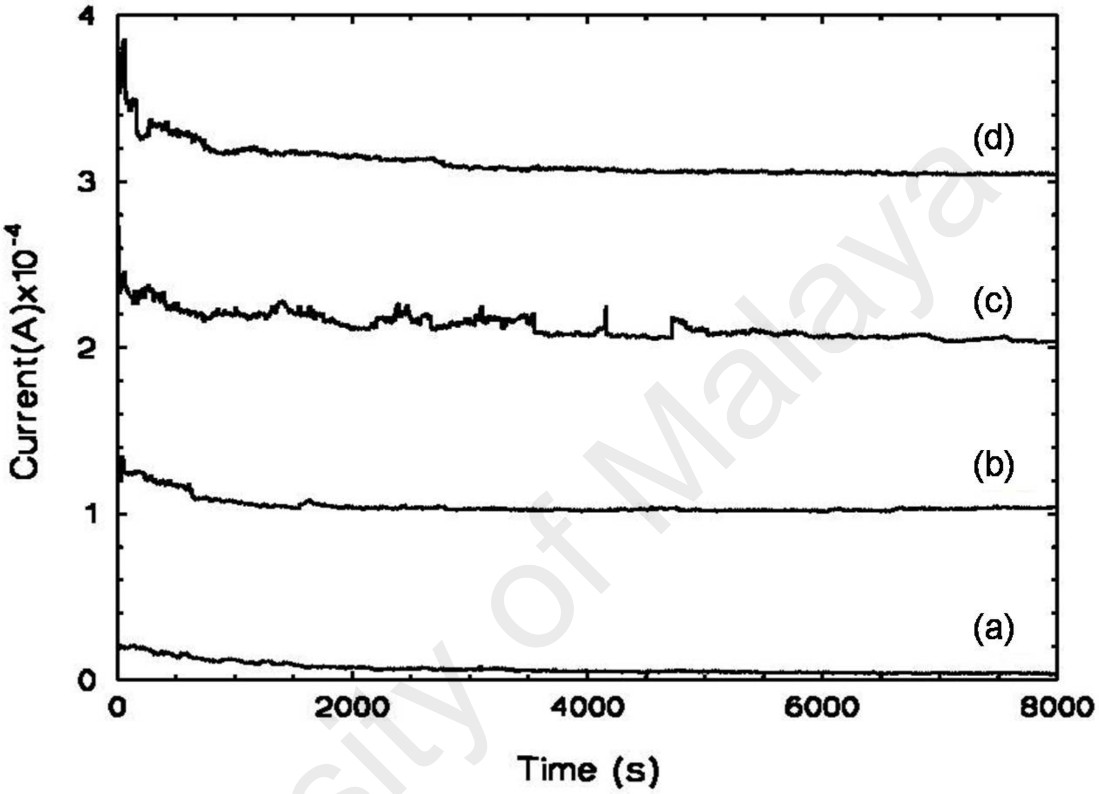

Figure 4.9: Stability of the emission current over time of (a) pure ZnO nanostructures, (b) 0.225 at. % Mg/Zn nanostructures, (c) 0.29 at.% Mg/Zn nanostructures, and (d) 0.45 at. % Mg/Zn nanostructures.

Results from this work are tabulated in Table 4.3, together with previously reported results for comparison. From the table, it can be seen that field emission properties obtained in present work is lower compared to previous literature. Although the turn-on, threshold electric field and field enhancement factors of ZnO nanostructures synthesized in this work is not as good as reported by Pan(Pan, et al., 2006)and Yousefi(Yousefi et al., 2010), the preparation of ZnO nanostructures in this work did not need any high temperature process compared to them which use thermal evaporation method. In addition, the differences in field emission properties are due to the difference in the experimental condition, such as the anode-cathode separation, level of doping and pressure of the measurement setup (Xiao et al., 2008).

Table 4.3: A comparison of field emission parameters of Mg-doped ZnO nanostructures from present work and other literatures**.**

ZnO Nanostructure	**Maximum current density (mA/cm^2)**	**Turn-on field value for (V/µm)**	**Threshold field value (V/µm)**	**Field Enhancement Factor, β**	**Reference**
Pure ZnO nanostructures	0.8 (10 V/ µm)	6.99 (1 µA/cm^2)	9.16 (100 µA/cm^2)	801	(this work)
0.225 at. % Mg/Zn nanostructures	0.9 (10 V/ µm)	6.35(1 µA/cm^2)	9.17(100 µA/cm^2)	965	
0.29 at. % Mg/Zn nanostructures	2.4 (10 V/ µm)	6.07(1 µA/cm^2)	8.62(100 µA/cm^2)	955	
0.45 at. % Mg/Zn nanostructures	3.2 (10 V/ µm)	5.99(1 µA/cm^2)	8.49(100 µA/cm^2)	786	
Mg-doped ZnO tetrapods (100-300 nm)	0.76 (6.0 V µm^{-1})	2.6	n/a	2327	(Pan, et al., 2006)
Mg-doped ZnO tetrapods (80 nm)	0.58 (6.0 V µm^{-1})	2.8		1690	
ZnMgO/Au (10nm) nanowires	n/a	0.78 (10 mA/cm^2)	1.22 (100 mA/cm^2)	2310	(Yousefi et al., 2010)
ZnMgO/Au (30nm) nanowires		1.62 (10 mA/cm^2)	2.32 (100 mA/cm^2)	1140	

4.4 Conclusion

ZnO nanostructures were synthesized using sol-gel method and have been tested for field electron emission application. The differences in deposition time influenced the diameter size of the rods. ZnO nanorods have been observed for sample synthesized at 2, 3 and 4 hours, while at 0.5 hour only nanoparticles was formed. For field electron emission measurement, the properties were slightly changed for ZnO nanorods prepared at different deposition time. The turn-on field and threshold field value decreased as the deposition time increased. The turn-on field for the ZnO nanorods synthesized at 0.5 hour to 4 hours deposition time were in the range of 6.92 – 5.21 V/μm, while threshold value were in the range of 9.45 – 8.79 V/μm, respectively. The field enhancement factor β also changed with value of of 3845- 5823 for the ZnO nanorods synthesized at 0.5 hour to 4 hours deposition time.

Another measurement on field electron emission was tested on pure ZnO nanorods and various doping level of Al-doped ZnO nanorods (0.13, 0.16 and 0.19 at. % Al/Zn). Different amount of doping level and geometry of ZnO and Al-doped ZnO nanorods gave effect to the FEE properties. 0.16at.% Al/Zn nanorods and 0.19at. % Al/Zn nanorodswhich grew perpendicular to substrate and have a sharp tip showed a lower turn-on and threshold field value compared to pure ZnO nanorods. The turn-on field value is 7.2, 6.6, 6.0 and 5.8 V/μm for pure ZnO nanorods, 0.13, 0.16 and 0.19at. % Al/Zn nanorods, respectively. The variation in the turn-on and threshold field can be attributed to the amount of doping level and morphological features of the ZnO nanorods. For this experiment, there are two region of low and high electric field that resulting two field enhancement factor β_H and β_L for each samples. The highest calculated $\beta_{H\,=}$ 592.88was obtained from0.16 at. % Al/Zn nanorods, while $\beta_{L\,=}$ 618.66

was calculated from pure ZnO nanorods. Generally, the β values showed no clear correlation with Al doping level.

Pure ZnO and Mg-doped ZnO nanostructures have been synthesized using CA juice as a reducing agent by a biomolecules assisted sol-gel method and the field electron emission measurement was conducted. Field electron emission measurements yielded a general trend of decreasing turn-on and threshold field values with increasing Mg doping level. Threshold electric field values of 6.99, 6.35, 6.07 and 5.99 V/μm were measured for pure ZnO, 0.225 at. % Mg/Zn nanostructures, 0.29 at.% Mg/Zn nanostructures and 0.45 at.% Mg/Zn nanostructures, respectively. The turn on field values was decreased as the doping level of Mg increased with value of 916, 917, 8.62 and 8.49 V/μm. The field enhancement factor, which significantly depended on the emitter geometry, showed no clear trend. Almost equal field enhancement factor values of 801, 965, 955 and 786 for pure ZnO, 0.225 at. % Mg/Zn nanostructures, 0.29 at.% Mg/Zn nanostructures and 0.45 at.% Mg/Zn nanostructures was obtained which might be attributed to similar geometrical structure of the samples. In general, this study has demonstrated that the use of CA juiceas a green reagent is viable for the synthesis ZnO nanostructures with good field electron emission features.

CHAPTER 5: SILVER NANOPARTICLES DECORATED MICROSTRUCTURED AND NANOSTRUCTURED ZNO AS PHOTOCATALYSTS FOR PHOTODEGRADATION OF DYE

5.1 Introduction

Industrial wastewater contains various organic and inorganic pollutants, which are generally toxic and resistant. The effluents containing dyes is highly toxic, contains chemicals with high concentration of heavy metals create severe environmental pollutions. The dye effluent contaminates the surface and ground water and can harm ecological resources including water quality, soils, plants, animal and also human health. Textile industry is one of an example that produces a large quantity of highly coloured effluents. Figure 5.1 shows the photograph of dye pollution produced from textile industries.

Figure 5.1: Images show the dye pollution produced by textile industries**.**

Much attention has been devoted to develop effective technologies for the removal of organic pollutants from aqueous media. Recently, technologies including biodegradation, adsorption, and oxidation processes have been developed (Chan et al., 2011). However, each of these water removal processes has a limitation for a large scale implementation. For that reason, photocatalysis is a promising technique for waste water treatment due to its applicability and simplicity (Panthi et al., 2015).

Photocatalysis is a catalytic reaction involving light absorption by a catalyst or a substrate (Parmon, Emeline, & Serpone, 2002). A photocatalyst is defined as a substance which is activated by adsorbing a photon and is capable of accelerating a reaction without being consumed. To meet the need for practical application, photocatalyst should have the high photocatalytic activity, non-toxic, cost effective and high yield. Oxide-based materials such as TiO_2, CeO_2 and ZnO have attracted much interest due to their important photocatalytic activity. Their bandgap are in the range of uv-visible light and the electron required for initiating the photo-oxidation reaction can be easily excited.

Recently, zinc oxide has received much attention because of its unique properties and potential application in various areas. The band gap of ZnO (3.25 eV) and TiO_2 (3.05 -3.2 eV) are almost similar,so it is expected that ZnO to have the same photocatalytic ability as TiO_2(Tian et al., 2012). As a photocatalyst, ZnO exhibit large initial rates of activity due to the presence of active sites with higher surface reactivity (Chang et al., 2013). For ZnO, photogenerated electrons and holes recombine easily. Figure 5.2 illustrate the photocatalytic mechanism of ZnO.

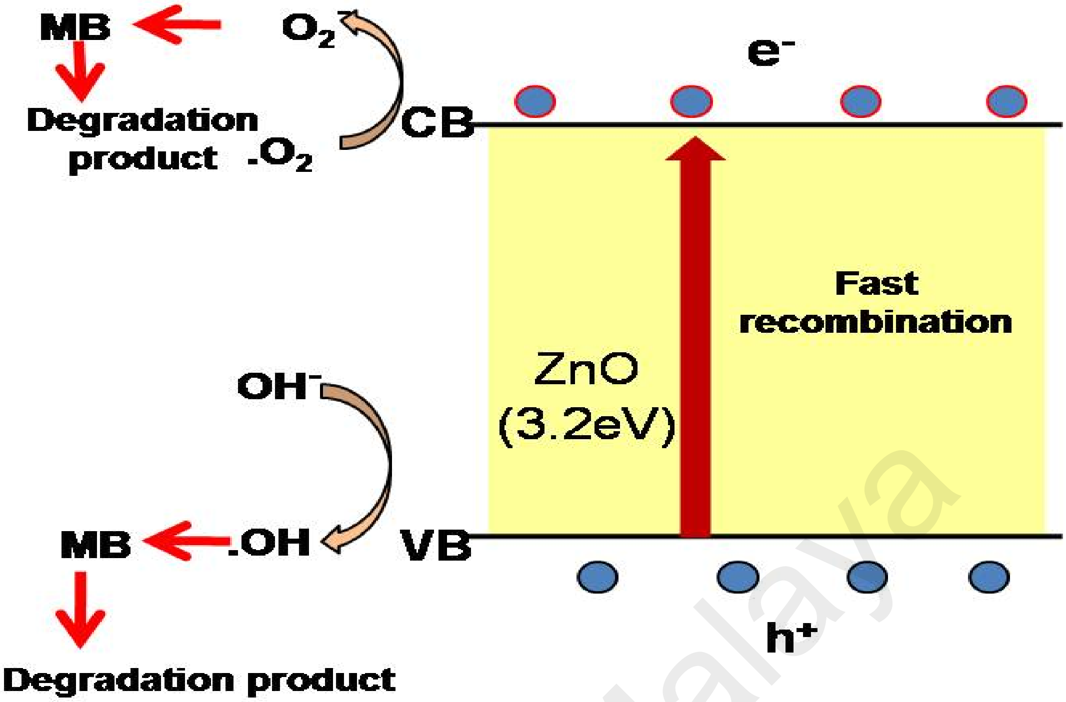

Figure 5.2: Schematic illustration of the fast recombination mechanism related to photocatalytic activities of ZnO.

The mechanism of photodegradation of methelyne blue (MB) dye using ZnO as photocatalyst under uv light illumination can be explained on the basis of photo-excitation (Panthi et al., 2015)(Inamur et al., 2013). When ZnO particles were illuminated by uv light with energy per photon greater than the band gap, electrons in the valence band are excited to the conduction band creating the electron–hole pairs. Holes could will react with OH^-adhering to the surfaces of ZnO particles to form highly reactive hydroxyl radicals (•OH). Meanwhile, oxygen acted as an electron acceptor by forming a superoxide radical anion ($\bullet O_2^-$). MB will be degraded through direct oxidation by the •OH and $\bullet O_2^-$ radical.

The most efficient way to accelerate the charge carrier separation and improve the catalytic activity is by modifying the surface structure of ZnO by decoration with transition metal such as Ag (Wang et al., 2012), iron (Kumar et al., 2014), magnesium (Lu et al., 2011). It is widely accepted that Ag nanoparticles on ZnO surface act as electron trapping agents thus improve the separation efficiency of photogenerated electron-hole which enhanced the photocatalytic activity (Xie et al., 2010)(Yin et al., 2012). Nevertheless, one of major drawback of ZnO photocatalyst is the low quantum efficiency of ZnO due to the fast recombination of photogenerated electron-hole pairs which significantly decreased the photocatalytic activity of ZnO (Xie et al., 2010)(Faisal et al., 2013). To overcome this limitation, decoration of ZnO with noble metals such as Ag is one of the efficient ways. Decoration of ZnO and Ag is now an exciting area in research for developing photocatalytic application, however the photocatalytic mechanism is complicated and still controversy. Figure 5.3 shows the possible mechanism of Ag decorated ZnO that have been reported by a few researchers (Lu et al., 2008)(Guo et al., 2013)(Ren et al., 2010).

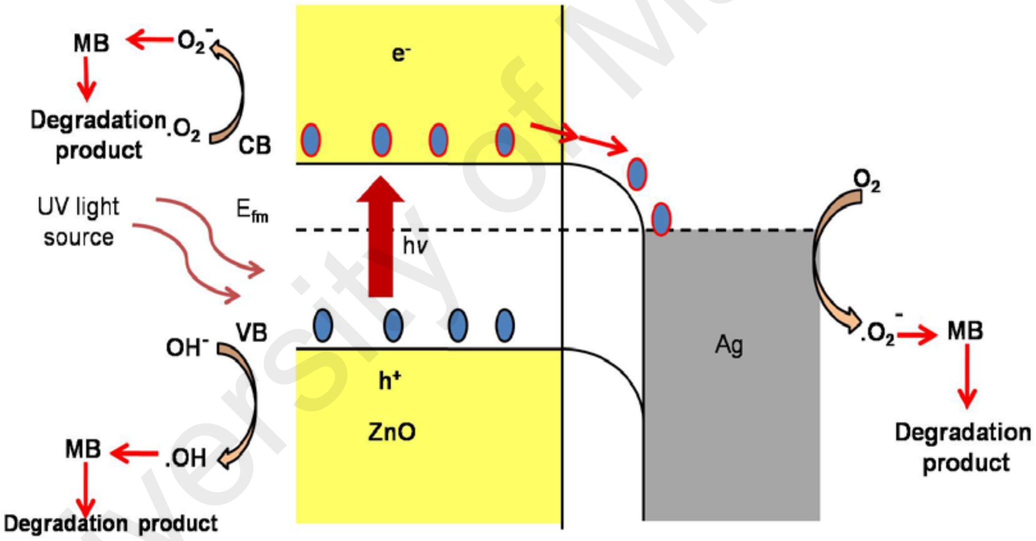

Figure 5.3: Proposed schematic mechanism of photodegradation activities of AgNPs decorated microstructured ZnO.

When Ag decorated ZnO was irradiated by uv light, some e^- of ZnO in the VB will be excited to the CB with the same amount of holes h^+ coming out in the VB. The bottom energy level of CB of ZnO is higher than the equilibrium Fermi energy level (E_{fm}) of Ag/ZnO heterostructure, so photoexcited electrons will transfer from ZnO particles to Ag particles driven by the potential energy (Lu et al., 2008)(Guo et al., 2013). It has been proposed that a Schottky barrier formed at the interface between metal and semiconductor, while the holes can remain on the semiconductor surfaces. Therefore, Ag particles or clusters on the surface of ZnO particles work as an electron sink, and they prevent the recombination of photoinduced electrons and holes which prolongs the lifetime of photogenerated pairs. And then the adsorbed O_2 as electronic acceptors can easily trap photoelectrons and produce a superoxide anion radical ($^{\bullet}O_2^{-}$), while superoxide anion radical and photoinduced holes can also readily react with H^+ or OH^- to generate hydroxyl radical species ($^{\bullet}OH$), and both radical groups ($^{\bullet}O_2^{-}$ − and $^{\bullet}OH$) are highly reactive toward MB degradation and from this it can be suggested that, various contents of surface hydroxyl on the ZnO surface which caused by different Ag content did influenced the photocatalytic activity (Gao et al., 2011). The photocatalytic reaction process can be proposed as follows (Chai, Wang, Cheng, Zhou, & Zhang, 2014)(Dermenci et al., 2014)(Zhang et al., 2011):

$$ZnO + hv\ (uv) \rightarrow ZnO\ (e_{cb}^{-} + h_{vb}^{+}) \quad (5.1)$$

$$h_{vb}^{+} + OH^{-} \rightarrow {}^{\bullet}OH \quad (5.2)$$

$$h^{+} + H_2O \rightarrow {}^{\bullet}OH + H^{+} \quad (5.3)$$

$$Ag^{+} + e_{cb}^{-} \rightarrow Ag \quad (5.4)$$

$$e_{cb}^{-} + O_2 \rightarrow {}^{\bullet}O_2^{-} \quad (5.5)$$

$${}^{\bullet}O_2^{-} + H^{+} \rightarrow {}^{\bullet}OH_2 \quad (5.6)$$

$$2{}^{\bullet}OH_2 \rightarrow H_2O_2 + O_2 \quad (5.7)$$

$${}^{\bullet}OH + MB \rightarrow \text{Degaradation products} \quad (5.8)$$

In this work, a sol-gel method was used to synthesize the pure ZnO and silver nanoparticles decorated micro- and nanostructured ZnO at various Ag content. The obtained samples then were applied for the photodegradation measurement of MB under uv light irradiation.

5.2 Photodegradation measurement of MB using AgNPs decorated micro- and nanostructured ZnO as photocatalyst under uv irradiation.

Figure 5.4 shows the photodegradation measurement setup that consists of 100 mL MB solution with concentration of 10 mg/L and uv light source with peak intensity at 254 nm.

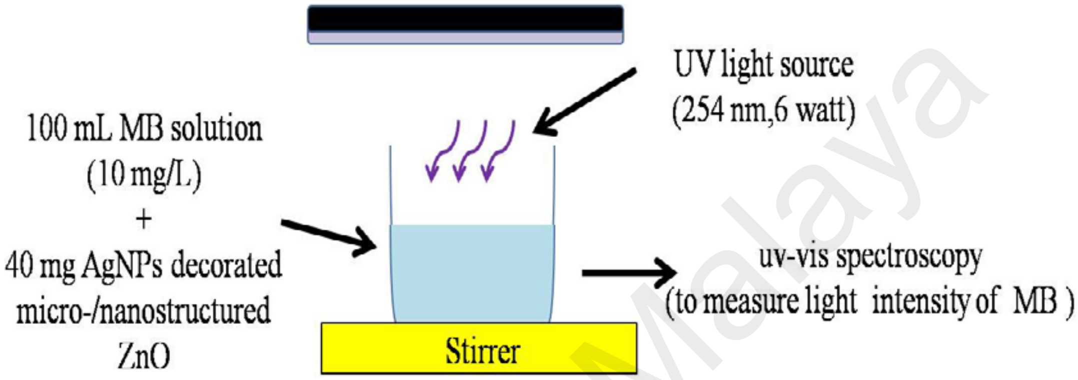

Figure 5.4: Setup for photodegradation of MB dye under UV light irradiation.

The experiments were carried out as follows: 40 mg of pure ZnO or AgNPs decorated micro- or nanostructured ZnO were added to the MB solution. Prior to irradiation, the suspensions were stirred in the dark for 30 minutes to achieve the maximum adsorption of the dye on the surface of the catalysts. Photodegradation process of MB was conducted under uv light under constant stirring. 5 ml of the MB solutions were collected at 10 minutes intervals for AgNPs decorated microstructured ZnO photocatalyst while 30 minutes interval for AgNPs decorated nanostructured ZnO photocatalyst. The MB concentration was evaluated using uv-vis spectroscopy based on the characteristic of MB absorption peak at 664 nm. The process was repeated for all samples.

5.3 Results and discussion

5.3.1 Photodegradation of MB using AgNPs decorated microstructured ZnO as photocatalyst under uv irradiation

The preparation of pure and AgNPs decorated microstructured ZnO samples for the photodegradation process was discussed earlier in Chapter 3 (Section 3.5.1, page 112). Decoration of ZnO with Ag was prepared by the sol-gel method. Based on EDX analysis, the amount of Ag incorporated was 2.33, 4.36, 11.48, 19.90, 40.40 and 61.31 at. %, respectively. From FESEM results in Chapter 3 (Section 3.5.2, page 114) confirmed that the structure of the ZnO sample consist of particles in average size less than 500 nm. Ag particles formed on the ZnO surface, indicating that Ag was not incorporated into the ZnO lattice. All samples were used as photocatalyst in the photodegradation of MB.

The absorption spectra of photodegradation of MB solutions using pure ZnO or AgNPs decorated microstructured ZnO under uv light irradiation are shown in Figure 5.5. Figure 5.5 (a) shows a typical absorption spectrum of MB aqueous solution without presence of photocatalyst at wavelength range between 500 – 750 nm under uv light irradiation for duration of 60 minutes. Degradation process did not occur without photocatalyst in the MB solution. Figure 5.5 shows the uv–vis absorbance spectra of MB aqueous solutions for (b) pure ZnO and AgNPs decorated microstructured ZnO at Ag content of (c) 2.33 at. %, (d) 4.36 at.%, (e) 11.48 at.%, (f) 19.90 at.%, (g) 40.40 at.%, and (h) 61.31 at. %, respectively. Similar pattern of spectrums were obtained for all samples. The characteristic absorption peaks at 664 nm gradually declined with time in the presence of pure ZnO and Ag decorated microstructured ZnO. The curve of absorption is nearly horizontal after hit 60 minutes.

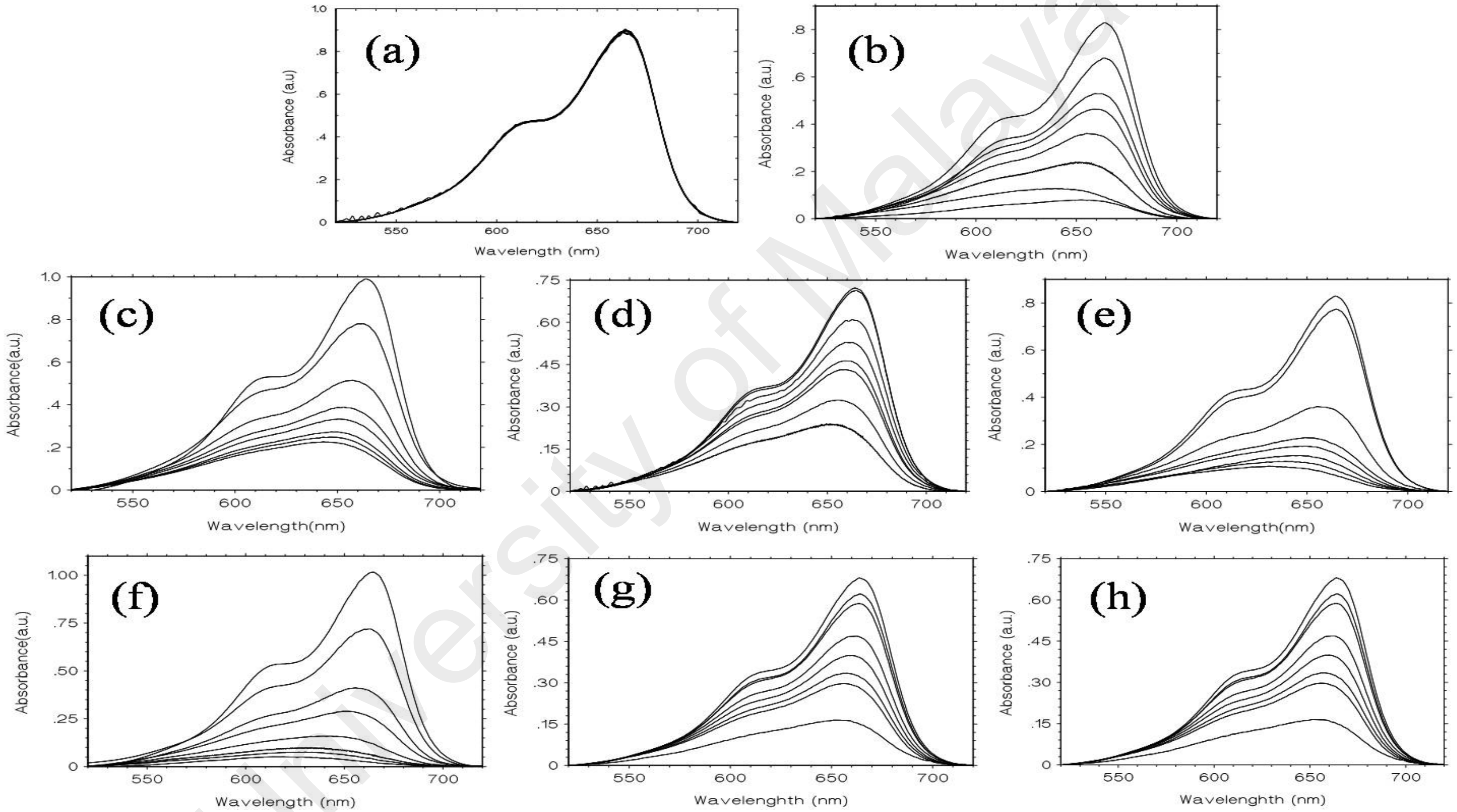

Figure 5.5: The time-dependent absorption spectra of MB solution in the presence of catalyst of (a) without catalyst, (b) pure ZnO, AgNPs decorated microstructured ZnO at Ag content of (c) 2.33 at. %, (d) 4.36 at. %, (e) 11.48 at. % (f) 19.90 at.% (g) 40.40 at.%, and (h) 61.31 at. %.

Figure 5.6 shows the photodegradation efficiency curves of the pure ZnO, 2.33, 4.36, 11.48, 19.90, 40.40, and 61.31 at. % AgNPs decorated microstructured ZnO over irradiation time. Photodegradation efficiency is defined as the number of molecules of a given photocatalytic process formed per photon of light of a given energy impinging on the photocatalytic system (Parmon et al., 2002).

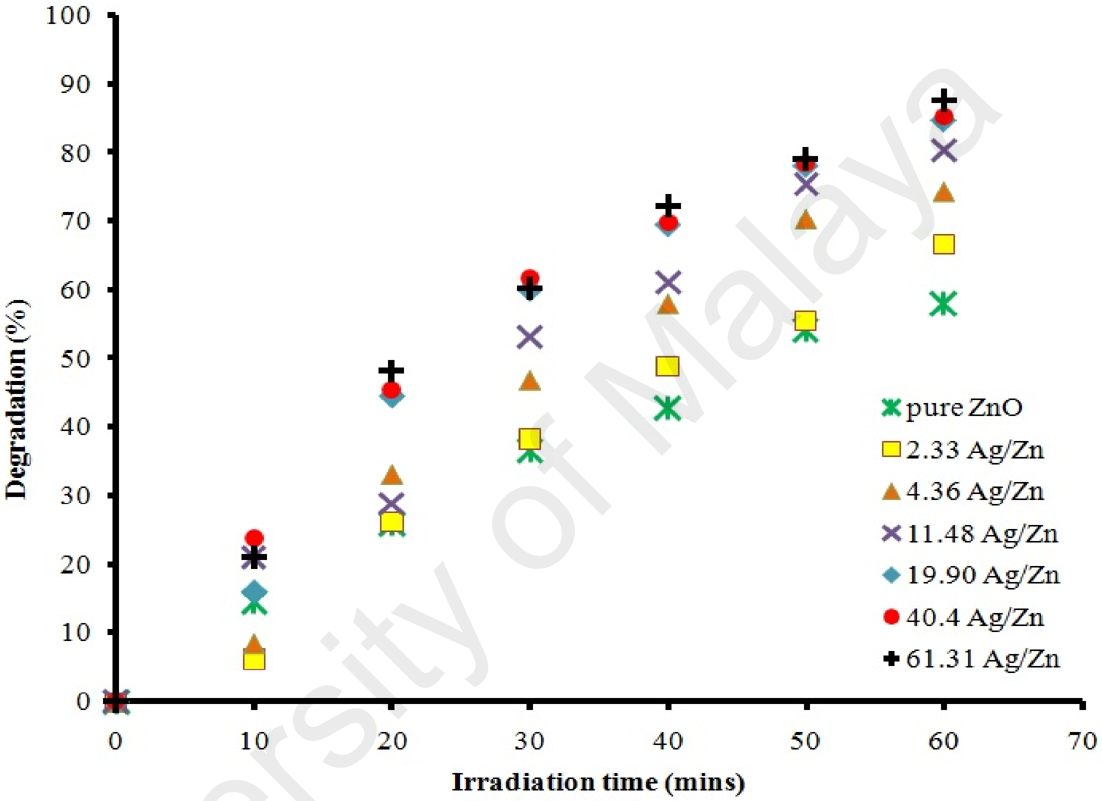

Figure 5.6: The photodegradation efficiency curve of MB under UV-light in the presence of pure ZnO and AgNPs decorated microstructured ZnO.

The photodegradation effeciency is calculated by the following equation:

$$\text{Photodegradation efficiency}(\%)= \left(\frac{C_0\text{-}C}{C_0}\right) \text{X } 100 \qquad (5.9)$$

Where C_o is the concentration at t = 0, while C is the concentration at time = t. As shown in Figure 5.6, the photodegradation efficiency of MB is about 57.98 %, 66.60 %, 74.38 %, 80.48 %, 85.25 %, 85.35 % and 87.74 % for pure ZnO, 2.33, 4.36, 11.48, 19.90, 40.40, and 61.31 at. % of AgNPs decorated microstructured ZnO, respectively when the reaction was performed under uv light irradiation for 60 minutes. It was evident that the degradation of MB after 60 minutes increased with increasing Ag content. From Figure 5.6, pure ZnO exhibits the lowest efficiency among all photocatalysts; while 61.31 at. % AgNPs decorated microstructured ZnO shows the highest photodegradation efficiency.

Figure 5.7 shows the change of photodegradation efficiency at 60 minutes irradiation time with respect to pure ZnO.

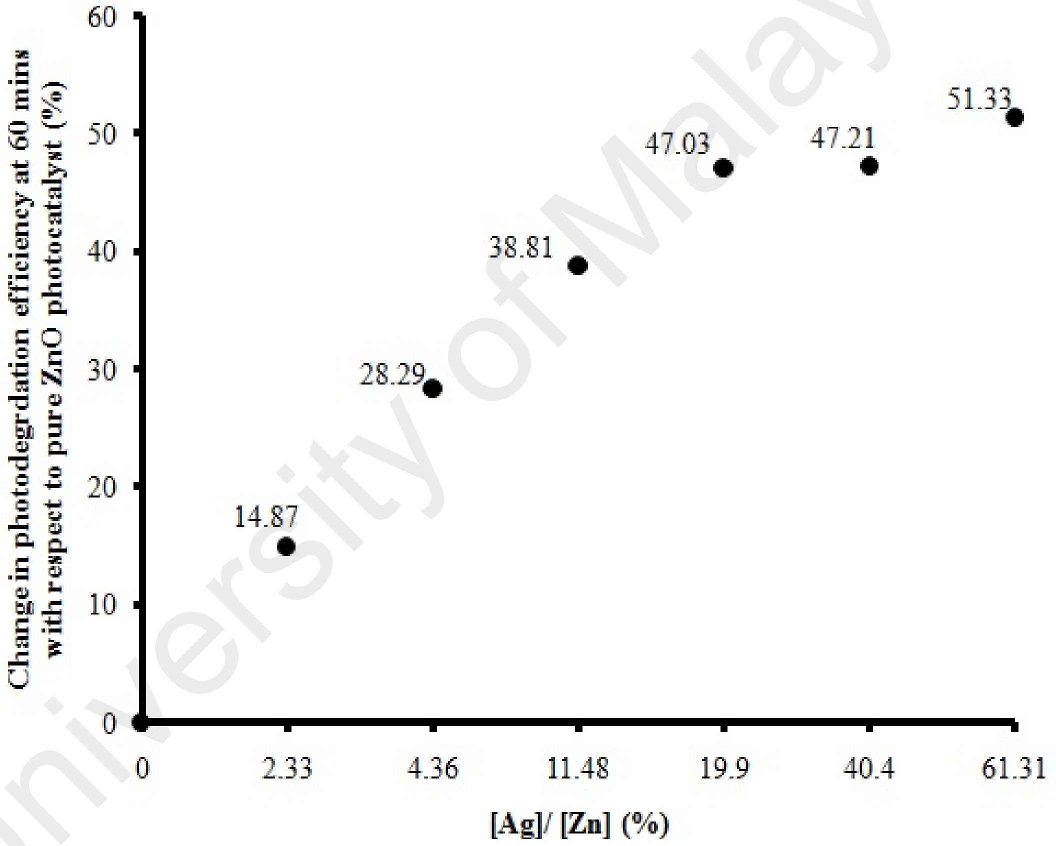

Figure 5.7: Change in photodegradation efficiency at 60 minutes irradiation time with respect to pure ZnO.

The change of photodegradation efficiency was increased monotonously as higher Ag content was used. The change of photodegradation efficiency of 2.33 at. % AgNPs decorated ZnO microstructures increased from 14.87 % to 51.33 % for 61.31 at. % AgNPs decorated ZnO microstructures after 60 minutes irradiation time, The photodegradation rate constant, *k* of pure ZnO and AgNPs decorated microstructured ZnO at different Ag contents were evaluated and quantified by plotting a first order decay plot of the characteristic MB absorption peak 664 nm. The photodegradation rate constant, *k*, can be obtained from the pseudo-first kinetics model of photocatalysis according to the following Equation 5.10:

$$\ln\left(\frac{C}{C_0}\right) = -kt \qquad \textbf{(5.10)}$$

Where *k* is the photodegradation rate constant, C_o and C are the MB initial concentration and the concentration of solution after the degradation time of t, respectively.

Figure 5.8 shows the graph of ln (C/C_o) vs irradiation time, t for pure ZnO and AgNPs decorated microstructured ZnO at various Ag contents.

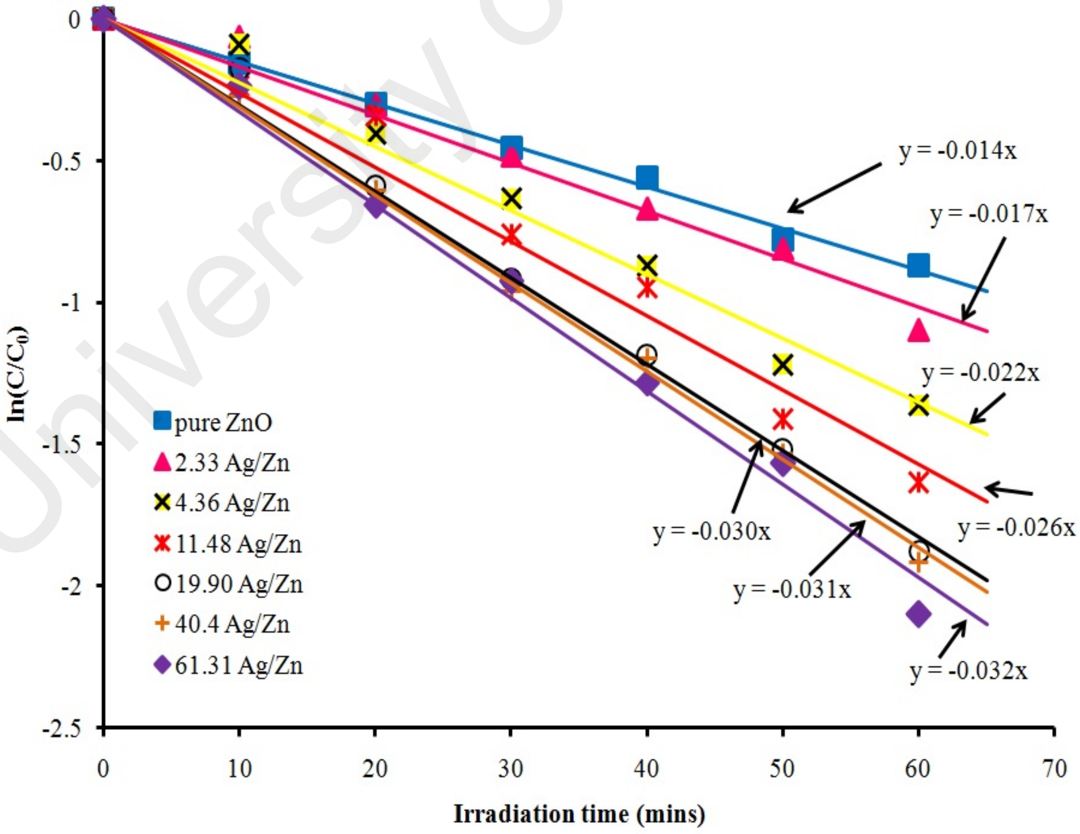

Figure 5.8: The curves of ln(C/C_0) versus time for photodegradation of MB using pure ZnO and AgNPs decorated microstructured ZnO.

This linear ln (C/C_o) vs t plot revealed that the photodegradation of MB follows pseudo-first-order reaction kinetics. The calculated photodegradation rate constant, *k* of different photocatalyst inferred from the gradients of the straight lines were 0.014, 0.017, 0.022, 0.026, 0.030, 0.031 and 0.032 min^{-1} for pure ZnO, 2.33, 4.36, 11.48, 19.90, 40.40, and 61.31 at. % of AgNPs decorated microstructured ZnO, respectively. The value of *k* for 61.31 at.% of AgNPs decorated microstructured ZnO was greater than twice of pure ZnO.

Figure 5.9 shows the photodegradation rate constant, *k* as a function of Ag contents. From the graph, the photodegradation rate constant, *k* was increased as the Ag contents increased. AgNPs decorated microstructured ZnO photocatalyst showed a higher k value compared to pure ZnO. The photodegradation rate constant, *k* marked increased for sample with AgNPs content up to 19.90 at. % and showed saturation behaviour at AgNPs content of 40.40 and 61.31 at. %. This situation might be due to an excessive Ag content which resulting in agglomeration of particles hence the photodegradation rate will saturate.

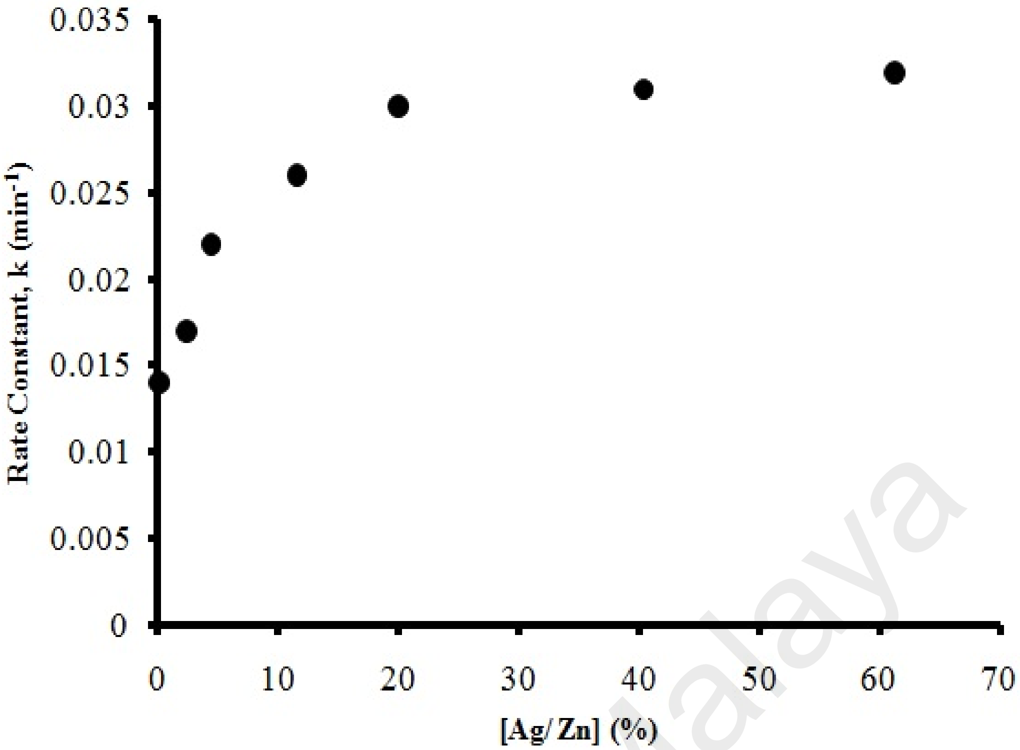

Figure 5.9: Photodegradation rate constant, *k* as a function of Ag content.

A number of studies have reported that the photocatalytic performance was reduced when the more Ag is loaded (Ren et al., 2010)(Height et al., 2006)(Chai et al., 2014). They reported that larger amount of Ag increased the size of Ag particles which significantly inhibitedthe recombination of the electron-hole pairs. This argument was supported by Saravanan (Saravanan et al., 2013) and Cheng (Cheng et al., 2013) who reported there exist an optimum amount of Ag for enhancing the degradation process. The optimum amounts of Ag acts as an electron-hole separation and hence increases the photocatalytic activity. At below optimum value, the improved activity is mainly due to the better charge separation than that of ZnO and the rate of electron transfer to dissolve the oxygen will increased. An appropriate silver content is the important factor in determining the maximum improvement of photodegradation activity.

Figure 5.10 shows the photograph of photodegradation of MB solution under uv light irradiation using AgNPs decorated microstructured ZnO. The MB solution appeared colourless after 40 minutes irradiation time.

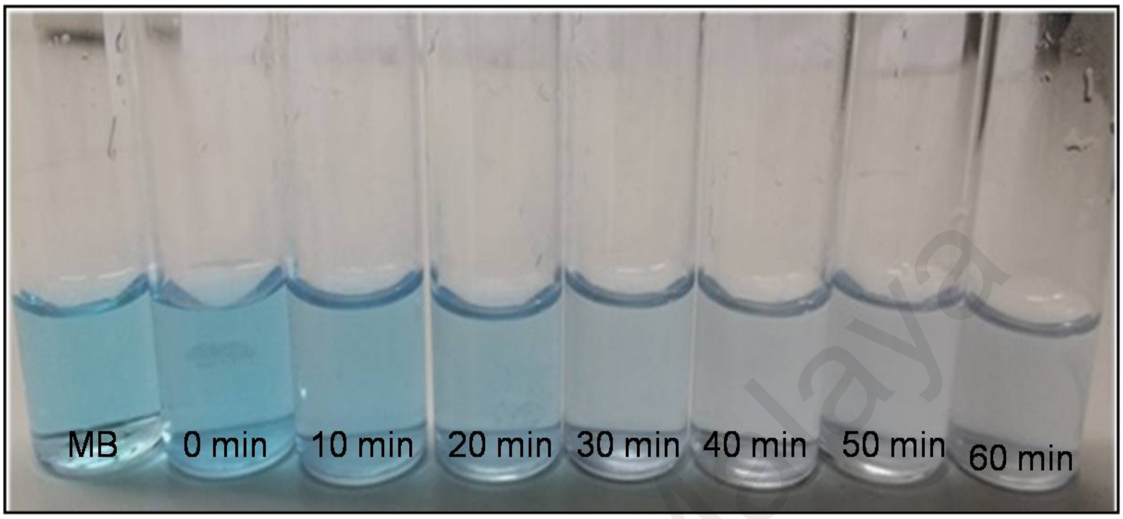

Figure 5.10: The color-change sequence of MB solution in the presence of AgNPs decorated microstrctured ZnO within irradiation times of 60 minutes.

In summary, the photodegradation rate constant, *k* increased with Ag content as 0.014, 0.017, 0.022, 0.026, 0.030, 0.031 and 0.032 min^{-1} for for pure ZnO, 2.33, 4.36, 11.48, 19.90, 40.40, and 61.31 at. % of AgNPs decorated microstructured ZnO, respectively. The improved performance of photodegradation of Ag decorated microstructured ZnO is due to existence of Ag element which acted as electron sinks to enhance the separation of photoexcited electrons fromholes.

5.3.2 Photodegradation of MB using AgNPs decorated nanostructured ZnO as photocatalyst under uv irradiation

The preparation of pure and AgNPs decorated nanostructured ZnO samples for the photodegradation process by the sol-gel technique was discussed earlier in Chapter 3 (Section 3.5.1, page 112). The amount of Ag incorporateds varied at 0.85, 1.11, 1.97, 2.08, 3.87 and 7.11 at. % . FESEM results in Chapter 3 (Section 3.5.3, page 125) confirmed that the structure of the sample consist of particles in average size of 30 -50 nm. Ag particles formed on the ZnO surface, indicating that Ag was not incorporated into the ZnO lattice. All samples (pure ZnO, 0.85, 1.11, 1.97, 2.08, 3.87 and 7.11 at. % of AgNPs decorated nanostructured ZnO) were used as photocatalyst in the photodegradation of MB.

Figure 5.11 (a-g) shows a typical absorption spectra of photodegradation of MB under uv irradiation at time between 0 and 240 minutes for (a) pure ZnO, (b) 0.85, (c) 1.11, (d) 1.97, (e) 2.08, (f) 3.87, and (h) 7.11 at.% of AgNPs decorated nanostructured ZnO, respectively. The absorbance intensities of MB gradually decreased in the presence of pure ZnO and AgNPs decorated nanostructured ZnO with the increase of irradiation time, indicating the degradation of the dye molecules.

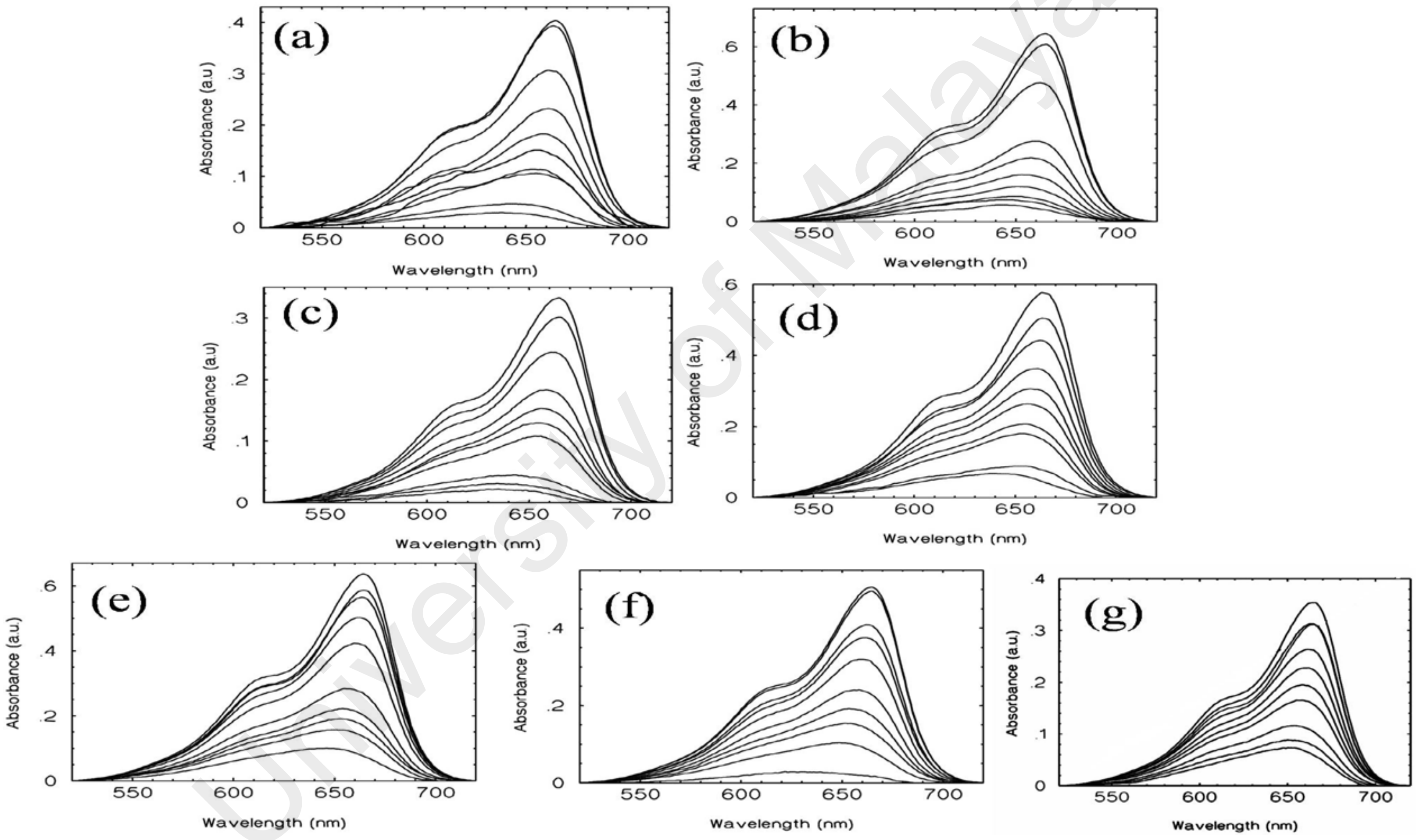

Figure 5.11: The time-dependent absorption spectra of MB solution in the presence of catalyst (a) pure ZnO, AgNPs decorated nanostructured ZnO at Ag content of (b) 0.85 at. %, (c) 1.11 at.%, (d) 1.97 at.%, (e) 2.08 at. %, (f) 3.87 at.% and (g) 7.11 at. %.

Figure 5.12 shows the photodegradation efficiency curve over irradiation time of pure ZnO and AgNPs decorated nanostructured ZnO of Ag content 0.85 at. %, 1.11 at.%, 1.97 at.%, 2.08 at.%, 3.87 at.%, and 7.11 at. %

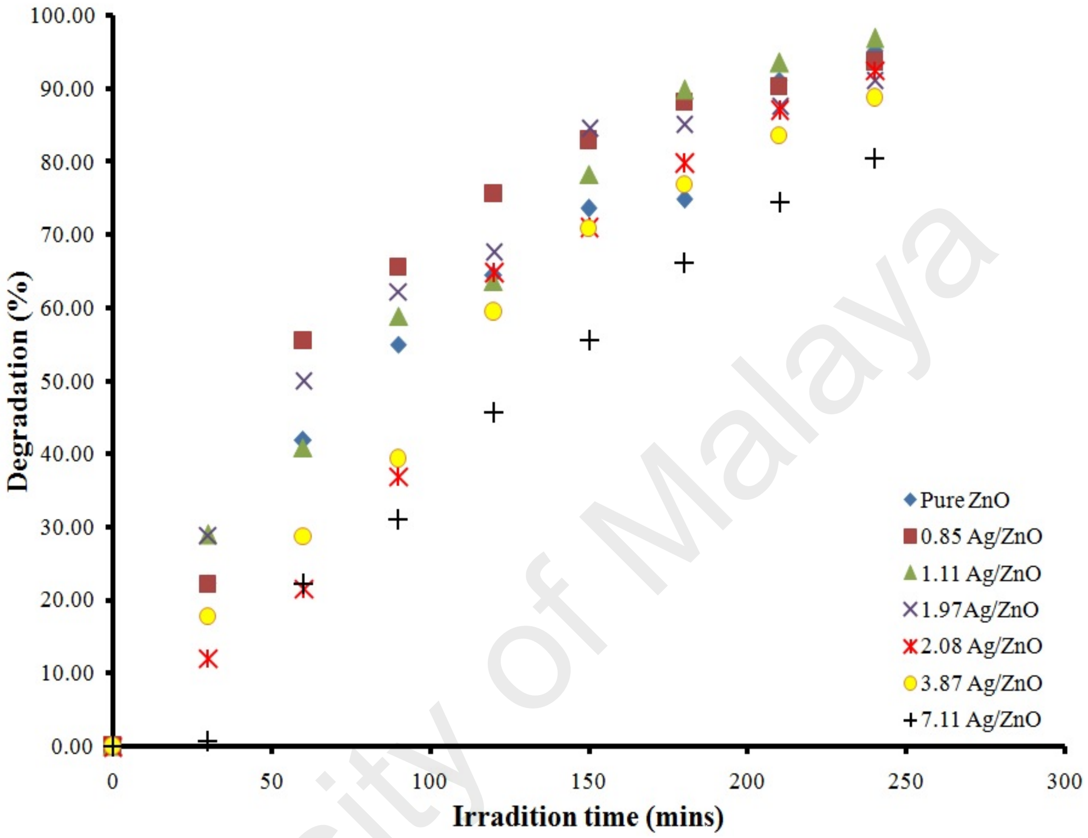

Figure 5.12: The photodegradation efficiency curve of MB under uv-light in the presence of pure ZnO and AgNPs decorated nanostructured ZnO photocatalyst.

The photodegradation efficiency was calculated from raw data using Equation 5.9 (Section 5.3.1, page 169) stated earlier. From the graph, (Figure 5.12) pure ZnO showed about 95.3 % followed by AgNPs decorated nanostructured ZnO at Ag content of 0.85 and 1.11 at. % with photodegradation efficiency after 240 minutes of about 93.7 % and 96.9 %, respectively. The calculated photodegaradation efficiency for AgNPs decorated nanostructured ZnO at Ag content of 1.97 at. % decreased to 91.3 % and increased to 92.5 % for AgNPs decorated nanostructured ZnO at Ag content of 2.08 at. % photocatalyst. The photodegradation efficiency was observed to decrease for AgNPs decorated nanostructured ZnO at Ag content of 3.87 and 7.11 at. % photocatalyst with value of 88.7 % and 80.5 %. From the graph (Figure 5.12), AgNPs decorated nanostructured ZnO at Ag content of 1.11 at. % photocatalyst showed the highest photodegradation efficiency of 96.9 %.

Figure 5.13 shows the change in photodegradation efficiency at 240 minutes irradiation time with respect to pure ZnO photocatalyst.

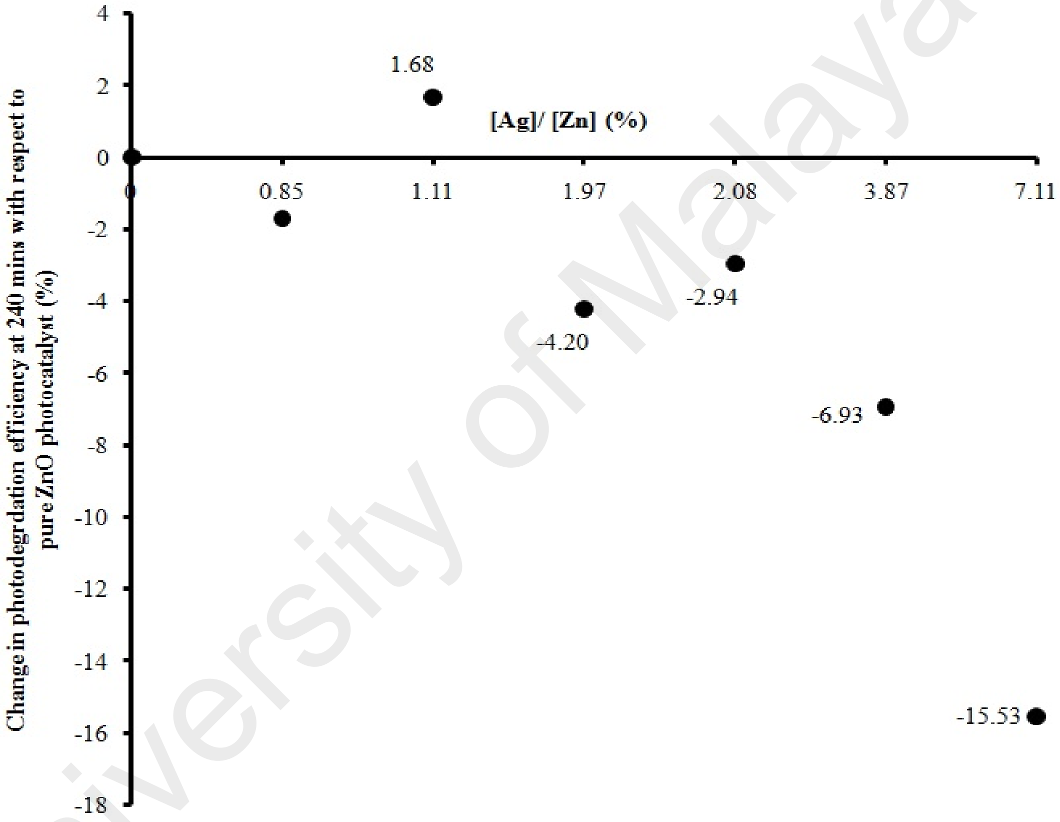

Figure 5.13: Change in photodegradation efficiency at 240 minutes irradiation time with respect to pure ZnO photocatalyst.

The change in photodegradation efficiency initially decreased to -1.68 % as 0.85 at % when AgNPs decorated nanostructured ZnO photocatalyst was used. Then, the change in photodegradation efficiency increased to 1.68 % as 1.11 at % of AgNPs decorated nanostructured ZnO was used. The change in photodegradation efficiency decreased when higher Ag contents were used at about -4.20 %, -2.94 %, -6.93 % and -15.53 %

for AgNPs decorated nanostructured ZnO at Ag contents of 1.97 at. %, 2.08 at.%, 3.87 at.% and 7.11 at.%, respectively.

The photodegradation of MB in the presence of pure ZnO and AgNPs decorated nanostructured ZnO photocatalyst was further analyzed using first order kinetics as in Equation 5.2 stated earlier in Section 5.3.1. The plot of ln (C/C_o) vs irradiation time is shown in Figure 5.14.

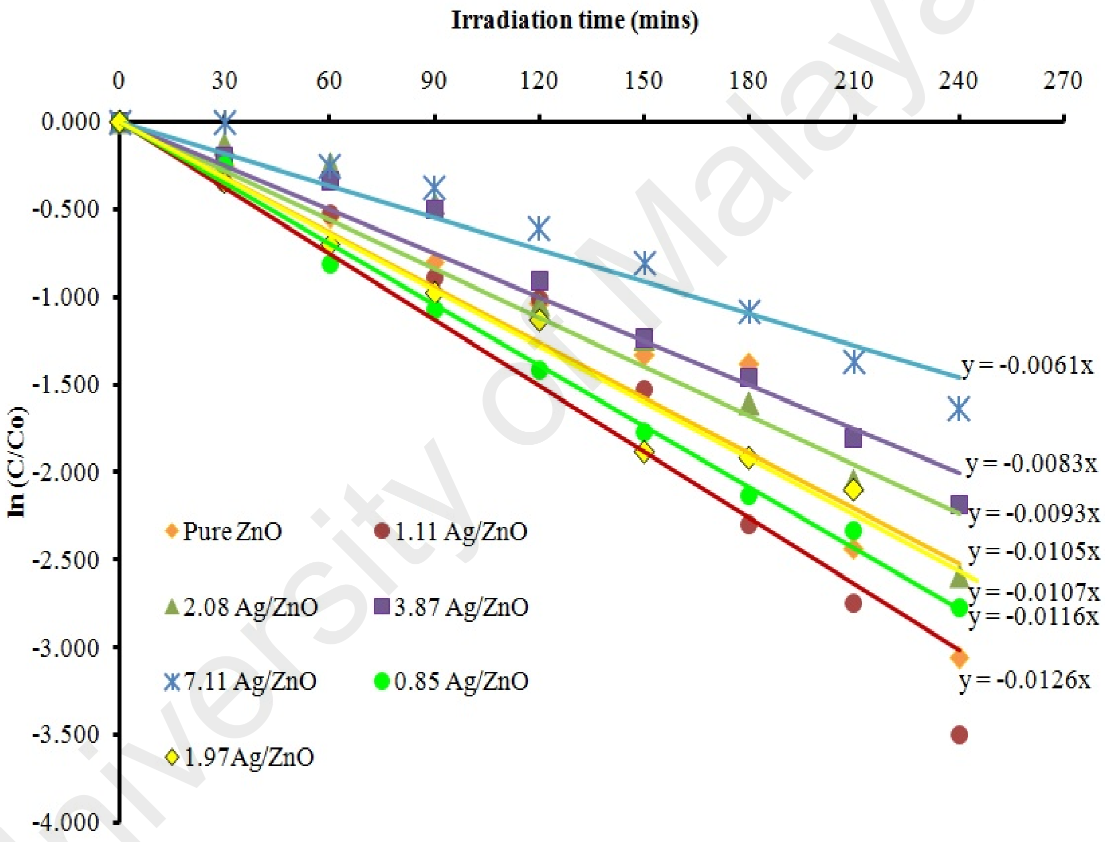

Figure 5.14: The photodegradation curves of ln(C/C_0) versus time for photodegradation of MB using pure ZnO and AgNPs decorated nanostructured ZnO photocatalyst.

From Figure 5.14, the photodegradation rate constant, *k*, for pure ZnO photocatalyst was 0.0105 min^{-1}. The *k* value increased to 0.0116 and 0.0126 min^{-1} for Ag content in the sample at 0.85 and 1.11 at. %. The photodegradation activity reduced at Ag content of 1.97 to 7.11 at. % with *k* at 0.0107, 0.093, 0.083 and 0.061 min^{-1} for Ag contents of 1.97

at.%, 2.08 at.%, 3.87 at.% and 7.11 At.%, respectively. The photocatalytic activities increased as the concentration increased from 0.5 to 1.5 wt. % of Ag and started to decrease for Ag content from 2.0 to 8.0 wt. %. AgNPs decorated nanostructured ZnO at Ag content of 1.11 at. % showed the highest *k* value.

Similar results were reported previously under different photodegradation measurement conditions. Gu et al. (Gu et al., 2009) synthesized dendrite-like Ag/ZnO heterostucture nanocrystal and investigated the photocatalytic of pure ZnO and ZnO@Ag heterostructures at Ag concentrations of 3 to 11 atom %. The photocatalytic activity increased with increasing Ag content from 3 to 8 atom %, but decreased when Ag content higher than 8.0 atom %. Sun et al. (Sun et al., 2012) evaluated the photocatalytic performance of Ag/ZnO heterostructured nanocrystals with Ag content was varied from 0.5 to 8.0 wt. %. The results showed that the photocatalytic activity of Ag/ZnO nanocrystal increased at Ag content from 0.5 to 1.5 wt. %, and further increasing the Ag content up to 8.0 wt. % leads to a decrease of photocatalytic activity. Gao et al. (Gao et al., 2011) synthesized hierarchical Ag/ZnO micro/nanostructure and evaluated the Ag/ZnO micro/nanostructure at various Ag content from 0.35 to 2.90 at. %. They reported that as the Ag content increases, the photocatalytic performance of the Ag/ZnO has not been enhanced monotonously and 1.81 at. % Ag achieved the highest photocatalytic performance.

Figure 5.15 shows the photodegradation rate constant, *k* as a function of Ag content for pure ZnO and AgNPs decorated nanostructured ZnO at various Ag content.

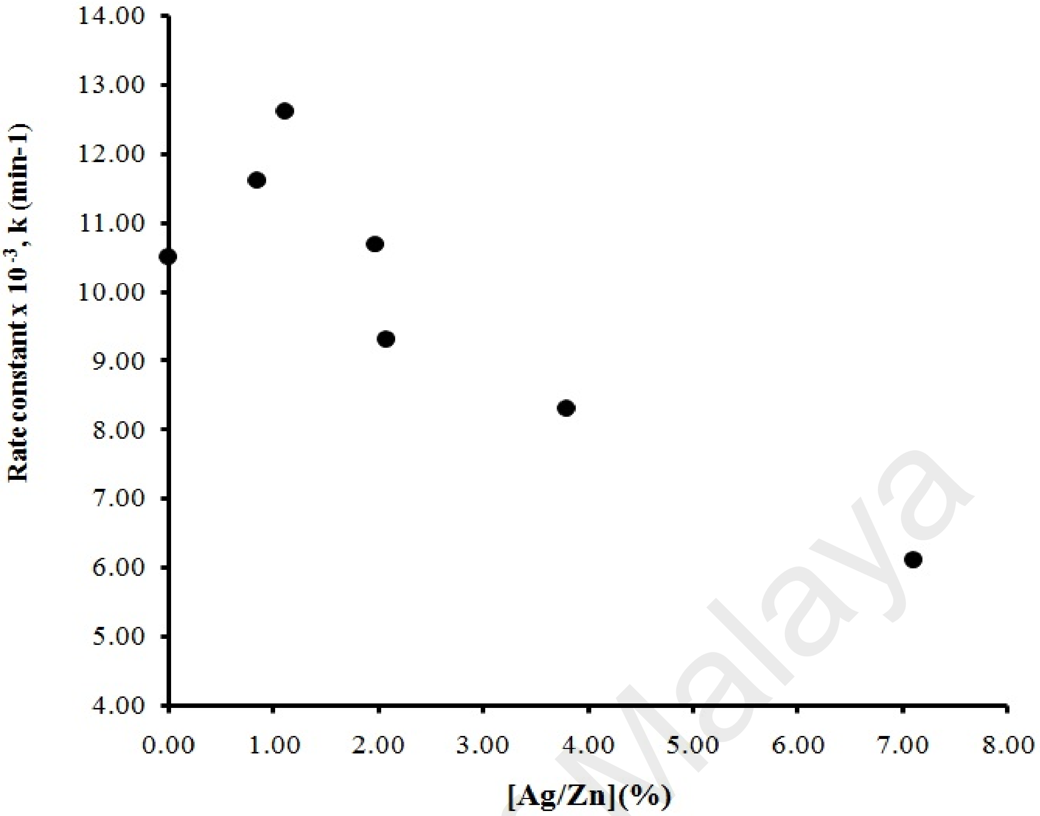

Figure 5.15: Photodegradation rate constant, *k* as a function of Ag content.

The photodegradation rate constant, *k* initially increased as the AgNPs decorated nanostructured ZnO at Ag content of 0.85 and 1.11 at. % was used. However, the *k* value decreased at higher Ag contents 1.97 to 7.11 at. %. AgNPs decorated nanostructured ZnO at Ag content of 1.11 at. % achieved the highest *k* value. Higher amount of Ag lead to the decreasing of photodegradation rate constant.

Figure 5.16 shows the photograph of photodegradation of MB solution under uv light irradiation using AgNPs decorated nanostructured ZnO. The MB appeared colourless after 180 minutes irradiation time.

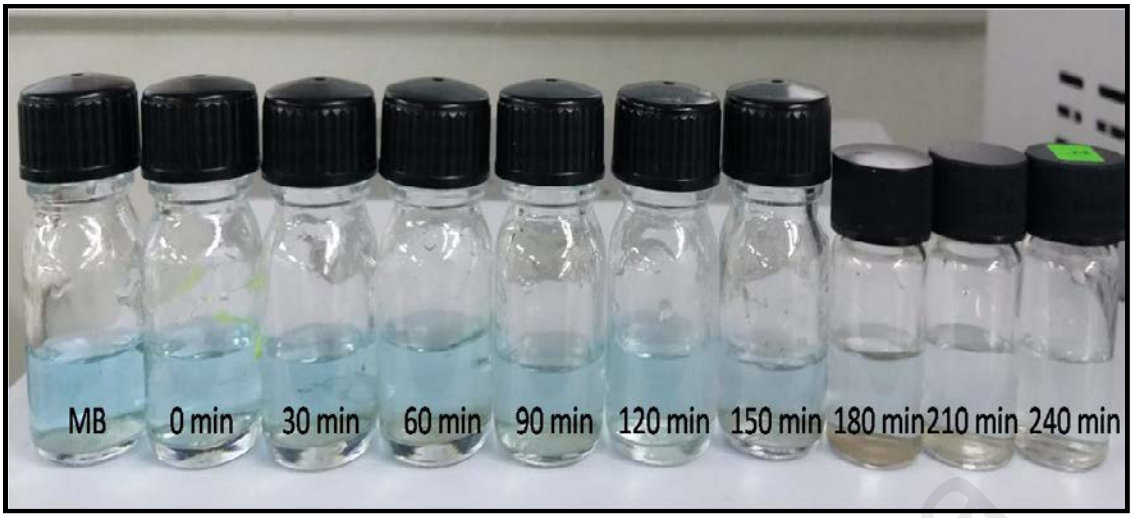

Figure 5.16: The colour-change sequence of MB dye solution in the presence of AgNPs decorated nanostructured ZnO within irradiation times of 240 minutes.

Table 5.1 shows the results of photodegradation rate constant, *k* of AgNPs decorated micro- and nanostructured ZnO from present work and results reported in the literature. Previous work also reported that, the ZnO in nanowires and nanorods structures show highest photodegradation rate constant compared to ZnO nanoparticles as briefly stated in Table 5.1. Piella et al. reported that different size and shape of nanostructures can affect the photocatalytic activity (Piella et al., 2013). She reported that, small particles exhibit a higher photocatalytic activity compared to larger particles. She also stated that, a flat surface such as stamp or belt-like shapes have a higher photocatalytic activity compared to spheres due to high coordination of atom. Zhoa et al. (Zhao et al., 2014) also reported that photocatalyst with higher surface energy show better photocatalytic activity. He observed that, ZnO shape of nanosheets composed flower-like and twining-hexagonal disk have larger area of (0001) plane than ZnO shape of sphere, hence exhibit higher photocatalytic activities.

In this work, AgNPs decorated microstructure with particle size less than 500 nm ZnO shows an increase of photodegradation rate with increasing of Ag content. The photodegradation rate for pure ZnO is 0.014 min^{-1} and increased up to 0.032 min^{-1} for the highest AgNPs decorated microstructured ZnO at Ag content of 61.31 at.%. A different trend of photodegradation rate constant was observed for AgNPs decorated nanostructured ZnO. The particle size for AgNPs decorated nanostructured ZnO is an average of 30 and 50 nm. A trend of increasing was observed up to 1.11 at.% Ag content and decreased with increasing Ag content of 1.97 at.%. The highest Ag content of 7.11 at. % of AgNPs decorated microstructured ZnO shows a half value of photodegradation rate constant of pure ZnO. Gu et al. (Gu et al., 2009) reported a photocatalytic effect of dendrite-like ZnO/Ag with a diameter of 50 to 400 nm and length of 1 μm. They observed that, the photodegradation rate constant was increased when Ag content up to 8 at. % (k=0.0024 min^{-1}) and decreased when exceed 11 at. % (k= 0.0022 min^{-1}). A photodegradation rate constant of Ag/ZnO nanoparticles reported by Whang et al. (Whang, Hsieh, & Chen, 2012) shows an increased of value of $5.47\mathrm{x}10^{-3}$ min^{-1} compared to pure ZnO with value of $1.37\mathrm{x}10^{-3}$ min^{-1}. A study by Chang et al. (Chang et al., 2013) reported the photocatalytic study of Ag microplate/ZnO nanowire with diameter of 20 to 50 nm and length size of 0.5 to 1 μm. The Ag content was varied from 0.34 up to 20.54 at. %. They observed a similar trend of photodegradation rate constant as our AgNPs decorated microstrctured ZnO photocatalyst where the photodegradation rate was steadily increased with increasing Ag content. Ren et al. (Ren et al., 2010) was studied the phocatalytic effect on the Ag particulates/ZnO nanorods with diameter of the rod in the range of 100 and 125 nm and length size of 1 μm. They observed a similar trend of photodegradation rate as our AgNPs decorated nanostructured ZnO photocatalyst. The photodegradation rate was increased up to 0.05 M Zn/Ag photocatalyts (k= $7.63\mathrm{x}10^{-3}$ min^{-1}). At higher concentration of 0.1 M and 0.2 M, the photodegration rate reduced at value of $7.17\mathrm{x}10^{-3}$ and 6.08x10-3 min^{-1}. It can be concluded that, different structures and size of Ag/Zn with different Ag content resulting a different trend of photodegradation rate value.

Table 5.1: Summary of photocatalytic studies of Ag/ZnO photocatalyst for the photodegradation of MB.

Structure	**Photodegradation rate constant, *k***	**Ref.**
Ag decorated microstructured ZnO (particle size: average size less than 500 nm)	PureZnO: 0.014 min^{-1} 2.33 at. % Ag/Zn: 0.017 min^{-1} 4.36 at. % Ag/Zn: 0.022 min^{-1} 11.48 at. % Ag/Zn: 0.026 min^{-1} 19.90 at. % Ag/Zn: 0.030 min^{-1} 40.40 at. % Ag/Zn: 0.031 min^{-1} 61.31 at. % Ag/Zn: 0.032 min^{-1} The rate constant increased as Ag content increased	This work
Ag decorated nanostructured ZnO (particle size: average size about 30- 50 nm)	Pure ZnO: 0.0105 min^{-1} 0.85 at. % Ag/Zn: 0.0116 min^{-1} 1.11 at. % Ag/Zn: 0.0126 min^{-1} 1.97 at. % Ag/Zn: 0.0107 min^{-1} 2.08 at. % Ag/Zn: 0.0093 min^{-1} 3.87 at. % Ag/Zn: 0.0083 min^{-1} 7.11 at. % Ag/Zn: 0.0061 min^{-1} The rate constant value increased from pure ZnO – 1.11 at.% Ag/Zn photocatalyst, and decrease when exceed 1.11 at. % Ag/Zn.	This work

‘Table 5.1,continued’: Summary of photocatalytic studies of Ag/ZnO photocatalyst for the photodegradation of MB.

Structure	Photodegradation rate constant, *k*	Ref.
Ag nanowire (length: 5 to 20 µm, diameter: 100-800 nm) Dendrite-like ZnO@Ag heterostructure nanocrystals (diameter ZnO nanorods: 50 to 400 nm,length: 1 µm)	ZnO100= 0.0015 min^{-1} ZnO97:Ag3.0= 0.0016 min^{-1} ZnO92:Ag8.0 =0.0024 min^{-1} ZnO89:Ag11.0= 0.0022 min^{-1} The rate constant increase when Ag content up to 8 at.% but decrease when Ag content of 11at.%	(Gu et al., 2009)
Ag/ZnO nanoparticles	Pure ZnO: 1.37 × 10^{-3} min^{-1} ZnO:98:Ag 2.0: 5.47 × 10^{-3} min^{-1} The rate constant increased	(Whang et al., 2012)
Ag microplate ZnO nanowire diameter (20–50 nm) and long length (0.5–1 µm)	ZnO100= 4.88 x10^{-3} min^{-1} ZnO99.64:Ag0.36= 5.05 x10^{-3} min^{-1} ZnO98.66:Ag1.34= 5.87 x10^{-3} min^{-1} ZnO94.88:Ag5.12= 6.60 x10^{-3} min^{-1} ZnO79.46:Ag20.54= 6.66 x10^{-3} min^{-1} The rate constant increased	(Chang et al., 2013)

'Table 5.1, continued': Summary of photocatalytic studies of Ag/ZnO photocatalyst for the photodegradation of MB.

Structure	Photodegradation rate constant, *k*	Ref.
Ag particulates ZnO nanorods (diameters of the nanorods ranged from 100 to 125 nm and the length was about 1.0 μm)	Pure ZnO= $5.16\times10^{-3}\text{min}^{-1}$ ZnO/Ag (0.02M)= $5.69\times10^{-3}\ \text{min}^{-1}$ ZnO/Ag (0.05M)= $7.63\times10^{-3}\text{min}^{-1}$ ZnO/Ag (0.1M)= $7.17\times10^{-3}\text{min}^{-1}$ ZnO/Ag (0.2M):= $6.08\times10^{-3}\text{min}^{-1}$ The rate constant increase when Ag concentration up to 0.1M but decrease when higher concentration (0.2M) applied	(Ren et al., 2010)

In this work, different trend of photodegradation rate constant, *k*was observed for AgNPs decorated micro- and nanostructured ZnO photocatalyst. For AgNPs decorated microstructred ZnO photocatalysts, a correlation was observed where a steady increase in the photodegradation rate constant, *k*with increasing Ag content. As for the AgNPs decorated nanostructured ZnO photocatalysts, a trend of increasing photodegradation rate constant, *k* was observed up to 1.11 at % Ag content. At higher Ag content, the photodegration rate constant, *k* reduced with increasing Ag content. At 2.08 at. % Ag content, the photodegradation rate constant, *k* was lower than that afforded using pure ZnO nanostructures. At the highest Ag content of 7.11 at. % the photodegradation rate constant, *k*was also half of that due to pure ZnO nanostructures. We believe that a shielding effect has significantly reduced the efficiency when using Ag decorated nanosized ZnO. As evident from HRTEM images (see Chapter 3, Figure 3.46 and Figure 3.53), the AgNPs were relatively small compared to the microsized ZnO but were of similar size to the nanosized ZnO. As such, there is a strong possibility that the AgNPs decorating the ZnO NPs shielded the uv light from hitting the ZnO NPs. This resulted in the reduced photodegradation efficiency. As for the AgNPs decorated microstructured ZnO, the relatively small sized Ag AgNPs attached to the ZnO surface, effectively provided little uv light shielding effect. The shielding effect can be visualized using Figure 5.17.

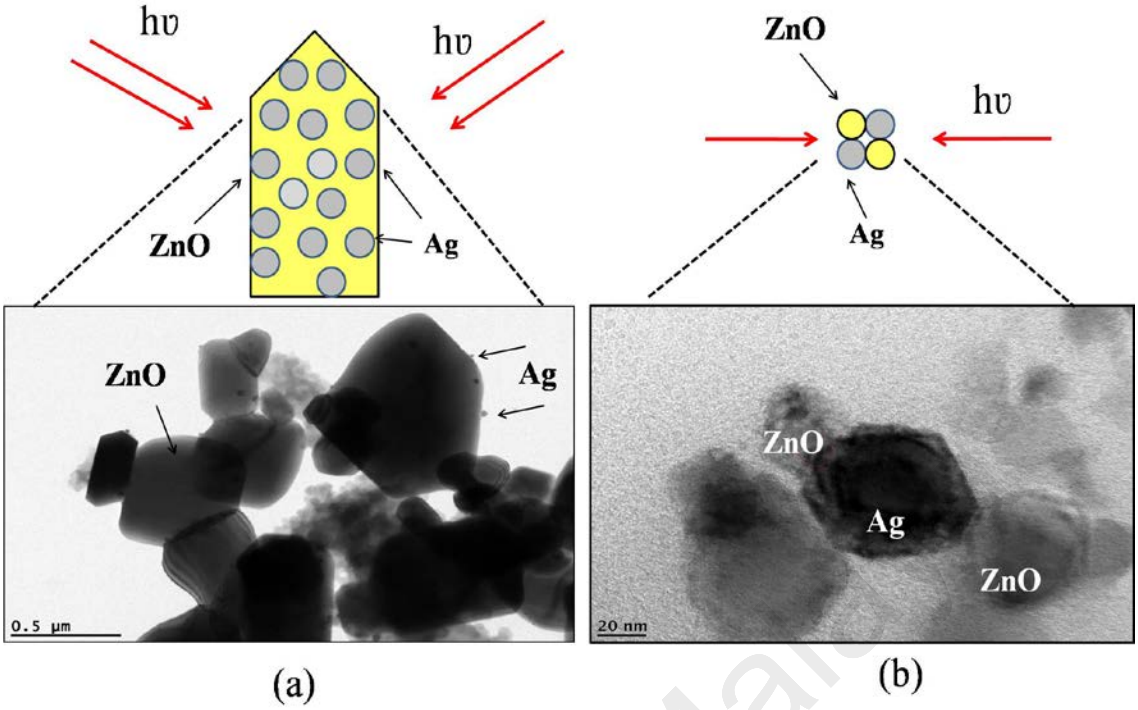

Figure 5.17: Visualization of shielding effect of AgNPs decorated (a) microstructured and (b) nanostructured ZnO photocatalysts.

In Figure 5.17 (a), for AgNPs decorated microstructured ZnO, the area exposed to uv light were constant in any direction where uv light will fall on the ZnO particles. In Figure 5.17 (b), the size of the AgNPs and the ZnO NPs were almost similar. Here there is a possibility that uv light will be shielded from the ZnO NPs, thus hampering the photocatalytic process and resulting in the reduction of the photodegradation rate constant.

In summary, the photodegradation efficiency increased for AgNPs decorated nanostructured ZnO at Ag content of 0.85 and 1.11 at. %, and reduced when Ag content exceed 1.11 at. %. Similar trend for the photodegradation rate constant, *k* was observed. The *k* value was increased as the Ag content increased from with value of 0.0105, 0.0016 and 0.00126 min^{-1} for pure ZnO, 0.85 and 1.11 at. % AgNPs decorated nanostructured ZnO. The *k* value was reduced with value of 0.0107, 0.0093, 0.0083 and 0.0061 min^{-1} for AgNPs decorated nanostructured ZnO at Ag content of 1.97, 2.08, 3.87

and 7.11 at. %, respectively. An appropriate amount of Ag on ZnO surface can produce the Schottky barrier, which effectively capture and transfer the photogenerated electrons, and thus suppress the recombination of the photogenerated electron–hole pairs. However, when more Ag content is loaded, the particles size of Ag will increase, which is disadvantage to inhibit the recombination of the electron–hole pairs.

5.4 Conclusions

AgNPs decorated micro- and nanostructured ZnO photocatalyst were synthesized using sol- gel method. The photodegradation of MB is much more rapidly in the presence of Ag compared to pure ZnO photocatalyst for AgNPs decorated microstructured ZnO photocatalyst. The photodegradation rate was observed to increase steadily with increased in Ag content. The photodegradation rate constant, *k* value is 0.014, 0.017, 0.022, 0.026, 0.030, 0.031 and 0.032 min^{-1} for pure ZnO, 2.33, 4.36, 11.48, 19.90, 40.40, and 61.31 at. % of AgNPs decorated microstructured ZnO photocatalyst. Presence of the 61.31 at. % Ag content of AgNPs decorated microstructured ZnO after 60 minutes uv irradiation, almost 90 % degradation efficiency was achieved along with highest photodegradation rate. It can conclude that addition of Ag enhanced the activity of ZnO and the highest amount of Ag was proven to be an efficient photocatalyst. By contrast, for AgNPs decorated nanostructured ZnO photocatalyst, as the Ag content increases, the photodegradation activity does not enhance monotonously. The photodegradation efficiency was increased for AgNPs decorated nanostructured ZnO at Ag content of 0.85 and 1.11 at. %, and started to reduce when Ag content exceed 1.11 at. %. Similar trend for the photodegradation rate constant, *k* was observed where initially the *k* value was increased as the Ag content increased to 1.11 at. % with value of 0.0105, 0.0016 and 0.00126 min^{-1} for pure ZnO, 0.85 and 1.11 AgNPs decorated nanostructured ZnO photocatalyst. The *k* value started to reduce with value of 0.0107, 0.0093, 0.0083 and 0.0061 min^{-1} for AgNPs decorated nanostructured ZnO at Ag content of 1.97, 2.08, 3.87 and 7.11 at. % photocatalyst, respectively. Hence, AgNPs decorated nanostructured ZnO at Ag content of 1.11 at. %, has been observed as the efficient photocatalyst to achieve the highest photodegradation rate as the photodegradation efficiency of 96.9 % was achieved along with highest photodegradation rate. When semiconductor and metal material was used, Schottky barrier will generated at the interface between ZnO and Ag resulting in an efficient electron’s channel from the bulk of ZnO to the newly formed interface. The accumulation of electrons on metal deposits could attract the photogenerated holes to the metal sites and this may encourage the recombination of charge carriers and the metal deposits conversely behave as recombinant centres (Pyne et al., 2012)(Yang et al., 2011). Unfortunately, when higher Ag contents were added, resulting over accumulation of electrons on the surface, it might decrease the catalytic efficiency of the semiconductor due to the excessive of Ag content that will shield the uv light adsorption of ZnO, and make it difficult to trigger the photocatalyst. Ag particles reversely behave as recombination centres of charge carriers after the Ag content exceeds the optimal value hence decrease the photocatalytic activities.

CHAPTER 6: CONCLUSION AND FUTURE WORKS

6.1 Conclusion

Sol-gel method was used to synthesis ZnO using conventional reagent i.e HMTA and biomaterial sources i.e *Citrus aurantifolia* (CA) as the reducing agent. Using HMTA, in glass substrate shows the efficient substrate to growth the ZnO nanorods, while stainless steel was the least efficientterms of growth rate. This situation was due to the reactivity of the metallic substrate with the chemicals during the synthesis.Doping with ferum andaluminum at different concentration were verified by shifts in the XRD peak of the zinc oxide (001) diffraction plane towards smaller or higher angle indicates the doping effect. Also observed was the increase in the lattice constants "a" and "c" indicating Fe^{2+} or Fe^{3+} substitution of Zn^{2+} in the ZnO lattice. EDX analysis also verified the doping effect of Fe or Al-doped ZnO nanorods.

Biosynthesis sol-gel method was demonstrated by substituting the conventional reducing agent i.e. HMTAwith CA. To our best knowledge, this is the first study to report the ZnO nanorods synthesized using CAjuice. Enhancement of ZnO formation was observed in neutral and alkaline compared to acidic starting solution. This was due to the abundance of OH^- ions in non acidic solutions which promoted the formation of the $Zn(OH)_2$ intermediate species. A study of in-situ high temperature XRD effect shows that the average particle size and lattice parameter (‘a’ and ‘c’) were significantly affected by the increase of temperature. The lattice parameter and average crystallite size increased as temperature increases. Similar morphology was observed for pure and different level of doping of Mg-doped ZnO nanostructures synthesized using CA juice. The level of doping increased as concentration of Mg increased. XRD peak that shifted toward higher angle and EDX analysis indicated doping.

For field electron emission study, the field enhancement factor, β, was influenced solely by the geometry of the ZnO cathodes samples. Doping (Al and Mg) have the effect of reducing the turn-on and threshold electric field. For ZnO nanorods prepared at different deposition time, the turn-on field values of 5.21, 5.45, 6.21and 6.92V/μm were obtained for samples deposited for 4, 3, 2.5 and 0.5 hours respectively. The threshold values were 10.45, 10.12, 9.39 and 9.12 V/μm or samples deposited for 4, 3, 2.5 and 0.5 hours, respectively. The field enhancement factor, β also increased with deposition time. For pure and Al doped ZnO at different Al concentrations (0.13, 0.16 and 0.19 at. %), enhanced FEE properties in terms of the lowering of turn on and threshold field values was observed. The turn-on field values are 7.2, 6.6, 6.0 and 5.8 V/μm for pure ZnO, 0.13, 0.16 and 0.19 at. % Al-doped ZnO. The threshold field values are 8.79, 8.63, 8.54 and 8.49 for pure ZnO, 0.13, 0.16 and 0.19 at. % Al-doped ZnO, respectively.FEE properties of the pure and Mg-doped ZnO nanostructures showed a clear trend of decreasing turn-on and threshold electric field values with increasing Mg doping level. The turn-on field values are 6.99, 6.35, 6.07 and 5.99 V/μm for pure ZnO, 0.225, 0.29 and 0.45 at. % Mg-doped ZnO nanostructures. The threshold field values are 9.16, 9.17, 8.62 and 8.49 V/μm for pure ZnO, 0.225, 0.29 and 0.45 at. % Mg-doped ZnO nanostructures.The field enhancement factor,βwas almost constant due to the similar geometrical features of ZnO nanostructres samples.

Effect of Ag levels in AgNPs decorated nanostructured ZnO synthesized using HMTA as photocatalyst for photodegradation of MB under uv light showed increased in photodegradation efficiency up to 1.11 at. % Ag content. Beyond this value, the efficiency measured in terms of photodegradation rate constant, reduced with increasing Ag content. The trend of reducing photodegradation efficiency was not observed when microsized ZnO was decorated with nanosized AgNPs, up to Ag content of 61.31 at. %.

This phenomena was explained in terms of light shield in the AgNPs decorated nanostructured ZnO samples.

6.2 Future work

Sol-gel synthesis is a very efficient and promising technique for the growth ZnO nanostructures. For future, more work is still need to be concerned to obtain precise and optimum control parameter for enhancing ZnO nanostructures properties such as crystallinity, electrical and optical. It would be interesting to see how the properties changed as size, structure and formation changed. In addition, the used of other type of biomaterial as a reducing agent also could be used as it is nontoxic and economical for the synthesis of ZnO. Further experimentation and investigation on doped-ZnO nanostructures is also recommended. It would be interesting to assess the effects of other type of dopant and co-dopant as it is well known that doping process can enhance the properties of ZnO nanostructures. A more detailed study using another characterization method such as XPS, TGA, HRTEM and SAED can added more information and knowledge on the prepared ZnO nanostructures. For future work, we also expect that more measurement on field electron emission could be employed for various samples of ZnO nanostructures. In addition the modification of ZnO nanostructures and microstructures with other material such as graphene, titanium dioxide and other metal is expected to give effect to the photocatalytic activity of dye.

REFERENCES

Adhyapak, P. V, Meshram, S. P., Amalnerkar, D. P., & Mulla, I. S. (2014). Structurally enhanced photocatalytic activity of fl ower-like ZnO synthesized by PEG-assited hydrothermal route. *Ceramics International*, *40*, 1951–1959.

Ahmed, F., Arshi, N., Anwar, M. S., Danish, R., & Koo, B. H. (2013). Facile growth of ZnO nanorod arrays by a microwave-assisted solution method for oxygen gas sensing. *Thin Solid Films*, *547*, 168–172. doi:10.1016/j.tsf.2013.03.099

Ahmed, F., Arshi, N., Anwar, M. S., Lee, S. H., Byon, E. S., Lyu, N. J., & Koo, B. H. (2012). Effect of Ni substitution on structural, morphological and magnetic properties of Zn1-xNixO nanorods. *Current Applied Physics*, *12*, S174–S177. doi:10.1016/j.cap.2012.02.054

Al-Owais, A. a. (2013). Synthesis and magnetic properties of hexagonally packed ZnO nanorods. *Arabian Journal of Chemistry*, *6*(2), 229–234. doi:10.1016/j.arabjc.2011.11.001

Alvi, N. H., Willander, M., & Nur, O. (2010). Superlattices and Microstructures The effect of the post-growth annealing on the electroluminescence properties of n-ZnO nanorods / p-GaN light emitting diodes. *Superlattices and Microstructures*, *47*(6), 754–761. doi:10.1016/j.spmi.2010.03.002

Baruah, S., & Dutta, J. (2009). pH-dependent growth of zinc oxide nanorods. *Journal of Crystal Growth*, *311*(8), 2549–2554. doi:10.1016/j.jcrysgro.2009.01.135

Baviskar, P. K., Nikam, P. R., Gargote, S. S., Ennaoui, A., & Sankapal, B. R. (2013). Controlled synthesis of ZnO nanostructures with assorted morphologies via simple solution chemistry. *Journal of Alloys and Compounds*, *551*, 233–242. doi:10.1016/j.jallcom.2012.10.052

Behera, D., & Acharya, B. S. Ã. (2008). Nano-star formation in Al-doped ZnO thin film deposited by dip-dry method and its characterization using atomic force microscopy , electron probe microscopy , photoluminescence and laser Raman spectroscopy. *Journal of Luminescence*, *128*, 1577–1586. doi:10.1016/j.jlumin.2008.03.006

Bhattacharya, S., De, D., Adhikari, S. M., Saha, S., Chatterjee, K. M., Choudhury, S., & Ghatak, K. P. (2011). Simple theoretical analysis of the Fowler-Nordheim field emission from microstructures and quantum wires of optoelectronic materials. *Superlattices and Microstructures*, *50*, 609–627. doi:10.1016/j.spmi.2011.07.007

Brinker, C. J., & Scherer, G. W. (1990). *SOL-GEL SCIENCE- The Physics and Chemistry of Sol-Gel Processing*. Academic Press.

C.Suryanarayana, & Norton, M. G. (1998). *X-Ray Diffraction*. Springer.

Calleja, J. M., & Cardona, M. (1977). Resonant raman scattering in ZnO. *Physical Review B*, *16*(8), 3753–3761.

Cetin, S. S., Uslu, I., Aytimur, A., & Ozcelik, S. (2012). Characterization of Mg doped ZnO nanocrystallites prepared via electrospinning. *Ceramics International*, *38*(5), 4201–4208. doi:10.1016/j.ceramint.2012.02.003

Chai, B., Wang, X., Cheng, S., Zhou, H., & Zhang, F. (2014). One-pot triethanolamine-assisted hydrothermal synthesis of Ag/ZnO heterostructure microspheres with enhanced photocatalytic activity. *Ceramics International*, *40*(1), 429–435. doi:10.1016/j.ceramint.2013.06.019

Chan, S. H. S., Yeong Wu, T., Juan, J. C., & Teh, C. Y. (2011). Recent developments of metal oxide semiconductors as photocatalysts in advanced oxidation processes (AOPs) for treatment of dye waste-water. *Journal of Chemical Technology & Biotechnology*, *86*(9), 1130–1158. doi:10.1002/jctb.2636

Chang, C.-W., Wu, H.-T., Huang, S.-H., Chen, C.-K., Un, I.-W., & Yen, T.-J. (2013). Single-crystalline heterostructure of ZnO nanowire arrays on large Ag microplates and its photocatalytic activity. *Acta Materialia*, *61*(18), 6993–6999. doi:10.1016/j.actamat.2013.08.013

Chen, A. J., Wu, X. M., Sha, Z. D., Zhuge, L. J., & Meng, Y. D. (2006). Structure and photoluminescence properties of Fe-doped ZnO thin films. *Journal of Physics D: Applied Physics*, *39*(22), 4762–4765. doi:10.1088/0022-3727/39/22/004

Chen, J., Lei, W., Chai, W., Zhang, Z., Li, C., & Zhang, X. (2008). High field emission enhancement of ZnO-nanorods via hydrothermal synthesis. *Solid-State Electronics*, *52*, 294–298. doi:10.1016/j.sse.2007.09.010

Chen, J. T., Wang, J., Zhuo, R. F., Yan, D., Feng, J. J., Zhang, F., & Yan, P. X. (2009). The effect of Al doping on the morphology and optical property of ZnO nanostructures prepared by hydrothermal process. *Applied Surface Science*, *255*(7), 3959–3964. doi:10.1016/j.apsusc.2008.10.086

Chen, Z. C., Zhuge, L. J., Wu, X. M., & Meng, Y. D. (2007). Initial study on the structure and optical properties of Zn1−xFexO films. *Thin Solid Films*, *515*(13), 5462–5465. doi:10.1016/j.tsf.2007.01.015

Cheng, Y., An, L., Lan, J., Gao, F., Tan, R., Li, X., & Wang, G. (2013). Facile synthesis of pompon-like ZnO-Ag nanocomposites and their enhanced photocatalytic performance. *Materials Research Bulletin*, *48*(10), 4287–4293. doi:10.1016/j.materresbull.2013.06.051

Chiu, S. H., & Huang, J. C. A. (2012). Chemical bath deposition of ZnO and Ni doped ZnO nanorod. *Journal of Non-Crystalline Solids*, *358*(17), 2453–2457. doi:10.1016/j.jnoncrysol.2011.12.053

Collins, P. G., & Zettl, a. (1997). Unique characteristics of cold cathode carbon-nanotube-matrix field emitters. *Physical Review B*, *55*(15), 9391–9399. doi:10.1103/PhysRevB.55.9391

Damen, T. C., Porto, S. P. S., & Tell, B. (1966). Raman Effect in ZnO. *Physical Review*, *142*(2), 570–573.

Darroudi, M., Sabouri, Z., Kazemi, R., Khorsand, A., & Kargar, H. (2013). Sol – gel synthesis , characterization , and neurotoxicity effect of zinc oxide nanoparticles using gum tragacanth. *Ceramics International*, *39*, 9195–9199. doi:10.1016/j.ceramint.2013.05.021

De Moura, a. P., Lima, R. C., Moreira, M. L., Volanti, D. P., Espinosa, J. W. M., Orlandi, M. O., … Longo, E. (2010). ZnO architectures synthesized by a microwave-assisted hydrothermal method and their photoluminescence properties. *Solid State Ionics*, *181*(15-16), 775–780. doi:10.1016/j.ssi.2010.03.013

Dermenci, K. B., Genc, B., Ebin, B., Olmez-Hanci, T., & Gürmen, S. (2014). Photocatalytic studies of Ag/ZnO nanocomposite particles produced via ultrasonic spray pyrolysis method. *Journal of Alloys and Compounds*, *586*(3), 267–273. doi:10.1016/j.jallcom.2013.10.004

Deus, R. C., Foschini, C. R., Moura, F., Garcia, F. G., & Simo, A. Z. (2014). Photoluminescence emission at room temperature in zinc oxide. *Materials Research Bulletin*, *50*, 12–17.

Dinesha, M. L., Jayanna, H. S., Ashoka, S., & Chandrappa, G. T. (2009). Temperature dependent electrical conductivity of Fe doped ZnO nanoparticles prepared by solution combustion method. *Journal of Alloys and Compounds*, *485*, 538–541. doi:10.1016/j.jallcom.2009.06.022

Ding, J., Yan, X., & Xue, Q. (2012). Study on field emission and photoluminescence properties of ZnO/graphene hybrids grown on Si substrates. *Materials Chemistry and Physics*, *133*(1), 405–409. doi:10.1016/j.matchemphys.2012.01.051

Djurišić, A. B., Leung, Y. H., Tam, K. H., Hsu, Y. F., Ding, L., Ge, W. K., … Phillips, D. L. (2007). Defect emissions in ZnO nanostructures. *Nanotechnology*, *18*(9), 095702. doi:10.1088/0957-4484/18/9/095702

Djurišić, A. B., Ng, A. M. C., & Chen, X. Y. (2010). ZnO nanostructures for optoelectronics: Material properties and device applications. *Progress in Quantum Electronics*, *34*(4), 191–259. doi:10.1016/j.pquantelec.2010.04.001

Duan, L., Zhang, W., Yu, X., Wang, P., Jiang, Z., Luan, L., … Li, D. (2013). Stable p-type ZnO films dual-doped with silver and nitrogen. *Solid State Communications*, *157*, 45–48. doi:10.1016/j.ssc.2012.12.029

Ekthammathat, N., Thongtem, T., Phuruangrat, A., & Thongtem, S. (2013). Growth of hexagonal prism ZnO nanorods on Zn substrates by hydrothermal method and their photoluminescence. *Ceramics International*, *39*, S501–S505. doi:10.1016/j.ceramint.2012.10.122

Eskandari, M., Ahmadi, V., & Ahmadi, S. H. (2010). Growth of Al-doped ZnO nanorod arrays on the substrate at low temperature. *Physica E*, *42*(5), 1683–1686. doi:10.1016/j.physe.2010.01.024

Faisal, M., Ismail, A. A., Ibrahim, A. A., Bouzid, H., & Al-Sayari, S. A. (2013). Highly efficient photocatalyst based on Ce doped ZnO nanorods: Controllable synthesis and enhanced photocatalytic activity. *Chemical Engineering Journal*, *229*, 225–233. doi:10.1016/j.cej.2013.06.004

Fan, Z., & Lu, J. G. (2005). Zinc Oxide Nanostructures: Synthesis and Properties. *Journal of Nanoscience and Nanotechnology*, *5*(10), 1561–73. doi:10.1166/jnn.2005.182

Fang, C., Wu, J., Lee, L., & Hsien, Y. (2008). ZnO : Al nanostructures synthesized on pre-deposited aluminum (Al)/ Si template : Formation , photoluminescence and electron field emission. *Thin Solid Films*, *517*(3), 1262–1267. doi:10.1016/j.tsf.2008.06.037

Feng, Q., Tang, D., Jiang, E., Gu, S., & Han, S. (2013). Solution growth of vertical aligned ZnO nanorod arrays on ZnO seed layers fabricated by Langmuir–Blodgett method. *Journal of Alloys and Compounds*, *578*, 228–234. doi:10.1016/j.jallcom.2013.05.013

Fonoberov, V., & Balandin, A. (2004). Interface and confined optical phonons in wurtzite nanocrystals. *Physical Review B*, *70*(23), 233205. doi:10.1103/PhysRevB.70.233205

Fowler, R. H., & Nordheim, L. (1928). Electron Emission in Intense Electric Fields. *Proc. R. Soc. Lond. A*, *119*, 173–181. doi:10.1098/rspa.1928.0091

Fransen, M. ., van Rooy, T. ., & Kruit, P. (1999). Field emission energy distributions from individual multiwalled carbon nanotubes. *Applied Surface Science*, *146*, 312–327. doi:10.1016/S0169-4332(99)00056-2

Fu, D., Han, G., & Meng, C. (2012). Size-controlled synthesis and photocatalytic degradation properties of nano-sized ZnO nanorods. *Materials Letters*, *72*, 53–56. doi:10.1016/j.matlet.2011.12.047

Fu, L., & Fu, Z. (2015). Plectranthus amboinicus leaf extract – assisted biosynthesis of ZnO nanoparticles and their photocatalytic activity. *Ceramics International*, *41*, 2492–2496.

Gao, P., Ng, K., & Sun, D. D. (2013). Sulfonated graphene oxide–ZnO–Ag photocatalyst for fast photodegradation and disinfection under visible light. *Journal of Hazardous Materials*, *262*, 826–835.

Gao, S., Jia, X., Yang, S., Li, Z., & Jiang, K. (2011). Hierarchical Ag/ZnO micro/nanostructure: Green synthesis and enhanced photocatalytic performance. *Journal of Solid State Chemistry*, *184*(4), 764–769. doi:10.1016/j.jssc.2011.01.025

Gayen, R. N., Dalui, S., Rajaram, a., & Pal, a. K. (2009). Modulation of field emission properties of vertically aligned ZnO nanorods with aspect ratio and number density. *Applied Surface Science*, *255*(9), 4902–4906. doi:10.1016/j.apsusc.2008.12.033

Georgekutty, R., Seery, M. K., & Pillai, S. C. (2008). A Highly Efficient Ag-ZnO Photocatalyst: Synthesis, Properties, and Mechanism. *The Journal of Physical Chemistry C*, *112*(35), 13563–13570. doi:10.1021/jp802729a

Giri, P. K., Bhattacharyya, S., Chetia, B., Kumari, S., Singh, D. K., & Iyer, P. K. (2011). High-Yield Chemical Synthesis of Hexagonal ZnO Nanoparticles and Nanorods with Excellent Optical Properties. *Journal of Nanoscience and Nanotechnology*, *11*(xx), 1–6. doi:10.1166/jnn.2011.5113

Gokarna, A., Kim, J.-H., Leroy, F., Patriarche, G., Roussel, P., Bougrioua, Z., … Cho, Y.-H. (2013). Structural and photoluminescence studies of highly crystalline un-annealed ZnO nanorods arrays synthesized by hydrothermal technique. *Journal of Luminescence*, *144*, 234–240. doi:10.1016/j.jlumin.2013.07.031

Gondal, M. A., Drmosh, Q. A., Yamani, Z. H., & Saleh, T. A. (2009). Synthesis of ZnO2 nanoparticles by laser ablation in liquid and their annealing transformation into ZnO nanoparticles. *Applied Surface Science*, *256*(1), 298–304. doi:10.1016/j.apsusc.2009.08.019

Gu, C., Cheng, C., Huang, H., Wong, T., Wang, N., & Zhang, T.-Y. (2009). Growth and Photocatalytic Activity of Dendrite-like ZnO @ Ag Heterostructure Nanocrystal. *Crystal Growth & Design*, *9*(7), 3278–3285.

Guo, X., Ma, J., & Ge, H. (2013). Preparation, characterization, and photocatalytic performance of pear-shaped ZnO / Ag core – shell submicrospheres. *Journal of Physics and Chemistry of Solids*, *74*, 784–788.

Hadis, M., & Özgur, Ü. (2009). General Properties of ZnO. In *Zinc Oxide: Fundamentals, Materials and Device Technology*.

Hassan, M. M., Ahmed, A. S., Chaman, M., Khan, W., Naqvi, A. H., & Azam, A. (2012). Structural and frequency dependent dielectric properties of Fe 3 + doped ZnO nanoparticles. *Materials Research Bulletin*, *47*, 3952–3958.

Height, M. J., Pratsinis, S. E., Mekasuwandumrong, O., & Praserthdam, P. (2006). Ag-ZnO catalysts for UV-photodegradation of methylene blue. *Applied Catalysis B: Environmental*, *63*(3-4), 305–312. doi:10.1016/j.apcatb.2005.10.018

Hong, R. Y., Qian, J. Z., & Cao, J. X. (2006). Synthesis and characterization of PMMA grafted ZnO nanoparticles. *Powder Technology*, *163*(3), 160–168. doi:10.1016/j.powtec.2006.01.015

Hong, W.-K., Jo, G., Kwon, S.-S., Song, S., & Lee, T. (2008). Electrical Properties of Surface-Tailored ZnO Nanowire Field-Effect Transistors. *IEEE Transactions on Electron Devices*, *55*(11), 3020–3029. doi:10.1109/TED.2008.2005156

Hsiao, C.-H., Huang, C.-S., Young, S.-J., Guo, J.-J., Liu, C.-W., & Chang, S.-J. (2013). Optical and Structural Properties of Ga-Doped ZnO Nanorods. *Journal of Nanoscience and Nanotechnology*, *13*(12), 8320–8324. doi:10.1166/jnn.2013.7938

Hu, H., Yu, K., Zhu, J., & Zhu, Z. (2006). ZnO nanostructures with different morphologies and their field emission properties. *Applied Surface Science*, *252*(24), 8410–8413. doi:10.1016/j.apsusc.2005.11.060

Huang, J.-S., & Lin, C.-F. (2008). Influences of ZnO sol-gel thin film characteristics on ZnO nanowire arrays prepared at low temperature using all solution-based processing. *Journal of Applied Physics*, *103*(1), 014304. doi:10.1063/1.2828172

Huang, N., Zhu, M. W., Gao, L. J., Gong, J., Sun, C., & Jiang, X. (2011). A template-free sol–gel technique for controlled growth of ZnO nanorod arrays. *Applied Surface Science*, *257*(14), 6026–6033. doi:10.1016/j.apsusc.2011.01.112

Huang, S. H., Chen, Z., Shen, X. C., Zhu, Z. Q., & Yu, K. (2008). Raman scattering of single tetrapod-like ZnO nanostructure synthesized by catalyst-free rapid evaporation. *Solid State Communications*, *145*(7-8), 418–422. doi:10.1016/j.ssc.2007.11.014

Huang, Y., Yu, K., & Zhu, Z. (2007). Synthesis and field emission of patterned ZnO nanorods. *Current Applied Physics*, *7*, 702–706. doi:10.1016/j.cap.2007.03.009

Inamur, Q., Ahmad, M., Kumar, S., & Lohani, M. B. (2013). Hexagonal ZnO nanorods assembled flowers for photocatalytic dye degradation : Growth , structural and optical properties. *Superlattices and Microstructures*, *64*, 495–506.

Jamali, F., Joag, D. S., More, M. A., Singh, J., & Srivasatva, O. N. (2010). Low temperature growth of aligned ZnO nanowires and their application as field emission cathodes. *Materials Chemistry and Physics*, *120*(2-3), 691–696. doi:10.1016/j.matchemphys.2009.12.022

Janotti, A., & Walle, C. G. Van De. (2009). Fundamentals of zinc oxide as a semiconductor. *REPORTS ON PROGRESS IN PHYSICS*, *72*. doi:10.1088/0034-4885/72/12/126501

Ji, Z., Song, Y., Xiang, Y., Liu, K., Wang, C., & Ye, Z. (2004). Characterization of MgxZn1-xO thin films prepared by sol – gel dip coating. *Journal of Crystal Growth*, *265*, 537–540. doi:10.1016/j.jcrysgro.2004.02.083

Jia, G. Z., Wang, Y. F., & Yao, J. H. (2012). Fabrication and strain investigation of ZnO nanorods on Si composing sol – gel and chemical bath deposition method. *Journal of Physical and Chemistry of Solids*, *73*(3), 495–498. doi:10.1016/j.jpcs.2011.11.032

Jin, H., Li, Y., Li, J., & Gu, C. (2009). Field emission from ZnO nanostructures with different morphologies. *Microelectronic Engineering*, *86*(4-6), 1159–1161. doi:10.1016/j.mee.2009.02.005

Johnson, S., Markwitz, a., Rudolphi, M., Baumann, H., Oei, S. P., Teo, K. B. K., & Milne, W. I. (2006). Field emission properties of self-assembled silicon nanostructures formed by electron beam annealing. *Current Applied Physics*, *6*(3), 503–506. doi:10.1016/j.cap.2005.11.049

Jung, H. J., Lee, S., Choi, H. C., & Choi, M. Y. (2013). Various shaped-ZnO nanocrystals via low temperature synthetic methods: Surfactant and pH dependence. *Solid State Sciences*, *21*, 26–31. doi:10.1016/j.solidstatesciences.2013.04.004

Kai, H., Jianguo, L., Li, Z., Zhen, T., Jiangying, Y., Ping, L., & Feng, L. (2012). Effect of magnesium doping on the light-induced hydrophilicity of ZnO thin films. *Journal of Semiconductors*, *33*(5), 1–5. doi:10.1088/1674-4926/33/5/053003

Kao, P.-C., Chu, S.-Y., Li, B.-J., Chang, J.-W., Huang, H.-H., Fang, Y.-C., & Chang, R.-C. (2009). Low temperature solution-synthesis and photoluminescence properties of ZnO nanowires. *Journal of Alloys and Compounds*, *467*(1-2), 342–346. doi:10.1016/j.jallcom.2007.11.119

Karthikeyan, B., & Pandiyarajan, T. (2010). Simple room temperature synthesis and optical studies on Mg doped ZnO nanostructures. *Journal of Luminescence*, *130*(12), 2317–2321. doi:10.1016/j.jlumin.2010.07.011

Karunakaran, C., Rajeswari, V., & Gomathisankar, P. (2010). Antibacterial and photocatalytic activities of sonochemically prepared ZnO and Ag–ZnO. *Journal of Alloys and Compounds*, *508*(2), 587–591. doi:10.1016/j.jallcom.2010.08.128

Kenanakis, G., & Katsarakis, N. (2014). ZnO nanowires on glass via chemical routes: A prospective photocatalyst for indoors applications. *Journal of Environmental Chemical Engineering*, *2*, 1416–1422. doi:10.1016/j.jece.2014.06.016

Khalil, M. M. H., Ismail, E. H., & El-Magdoub, F. (2012). Biosynthesis of Au nanoparticles using olive leaf extract. *Arabian Journal of Chemistry*, *5*(4), 431–437. doi:10.1016/j.arabjc.2010.11.011

Khan, A., Jadwisienczak, W. M., Lozykowski, H. J., & Kordesch, M. E. (2007). Catalyst-free synthesis and luminescence of aligned ZnO nanorods. *Physica E: Low-Dimensional Systems and Nanostructures*, *39*(2), 258–261. doi:10.1016/j.physe.2007.05.025

Khusaimi, Z., Amizam, S., Mamat, M. H., Ahmad, M. K., Abdullah, N., & Rusop, M. (2010). Synthesis and Reactivity in Inorganic , Metal-Organic , and Nano-Metal Chemistry Controlled Growth of Zinc Oxide Nanorods by Aqueous-Solution Method Controlled Growth of Zinc Oxide Nanorods by Aqueous-Solution Method. *Synthesis and Reactivity in Inorganic, Metal-Organic, and Nano-Metal Chemistry*, *40*, 190–194. doi:10.1080/15533171003629147

Kim, D. Y., Kim, J. Y., Chang, H., Kim, M. S., Leem, J.-Y., Ballato, J., & Kim, S.-O. (2012). Low-temperature growth of multiple-stack high-density ZnO nanoflowers/nanorods on plastic substrates. *Nanotechnology*, *23*(48), 485606. doi:10.1088/0957-4484/23/48/485606

Kim, T. Y., Kim, J. Y., Kumar, M. S., Suh, E. K., & Nahm, K. S. (2004). Influence of ambient gases on the morphology and photoluminescence of ZnO nanostructures synthesized with nickel oxide catalyst. *Journal of Crystal Growth*, *270*(3-4), 491–497. doi:10.1016/j.jcrysgro.2004.07.009

Kim, Y. Y., Kang, S. W., Kong, B. H., & Ã, H. K. C. (2007). Epitaxial growth of high-temperature ZnO layers on sapphire substrate by magnetron sputtering. *Physica B*, *402*, 408–412. doi:10.1016/j.physb.2007.08.199

Kong, J., Fan, D., & Zhu, Y. (2012a). Synthesis and Raman spectra of hammer-shaped ZnO nanostructures via thermal evaporation growth. *Materials Science in Semiconductor Processing*, *15*(3), 258–263. doi:10.1016/j.mssp.2011.10.010

Kong, J., Fan, D., & Zhu, Y. (2012b). Synthesis and Raman spectra of hammer-shaped ZnO nanostructures via thermal evaporation growth. *Materials Science in Semiconductor Processing*, *15*(3), 258–263. doi:10.1016/j.mssp.2011.10.010

Kumar, K., Chitkara, M., Sandhu, I. S., Mehta, D., & Kumar, S. (2014). Photocatalytic, optical and magnetic properties of Fe-doped ZnO nanoparticles prepared by chemical route. *Journal of Alloys and Compounds*, *588*, 681–689. doi:10.1016/j.jallcom.2013.11.127

Kumar, P., Singh, J. P., Kumar, Y., Gaur, A., Malik, H. K., & Asokan, K. (2012). Investigation of phase segregation in Zn1−xMgxO systems. *Current Applied Physics*, *12*(4), 1166–1172. doi:10.1016/j.cap.2012.02.042

Kuo, S.-T., Tuan, W.-H., Shieh, J., & Wang, S.-F. (2007). Effect of Ag on the microstructure and electrical properties of ZnO. *Journal of the European Ceramic Society*, *27*(16), 4521–4527. doi:10.1016/j.jeurceramsoc.2007.02.215

Kwok, W. M., Djurišić, A. B., Leung, Y. H., Li, D., Tam, K. H., Phillips, D. L., & Chan, W. K. (2006). Influence of annealing on stimulated emission in ZnO nanorods. *Applied Physics Letters*, *89*(18), 183112. doi:10.1063/1.2378560

Lee, C. J., Lee, T. J., Lyu, S. C., Zhang, Y., Ruh, H., & Lee, H. J. (2002). Field emission from well-aligned zinc oxide nanowires grown at low temperature. *Applied Physics Letters*, *81*(2002), 3648–3650. doi:10.1063/1.1518810

Lee, J.-H., Chung, Y.-W., Hon, M.-H., & Leu, I.-C. (2009). Density-controlled growth and field emission property of aligned ZnO nanorod arrays. *Applied Physics A*, *97*(2), 403–408. doi:10.1007/s00339-009-5226-y

Lee, K. M., Park, K. H., Koh, K. H., & Lee, S. (2007). Synthesis of High Quality ZnO Nanorods by Low Temperature Wet Chemical Process. *IEEE*, 775–778.

Lee, W., Jeong, M.-C., Kim, M. J., & Myoung, J.-M. (2007). Field emission characteristics of ZnO nanoneedle array cell under ultraviolet irradiation. *Physics Letters A*, *370*(3-4), 345–350. doi:10.1016/j.physleta.2007.05.106

Li, C., Fang, G., Fu, Q., Su, F., Li, G., Wu, X., & Zhao, X. (2006). Effect of substrate temperature on the growth and photoluminescence properties of vertically aligned ZnO nanostructures. *Journal of Crystal Growth*, *292*(1), 19–25. doi:10.1016/j.jcrysgro.2006.03.061

Li, C., Fang, G., Yuan, L., Liu, N., Li, J., Li, D., & Zhao, X. (2007). Field electron emission improvement of ZnO nanorod arrays after Ar plasma treatment. *Applied Surface Science*, *253*(20), 8478–8482. doi:10.1016/j.apsusc.2007.04.040

Li, M.-K., Wang, D.-Z., Ding, Y.-W., Guo, X.-Y., Ding, S., & Jin, H. (2007). Morphology and field emission from ZnO nanowire arrays synthesized at different temperature. *Materials Science and Engineering: A*, *452-453*, 417–421. doi:10.1016/j.msea.2006.10.089

Li, Q., Bian, J., Sun, J., Wang, J., Luo, Y., Sun, K., & Yu, D. (2010). Controllable growth of well-aligned ZnO nanorod arrays by low-temperature wet chemical bath deposition method. *Applied Surface Science*, *256*(6), 1698–1702. doi:10.1016/j.apsusc.2009.09.097

Liao, L., Li, J. C., Wang, D. F., Liu, C., & Fu, Q. (2005). Electron field emission studies on ZnO nanowires. *Materials Letters*, *59*(19-20), 2465–2467. doi:10.1016/j.matlet.2005.03.014

Lin, J., Huang, B., & Lin, T. (2014). Hybrid structure of graphene sheets / ZnO nanorods for enhancing electron field emission properties. *Applied Surface Science*, *289*, 384–387.

Ling-min, Y., Xin-hui, F., Li-jun, Q., & Wen, Y. (2011). Field emission property of printed CNTs-mixed ZnO nanoneedles. *Applied Surface Science*, *257*(15), 6332–6335. doi:10.1016/j.apsusc.2011.01.069

Liu, J., Huang, X., Li, Y., Ji, X., Li, Z., He, X., & Sun, F. (2007). Vertically Aligned 1D ZnO Nanostructures on Bulk Alloy Substrates: Direct Solution Synthesis, Photoluminescence, and Field Emission. *Journal of Physical Chemistry C*, *111*(13), 4990–4997. doi:10.1021/jp067782o

Liu, J., Weng, W., Ding, W., Cheng, K., Du, P., Shen, G., & Han, G. (2005). Sol–gel derived (Li, Mg): ZnO films with high c-axis orientation and electrical resistivity. *Surface and Coatings Technology*, *198*(1-3), 274–277. doi:10.1016/j.surfcoat.2004.10.081

Liu, K., Yang, B., Yan, H., Fu, Z., Wen, M., Chen, Y., & Zuo, J. (2009). Effect of Ag doping on the photoluminescence properties of ZnO films. *Journal of Luminescence*, *129*(9), 969–972. doi:10.1016/j.jlumin.2009.04.021

Liu, R., Pan, A., Fan, H., Wang, F., Shen, Z., Yang, G., … Zou, B. (2007). Phonon-assisted stimulated emission in Mn-doped ZnO nanowires. *Journal of Physics: Condensed Matter*, *19*(13), 136206. doi:10.1088/0953-8984/19/13/136206

Liu, W. C., & Cai, W. (2008). One-dimensional and quasi-one-dimensional ZnO nanostructures prepared by spray-pyrolysis-assisted thermal evaporation. *Applied Surface Science*, *254*(10), 3162–3166. doi:10.1016/j.apsusc.2007.10.089

Liu, X. (2004). Growth mechanism and properties of ZnO nanorods synthesized by plasma-enhanced chemical vapor deposition. *Journal of Applied Physics*, *95*(6), 3141. doi:10.1063/1.1646440

Liu, Y., Li, C., Wang, J., Fan, X., Yuan, G., & Xu, S. (2015). Field emission properties of ZnO nanorod arrays by few seed layers assisted growth. *Applied Surface Science*, *331*, 497–503.

Liu, Y., Li, S., Lv, H., Ping, D., Li, S., Li, Z., & Tang, H. (2014). Self-assembly synthesis of ZnO with adjustable morphologies and their photocatalytic performance. *Ceramics International*, *40*(2), 2973–2978. doi:10.1016/j.ceramint.2013.10.011

Liu, Y., Zhang, H., An, X., Gao, C., Zhang, Z., Zhou, J., … Xie, E. (2010). Effect of Al doping on the visible photoluminescence of ZnO nanofibers. *Journal of Alloys and Compounds*, *506*(2), 772–776. doi:10.1016/j.jallcom.2010.07.067

Lopez, O. E., Tucker, A. L., Singh, K. R., Mamer, S. B., Sadoqi, M., & Xu, H. (2014). Synthesis of zinc oxide nanowires on seeded and unseeded gold substrates : Role of seed nucleation and precursor concentration. *Superlattices and Microstructures*, *75*, 358–370.

Lu, W., Gao, S., & Wang, J. (2008). One-Pot Synthesis of Ag/ZnO Self-Assembled 3D Hollow Microspheres with Enhanced Photocatalytic Performance. *The Journal of Physical Chemistry C*, *112*(43), 16792–16800. doi:10.1021/jp803654k

Lu, X., Liu, Z., Zhu, Y., & Jiang, L. (2011). Sonochemical synthesis and photocatalytic property of zinc oxide nanoparticles doped with magnesium(II). *Materials Research Bulletin*, *46*(10), 1638–1641. doi:10.1016/j.materresbull.2011.06.015

Mahmood, K., Park, S. Bin, & Sung, H. J. (2013). Enhanced photoluminescence, Raman spectra and field-emission behavior of indium-doped ZnO nanostructures. *Journal of Materials Chemistry C*, *1*(18), 3138. doi:10.1039/c3tc00082f

Maiti, U. N., Nandy, S., Karan, S., Mallik, B., & Chattopadhyay, K. K. (2008). Enhanced optical and field emission properties of CTAB-assisted hydrothermal grown ZnO nanorods. *Applied Surface Science*, *254*(22), 7266–7271. doi:10.1016/j.apsusc.2008.05.311

Mamat, M. H., Khusaimi, Z., Malek, M. F., Musa, M. Z., Rusop, M., Hashim, A. M., & Arora, V. K. (2011). Ultra-violet Sensing Characteristic and Field Emission Properties of Vertically Aligned Aluminum Doped Zinc Oxide Nanorod Arrays. *AIP*, *440*(2011), 440–445. doi:10.1063/1.3587035

Mamat, M. H., Khusaimi, Z., Musa, M. Z., Sahdan, M. Z., & Rusop, M. (2010). Novel synthesis of aligned Zinc oxide nanorods on a glass substrate by sonicated sol – gel immersion. *Materials Letters*, *64*(10), 1211–1214. doi:10.1016/j.matlet.2010.02.053

Minami, T., Miyata, T., & Yamamoto, T. (1998). Work function of transparent conducting multicomponent oxide thin films prepared by magnetron sputtering. *Surface and Coatings Technology*, *108-109*, 583–587. doi:10.1016/S0257-8972(98)00592-1

Mittal, A. K., Chisti, Y., & Banerjee, U. C. (2013). Synthesis of metallic nanoparticles using plant extracts. *Biotechnology Advances*, *31*(2), 346–56. doi:10.1016/j.biotechadv.2013.01.003

Mousavi, S. H., Haratizadeh, H., & Minaee, H. (2011). The effect of morphology and doping on photoluminescence of ZnO nanostructures. *Optics Cimmunications*, *284*(2), 3558–3561. doi:10.1016/j.optcom.2011.03.078

Navale, S. C., Sheini, F. J., Patil, S. S., Mulla, I. S., Joag, D. S., More, M. a., & Gosavi, S. W. (2009). Field Emission Properties of Al-Doped ZnO Nanostructures. *Journal of Nano Research*, *5*, 231–237. doi:10.4028/www.scientific.net/JNanoR.5.231

Ni, Y., Yang, S., Hong, J., & Zhen, P. (2008). Microwave-assisted preparation , characterization and properties of columnar hexagonal-shaped ZnO microcrystals. *Scripta Materialia*, *59*, 127–130. doi:10.1016/j.scriptamat.2008.02.044

Nor, R. M. (2011). Field electron emission properties of carbon nanotube films deposited by electrophoresis. *Materials Research Innovations*, *15*, 82–85. doi:10.1179/143307511X1303189074

Nunes, P., Fortunato, E., Tonello, P., Braz Fernandes, F., Vilarinho, P., & Martins, R. (2002). Effect of different dopant elements on the properties of ZnO thin films. *Vacuum*, *64*(3-4), 281–285. doi:10.1016/S0042-207X(01)00322-0

Ong, W. L., Lim, S. X., Sow, C. H., Zhang, C., & Ho, G. W. (2010). Synthesis and field emission properties of well-aligned ZnO nanowires on buffer layer. *Thin Solid Films*, *518*(24), e139–e142. doi:10.1016/j.tsf.2010.03.101

Palmqvist, A. E. C. (2003). Synthesis of ordered mesoporous materials using surfactant liquid crystals or micellar solutions. *Curr. Opin. Colloid Interface Sci.*, *8*, 145–155. doi:10.1016/S1359-0294

Pan, H., Luo, J., Sun, H., Feng, Y., Poh, C., & Lin, J. (2006). Hydrogen storage of ZnO and Mg doped ZnO nanowires. *Nanotechnology*, *17*(12), 2963–2967. doi:10.1088/0957-4484/17/12/023

Pan, H., Zhu, Y., Sun, H., Feng, Y., Sow, C.-H., & Lin, J. (2006). Electroluminescence and field emission of Mg-doped ZnO tetrapods. *Nanotechnology*, *17*(20), 5096–5100. doi:10.1088/0957-4484/17/20/009

Pan, N., Xue, H., Yu, M., & Cui, X. (2010). Tip-morphology-dependent field emission from ZnO nanorod arrays. *Nanotechnology*, *225707*. doi:10.1088/0957-4484/21/22/225707

Panda, S. K., & Jacob, C. (2009). ZnO nanostructures growth with silver catalyst-Effect of annealing. *Physica E: Low-Dimensional Systems and Nanostructures*, *41*(5), 792–796. doi:10.1016/j.physe.2008.12.020

Panin, G. N., Baranov, A. N., Khotina, I. A., & Kang, T. W. (2008). Luminescent Properties of ZnO / MgO Nanocrystal / Polymer Composite Structure. *Journal Of The Korean Physical Society*, *53*(5), 2943–2946.

Panthi, G., Park, M., Kim, H., Lee, S., & Park, S. (2015). Electrospun ZnO hybrid nanofibers for photodegradation of wastewater containing organic dyes : A review. *Journal of Industrial and Engineering Chemistry*, *21*, 26–35.

Park, K. C., Ma, D. Y., & Kim, K. H. (1997). The physical properties of Al-doped zinc oxide films prepared by RF magnetron sputtering. *Thin Solid Films*, *305*(1-2), 201–209. doi:10.1016/S0040-6090(97)00215-0

Parmon, V., Emeline, A. V, & Serpone, N. (2002). Glossary of terms in photocatalysis and radiocatalysis, A preliminary version of IUPAC's Project #2001-036-1. *Journal of Photochemistry and Photobiology A: Chemistry*, *4*. doi:10.1016/S1010-6030(01)00659-1

Patra, M. K., Manzoor, K., Manoth, M., Vadera, S. R., & Kumar, N. Ã. (2008). Studies of luminescence properties of ZnO and ZnO : Zn nanorods prepared by solution growth technique. *Journal of Luminescence*, *128*, 267–272. doi:10.1016/j.jlumin.2007.08.005

Philip, D. (2010). Green synthesis of gold and silver nanoparticles using Hibiscus rosa sinensis. *Physica E: Low-Dimensional Systems and Nanostructures*, *42*(5), 1417–1424. doi:10.1016/j.physe.2009.11.081

Piella, J., Bastús, N. G., Casals, E., & Puntes, V. (2013). Characterizing Nanoparticles Reactivity: Structure-Photocatalytic Activity Relationship. *Journal of Physics: Conference Series*, *429*, 012040. doi:10.1088/1742-6596/429/1/012040

Prabakar, K., & Kim, H. (2010). Growth control of ZnO nanorod density by sol – gel method. *Thin Solid Films*, *518*(24), e136–e138. doi:10.1016/j.tsf.2010.03.103

Prathna, T. C., Chandrasekaran, N., Raichur, A. M., & Mukherjee, A. (2011). Biomimetic synthesis of silver nanoparticles by Citrus limon (lemon) aqueous extract and theoretical prediction of particle size. *Colloids and Surfaces. B, Biointerfaces*, *82*(1), 152–9. doi:10.1016/j.colsurfb.2010.08.036

Pung, S.-Y., Lee, W.-P., & Aziz, A. (2012). Kinetic Study of Organic Dye Degradation Using ZnO Particles with Different Morphologies as a Photocatalyst. *International Journal of Inorganic Chemistry*, *2012*, 1–9. doi:10.1155/2012/608183

Pyne, S., Sahoo, G. P., Bhui, D. K., Bar, H., Sarkar, P., Samanta, S., … Misra, A. (2012). Enhanced photocatalytic activity of metal coated ZnO nanowires. *Spectrochimica Acta. Part A, Molecular and Biomolecular Spectroscopy*, *93*, 100–5. doi:10.1016/j.saa.2012.02.050

Qiu, J., Li, X., He, W., Park, S.-J., Kim, H.-K., Hwang, Y.-H., … Kim, Y.-D. (2009). The growth mechanism and optical properties of ultralong ZnO nanorod arrays with a high aspect ratio by a preheating hydrothermal method. *Nanotechnology*, *20*(15), 155603. doi:10.1088/0957-4484/20/15/155603

Rackauskas, S., Mustonen, K., Järvinen, T., Mattila, M., Klimova, O., Jiang, H., … Nasibulin, A. G. (2012). Synthesis of ZnO tetrapods for flexible and transparent UV sensors. *Nanotechnology*, *23*(9), 095502. doi:10.1088/0957-4484/23/9/095502

Rajabi, M., Dariani, R. S., & Zad, a. I. (2011). Comparative study of ZnO nanostructures grown on silicon (1 0 0) and oxidized porous silicon substrates with and without Au catalyst by chemical vapor transport and condensation. *Journal of Alloys and Compounds*, *509*(11), 4295–4299. doi:10.1016/j.jallcom.2011.01.041

Ramesh Yadav, A., Chauhan, A. S., Rekha, M. N., Rao, L. J. M., & Ramteke, R. S. (2004). Flavour quality of dehydrated lime [Citrus aurantifolia (Christm.) Swingle]. *Food Chemistry*, *85*(1), 59–62. doi:10.1016/j.foodchem.2003.06.002

Ramgir, N. S., Late, D. J., Bhise, A. B., Mulla, I. S., More, M. a, Joag, D. S., & Pillai, V. K. (2006). Field emission studies of novel ZnO nanostructures in high and low field regions. *Nanotechnology*, *17*(11), 2730–2735. doi:10.1088/0957-4484/17/11/003

Raoufi, D. (2013). Synthesis and microstructural properties of ZnO nanoparticles prepared by precipitation method. *Renewable Energy*, *50*, 932–937. doi:10.1016/j.renene.2012.08.076

Raveendran, P., Fu, J., & Wallen, S. L. (2003). Completely " Green " Synthesis and Stabilization of Metal Nanoparticles Completely " Green " Synthesis and Stabilization of Metal Nanoparticles. *J. Am. Chem. Soc.*, *125*, 13940–13941. doi:10.1021/ja029267j

Reddy, A. J., Kokila, M. K., Nagabhushana, H., Chakradhar, R. P. S., Shivakumara, C., Rao, J. L., & Nagabhushana, B. M. (2011). Structural, optical and EPR studies on ZnO:Cu nanopowders prepared via low temperature solution combustion synthesis. *Journal of Alloys and Compounds*, *509*(17), 5349–5355. doi:10.1016/j.jallcom.2011.02.043

Rekha, K., Nirmala, M., Nair, M. G., & Anukaliani, a. (2010). Structural, optical, photocatalytic and antibacterial activity of zinc oxide and manganese doped zinc oxide nanoparticles. *Physica B: Condensed Matter*, *405*(15), 3180–3185. doi:10.1016/j.physb.2010.04.042

Ren, C., Yang, B., Wu, M., Xu, J., Fu, Z., Iv, Y., … Zhu, C. (2010). Synthesis of Ag/ZnO nanorods array with enhanced photocatalytic performance. *Journal of Hazardous Materials*, *182*(1-3), 123–1299. doi:10.1016/j.jhazmat.2010.05.141

Ren, Z. F.Jo, S. H., Lao, J. Y., Farrer, R. a., Baldacchini, T., & Fourkas, J. T. (2003). Field-emission studies on thin films of zinc oxide nanowires. *Applied Physics Letters*, *83*(23), 4821. doi:10.1063/1.1631735

Rezapour, M., & Talebian, N. (2014). Synthesis and investigation of Indium doping and surfactant on the morphological, optical and UV/Vis photocatalytic properties of ZnO nanostructure. *Ceramics International*, *40*(2), 3453–3460. doi:10.1016/j.ceramint.2013.09.085

Ruan, H. B., Fang, L., Qin, G. P., Wu, F., Yang, T. Y., Li, W. J., & Kong, C. Y. (2012). Raman scattering and electrical properties of Zn1−xMnxO films. *Journal of Alloys and Compounds*, *531*, 77–81. doi:10.1016/j.jallcom.2012.03.116

Samat, N. A., & Nor, R. M. (2013). Sol – gel synthesis of zinc oxide nanoparticles using *Citrus aurantifolia* extracts. *Ceramics International*, *39*, S545–S548. doi:10.1016/j.ceramint.2012.10.132

Sangeetha, G., Rajeshwari, S., & Venckatesh, R. (2011). Green synthesis of zinc oxide nanoparticles by aloe barbadensis miller leaf extract : Structure and optical properties. *Materials Research Bulletin*, *46*(12), 2560–2566. doi:10.1016/j.materresbull.2011.07.046

Saravanan, R., Karthikeyan, N., Gupta, V. K., Thirumal, E., Thangadurai, P., Narayanan, V., & Stephen, A. (2013). ZnO/Ag nanocomposite: an efficient catalyst for degradation studies of textile effluents under visible light. *Materials Science & Engineering C*, *33*(4), 2235–44. doi:10.1016/j.msec.2013.01.046

Sengupta, J., Ahmed, A., & Labar, R. (2013). Structural and optical properties of post annealed Mg doped ZnO thin films deposited by the sol–gel method. *Materials Letters*, *109*, 265–268. doi:10.1016/j.matlet.2013.07.104

Sheini, F. J., Joag, D. S., & More, M. a. (2010). Electrochemical synthesis of Sn doped ZnO nanowires on zinc foil and their field emission studies. *Thin Solid Films*, *519*(1), 184–189. doi:10.1016/j.tsf.2010.07.106

Song, C., Lin, Y., Wang, D., & Hu, Z. (2010). Facile synthesis of Ag/ZnO microstructures with enhanced photocatalytic activity. *Materials Letters*, *64*(14), 1595–1597. doi:10.1016/j.matlet.2010.04.033

Song, Y., Yin, W., Fernandes, C., & Ruda, H. E. (2013). Fabrication of one-dimension ZnSe and ZnO nanostructures via anodic alumina template assisted vapor-liquid-solid growth process. *Thin Solid Films*, *548*, 130–137. doi:10.1016/j.tsf.2013.09.029

Srinivasan, G., Kumar, R. T. R., & Kumar, J. (2007). Influence of Al dopant on microstructure and optical properties of ZnO thin films prepared by sol – gel spin coating method. *Optical Materials*, *30*, 314–317. doi:10.1016/j.optmat.2006.11.075

Srivastava, A. K., Deepa, M., Bahadur, N., & Goyat, M. S. (2009). Influence of Fe doping on nanostructures and photoluminescence of sol – gel derived ZnO. *Materials Chemistry and Physics*, *114*, 194–198. doi:10.1016/j.matchemphys.2008.09.005

Steiner, T. (2004). *Semiconductor nanostructures for optoelectronic applications*.

Sugunan, A., Warad, H. C., Boman, M., & Dutta, J. (2006). Zinc oxide nanowires in chemical bath on seeded substrates: Role of hexamine. *Journal of Sol-Gel Science and Technology*, *39*(1), 49–56. doi:10.1007/s10971-006-6969-y

Sun, F., Tan, F., Wang, W., Qiao, X., & Qiu, X. (2012). Facile synthesis of Ag/ZnO heterostructure nanocrystals with enhanced photocatalytic performance. *Materials Research Bulletin*, *47*(11), 3357–3361. doi:10.1016/j.materresbull.2012.07.025

Sun, Q., Wang, Y., Yuan, X., Li, Y., Yang, J., & Jin, H. (2013). Comparative studies on the structural and luminescent properties of ZnO micro and nanostructures prepared by different hydrothermal growth. *Superlattices and Microstructures*, *64*(388), 535–542.

Sun, X. (2006). Designing efficient field emission into ZnO. *SPIE Newsroom*, 10–13. doi:10.1117/2.1200602.0101

Tam, K. H., Cheung, C. K., Leung, Y. H., Djurisić, a B., Ling, C. C., Beling, C. D., … Djuris, A. B. (2006). Defects in ZnO nanorods prepared by a hydrothermal method. *The Journal of Physical Chemistry. B, 110*(42), 20865–71. doi:10.1021/jp063239w

Tan, W. K., Abdul Razak, K., Lockman, Z., Kawamura, G., Muto, H., & Matsuda, A. (2014). Synthesis of ZnO nanorod–nanosheet composite via facile hydrothermal method and their photocatalytic activities under visible-light irradiation. *Journal of Solid State Chemistry*, *211*, 146–153. doi:10.1016/j.jssc.2013.12.026

Tian, C., Zhang, Q., Wu, A., Jiang, M., Liang, Z., Jiang, B., & Fu, H. (2012). Cost-effective large-scale synthesis of ZnO photocatalyst with excellent performance for dye photodegradation. *Chemical Communications*, *48*(23), 2858–60. doi:10.1039/c2cc16434e

Tian, X., Pan, Z., Zhang, H., Xie, Y., Zeng, X., Xiao, C., … Wei, Z. (2013). Preparation and characterization of vertically aligned ZnO microrods on glass substrate. *Materials Letters*, *97*, 71–73. doi:10.1016/j.matlet.2013.01.116

Uhm, Y. R., Sun Han, B., Rhee, C. K., & Choi, S. J. (2013). Photocatalytic Characterization of Fe- and Cu-Doped ZnO Nanorods Synthesized by Cohydrolysis. *Journal of Nanomaterials*, *2013*, 1–6. doi:10.1155/2013/958586

Uthirakumar, P., Karunagaran, B., Nagarajan, S., Suh, E.-K., & Hong, C.-H. (2007). Nanocrystalline ZnO particles: Low-temperature solution approach from a single molecular precursor. *Journal of Crystal Growth*, *304*(1), 150–157. doi:10.1016/j.jcrysgro.2007.01.035

Van Dijken, A., Meulenkamp, E. ., Vanmaekelbergh, D., & Meijerink, A. (2000). The luminescence of nanocrystalline ZnO particles: the mechanism of the ultraviolet and visible emission. *Journal of Luminescence*, *87-89*, 454–456. doi:10.1016/S0022-2313(99)00482-2

Vanheusden, K., Warren, W. L., Seager, C. H., Tallant, D. R., Voigt, J. a., & Gnade, B. E. (1996). Mechanisms behind green photoluminescence in ZnO phosphor powders. *Journal of Applied Physics*, *79*(10), 7983. doi:10.1063/1.362349

Vu, T. T., Río, L. del, Valdés-Solís, T., & Marbán, G. (2013). Stainless steel wire mesh-supported ZnO for the catalytic photodegradation of methylene blue under ultraviolet irradiation. *Journal of Hazardous Materials*, *246-247*, 126–34. doi:10.1016/j.jhazmat.2012.12.009

Wagner, R. S., & Ellis, W. C. (1965). The vapor-liquid-solid mechanism of crystal growth and its application to silicon. *Transactions of the Metallurgical Society of AIME*, *233*(June), 1053–1064.

Wang, B., Callahan, M. J., Xu, C., Bouthillette, L. O., Giles, N. C., & Bliss, D. F. (2007). Hydrothermal growth and characterization of indium-doped-conducting ZnO crystals. *Journal of Crystal Growth*, *304*, 73–79. doi:10.1016/j.jcrysgro.2007.01.047

Wang, C., Chen, Z., He, Y., Li, L., & Zhang, D. (2009). Structure, morphology and properties of Fe-doped ZnO films prepared by facing-target magnetron sputtering system. *Applied Surface Science*, *255*(15), 6881–6887. doi:10.1016/j.apsusc.2009.03.008

Wang, D., Wang, F., Tao, H., Han, X., Zhao, X., Zhang, T., … Qiu, W. (2013). Controllable synthesis of ZnO nanostructures with various morphologies. *Physics Procedia*, *48*, 235–240. doi:10.1016/j.phpro.2013.07.037

Wang, D., Zhang, J., Hu, Y., Li, G., Bi, Z., Zhang, X., … Hou, X. (2009). Fabrication and optical properties of spear-like ZnO nanostructures by chemical vapor deposition. *Materials Letters*, *63*(24-25), 2157–2159. doi:10.1016/j.matlet.2009.07.011

Wang, J.-L., Hsieh, T.-Y., Yang, P.-Y., Hwang, C.-C., Shye, D.-C., & Lee, I.-C. (2013). Oxygen annealing effect on field-emission characteristics of hydrothermally synthesized Al-doped ZnO nanowires. *Surface and Coatings Technology*, *231*, 423–427. doi:10.1016/j.surfcoat.2012.01.019

Wang, L., Hu, Q., Li, Z., Guo, J., & Li, Y. (2012). Microwave-assisted synthesis and photocatalytic performance of Ag-doped hierarchical ZnO architectures. *Materials Letters*, *79*, 277–280. doi:10.1016/j.matlet.2012.04.062

Wang, M., Kim, E. J., Hahn, S. H., Park, C., & Koo, K.-K. (2008). Controlled Crystal Growth and Crystallite Orientation in ZnO Films/Nanorods Prepared by Chemical Bath Deposition: Effect of Solvent. *Crystal Growth & Design*, *8*(2), 501–506. doi:10.1021/cg070467m

Wang, R. C., Liu, C. P., Huang, J. L., Chen, S.-J., Tseng, Y.-K., & Kung, S.-C. (2005). ZnO nanopencils: Efficient field emitters. *Applied Physics Letters*, *87*(1), 013110 (1–4). doi:10.1063/1.1977187

Wang, Z. L. (2004). Zinc oxide nanostructures: growth, properties and applications. *Journal of Physics: Condensed Matter*, *16*(25), R829–R858. doi:10.1088/0953-8984/16/25/R01

Weigand, C., Tveit, J., Ladam, C., Holmestad, R., Grepstad, J., & Weman, H. (2012). Epitaxial relationships of ZnO nanostructures grown by Au-assisted pulsed laser deposition on c- and a-plane sapphire. *Journal of Crystal Growth*, *355*(1), 52–58. doi:10.1016/j.jcrysgro.2012.06.038

Wen, F., Li, W., Moon, J., & Hyeok, J. (2005). Hydrothermal synthesis of ZnO : Zn with green emission at low temperature with reduction process. *Solid State Communications*, *135*, 34–37. doi:10.1016/j.ssc.2005.03.066

Whang, T.-J., Hsieh, M.-T., & Chen, H.-H. (2012). Visible-light photocatalytic degradation of methylene blue with laser-induced Ag/ZnO nanoparticles. *Applied Surface Science*, *258*(7), 2796–2801. doi:10.1016/j.apsusc.2011.10.134

Willander, M., Yang, L. L., Wadeasa, a., Ali, S. U., Asif, M. H., Zhao, Q. X., & Nur, O. (2009). Zinc oxide nanowires: controlled low temperature growth and some electrochemical and optical nano-devices. *Journal of Materials Chemistry*, *19*(7), 1006. doi:10.1039/b816619f

Wu, J.-J., & Liu, S.-C. (2002). Low-Temperature Growth of Well-Aligned ZnO Nanorods by Chemical Vapor Deposition. *Advanced Materials*, *14*(3), 215–218. doi:10.1002/1521-4095(20020205)14:3<215::AID-ADMA215>3.0.CO;2-J

Xiao, J., Zhang, G., Bai, X., Yu, L., Zhao, X., & Guo, D. (2008). Field emission from zinc oxide nanostructures and its degradation. *Vacuum*, *83*(2), 265–272. doi:10.1016/j.vacuum.2008.07.005

Xie, J., & Wu, Q. (2010). One-pot synthesis of ZnO/Ag nanospheres with enhanced photocatalytic activity. *Materials Letters*, *64*(3), 389–392. doi:10.1016/j.matlet.2009.11.026

Xie, W., Li, Y., Sun, W., Huang, J., Xie, H., & Zhao, X. (2010). Surface modification of ZnO with Ag improves its photocatalytic efficiency and photostability. *Journal of Photochemistry and Photobiology A: Chemistry*, *216*(2-3), 149–155. doi:10.1016/j.jphotochem.2010.06.032

Xu, C., Xu, G., Liu, Y., & Wang, G. (2002). A simple and novel route for the preparation of ZnO nanorods. *Solid State Communications*, *122*, 175–179.

Xu, J., Chang, Y., Zhang, Y., Ma, S., Qu, Y., & Xu, C. (2008). Effect of silver ions on the structure of ZnO and photocatalytic performance of Ag/ZnO composites. *Applied Surface Science*, *255*(5), 1996–1999. doi:10.1016/j.apsusc.2008.06.130

Xu, L., & Li, X. (2010). Influence of Fe-doping on the structural and optical properties of ZnO thin films prepared by sol – gel method. *Journal of Crystal Growth*, *312*, 851–855. doi:10.1016/j.jcrysgro.2009.12.062

Xu, S., & Wang, Z. L. (2011). One-Dimensional ZnO Nanostructures : Solution Growth and Functional Properties. *Nano Res*, *3*(9), 676–684. doi:10.1007/s12274-011-0160-7

Yang, J., Lang, J., Li, C., Yang, L., Han, Q., Zhang, Y., … Liu, X. (2008). Effects of substrate on morphologies and photoluminescence properties of ZnO nanorods. *Applied Surface Science*, *255*(5), 2500–2503. doi:10.1016/j.apsusc.2008.07.124

Yang, Z., Zhang, P., Ding, Y., Jiang, Y., Long, Z., & Dai, W. (2011). Facile synthesis of Ag/ZnO heterostructures assisted by UV irradiation: Highly photocatalytic property and enhanced photostability. *Materials Research Bulletin*, *46*(10), 1625–1631. doi:10.1016/j.materresbull.2011.06.016

Ye, N., & Chen, C. C. (2012). Investigation of ZnO nanorods synthesized by a solvothermal method , using Al-doped ZnO seed films. *Optical Materials*, *34*(4), 753–756. doi:10.1016/j.optmat.2011.10.013

Yilmazoglu, O., Biethan, J.-P., Evtukh, a., Semenenko, M., Pavlidis, D., Hartnagel, H. L., & Litovchenko, V. (2012). Field emission from ZnO whiskers under intervalley electron redistribution. *Applied Surface Science*, *258*(11), 4990–4993. doi:10.1016/j.apsusc.2012.01.153

Yin, M., Liu, M., & Liu, S. (2014). Diameter regulated ZnO nanorod synthesis and its application in gas sensor optimization. *Journal of Alloys and Compounds*, *586*(3), 436–440. doi:10.1016/j.jallcom.2013.10.081

Yin, X., Que, W., Fei, D., Shen, F., & Guo, Q. (2012). Ag nanoparticle/ZnO nanorods nanocomposites derived by a seed-mediated method and their photocatalytic properties. *Journal of Alloys and Compounds*, *524*, 13–21. doi:10.1016/j.jallcom.2012.02.052

Yin, Y. T., Que, W. X., & Kam, C. H. (2009). ZnO nanorods on ZnO seed layer derived by sol–gel process. *Journal of Sol-Gel Science and Technology*, *53*(3), 605–612. doi:10.1007/s10971-009-2138-4

Yogamalar, N. R., & Bose, A. C. (2013). Synthesis, Dopant Study and Device Fabrication of Zinc Oxide Nanostructures: Mini Review. *Progress in Nanotechnology and Nanomaterials*, *2*(1), 1–20. Retrieved from http://www.academicpub.org/pnn/paperInfo.aspx?paperid=2678

Yousefi, R., Sheini, F. J., Muhamad, M. R., & More, M. A. (2010). Characterization and field emission properties of ZnMgO nanowires fabricated by thermal evaporation process. *Solid State Sciences*, *12*(7), 1088–1093. doi:10.1016/j.solidstatesciences.2010.04.019

Yu, K., Li, L., Wang, Y., & Zhu, Z. (2010). Photoluminescence and field emission properties of Sn-doped ZnO microrods. *Applied Surface Science*, *256*(11), 3361–3364. doi:10.1016/j.apsusc.2009.12.034

Yu, K., Zhang, Y., Xu, R., Ouyang, S., Li, D., & Luo, L. (2005). Efficient field emission from tetrapod-like zinc oxide nanoneedles. *Materials Letters*, *59*, 1866–1870. doi:10.1016/j.matlet.2005.02.001

Yun, S., Lee, J., Yang, J., & Lim, S. (2010). Hydrothermal synthesis of Al-doped ZnO nanorod arrays on Si substrate. *Physica B*, *405*(1), 413–419. doi:10.1016/j.physb.2009.08.297

Zeng, J.-L., Zhang, X.-W., Yie Tan, J. Z., Bian, J.-C., Li, Z., Chen, Z.-D., … Yang, F. (2013). Full-color photoluminescence of ZnO nanorod arrays based on annealing processes. *Journal of Luminescence*, *135*, 201–205. doi:10.1016/j.jlumin.2012.10.016

Zhang, D., Liu, X., & Wang, X. (2011). Growth and photocatalytic activity of ZnO nanosheets stabilized by Ag nanoparticles. *Journal of Alloys and Compounds*, *509*(15), 4972–4977. doi:10.1016/j.jallcom.2011.01.145

Zhang, G., Wei, L., Chen, Y., Mei, L., & Jiao, J. (2013). Field emission property of ZnO nanoneedle arrays with differentmorphology. *Materials Letters*, *96*, 131–134. doi:10.1016/j.matlet.2013.01.028

Zhang, R., Yin, P., Wang, N., & Guo, L. (2009). Photoluminescence and Raman scattering of ZnO nanorods. *Solid State Sciences*, *11*(4), 865–869. doi:10.1016/j.solidstatesciences.2008.10.016

Zhang, Y., Du, G., Liu, D., Zhu, H., Cui, Y., Dong, X., & Yang, S. (2004). Structural and optical properties of MgxZn1−xO thin films grown by metal-organic chemical vapor deposition. *Journal of Crystal Growth*, *268*(1-2), 140–143. doi:10.1016/j.jcrysgro.2004.04.110

Zhang, Y., Ram, M. K., Stefanakos, E. K., & Goswami, D. Y. (2012). Synthesis , Characterization , and Applications of ZnO Nanowires. *Journal of Nanomaterials, 2012*. doi:10.1155/2012/624520

Zhang, Z., Huang, J., He, H., Lin, S., Tang, H., Lu, H., & Ye, Z. (2009). Solid-State Electronics The influence of morphologies and doping of nanostructured ZnO on the field emission behaviors. *Solid State Electronics*, *53*(6), 578–583. doi:10.1016/j.sse.2009.03.024

Zhao, M., Wang, X., Ning, L., He, H., Jia, J., Zhang, L., & Li, X. (2010). Synthesis and optical properties of Mg-doped ZnO nanofibers prepared by electrospinning. *Journal of Alloys and Compounds*, *507*(1), 97–100. doi:10.1016/j.jallcom.2010.07.093

Zhao, X., Li, M., & Lou, X. (2014). Sol – gel assisted hydrothermal synthesis of ZnO microstructures : Morphology control and photocatalytic activity. *Advanced Powder Technology*, *25*, 372–378.

Zhou, H., Yi, D., Yu, Z., Xiao, L., & Li, J. (2007). Preparation of aluminum doped zinc oxide films and the study of their microstructure , electrical and optical properties. *Thin Solid Films*, *515*, 6909–6914. doi:10.1016/j.tsf.2007.01.041

Zi-qiang, X., Ã, D. H., Yan, L., & Hang, C. (2006). Al-doping effects on structure , electrical and optical properties of c-axis-orientated ZnO : Al thin films. *Materials Science in Semiconductor Processing*, *9*, 132–135. doi:10.1016/j.mssp.2006.01.082

Znaidi, L., Soler Illia, G. J. a. a., Benyahia, S., Sanchez, C., & Kanaev, a. V. (2003). Oriented ZnO thin films synthesis by sol–gel process for laser application. *Thin Solid Films*, *428*(1-2), 257–262. doi:10.1016/S0040-6090(02)01219-1

LIST OF PUBLICATIONS

1. H.A. Rafaie, N.A. Samat, R. Md. Nor, “Effect of pH on the growth of zinc oxide nanorods using *Citrus aurantifolia* extracts”, Materials Letters 137 (2014) 297–299
2. Hartini Ahmad Rafaie, Roslan Md. Nor and Yusoff Mohd Amin, “Magnesium doped ZnO nanostructures synthesis using *Citrus aurantifolia*extracts: Structural and field electron emission properties”, Mater. Express, Vol. 5, No. 3, 2015
3. Hartini Ahmad Rafaie, Roslan Md. Nor and Yusoff Mohd Amin, “Effect of growth time to the structural and field emission properties of ZnO nanorods by sol-gel method”, Advanced Materials Research Vol. 1109 (2015) pp 15-19
4. H.A. Rafaie, R.Md. Nor, N.A. Samat, Synthesis And Characterization Of Zinc Oxide Nanostructures Using *Citrus aurantifolia* Extracts, Advanced Materials Research Vol. 1109 (2015) pp 20-24
5. H.A. Rafaie, R.Md. Norand Y.M. Amin, Structural and Field Electron Emission Properties of Pure and Al-Doped ZnO Nanorods Prepared by Sol-gel Method, Advanced Material Research, Vol. 1133 (2015) pp 515-519
6. M. Batumalay, Z. Harith, H.A. Rafaie, F. Ahmad, M. Khasanah, S.W. Harun, R.M. Nor, H. Ahmad, “Tapered plastic optical fiber coated with ZnO nanostructures for the measurement of uric acid concentrations and changes in relative humidity”, Sensors and Actuators A 210 (2014) 190–196
7. Hazli Rafis, N. Irawati, H.A.Rafaie, H.Ahmad, S.W.Harun. R.M.Nor, Detection of different concentration of uric acid using tapered silica optical sensor coated with zinc oxide (ZnO), Jurnal Teknologi, 74:8 (2015) 55-58
8. A.Lokman, S.W. Harun, Z.Harith, H.A. Rafaie, R.M.Mor, H. Arof, Inline Mach-Zehnder interferometer with ZnO nanowires coating for the measurement of uric acid concentrations, Sensors and Actuators A 234 (2015) 206-2011

9. Z. Harith, N.Irawati, H.A. Rafaie, M. Batumalay, S.W.Harun, R. M. Nor, H. Ahmad, Tapered plastic optical fiber coated with Al-doped ZnO nanostructures for detecting relative humidity, Accepted in IEEE Sensors Journal